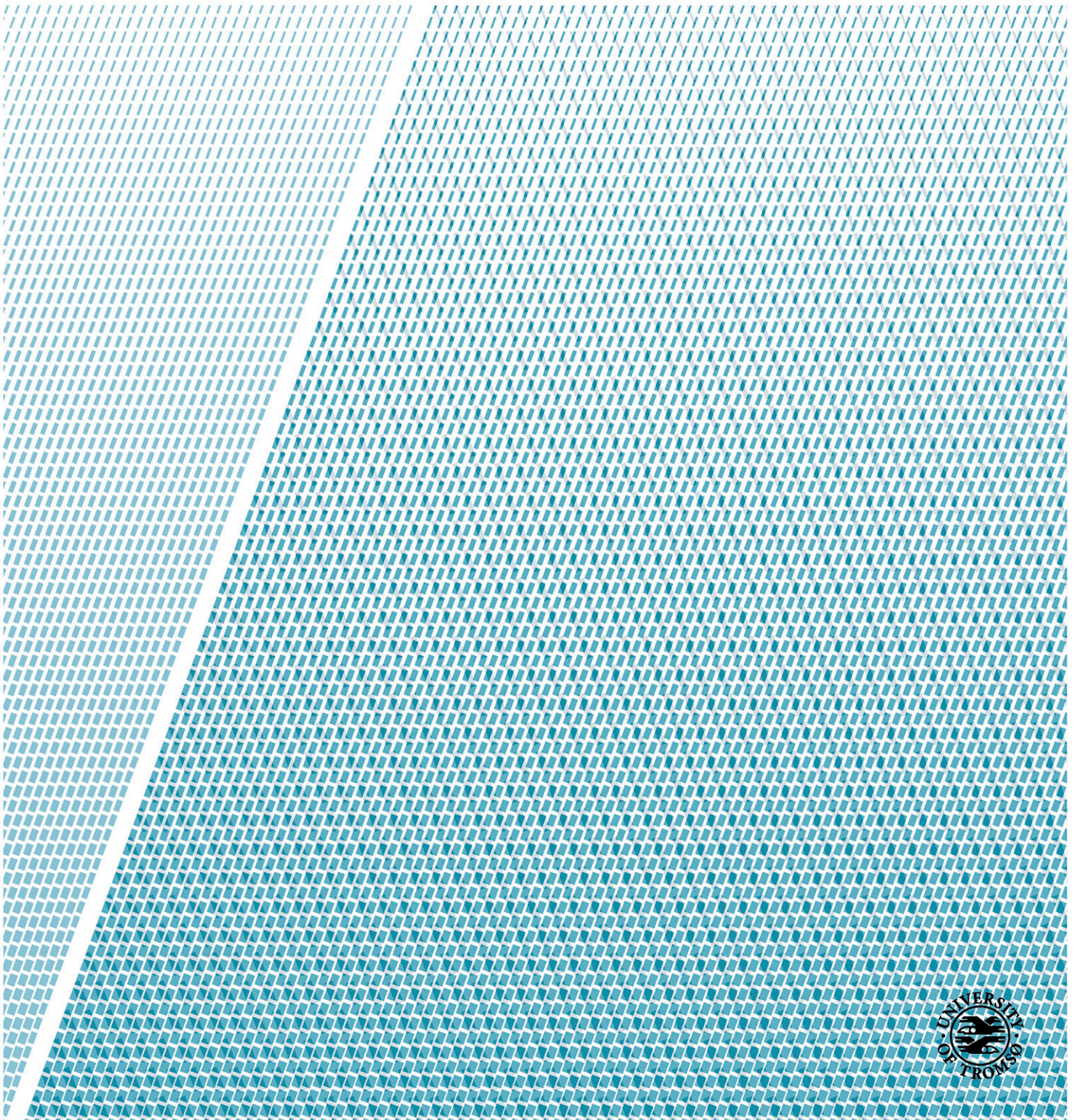# Sedimentary processes and paleoenvironments in Moskusoksefjord and Nordfjord, North-East Greenland

Ingrid Leirvik Olsen
GEO-3900 Master´s thesis in Geology
May 2015

Abstract

Multi-proxy analyses of five sediment cores (including lithostratigraphy, physical properties and XRF-scanning) and analyses of swath bathymetry and high resolution seismic data were integrated in order to reconstruct the Holocene glacial history and paleoenvironment of Moskusoksefjord and inner parts of Nordfjord, North-East Greenland.

In Moskusoksefjord, the large-scale bathymetry is divided into an inner-, middle- and outer basins, separated by relatively large deltas prograding into the fjord from both sides. Several slide scars and sediment lobes are also found, in addition to numerous channels. No glacial landforms have been observed in the study area apart from two transverse ridges in the outer basin of Moskusoksefjord which may represent buried glacial moraines. The seismostratigraphy revealed two main units with a stratified acoustic signature as well as MTDs of various dimensions. From their distribution, mass-transport activity in Moskusoksefjord and Nordfjord probably occurred episodically throughout the entire Holocene.

Suspension settling, as well as mass-transport deposits and ice-rafting from icebergs and sea-ice are the main sedimentary processes of both fjords. The two main sources of sediment were theWaltershausen Gletscher and the river coming from Badlandal at the fjord head of Moskusoksefjord. The estimated average sedimentation rates are 58 cm/ka for the last ~8 ka and 85-446 cm/ka for the last 1 ka. Ice-rafting was of higher relative importance with increasing influence away from the glacier margin. However, rafting of material from icebergs and sea ice has proven to be of less importance in the two studied fjords than in other East-Greenland fjords (cf. Smith and Andrews, 2000).

After retreating onto land during the warm Holocene Climate Optimum, Waltershausen Gletscher probably advanced into tidewater after a climate cooling ~6500 cal. yr. BP. An increase in the glacial activity continued through the Neoglaciation, with shorefast sea-ice suppressing iceberg rafting and an increase in the amount of laminations characterizing the time period. No clear glacial advance and little IRD are observed related to the Little Ice Age. In addition to the late cooling signal in the sediment cores, it is interpreted to indicate a late onset and a restricted advance of the Little Ice Age ice front in Moskusoksefjord and Nordfjord.

Forord

Først vil jeg rette en stor takk til mine to veiledere Jan Sverre Laberg og Matthias Forwick. Takk for all hjelp, inspirasjon og kunnskap. Takk for at dere er inkluderende og lar meg delta på tokt til nye og spennende områder. Det har vært et eventyr.

Masteroppgaven ble gjort mulig med finansiell støtte fra Det norske oljeselskap ASA. Innsamling av materiale ble utført av mannskapet på R/V Helmer Hanssen i august 2013 i samarbeid med TUNU-programmet ved Universitetet i Tromsø – Norges arktiske universitet. Radiokarbondateringer ble utført av Lukas Wacker fra Laboratory of Ion Beam Physics ved ETH Zürich, Sveits, mens ^{210}Pb og ^{137}Cs målinger ble foretatt av Witold Szczuciński fra Adam Mickiewicz University i Poznan, Poland. En ekstra takk til Witold som lot meg delta på en uforglemmelig tokt til Hornsund, Spitsbergen høsten 2014.

Ingvild Hald, Trine Dahl og Karina Monsen var veldig hjelpsomme i min periode på laben. De hjalp også til med å plukke foraminiferer til datering.

Jeg vil gjerne takke alle de fine folkene jeg har blitt kjent med gjennom mine 8 år som student ved UiT og UNIS. En spesiell takk sendes til Ida og Karoline som har gitt meg fem år med minneverdige turer, lange kaffepauser og lattermilde øyeblikk.

Til mine foreldre, besteforeldre og bror. Tusen takk for all oppmuntring, gode råd og finansiell støtte gjennom alle årene som student. Uten dere hadde det ikke vært mulig.
En takk sendes også til min «svigerfamilie» som tar imot meg når jeg trenger en avbrekk fra studiet.

Til slutt vil jeg rette en stor og takknemlig takk til min kjære Hans-Kristian. Takk for din tålmodighet og kjærlighet i både medgang og motgang. Du gjorde lange dager lettere.

Tusen hjertelig takk!

Ingrid Leirvik Olsen

Tromsø, 15. mai 2015

Contents

1. Introduction

1.1.   Objectives

This master thesis was carried out at University of Tromsø, The Arctic University of Norway from January 2014 to May 2015. In the project five sediment cores, swath bathymetry data and chirp sonar profiles from the two fjords Nordfjord and Moskusoksefjord, tributaries of the Kejser Franz Joseph Fjord, East Greenland (Fig. 1.1 and 1.2), were analyzed in order to:

- Establish seismo-and lithostratigraphies for the study area
- Describe and interpret the assemblage of sedimentary processes and products in order to reconstruct the glacial history and sedimentary paleoenvironment during the Holocene
- Link the study`s conclusions into the bigger picture of the geoscientific research of East Greenland fjords

1.2.   Background

The areas investigated in this study are Nordfjord and Moskusoksefjord, the two northern arms of Kejser Franz Joseph Fjord, on East Greenland (Fig. 1.2). Fjords act as efficient sediment traps and are relatively sensitive to environmental changes, making them excellent for high-resolution paleoclimatic and paleoenvironmental studies on a decadal to centennial timescale. The seafloor and shallow sub-seafloor in formerly glaciated Greenland fjords often contain well-preserved submarine glacial landforms and glacimarine sediments, revealing information on the characteristics and dynamics of outlet glaciers draining the Greenland Ice Sheet, the glaciation history and deglaciation of the study area as well as the following Holocene climatic and oceanographic changes (Evans et al., 2002; Jennings et al., 2002; Evans et al., 2009; Alley et al., 2010).

Information about East Greenland glaciation history is poorly constrained (Evans et al., 2002) due to the presence of all-year sea ice in East Greenland fjords. A warming climate and fluctuations in sea ice from the Arctic Ocean allows scientists to now study areas previously unattainable, providing valuable information about the Late Quaternary glacial-interglacial periods. By studying the paleoenvironment and sedimentary processes in East Greenland

fjords we are able to get a better understanding of natural climate changes. And as a consequence, get a better understanding of the ongoing processes of today.
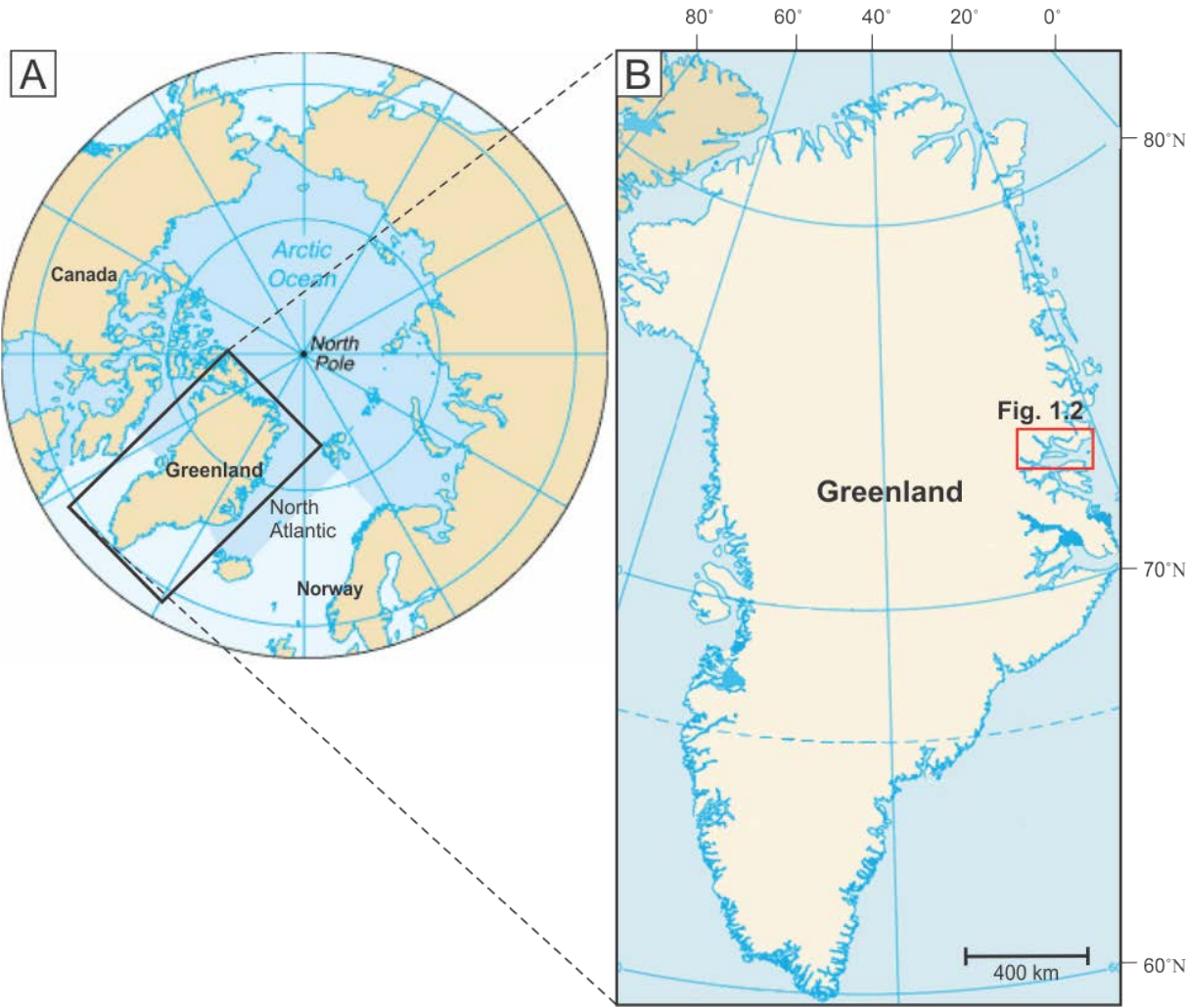
Figure 1.1: *A*: Overview map of the Arctic region. *B*: Greenland. The red box shows the study area detailed in Fig. 1.2.

Figure 1.2: Topographic map of Kejser Franz Joseph Fjord including the glaciers in the catchment area. Red box shows the study area.

1.2.1. Glacial history of North-East Greenland

The reconstruction of North-East Greenland glacial history have been addressed by several authors, but compared to studies on e.g. Svalbard, information about the glaciation history remains limited. Funder et al. (2011) presented a review of the work done on the Greenland Ice Sheet (GIS) up to 2011, and it becomes clear that only a few marine studies addressing the Late Weichselian deglaciation history and the Holocene paleoenvironment of the North-East Greenland fjords have been published. As a result, the maximum position of the GIS during the Last Glacial Maximum (LGM; ca 24-19 ka BP), the timing of the deglaciation, and the glacial dynamics of the GIS remains conceptual (Fig. 1.3), leaving the glacial history of the easterly fjords on Greenland poorly constrained. The GIS has waxed and waned in relation to glacial and interglacial periods, and have since the LGM lost about 40% of its area (Funder et al., 2004). The timing and extent of the Late Weichselian GIS have been debated based on a combination of both onshore and offshore studies (Hansen et al., 1999; Bennike & Björck, 2002; Evans et al., 2002; Ó Cofaigh et al., 2004; Wilken & Mienert, 2006; Evans et al., 2009). The maximum extent of the GIS during the Late Weichselian varies along North-East Greenland, reaching fjord mouth in some areas, and extending to the shelf break in others (Hubberten et al., 1995; Evans et al., 2002, Ó Cofaigh et al., 2004; Evans et al., 2009).

According to Evans et al. (2002) the GIS from Kejser Franz Joseph Fjord reached mid-shelf, as a minimum, during LGM, while Ó Cofaigh et al. (2004) believe the ice extended all the way to the shelf break. Low weathering limits on coastal mountains due to a thin ice sheet (Landvik, 1994) can either be interpreted as evidence for a mid-shelf position, or a low-gradient ice stream extending to the shelf break (Funder et al., 2011). OSL-dating done by Hansen et al. (1999) imply that the GIS was close to its LGM extent at ca. 60 ka BP, and stayed close to its maximum limit until its final collapse ca. 50 000 years later. The major fjord systems and cross-shelf troughs off Greenland worked as channels for fast-flowing, warm-based ice streams draining the interior basins of the ice sheet, separated by banks with grounded, less-dynamic ice (Funder et al., 2011). Also, Evans et al. (2002) interpreted the glacial ice flowing through Kejser Franz Joseph Fjord to be active, but grounded. Break-up and retreat of the GIS commenced at ca. 19 ka BP (Evans et al., 2002), and is said to have happened in two stages; initial retreat by calving and breakup of grounded ice due to a rise in sea-level (Bennike & Björk, 2002), and a second phase of slower retreat, notably driven by melting (Alley et al., 2010). Minimum dates for the last deglaciation of Geographical Society

Ø, located at the fjord mouth of Kejser Franz Joseph Fjord (Fig. 1.2), and inner Nordfjord have been estimated to be 10.2 ka BP and 9.5 ka BP, respectively (Bennike & Weidick, 2001).

Although Greenland ice cores show signals of Younger Dryas (YD 12.8-11.7 ka BP) cooling and subsequent warming, there is no evidence of glacial response on Greenland (Alley et al., 2010; Funder et al., 2011). Marienfeld (1992) reasoned no glacier advance during YD with the climate being too cold and dry, while Alley et al. (2010) suggested no evidence due to much of the ice-sheet margin being marine. However, the Preboreal Oscillation (PBO 11.5-11.4 ka BP) cooling is marked by a small glacial advance (Funder et al., 1998). Similar to the YD, no glacial response of the 8.2 ka event have been recorded in East Greenland. After 8 ka BP the ice margin retreated through the fjord system behind the present day ice limit, with local ice caps remaining on mountain plateaus (Bennike, 2008; Alley et al., 2010). North of Kejser Franz Joseph Fjord, at Hvalrosodden, the GIS is believed to have retreated up to 80 km (Simpson et al., 2009). After 4.5 ka BP, the ice grew again until its maximum position during the Little Ice Age (LIA 1300-1850 AD) (Jakobsen et al., 2008; Funder et al., 2011).

1.2.2. Holocene paleoclimate of East Greenland

The Holocene epoch began 11.7 ka BP and continues to present, marking the end of the YD and the Pleistocene epoch (2.58 Ma- 11.7 ka BP). Climate improved in the North Atlantic during the early Holocene with dry summers and higher summer temperatures than present, supported by high summer insolation (Wagner et al., 2000). Records based on pollen, molluscs and diatoms indicate the Holocene Climate Optimum to have lasted from 9 ka to 4-5 ka BP (Bennike & Weidick, 2001; Wagner et al., 2010), resulting in a retreat of the ice sheet from the coastline all over Greenland (Weidick, 1993). A short-lived cold interval ~8.3-8.2 ka BP, called the "8.2-event", has been described as a rapid cooling of $6 \pm 2°C$ at the GIS summit (Alley et al., 1997). The event can be linked to a decrease in methane concentrations, surface-water salinity and the North Atlantic thermohaline circulation with a consequent increase in sea ice (Alley et al., 1997; Alley, 2007), and is believed to be a result of the final collapse of the Laurentide Ice Sheet (Alley et al., 1997).

A regional climatic cooling leading to increased precipitation and a decline in temperature commenced 6.5 ka BP, documented by pollen assemblages found in lake sediments in the area of Kejser Franz Joseph Fjord (Wagner et al., 2000). The cold period referred to as the

Neoglaciation began before 4.5 ka BP and can be seen from evidence of glacier expansion all over Greenland (Bennike & Weidick, 2001). A weak Medieval Warm Period from 1 ka to 0.8 ka BP have by Johnsen et al. (1992) and Wagner et al. (2000) been interpreted from palynological evidence and $\delta^{18}O$ values. The climate continued to cool, reaching a culmination at the Little Ice Age (~800-100 years BP) (Levy et al., 2014). The Little Ice Age is well documented, e.g. by low values of biogeochemical parameters from lake sediments (Wagner et al., 2000), glacier expansion and changes in $\delta^{18}O$ values (Benn & Evans, 2010). After the Little Ice Age temperatures on Greenland increased and reached a maximum in the 1930s, cooled, and have increased again since the 1980s. A warming of 1.1˚C was observed at the ice sheet summit from 1991-2000 (Box, 2002).
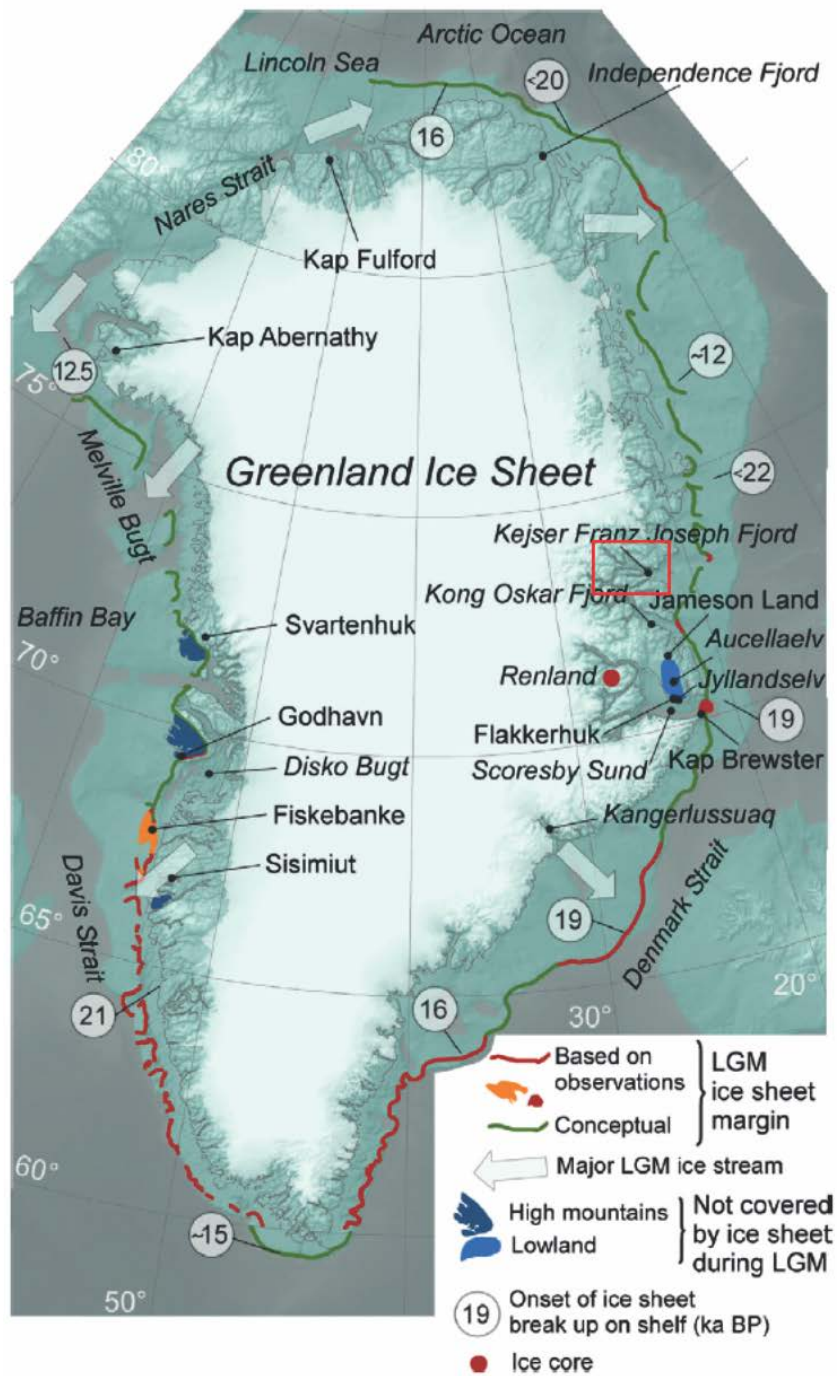
Figure 1.3: Reconstruction of the LGM Ice Sheet margin, ice flow, ice-free areas, dates for break-up of shelf-bound ice and localities. Red box show study area. (Modified from Funder et al., 2011).

2. Study area

2.1. Physiographic setting

Greenland is the largest island in the world with a total area of 2,166,086 km^2 and a total coastline of 44,087 km. The island is located between 59˚ to 83˚N and 11˚ to 74˚W northeast of Canada on the North American continent, between the Arctic Ocean and North Atlantic Ocean (Fig. 1.1). The study area, Kejser Franz Joseph Fjord, shown in Fig. 1.2 is located on the north-eastern coast of Greenland, and is a large, branched fjord system opening towards Foster Bugt and the Polar North Atlantic. The fjord system extends 220 km inland, covers an area of 2200 km^2 (Evans et al., 2002) and borders to Hudson Land in the north and Ymer Ø in the south. Kejser Franz Joseph Fjord comprises three main fjords; Nordfjord, Geologfjord and Isfjord, with several smaller fjords linked to the fjord system. The Inland Ice drains into the fjords via Waltershausen-, Adolf Hoel-, Jætte-, Gerrard de Geer- and Nordenskjøld Gletscher (Evans et al., 2002). The hinterland of the fjord system is characterized by an alpine landscape which inland becomes more plateaus as it continues below the GIS. The alpine mountains slopes down to coastal lowlands, contrasting the steep fjord walls carved out by glaciers. Today the mountains are covered by local plateau ice fields and cirques while the valleys are glacially abandoned. The coastal lowlands are cut by glacifluvial- and fluvial systems building deltas and alluvial fans along the fjord margins (Evans et al., 2002).

Nordfjord and Moskusoksefjord (73˚28'N to 73˚48'N and 22˚12'W to 24˚27'W) are separated by Gauss Halvø, and represent the northern arm of Kejser Franz Joseph Fjord. Moskusoksefjord is approximately 65 km long, 0.6 - 5 km wide and has a WNW-ESE orientation. Nordfjord is shorter with its 35 km, has a width of 13 km and generally follows an N-S trend. Waltershausen Gletscher terminates where the two fjords meet.

2.2. Bedrock geology

The bedrock in the area of Kejser Franz Joseph Fjord is mainly composed of Neoproterozoic to Ordovician Caledonian fold- and thrust belts and Devonian to Paleogene sedimentary and basaltic bedrocks (Henriksen et al., 2000; Andresen et al., 2007; Henriksen, 2008) (Fig. 2.1 and 2.2). The Caledonian bedrocks are found on Strindberg Land, Andrée Land and western Ymer Ø, constricted by an N-S trending extensional fault to the west and Devonian bedrocks

9

to the east. The Devonian bedrocks can be found on Hudson Land, Gauss Halvø and eastern Ymer Ø, whilst the outer part of the fjord, Hold with Hope and Traill Ø, are mainly composed of Paleogene basalts and Carboniferous-Cretaceous sediments, respectively. Archean to early Neoproterozoic crystalline complexes and sediments are exposed in the catchment area of Waltershausen Gletscher and Adolf Hoel Gletscher (Higgins et al., 2004; Andresen et al., 2007).

The N-S trending Caledonian mountain belt is made up by two very thick, folded sedimentary successions; the oldest Krummedal supracrustal sequence (~1000 Ma) and the youngest sequence consisting of Eleonore Bay Supergroup, Tillite Group and Kong Oscar Fjord Group (450-900 Ma). The Krummedal sequence comprises pale sandstones and darker mudstone which have metamorphosed under amphibolite facies into schist with local melting and granite formation. Above, the Eleonore Bay Supergroup, further divided into Nathorst Land-, Lyell Land-, Ymer Ø- and Andrée Land Group, is made up by a thick sequence dominated by sandstones, mudstone and carbonates. The overlying Tillite Group is mostly made up by a thick sequence of lithified glacial deposits, and on top is Kong Oscar Fjord Group with its sandstones, limestones and dolomites rich in fossils (Henriksen et al., 2000; Higgins et al., 2001; Henriksen, 2008). The Devonian sediments, known as Old Red Sandstones based on their recognizable red colour, comprise continental siliclastic sediments mainly composed of sandstones with intervening conglomerate, occasional mudstone and intervals of volanics. The sediments have been divided into four groups based on local tectonic events causing overthrust, faults and minor folding; Vilddal-, Kap Kolthoff-, Kap Graah- and Celsius Berg Group (Henriksen et al., 2000; Henriksen, 2008).
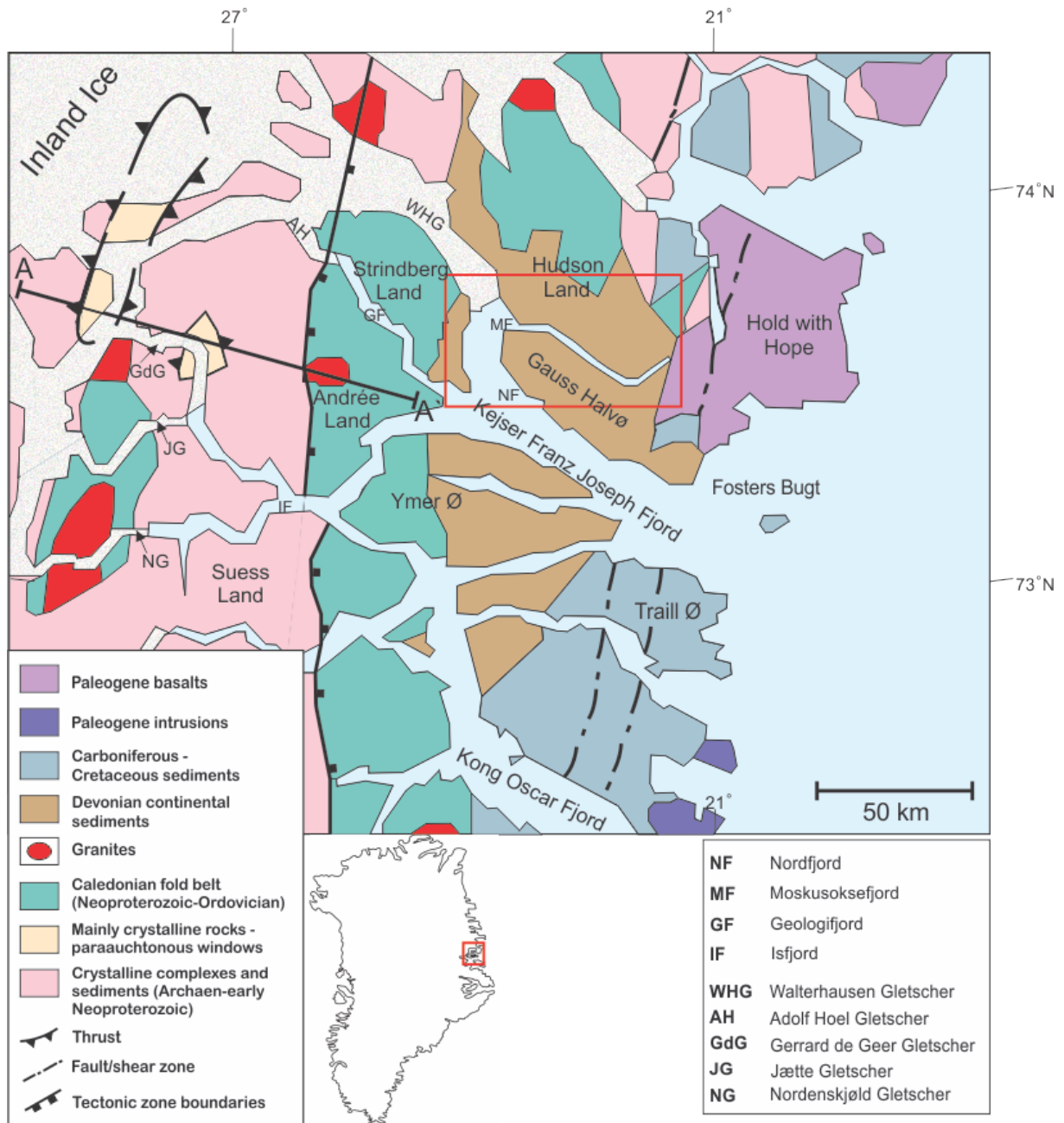
Figure 2.1: Geological map of Kejser Franz Joseph Fjord region (based on Higgins et al., 2004). Red box show study area. A-A` is a cross-section line (see Fig. 2.2).
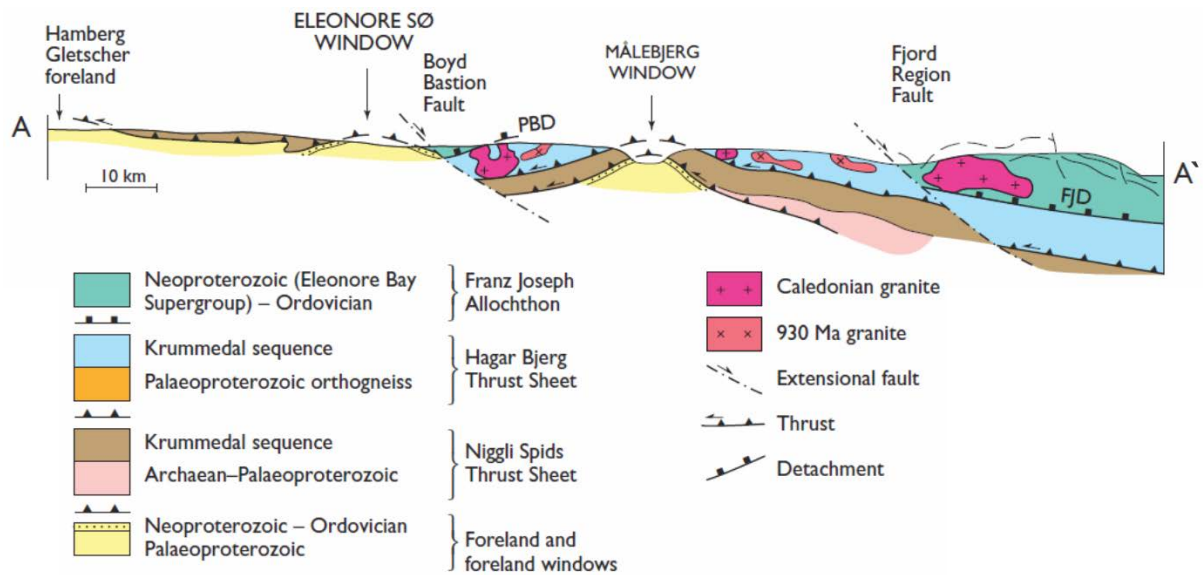
Figure 2.2: Cross-section of the bedrock stratigraphy in the Kejser Franz Joseph Fjord region, showing thrust sheet architecture. Vertical scale = horizontal scale. *PBD*: Petermann Bjerg Detachment, *FJD*: Franz Joseph Detachment **(modified from Higgins et al., 2004).**

2.3. Geomorphology

A "fjord" is a narrow, steep-sided and over-deepened marine basin, coastal trough or estuary. They are erosional landforms of glacial origin, formed as land-based glaciers expanded and carved into weak zones in the underlying bedrock (Powell, 2003; Howe et al., 2010), e.g. faults, lithology or fluvially eroded troughs (Forwick, 2013b). According to Hambrey (1994) East Greenland fjords often have a linear trend related to faults. Syvitski et al. (1987) described fjords as transitions between land and open oceans where fresh- and saltwater mixes and strong physical and chemical gradients are produced. Today fjords can be found along mid- to high latitude mountainous coastlines, e.g. Alaska, Norway, Greenland, Scotland, New Zealand and Antarctica (Fig. 2.3) (Farmer & Freeland, 1983; Powell, 2003; Howe et al., 2010).
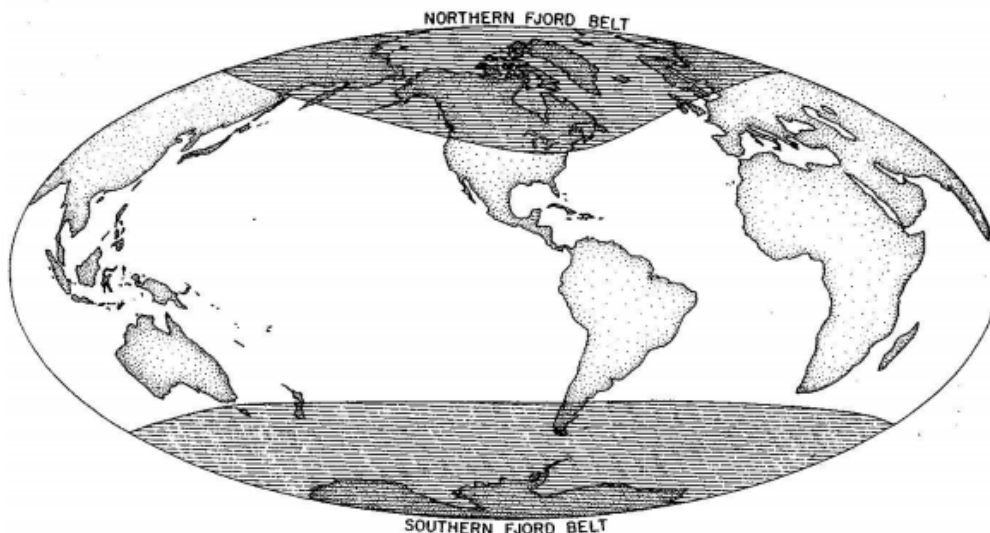
Figure 2.3: General distribution of fjords in the northern and southern hemisphere (Syvitski et al., 1987).

Hambrey (1994) suggested a classification of fjords based on glacier regime and influence, including Alaskan, Antarctica, Greenland and Svalbard regimes. Kejser Franz Joseph Fjord is a part of the "Greenland regime", characterized by cold, dynamic and floating glacier outlets from the Inland Ice terminating in the deep fjords (>200 meter). According to Domack & McClennen´s (1996) classification system based on climate, the fjord system is polar due to the presence of sea ice most of the year and calving glaciers. However, a mean summer temperature >0˚C would classify the fjord system as subpolar (Domack & McClennen, 1996). The third classification, by Syvitski et al. (1987), is based on a physical regime, with a medium to high sedimentation rate in Greenland fjords.

The geomorphology of a fjord is dependent on several parameters including geology, climate and glacial and postglacial history of the region. The shape of the fjord is dependent on both bedrock lithology and sediment infill; Moskusoksefjord, in particular, have a typical U-shaped form and smooth, continuous sea floor reflecting its narrow, steep physiography and proximity to numerous meltwater sources draping the sea floor (Syvitski et al., 1987; Evans et al., 2002). Along mountain slopes of fjords we often find terraces representing old shorelines, moraines formed at old ice margins, talus cones, and hanging valleys (Syvitski et al., 1987). The local marine limit on Ymer Ø is 70 m a.s.l (Funder & Hansen, 1996). As most fjords, Kejser Franz Joseph Fjord has an entrance sill and several basins separated by sills (Syvitski et al., 1987; Wassmann et al., 1996; Evans et al., 2002). A shallow sill is found at the intersection between Nordfjord and Kejser Franz Joseph Fjord (Evans et al., 2002), its presence may restrict sediment transport along the fjord bottom and the exchange of inner and outer fjord water (Syvitski et al., 1987). Sediment lobes can be seen along the fjord margins in both fjords.

2.4.   Glaciology

The GIS, a remnant of the Pleistocene ice ages (GEUS, 2003), is an uninterrupted, slightly domed ice cap, and covers approximately 81% of Greenland. It is the largest body of ice in the northern hemisphere and the second largest in the world, only overshadowed by the Antarctic Ice Sheet (Dahl-Jensen et al., 2009). The GIS covers an area of approximately 1.7 million km^2, reaches a thickness of more than 3 km, with an average thickness of 1600 meters (Alley et al., 2010). Total volume is 2.9 million km^3 (Dahl-Jensen et al., 2009). Today the inland ice of the GIS is largely separated from the sea by a more or less ice-free coast reaching up to 300 km width (Weidick & Bennike, 2007). Outlets from the ice sheet terminate either on land, in lakes or at sea. More than 50% of the ice mass loss is through melting and runoff, the rest is through calving at the front of tidewater glaciers (Gregory et al., 2004; Hanna et al., 2005; Benn & Evans, 2010).

In Kejser Franz Joseph Fjord and its tributary fjords there are five outlet glaciers of significant size (Waltershausen-, Jætte-, Adolf Hoel-, Gerrard de Geer- and Nordenskjøld Gletscher) and numerous smaller glaciers (Fig.1.2). The five outlet glaciers are fed by the Inland Ice and have a total glacier drainage basin of >8400 km^2 (Evans et al., 2002). Each year approximately 8 km^3 of ice calve into the Kejser Franz Joseph Fjord system, which comprises

3% of the total iceberg production in Greenland (Reeh, 1985). However, only Waltershausen Gletscher terminates directly into the fjord basins of Moskusoksefjord and Nordfjord.

Waltershausen Gletscher is a tidewater outlet glacier with a terminus width of 10.5 km. Like other outlet glaciers on North-East Greenland glacier front fluctuations have been relatively minor (Funder et al, 2011; Seale et al., 2011), with -0.13 km interannual front change from 2001-2005 and +0.15 km front change from 2005-2008 (Seale et al., 2011) (Fig. 2.4). Surges have been suggested for both Waltershausen Gletscher (Weidick, 1995) and Adolf Hoel Gletscher (Moon et al., 2012), but this has never been recorded.
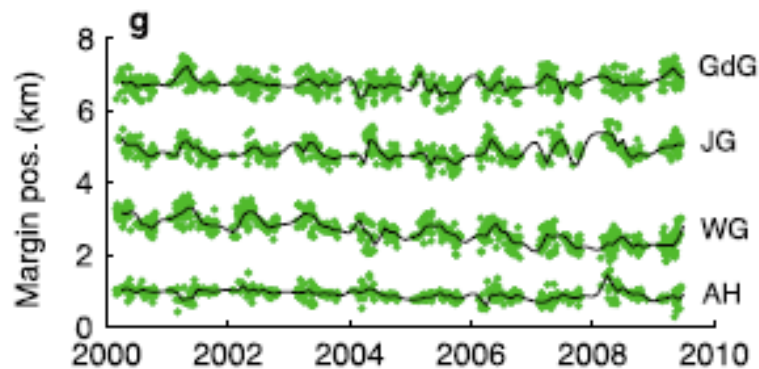
Figure 2.4: Changes in the relative position of calving glacier margins from 2000 - 2009 in Kejser Franz Joseph Fjord derived from automatic edge detection and brightness in MODIS imagery (modified from Seale et al., 2011). *GdG*: Gerrard de Geer Gletscher, *JG*: Jætte Gletscher, *WG*: Waltershausen Gletscher, *AH*: Adolf Hoel Gletscher.

2.5.   Sediment sources

The sedimentation accumulation rate in a fjord is dependent of both rainfall and summer temperature within the fjords drainage basin controlling the amount of discharge, the duration of the melt season and initiating episodic sedimentation events (Cowan & Powell, 1991). All the glaciers in the drainage basin of Nordfjord and Moskusoksefjord contribute to the fjords´ sediment supply, either from direct contact or through meltwater rivers. Based on its proximity, Waltershausen Gletscher acts as an important sediment source to the fjord basins of both Nordfjord and Moskusoksefjord, releasing sediments throughout the year (Evans et al., 2002). Sediments released at the glacier front can derive from various sources; supra-, en- or subglacial, iceberg-rafted debris, aeolian or lateral deltas. The presence of sea ice will impact the stability of a calving glacier front, affecting both production and the mobility of icebergs (Evans et al., 2002). Sedimentation rates are highest proximal to the glacier termini and decreases exponentially from the glacier front. The dominant sediment source to Greenland fjords is glacial flour (Heling, 1974).

Figure 2.5: Picture taken in Moskusoksefjord, showing various sediment sources.

Numerous glacifluvial and fluvial systems can be found along the fjord margins, fed by glacial meltwater, snow and precipitation (Fig. 2.5 and 2.6). Important sediment sources in Nordfjord (besides Waltershausen Gletscher) are river systems dissecting the coastal plains of Paralleldal on Gauss Halvø and Broget Dal on Strindbergs Land. Evans et al. (2002) proposed that the sediments in the fjord basin of outer Nordfjord comprise well-stratified sediments

draped by stratified glacimarine sediments, deposited from sediment gravity flows and suspension settling. They also stated that meltwater processes had greatly exceeded debris deposited from icebergs. In Moskusoksefjord, in addition to Paralleldal, a large, braided flood plain located in Badlandal at the fjord head releases large amounts of sediments during melt season. In both fjords river- and fan deltas of various sizes can be found along the fjord margins. Adolf Hoel Gletscher may also contribute as a sediment source to outer Nordfjord.
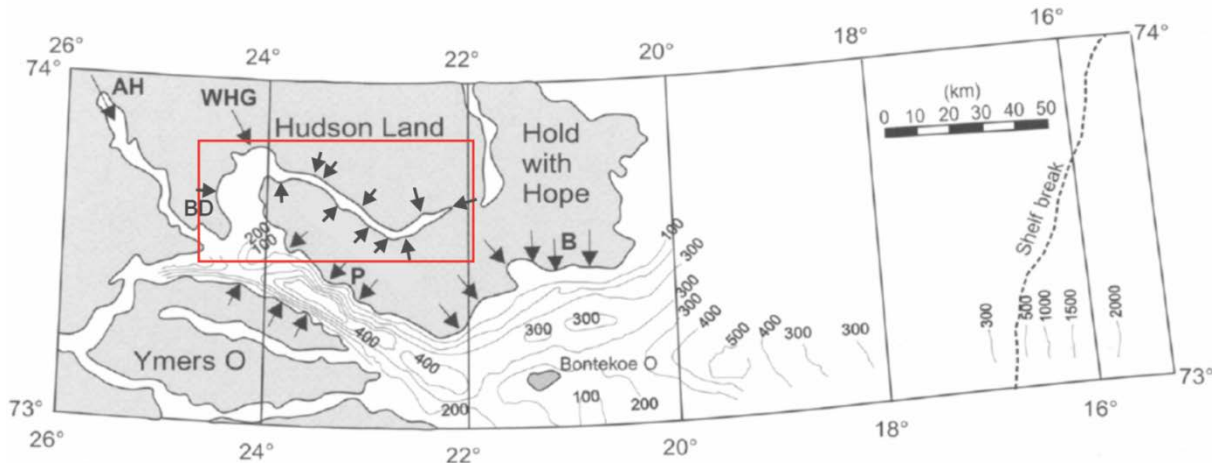
Figure 2.6: Bathymetric map of middle- and outer Kejser Franz Joseph Fjord. Arrows indicates source of meltwater to Moskusoksefjord, Nordfjord and Fosters Bugt. *AH*: Adolf Hoel Gletscher, *WHG*: Waltershausen Gletscher, *P*: Paralleldal, *B*: Badlandal, *BD*: Broget Dal (modified from Evans et al., 2002). Red box show study area.

Slope instabilities are common in fjords with steep slopes and high sedimentation rates. As a result they are often the site of gravity-driven depositional processes like slides, slumps, debris flows and turbidity flows (Syvitski et al., 1987; Nelson et al., 2011).

2.6.   Climate

The climate on Greenland is arctic to subarctic with cool summers and cold winters (CIA, 2014). The fact that the island stretches more than 2600 km from north to south, or almost 24 degrees of latitude from top to bottom, leads to great variations in climate (Cappelen et al., 2001). The regional climate of Kejser Franz Joseph Fjord is largely affected by the East Greenland Current transporting fresh, cold water and vast amounts of sea ice from the Arctic Ocean along the coast to the south where it joins the warm Irminger Stream (Weidick, 1995; Weidick & Bennike, 2007; Wagner et al., 2010). The width and areal extent of the sea ice belt is seasonally and climatically dependent (Weidick, 1995), and contributes to the regional winters normally being very cold due to the lack of open sea in the area, meanwhile during summer the fjords mostly stay relatively warm and sunny (Cappelen et al., 2001).

At present there are several meteorological stations performing climatic measurements along the outer coast of Greenland (Table 2-1). Precipitation data show a decrease from south to north (Ohmura & Reeh, 1991; Weidick, 1995; Weidick & Bennike, 2007), with a mean annual precipitation of 340 mm (Ohmura & Reeh, 1991). In Kejser Franz Joseph Fjord the mean precipitation is 200-300 mm/year, and the mean temperature is -9˚C (Cappelen et al., 2001). Due to the meteorological stations being situated at the outer coast, measurements of the precipitation from the coast and inland are lacking. Instead, Böcher et al. (1978) have used vegetation as indicators of the precipitation decreasing inland, showing that inland areas in the far northern East Greenland can stay desert-dry. Weidick (1995) described the area of Waltershausen Gletscher and Adolf Hoel Gletscher to be inland areas with low precipitation.

The wind system over Greenland differs during winter and summer time (Fig. 2.7), and is mainly dominated by two cyclons; Baffin Bay low in west and the Icelandic low in east. During winter, the southeast Greenland is hit by onshore winds, contributing to the high precipitation in east and dry winters in west. During summer this pattern changes; an additional low from the polar basin contributes to the summer climate. Due to advection from the west, the northeast has an increase in precipitation whilst the east becomes dryer (Ohmura & Reeh, 1991).

Table 2-1: Average temperatures for January and July, annual average temperatures, and average annual precipitation at selected stations, East Greenland (Weidick, 1995).

Station	Location		Average temperatures (°C)			Average annual precipitation (millimeters per year)
	°N lat	°W long	January	July	Annual	
Daneborg.................	74	20	−21.8	+3.7	−10.6	195
Kap Tobin................	70	22	−17.4	+2.7	−8.2	448
Aputitêq..................	68	32	−10.7	+2.2	−4.8	606
Angmagssalik.............	66	38	−7.3	+6.6	−1.6	930
Tingmiarmiut.............	63	42	−6.2	+5.7	−1.2	1,521
Prins Christianssund......	60	43	−3.3	+6.7	+0.9	2,480
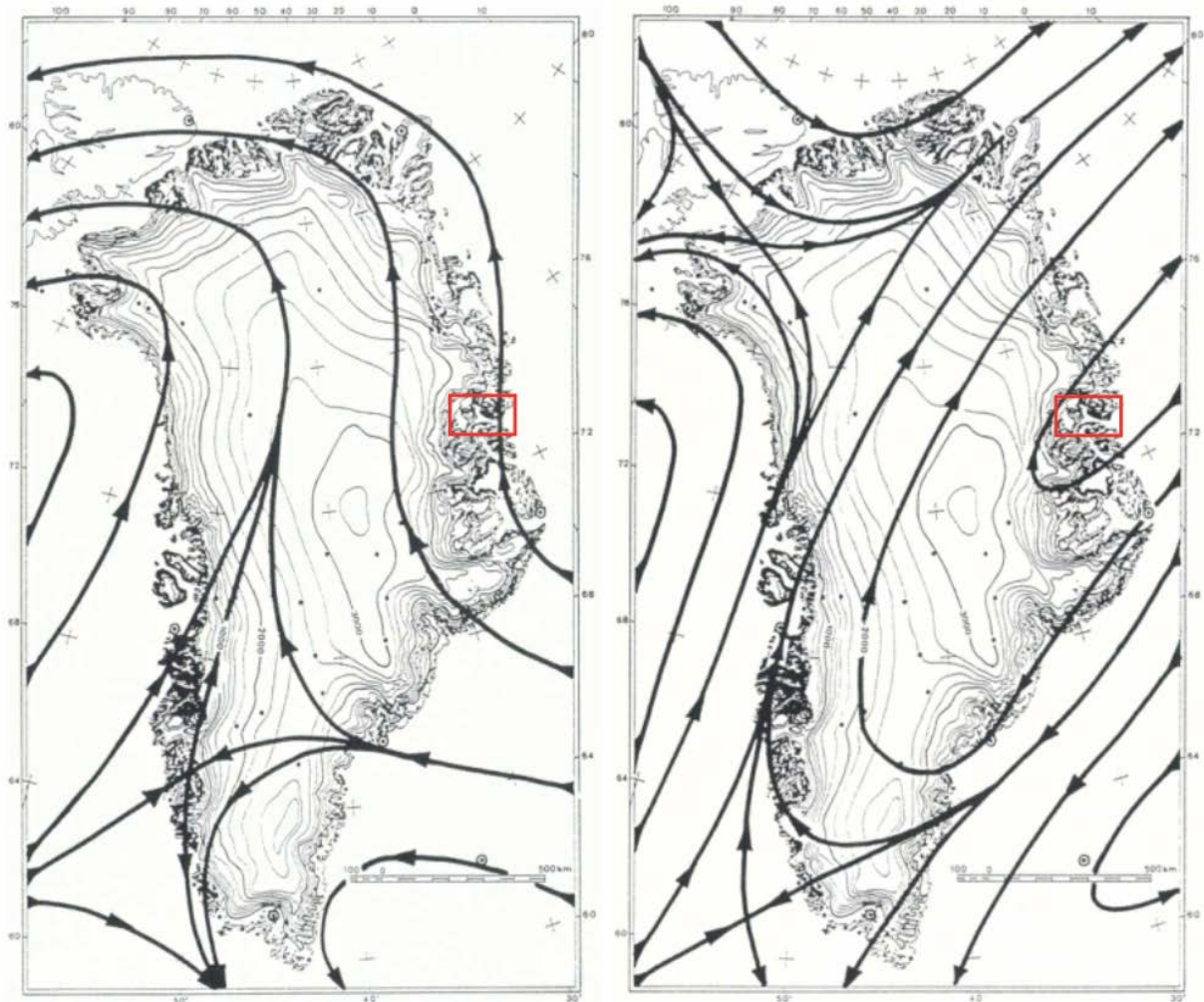
Figure 2.7: The general monthly wind pattern for 850 hPa (mbar) in January (left) and July (right). The concentration of stream lines is proportional to wind speed (Ohmura & Reeh, 1991). Red box show study area.

2.7. Oceanography

The east coast of Greenland is largely influenced by the East Greenland Current (EGC) carrying cold Polar Water (PW; 0-150 meter), warm Atlantic Intermediate Water (AIW; 150-800 meter) and Greenland Deep Water (GDW; >800 meter) southwards along the East Greenland shelf and slope through the Nordic Seas and Denmark Strait. The EGC is fed by fresh water from the Arctic Ocean through the Fram Strait and is constrained to the Greenland Continental Margin by its low density and geostrophic currents (Hopkins, 1991). When reaching Denmark Strait, the EGC joins the warmer Irminger Current at the East Greenland Front before it turns northward after passing Cape Farewell on the southern tip of Greenland (Jennings & Weiner, 1996; Alley et al., 2010) (Fig. 2.8). AIW carried by the EGC originates from two sources. The first source is recirculating Atlantic Water from the Arctic Ocean, which after circulating in the Arctic follows the EGC through the Fram Strait. The second

19

source is a southward turning branch from the West Spitsbergen Current (Jennings & Weiner, 1996). Transport values and current speed of the EGC have been attempted by several authors, but due to different methods and magnitude they come up with different results. According to Hopkins (1991) transport values of the EGC varies from 2-32 Sv, while Aagaard & Coachman (1968) have calculated a mean annual of 35 Sv. Calculated current speed ranges from 4 to 20-30 cm s^{-1} (Aagaard & Coachman, 1968; Foldvik et al., 1988; Bersch, 1995).
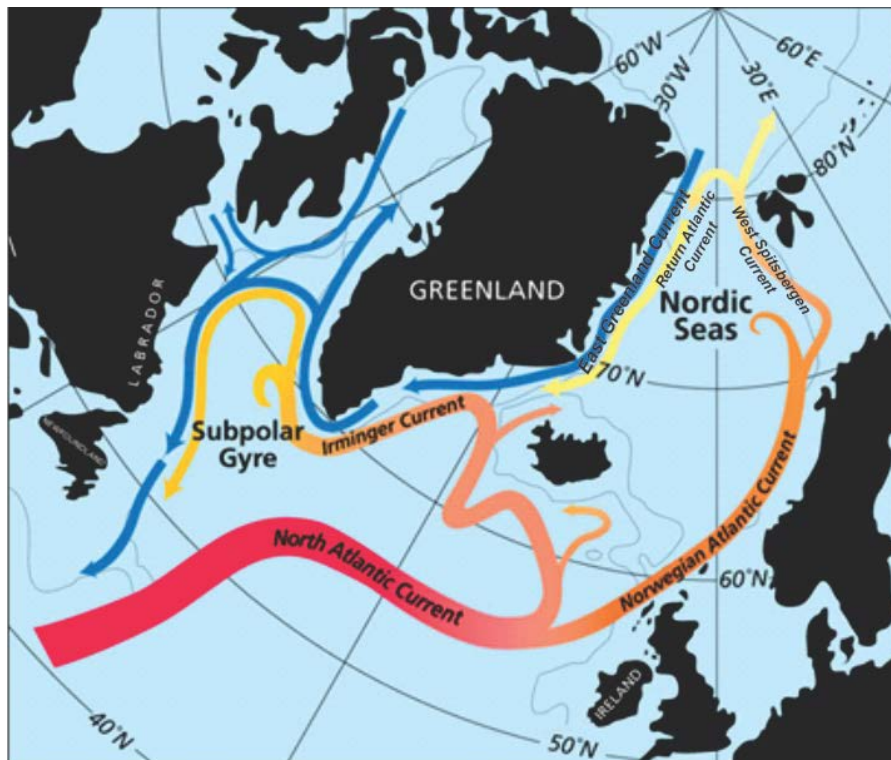
Figure 2.8: Ocean circulation in the North Atlantic and Nordic Seas (adapted from Watts (2010)).

The EGC carries sea ice and icebergs through the majority of the year (Smith & Andrews, 2000). As it flows southwards, icebergs and meltwater are added to the EGC by outlet glaciers along the coast, except between October and June when shorefast sea ice prevents drift (Jennings & Weiner, 1996; Evans et al., 2002).

Fjord circulation, in general, comprises an outward flowing surface layer and a compensating inward moving current. In Polar Regions, however, runoff may be limited to only a few months per year, weakening the fjord circulation (Syvitski et al., 1987). The general circulation and mixing in fjords are dependent on various factors together with the bathymetry and Coriolis Effect, affecting both sedimentological and biochemical gradients (Syvitski et

al., 1987). Farmer & Freeland (1983) divided the factors influencing the fjord into two main groups; "Buoyancy sources" (e.g. river discharge, gravitational circulation and exchange of surface heat or water) and "Turbulent kinetic energy sources" (e.g. wind, tides, convection by surface cooling and kinetic energy from rivers). High inputs of freshwater to the fjord and the presence of shallow sills creates a stratification of the water masses within a basin (Syvitski et al., 1987; Nielsen & Andersen, 2002). The water inside and below sill depth in Nordfjord and Moskusoksefjord would be entrapped, only renewed during certain periods of the year. Between these periods the water would stay stagnant and the vertical diffusion would lose its intensity as time passes (Stigebrandt, 1976).

Three water masses can be found in the fjord system of Kejser Franz Joseph Fjord (Fig. 2.9); (1) upper 25 meters holds warm (>0°C), low saline (<31‰) surface water that extends to the inner shelf, (2) very cold (<0°C), moderately high salinity (~31-34.5‰) PW found down to 200-300 meter water depth and (3) warm (0-3°C), high salinity (>34‰) AIW below 300 meter water depth (Bourke et al., 1987; Ó Cofaigh et al., 2001).
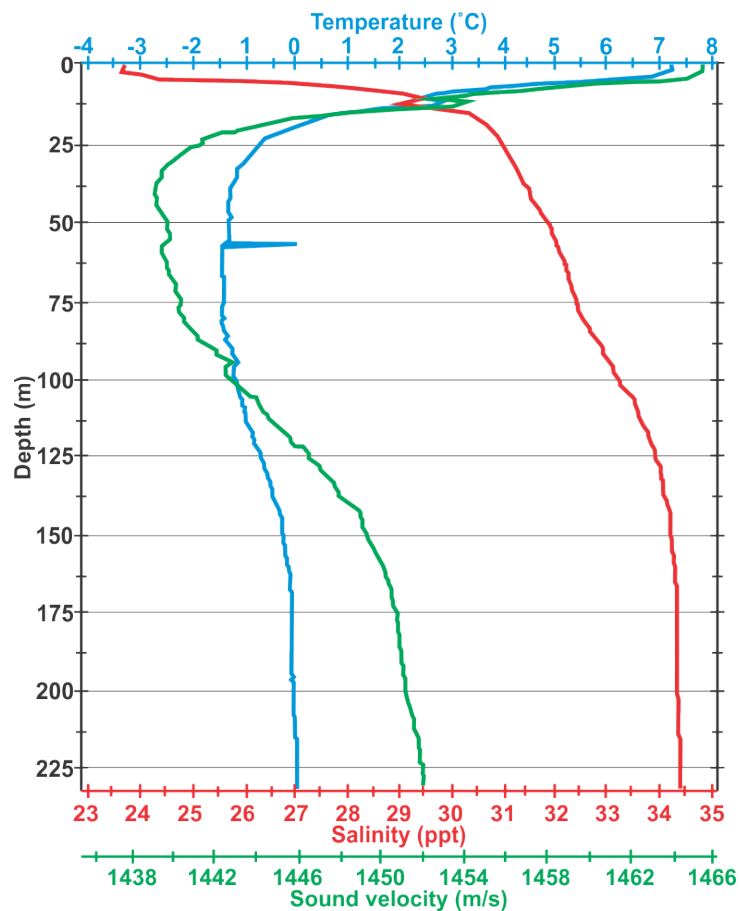
Figure 2.9: CTD profiles based on measurements performed during the scientific cruise to Kejser Franz Joseph Fjord in August 2013. The blue line represents the temperature, red line the salinity and the green line is the sound velocity.

21

3. Material and methods

The sediment cores, swath bathymetry data and chirp profiles (Fig. 3.1) were collected with the research vessel R/V Helmer Hanssen from UiT, the Arctic University of Norway during a scientific cruise in august 2013.

3.1. Swath bathymetry data/Multibeam

The Swath bathymetry sonar system is a high-resolution imaging system emitting a fan of beams to the seafloor, allowing the seabed to be scanned in high detail and with a wide coverage (Fig. 3.1). The multibeam system uses a large set of echo sounders, each pointing sideways to the acquisition direction in a specific angle to the vertical (Denbigh, 1989). The system swath width depends on water depth, at greater water depths the resolution decreases as the water depth increases. Multibeam allows us to collect data about seabed morphology and structure, water depth, slopes and the type and distribution of sediments on the sea floor. (Carter, 2012). The main source of error in swath bathymetry is acoustic interference (Denbigh, 1989). The bathymetry data show areas with different artefacts, e.g. straight lines or areas of hummocky appearance centered along lines (both parallel and transverse to the long axis of the fjord) and artificial "holes" and "bumps". In some areas data is lacking (Fig. 3.2).

The swath bathymetry data used in this study was collected using the Kongsberg Maritime Simrad EM 300 multibeam echo sounder. It is a hull-mounted system with a nominal operational frequency of approximately 30 kHz. The system consists of 135 beams, providing an angular coverage of up to 150° and a depth range from 10 to >5000 m. Both the angular coverage sector and beam pointing angles are variable with depth in order to maximize the use of beams (Kongsberg Maritime, 2003).

The available swath bathymetry data was interpreted and imaged using the Fledermaus v7 3D Visualization software, with a resolution of 10 m.
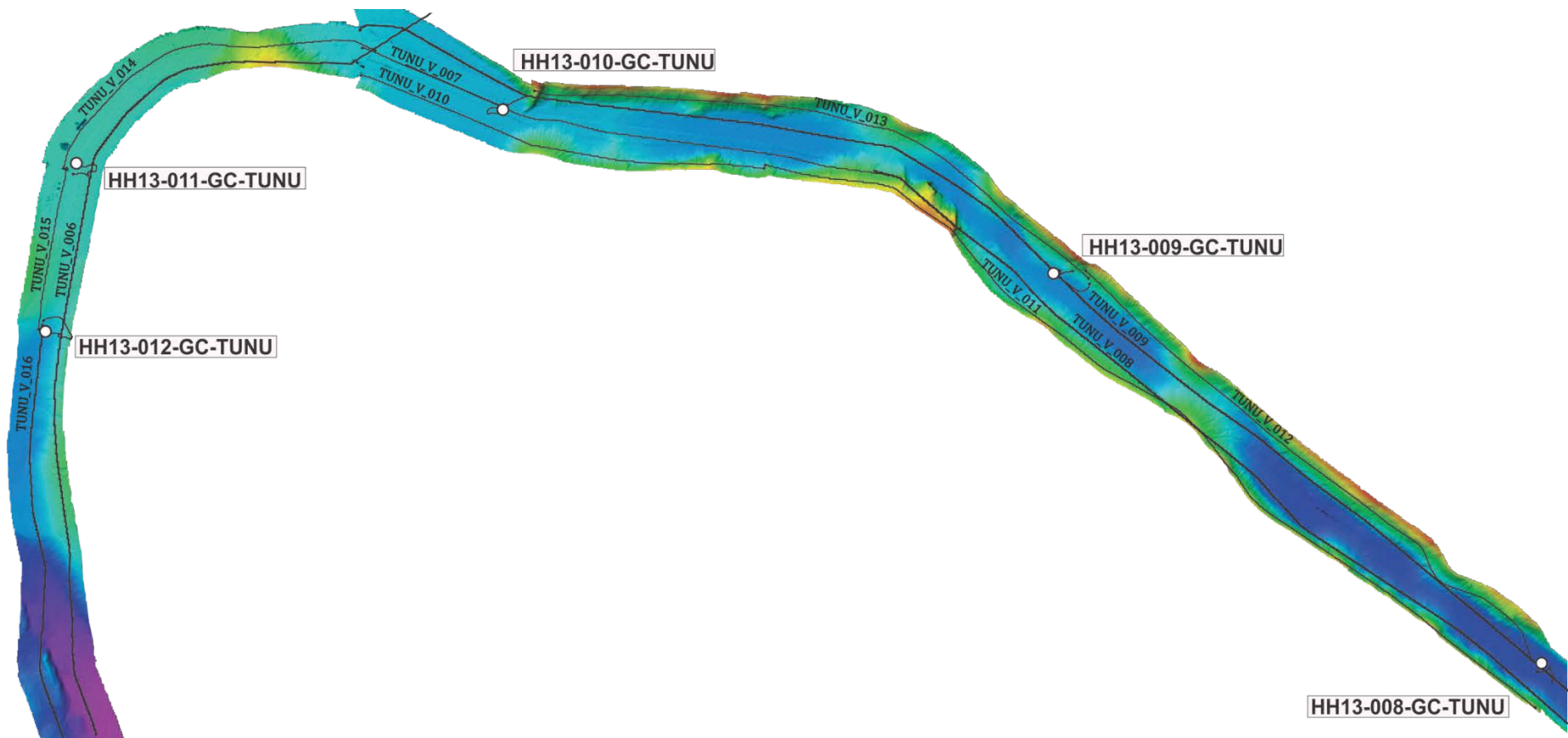
Figure 3.1: Overview of the obtained swath bathymetry. Black lines represent chirp profiles, and white circles reflect core locations.
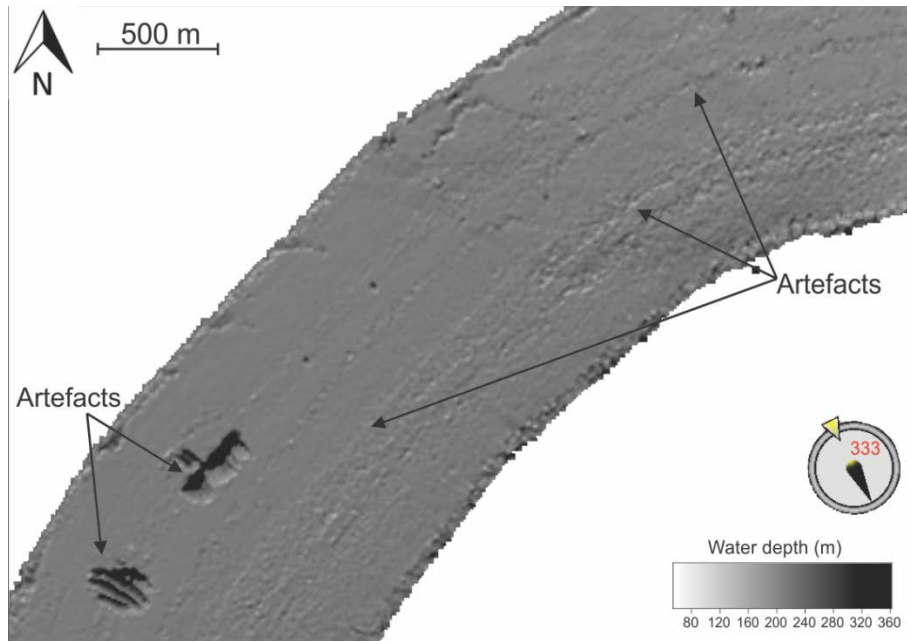
Figure 3.2: Shaded bathymetry image showing artefacts (for location see Fig. 4.1).

3.2.   Chirp Sonar

Chirp sonar is a quantitative acoustic measurement system using a wide-band, frequency-modulated sub bottom profiler. The measurement system can measure and determine acoustic attenuation and produce real-time artifact-free sediment profiles of the upper marine sediments. Unlike the multibeam echo sounder, the Chirp system can map the upper 30 meters of unconsolidated sediments. This allows us to gain useful information about the deposited material, helping us to classify the local marine bottom sediments and to get an idea of the solidity of the sediments (Schock et al., 1989; Quinn et al., 1998). The horizontal resolution is related to the source characteristics, the sediments compressional wave velocity, towfish altitude and the systems pulse rate, whereas the vertical resolution is dependent upon the bandwith of the source (Quinn et al., 1998). The Chirp system differentiates from the normal short-pulse, single frequency profilers, like springers and boomers, in the way the system transmits selectable computer-generated sweep-frequency pulses, usually between 400Hz and 20kHz (Quinn et al., 1998; Mosher and Simpkin, 1999).

In the chirp data set there may be noise creating multiples – reflections that have undergone more than one reflection. Multiples appear as delayed signals beneath the primary reflection. The distance between the primary and the first multiple is dependent on the extra travel time.

Multiples are produced with a reversed polarity, twice the angle of dip and with a weaker impedance contrast than the primary reflection.

All chirp sonar profiles were acquired with the EdgeTech 3300-HM hull-mounted sub-bottom profiler. The pulse frequency was 1.5-9.0 kHz and a 40 ms pulse length was used. The ship travelled at a speed between 7 and 11 knots and the shot rate was 1 Hz.
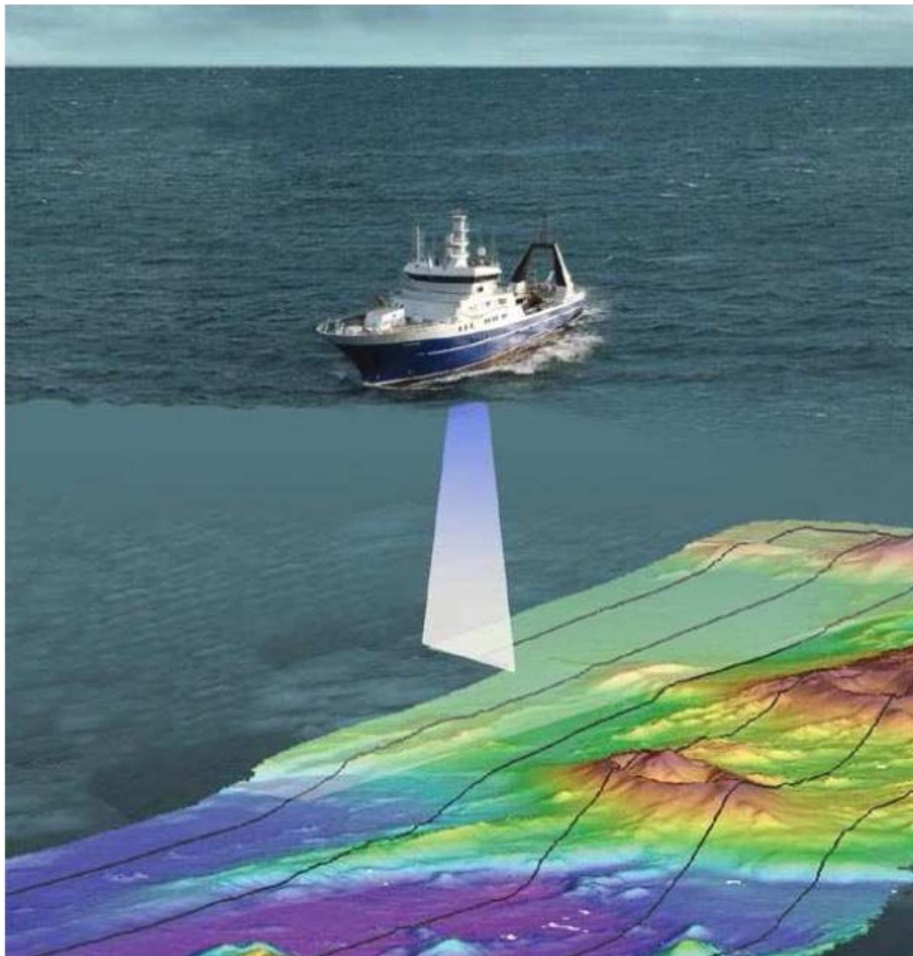
Figure 3.3: Example image of a multibeam survey (Pickrill & Barnes, 2003)

3.3.   Sediment cores

Five sediment gravity cores were collected in two fjords in North-East Greenland, august 2013. Location and information about the cores can be found in Table 3-1.

The gravity corer consisted of a 6 meter long steel barrel with a 1600kg weight attached. A 6 meter long plastic liner with an outer diameter of 11cm was placed and secured into the steel barrel with a core catcher and core cutter (Fig. 3.4). After retrieval, all five cores were split into ~100cm long sections, labeled and sealed with plastic caps at both ends. All cores have been stored at 4˚C.

Table 3-1: Gravity-corer locations and information about the cores.

Station	Date	Time (UTC)	Location	Latitude [N] Longitude [W]	Water depth [m]	Penetration [m]	Recovery [cm]	Comments
HH13-008-GC TUNU	10.08.2013	19:25	Moskusoksefjord	73˚37.238´ 023˚05.104´	256	>6	226	
HH13-009-GC TUNU	10.08.2013	20:55	Moskusoksefjord	73˚41.838´ 023˚27.354´	233	>6	283	
HH13-010-GC TUNU	10.08.2013	22:18	Moskusoksefjord	73˚43.595´ 023˚52.081´	227	>6	486	20-30 cm lost. Uppermost >20 cm heavily disturbed
HH13-011-GC TUNU	10.08.2013	23:22	Nordfjord	~73˚42.510´ ~024˚10.172´	209	>6	597	10 cm lost. Uppermost 10-20 cm heavily disturbed
HH13-012-GC TUNU	11.08.2103	~0:15	Nordfjord	73˚40.515´ 024˚10.939´	~210	>6	459	Uppermost ~10 cm heavily disturbed
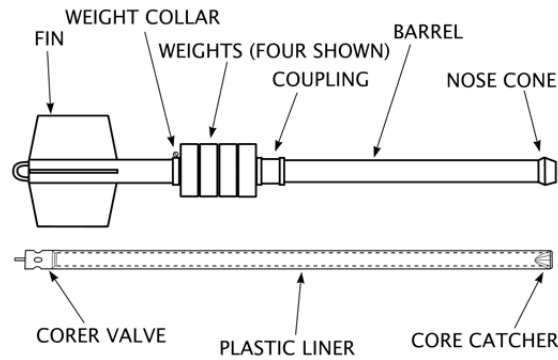
3.4. Laboratory work – sediment cores

The laboratory work was carried out at the Department of Geology at the University of Tromsø, The Arctic University of Norway, from March 2014 to February 2015.

All 22 core sections were examined and analyzed in the laboratory to determine geochemical elements, physical parameters, sediment grain-size and -distribution.

3.4.1. Multi Sensor Core Logger (MSCL)

Prior to opening, the cores were first logged with a GEOTEK Multi Sensor Core Logger (MSCL), a logging device providing continuous centimeter-scale measurements of the marine sediment cores (Fig. 3.5). The physical parameters that were measured were core diameter, temperature, gamma-ray attenuation, P-wave velocity and P-wave amplitude and magnetic susceptibility. As a result, the wet bulk density, p-wave velocity, acoustic impedance and fraction porosity were obtained for the measured sediment cores.

Temperature can influence the physical parameters, like the p-wave velocity and the magnetic susceptibility (Marum, 2013a), but to avoid this unwanted influence all cores were stored in the laboratory a while prior to measuring. The room temperature was measured by a thermometer placed on the apparatus, and the cores were assumed to have the same temperature. The core diameter was measured relative to a known reference diameter of 110 mm so that any deviation could be recorded. The different physical parameters of the GEOTEK MSCL were calibrated before use.
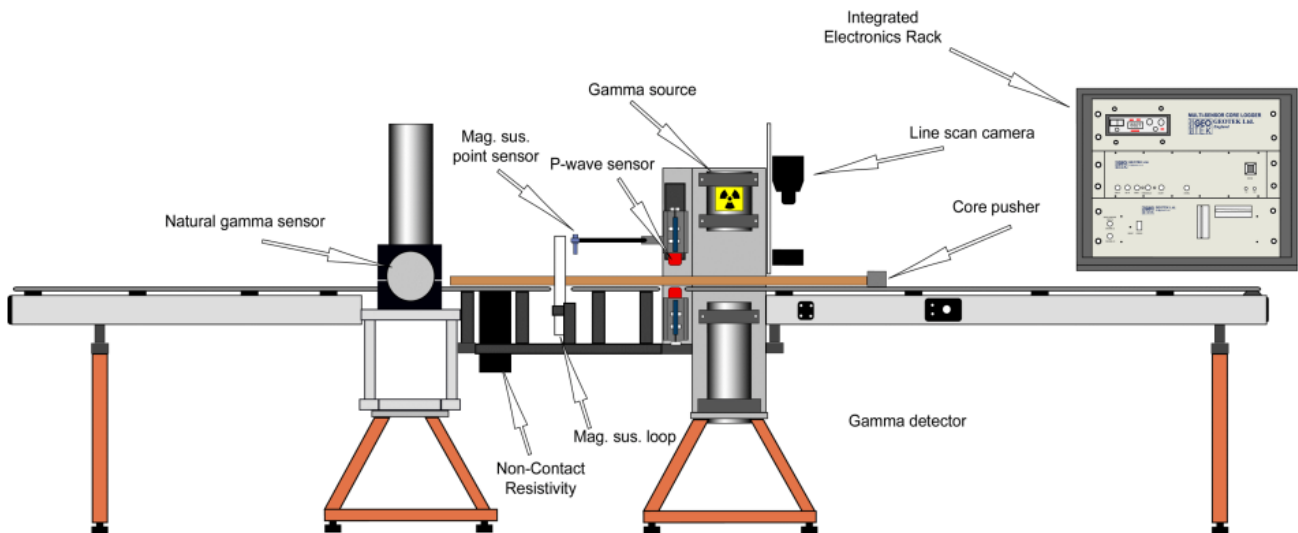
Figure 3.5: Principle sketch showing the setup of the Multi-Sensor Core Logger (GEOTEK, 2000)**. The MSCL used at the Department of Geology, University of Tromsø, has all instrumenst measuring horizontally, not vertically as in the sketch.**

3.4.1.1. *Wet-bulk density*

The bulk density of a material is defined as the mass of any particles of the material divided by the total volume they occupy. For sediments this is dependent of their mineral composition and compaction (GEOTEK, 2014a).

Radioactive ^{137}Cs emitting γ-rays with energies at 662 keV were used to calculate core diameter and electron density of the material. Photons propagating through the core interact with electrons and loose energy due to Compton scattering, causing γ-ray attenuation. This means that since the amount of γ-rays transmitted through the core is directly dependent of the number of electrons in the gamma ray beam, the core diameter and density can be determined (GEOTEK, 2014a). As the sediments measured in this study were wet, the obtained density is the wet bulk density.

3.4.1.2. *P-wave velocity*

P-waves (primary-waves) are compressional waves, which means that the material is alternately compressed and dilated in the direction of propagation as the waves propagate through a material. P-waves can, unlike S-waves (secondary-waves), travel through any material (GEOTEK, 2014a). The P-wave velocity is an important measure of the travel velocity of the acoustic signal generated through the material, and changes with the materials characteristics, e.g. porosity and density (Burger et al., 2006).

The GEOTEK MSCL produces a short P-wave pulse which propagates through the core and is detected by the receiver, measuring the P-wave travel time through the sediments (GEOTEK, 2014a). The propagation velocity of the P-wave through the core sediments is given by:

$$V = \frac{d}{t}$$

where d is the diameter of the sediment core, and t is the pulse travel time in the sediment (Marum, 2013a). For optimum contact the transducer was carefully moistened by water, and a good contact between transducer and core was strived.

3.4.1.3. Acoustic impedance and fraction porosity

The gamma density measurements reveal the wet-bulk density of the sediment cores. From these measurements it is possible to calculate the fraction porosity and the acoustic impedance. The acoustic impedance is a product of both the P-wave velocity and the wet-bulk density, and is given by the formula:

$$Z = V*p$$

where Z is the acoustic impedance, V is the P-wave velocity and p is the density (GEOTEK, 2014a).

3.4.1.4. Magnetic susceptibility

Magnetic susceptibility is "the degree of a magnetization of a material in an applied magnetic field" (GEOTEK, 2014a). The presence of either a paramagnetic, ferrimagnetic, ferromagnetic or antiferromagnetic material will create a positive response which will strengthen the magnetic field. However, ferrimagnetic minerals (e.g. magnetite) will produce values 3 or 4 times greater than antiferromagnetic minerals (e.g. hematite). If the ferrimagnetic concentration is low, paramagnetic (e.g. clay and ferromagnesian silicate minerals) and diamagnetic minerals (e.g. biogenic carbonate, silica) will contribute to the measurement record (Stoner et al., 1996), with a negative response being indicative of a diamagnetic material in the sample. The measurement of this physical parameter is used for correlating changes in the sedimentary environment, as well as inter-core correlation (GEOTEK, 2014a).

The magnetic susceptibility was measured by a Bartington loop sensor with a given magnetic field.

3.4.2. X-ray Photography

X-ray photography is a non-destructive method of imaging material with the use of electromagnetic radiation. X-rays are generated when a high voltage direct current is applied to a cathode causing electrons to flow through a vacuum tube and collide with an anode (Fujifilm, 2014). When an incoming electron from the cathode collide with an inner-shell electron in the anode, a characteristic X-ray is emitted as a result of an electron from an outer shells falls into the vacant inner shell and emitting excess energy (Schad, 2008).

The factors which determine the quality of radiographs are contrast, sharpness and density. Magnification and distortion in an image can be dependent on geometrical arrangements relative to the X-ray tube and/or detector, difference in thickness throughout the core or the angle of the X-ray beam relative to the core specimen and detector (Fujifilm, 2014).

X-ray photographs were taken of half-core sections using the GEOTEK MSCL-XCT X-ray core imaging system (Fig. 3.6). The values used for getting satisfying exposure were 120kV and 225μA, and an image was taken every 20mm.
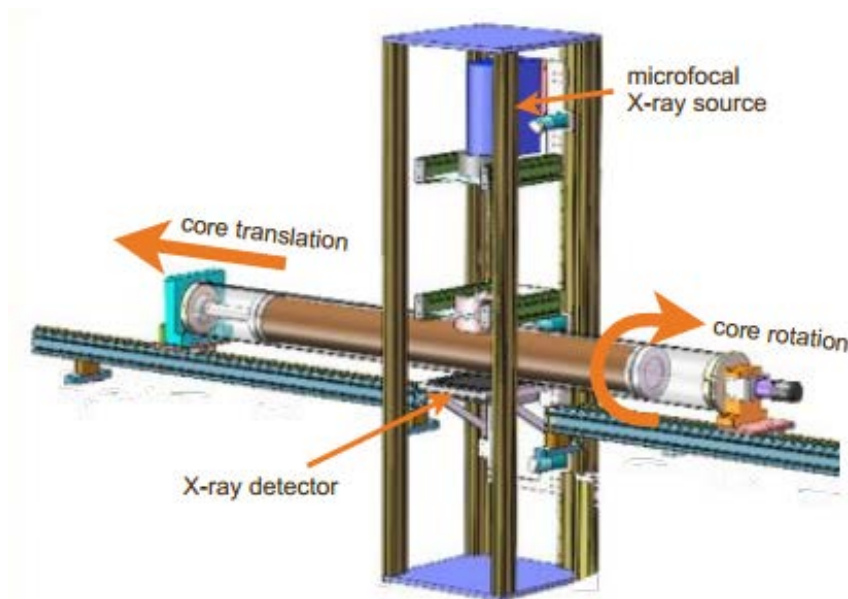

Figure 3.6: 3D model of the GEOTEK MSCL-XCT X-ray core imaging system (GEOTEK, 2014b)**.**

3.4.3. XRF-scan

X-Ray Fluorescence (XRF) core scanning is a non-destructive method used for analyzing elements on core surfaces (Marum, 2013b). The Avaatch XRF Core Scanner used X-rays from a radioactive source, rhodium (Rh), to excite and detect geochemical elements ranging

from Mg to U in the periodic table. When X-rays collide with matter, secondary, fluorescent X-rays are generated and measured for analysis of the geochemical composition of solids, liquids and powder (Beckhoff et al., 2006; Forwick, 2013a). For the best detection of lighter elements like Al, Si and Mg, a He atmosphere were used to reduce the friction on the secondary radiation caused by the presence of oxygen. To avoid misinterpretation of the results, usage of element ratios is highly recommended (Forwick, 2013a).

Measurements of the various elements are done in several runs with different currents (I), voltages (U) and filters applied. For measurements of light elements from Mg to Co 10kV is used, for Ni to Mo 30kV, and up to the heavy U 50kV is used (Forwick, 2013a).

Prior to measurement, the cores were adjusted to room temperature. Also, the core surfaces were smoothened and a 4μm ultralean film was applied to avoid contamination. Excess oxygen trapped between the film and sediments was removed. Values used were 10kV and 30kV with a measurement distance of 10mm.

In order to get an ideal measurement of the elements, the material should be homogenous, dry and have a flat surface. Comparison of XRF measurements conducted on wet sediments relative to dry sediment samples show that the intensity is largely reduced in light elements like Al and Si, whereas heavier elements remains relatively unaffected (Tjallingii et al., 2007; Weltje & Tjallingii, 2008; Hennekam & de Lange, 2012). The artefacts produced by these physical factors can be minimized by using element ratios instead of single element intensities, with every single element plotted against another element (e.g. Fe/Ca) or the sum of several elements (e.g. Ti/Sum) (Weltje & Tjallingii, 2008). The "sum" refers to all element count rates >10 000 during the 10 kV run.

Research in fjords using XRF data is relatively new and little is known about element interpretation within these environments. In other settings authors have attempted to correlate their results with the sediments´ provenance, composition and nature and the degree of terrestrial sediment discharge (Croudace et al., 2006; Rothwell et al., 2006; Calvert & Pedersen, 2007; Bertrand et al., 2012). Titanium (Ti) and zirconium (Zr) are both heavy and resistant minerals and are therefore often abundant in turbidite bases, while Kalium (K) is often associated with clay minerals, being enhanced in turbidite muds (Rothwell et al., 2006). Silicon (Si) is an important indicator for productivity, and along with aluminium (Al), iron (Fe), Ti and Zr also an indicator for terrigenous supply (McLennan et al., 2003; Croudace et

al., 2006; Bertrand et al., 2012). Carbon (C) is a carbonate indicator, and with Fe (Ca/Fe) also an indicator of biogenic carbonate:detrial clay ratio (Rothwell et al., 2006).

3.4.4. Sedimentological description and logging

A systematic description of the sediment surface of the working halves was carried out after opening. The surfaces were cleaned and described according to visual properties such as visible variations in grain size, clast-distribution, sedimentary structures (e.g. boundaries), bioturbation, fossils and general remarks. Color was determined with the help of the Munsell Soil Color Chart. Lithological logs were made to present these observations.

3.4.5. Grain-size analysis

3.4.5.1. Sampling and preparation

A total of 343 samples were taken and prepared for grain-size analysis. All five sediment cores were sub-sampled to perform grain-size distribution analysis. Sediment was sampled at intervals of 10 cm, with more frequent sampling in areas of interest/events. After sampling, the cups with sediments were dried in a heating cabinet for several days to be able to measure the sediments' water content. The samples were then treated with acetic acid (CH_3COOH) to eliminate carbonates and hydrogen peroxide (H_2O_2) to remove any organic matter present in the samples. The acetic acid was left over night, while the hydrogen peroxide had to be left for 4-5 days to complete the reaction. All samples were flushed twice with distilled water after the acetic acid treatment and centrifuged after the hydrogen peroxide in order to remove all the suspended organic material (especially the three cores from Moskusoksefjord contained much organic material). Finally, a few drops of calgon (sodium polyphosphate) were added to each sample, then placed in an ultrasonic bath, both to avoid the formation of clay aggregates (Hass et al., 2010). Immediately prior to measuring, all samples were shaken.

3.4.5.2. Measurements and statistics

The grain-size analysis was carried out with the LS 13 320 Laser Diffraction Particle Size Analyzer which only measures particles up to 2000 μm. Particles larger than this were therefore not included in the results, but are presented in the lithological logs as clasts. Due to too high concentrations indicated by the analyzer, most of the samples had to be diluted before measuring.

Classification of grain-sizes and associated terminology used in this study is based on the Udden-Wentworth grain-size for clastic sediments (Table 3-2) (Nichols, 2009). For describing the approximate relationship between the size fractions, Folk`s (1954) classification system for sand, silt and clay is used (Fig. 6.2).

Table 3-2: Overview of grain-sizes and associated descriptive terminology, based on Udden (1914) and Wentworth (1922). Modified from Nichols (2009).

mm	phi	Name	
256	−8	Boulders	
128	−7		
64	−6	Cobbles	Gravel
32	−5		
16	−4		
8	−3	Pebbles	
4	−2		
2	−1	Granules	
1	0	Very coarse sand	
0.5	1	Coarse sand	
0.25	2	Medium sand	Sand
0.125	3	Fine sand	
0.063	4	Very fine sand	
0.031	5	Coarse silt	
0.0156	6	Medium silt	
0.0078	7	Fine silt	Mud
0.0039	8	Very fine silt	
		Clay	

3.4.6. ^{210}Pb and ^{137}Cs dating

Two cm thick slices with approximately 20 g of sediments were collected every 10-50 cm from both HH13-008-GC-TUNU and HH13-012-GC-TUNU to perform a downcore analysis of the sediment accumulation rate. The sediments samples were dried so that the water content could be calculated, grounded and packed in sealed containers for further measurements.

3.4.6.1. Principle

^{210}Pb is a natural occurring radioisotope which in sediments can come from two sources; supported (autotochthonous) or excess (allochthonous) ^{210}Pb. The supported ^{210}Pb is a product of radioactive decay of uranium radioactive chain isotopes, and is produced in situ. Excess ^{210}Pb, on the other hand, is the product of decay of ^{222}Rn in the atmosphere, and is later deposited with the sediments (Sakuna et al., 2012). Excess ^{210}Pb is normally used for dating and will therefore be further discussed in this chapter. The signal of excess ^{210}Pb in sediments is a function of sedimentation rate, with maximum activity at the sediment surface, and can be indicative of changes in sedimentation rate, erosional events and presence of event layers. Low sedimentation rate will give a high excess ^{210}Pb and vice versa (Sakuna et al., 2012; Suckow, 2014). The radioisotope has an exponential decay with a half-life of 22.3 years and a dating range of up to 150 years. Its activity is measured by alpha spectroscopy of the granddaughter nuclide ^{210}Po, assuming secular equilibrium (Szczuciński et al., 2009; Suckow, 2014).

^{137}Cs is an artificial radionuclide that was introduced to the atmosphere by nuclear bomb-test, nuclear accidents (Chernobyl, Ukraine) and other discharges from nuclear installations. It is used as a radiotracer, with an onset around 1950, maximum peak in 1963 and the Chernobyl peak in 1986. The radionuclide has a half-life of 30 years and is often used for dating the last ~65 years (Pittauerova, 2009).

Possible uncertainties with using ^{210}Pb and ^{137}Cs for dating can be caused by sediment reworking (bioturbation, diagenetic processes) at the core site, grain-size variations within each core, loss of sediments from the top of the core during coring, cross-contamination during sampling, a wrong estimation of water content and dry bulk sediment, inaccurate radionuclide measurements and errors during the numerical calculation (Pittauerova, 2009).

3.4.6.2. Dating methods and calculation of the sediment accumulation rates

The activity of both ^{210}Pb and ^{137}Cs isotopes were measured with a gamma spectroscopy using a Canberra GX2520 high-purity coaxial germanium detector at the Institute of Geology, Adam Mickiewicz University in Poznan (Poland). Measurements for each sample took on average 24 hours. The decay activity was corrected for the date of sampling (Szczuciński, 2015).

Sediment accumulation rates were determined at the Institute of Geology, Adam Mickiewicz University in Poznan through complementary ^{210}Pb and ^{137}Cs analyses. The sediment accumulation rates were calculated from the decrease of excess ^{210}Pb activities with sediment depth in accordance with McKee et al. (1983). By subtracting the average supported activity taken from the sample below the region of radioactive decay from the total activity, the excess ^{210}Pb activities were determined. The independent sediment accumulation rates assessment was made using the first occurrence of ^{137}Cs as a marker of the early 1950s (taken as 1952), its maximum activity peak as ~1962 and younger secondary activity peak as Chernobyl-related 1986 marker (e.g., Robbins and Edgington 1975, Appleby 2008). Due to possible loss of core top sediment layers, sediment mixing, variations in sediment accumulation rates and low activities of excess ^{210}Pb, the calculated sediment accumulation rates must be treated as approximate values (Szczuciński, 2015).

3.4.7. Radiocarbon dating

3.4.7.1. Principle

Radiocarbon dating is a method based on measuring the decay of ^{14}C, and can be used for dating materials younger than 50 000 years. 14C is a natural occurring radioactive carbon isotope formed in the upper atmosphere when cosmic ray neutrons collide with ^{14}N atoms. After oxidation, CO_2 is created and mixed in the atmosphere and oceans where they enter plant material through photosynthesis and become a part of calcareous ($CaCO_3$) marine organisms through the carbon cycle. When organisms die, they are no longer in equilibrium with the atmosphere and biosphere, and the unstable ^{14}C will start to decay with a half-life of 5730 ± 40 years. By measuring the number of the unstable ^{14}C relative to the stable ^{12}C and ^{13}C information about when the organism died can be calculated (Bowman, 1990).

3.4.7.2. *Accelerator Mass Spectroscopy (AMS)*

The samples were prepared and measured at the Laboratory for Ion Beam Physics, ETH Zurich, using the Accelerator Mass Spectroscopy (AMS) method. AMS is performed by accelerating C-ions from the sediment samples and subjecting them to a magnetic field. Particles with the same velocity, but different mass, will deflect differently towards the applied magnetic field. The heaviest particles will deflect the least, making it possible to identify and measure the amount of ^{14}C present in the sample (Bowman, 1990; Higham et al., 2014). The Laboratory for Ion Beam Physics uses a new method capable of dating samples containing less than 100 µg carbonate. The method determines the radiocarbon content of carbonates by directly measuring the CO_2 produced by acid decomposition with a gas ion source AMS (for more information, see Wacker et al., 2013 & Bard et al., 2015).

3.4.7.3. *Calibration and marine reservoir effects*

The production rate of ^{14}C in the atmosphere is not constant due to different factors like the Earth's magnetic field, sunspot activity and the Suess effect. The concentration of ^{14}C in both atmosphere and in living organisms varies through time, resulting in a discrepancy between the radiocarbon age and calendar age (Bowman, 1990). With the AMS, the radiocarbon dates are calibrated to calendar years before present (cal. yr. BP).

The ^{14}C produced in the atmosphere is constantly supplied to the sea surface by an exchange at the ocean-atmosphere interface, and is believed to be in a state of equilibrium. However, as the water masses sinks, the supply of ^{14}C from the atmosphere is cut off and the decay of the unstable ^{14}C isotope occurs in a closed system. This radioactive decay will give a lower ^{14}C activity, and the ocean water will therefore have an increased apparent age called the marine reservoir effect (Mangerud, 1972). The average marine reservoir age is 440 years, and the regional marine reservoir age for East Greenland is 550 ± 54 years (Hjort, 1973; Håkansson, 1973). When dating calcareous marine organisms the ageing effect of the region has to be accounted and calculated for to avoid large regional variations.

The CALIB 7.1 software (Stuvier et al., 2015) was used in order to calibrate the radiocarbon ages obtained from the AMS dating. The program used the MARINE13 calibration curve (Reimer et al., 2013) with a global reservoir correction of 405 years. To accommodate for the difference between the East Greenland reservoir age and the model ocean, an additional regional difference (ΔR) was added. In this study, a ΔR of 166 ± 54 was applied (Hjort, 1973; Håkansson, 1973).

3.4.7.4.   *Radiocarbon dating and estimation of an age model*

The obtained radiocarbon dates were used for estimating an age model for the sediment cores. By using a linear interpolation and assuming a constant accumulation of sediments between the dated intervals, the boundaries between the time periods were estimated. However, studies show that uncertainties are to be expected, especially when there are only a few dates available (Telford et al., 2004).

4. Swath bathymetry

4.1. Introduction

A swath bathymetry data set has been used to identify, describe and interpret the submarine geomorphological landforms in both Nordfjord and Moskusoksefjord. In addition, chirp sonar profiles (Chapter 5) and sediment samples (Chapter 6) were used to do a more detailed interpretation of the sedimentary processes and products of the shallow sub-seafloor in both fjords. The study area extends from mid Moskusoksefjord to the point where Nordfjord opens up to Kejser Franz Joseph Fjord. The bathymetry data is ~53 km long and between 0.7 and 2 km wide. Large parts of Nordfjord (mostly the shallow-water parts) were not covered by the swath bathymetry survey. Since the data set from Nordfjord is very limited, the Moskusoksefjord data will be the focus of the following subchapter.

4.1.1. Large scale morphology

There are four basins within the study area; three are located in Moskusoksefjord and one in inner Nordfjord (Fig. 4.1). In Moskusoksefjord the inner-, middle- and outer basins are separated by relatively large deltas prograding into the fjord from both sides. Based on the data set a total of 18 deltas of various sizes have been identified (Fig. 4.1), as further detailed below. The water depth increases gradually from the fjord mouth towards the inner part of Moskusoksefjord. The outer basin has a maximum water depth of about 237 m, the middle reaches 245 m and the inner basin is the deepest with its 260 m. However, the deltas separating the outer- and middle basin form a threshold at 216 m, whilst the threshold between the middle- and inner basin is located at 210 m water depth.

The gradients of the fjord slopes reaches occasionally 30˚, with maximum gradients >40˚ on the NE slope in the middle basin. The seafloor of the basin floor appears as generally smooth, while a number of small- and large-scale landforms characterize the basin side walls. Here several slide scars and sediment lobes are found, and together with numerous grooves, they contribute to the rugged appearance of the fjord slopes. At the fjord mouth two transverse ridges have been observed. All landforms mentioned above are discussed in more detail below. In the studied part of Nordfjord the seafloor has a generally smooth appearance. However, a slide scar and several sediment lobes have been identified.
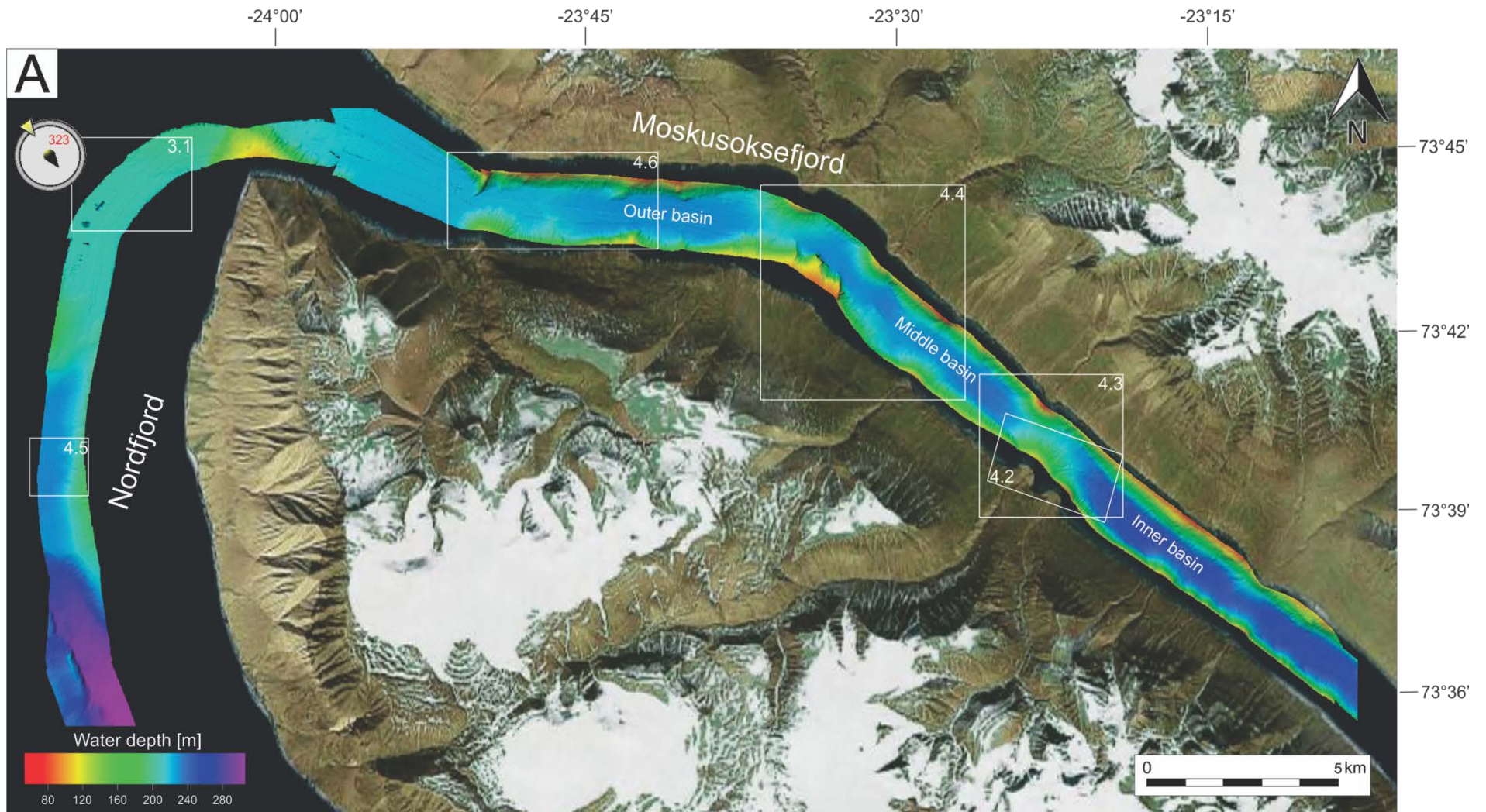
Figure 4.1: *A)* **Swath bathymetry data of Nordfjord and Moskusoksefjord, North-East Greenland. White boxes indicate the locations of areas shown in Fig. 3.1 and 4.2 – 4.6.**
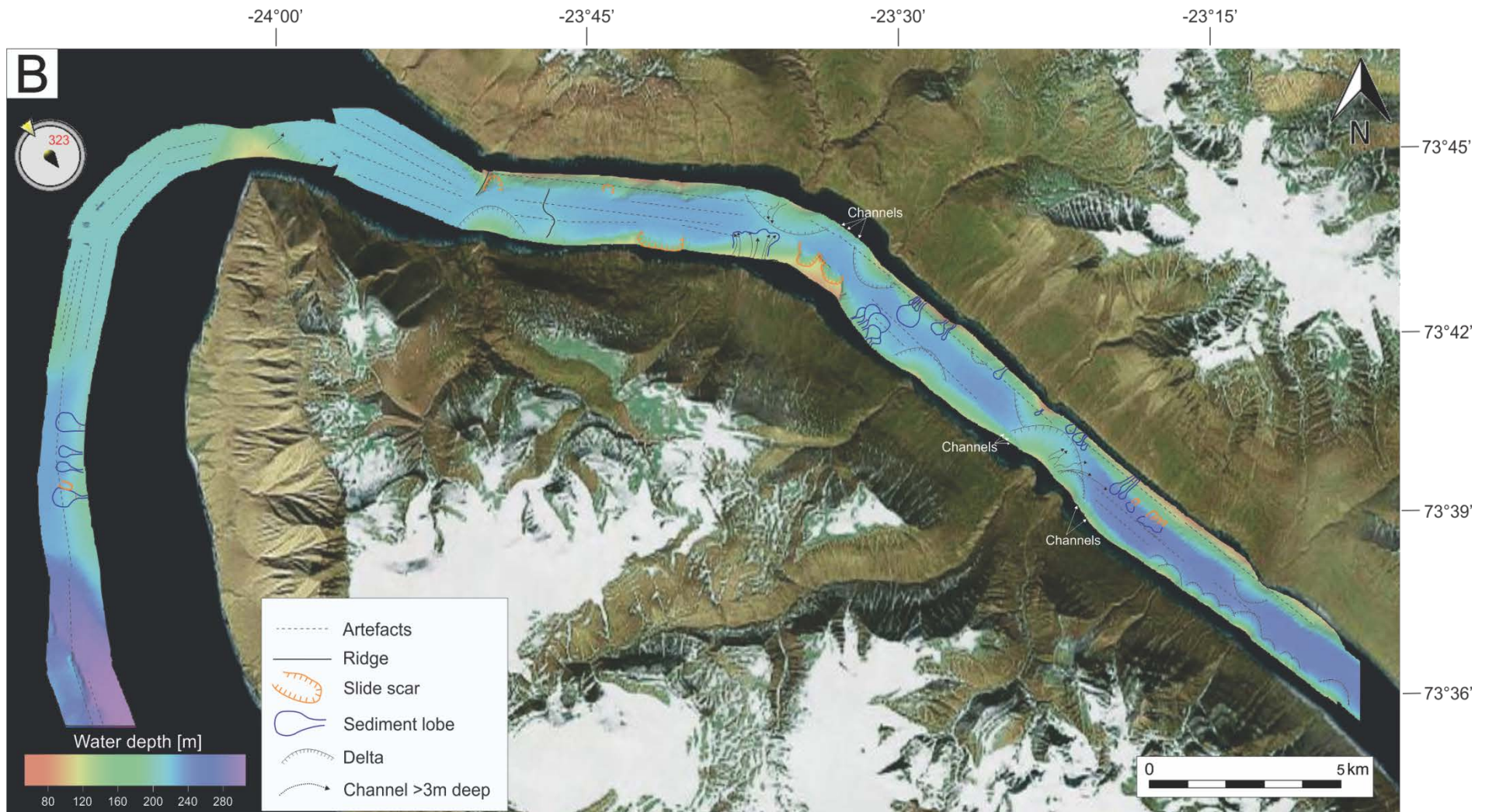
Figure 4.1: *B)* **The swath bathymetry data with interpretation and distribution of the large-scale morphology in Moskusoksefjord and Nordfjord, North-East Greenland.**

4.1.2. Deltas

A total of 18 deltas of different sizes are observed along the fjord sides in Moskusoksefjord (Fig. 4.1). 13 of the deltas are located along the S-SW fjord sidewall and five on the N-NE side. The different deltas in Moskusoksefjord can be divided into two groups based on their origin; fan deltas and river deltas. A fan delta is developed when an alluvial fan builds into standing water (Prior and Bornhold, 1990; Nichols, 2009). They are located in areas with steep fjord walls, have small catchment areas and generally consist of coarse sand and gravel (Prior and Borhold, 1990). River deltas, on the other hand, form where a river enters standing water and builds a sediment body (Nichols, 2009). In addition to different origins, fan deltas and river deltas also have different dimensions and slope gradients. The river deltas in Moskusoksefjord have a maximum width ranging from 1.5 to 2.3 km, with the largest delta located on the S-SW fjord side between the middle- and inner basin (see Fig. 4.2 and 4.3). The fan deltas, however, have maximum widths from 350 m and up to about 1.1 km.

In Moskusoksefjord there are 11 observed fan deltas, where ten of them are located along the S-SW fjord sidewall in the inner basin. The fan deltas in Moskusoksefjord have steep slope gradients, exceeding 30° in some areas.

Unlike the fan deltas of Moskusoksefjord, all river deltas surveyed have channels on their distal fan areas where the slope gradient is <10° (Fig. 4.2). The upper part of the deltas, where the slope gradient exceeds 15°, the slope surface generally appears to be smooth.
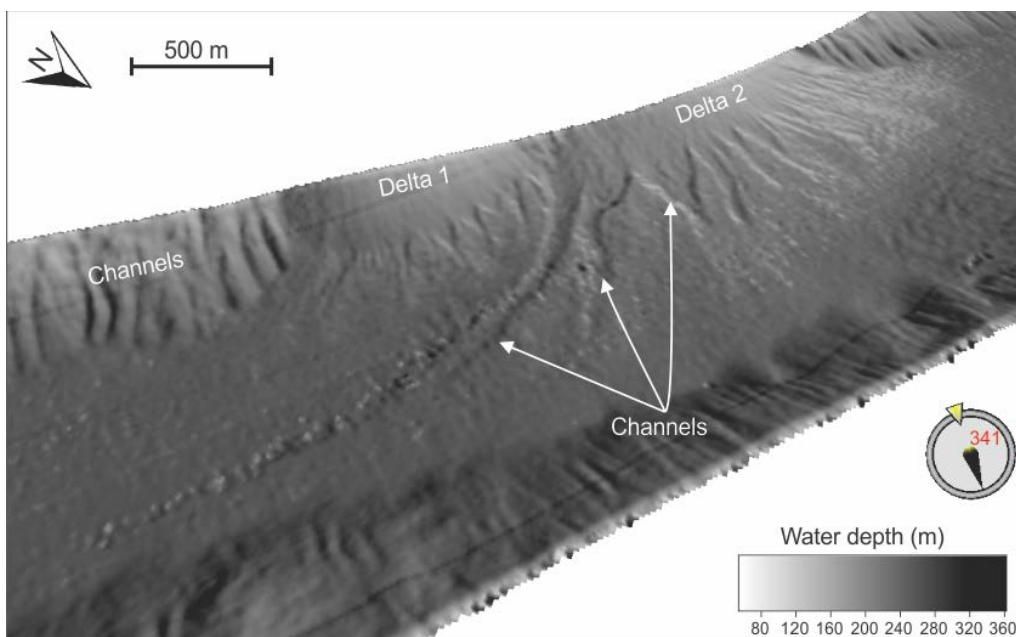
Figure 4.2: Shaded bathymetry image showing the morphology of two river deltas with accompanying channels in more detail (for location see fig. 4.1).
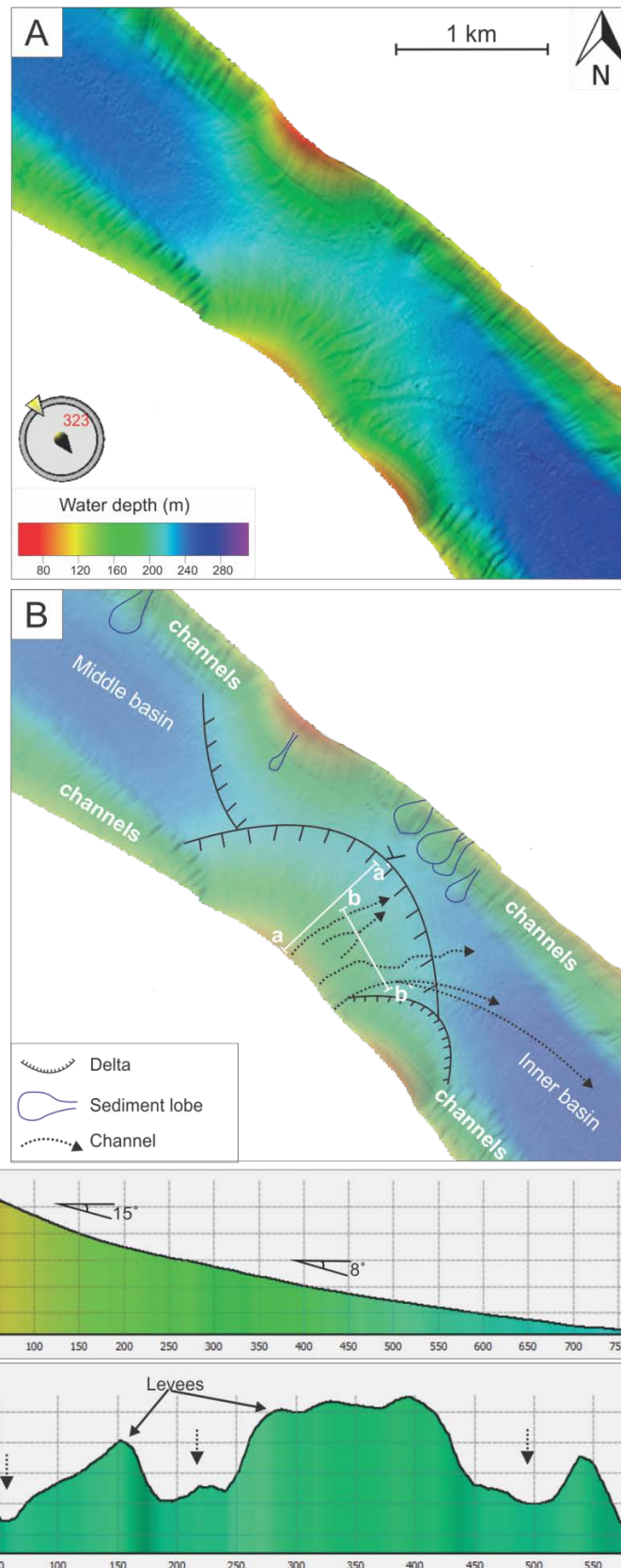
Figure 4.3: Swath bathymetry data and bathymetric profiles of the central part of Moskusoksefjord (see fig. 4.1 for location). Vertical exaggeration is 4.

A) **The two river deltas forming a threshold between the inner- and middle basin.** *B)* **Interpretation of the main morphological features.**

Slope profile *a* **shows the slope gradient of the river delta located on the W-SW fjord slope. Cross profile** *b* **shows the width, depth and form of the channels on the delta slope, located by black dotted arrows.**

4.1.3. Channels

Numerous downslope oriented, straight and shallow grooves have been identified along the fjord sides of Moskusoksefjord. They occur most frequently on the fjord sides in the middle basin and in the outer part of the innermost basin (Fig. 4.1). Here the fjord sides are steepest, exceeding 40˚ in some areas.

The longest, widest and deepest is observed on the southern delta separating the middle- and inner basin (Fig. 4.2 and 4.3). It has a depth ranging from 2-6 m, width of 10-150 m and can be followed approximately 2.2 km curving in a southeasterly direction into the fjord bottom where it terminates. The floor of the feature is uneven with a thalweg following the outer bend. Some of the grooves end downslope with thin splays (Fig. 4.2). Most of the features have adjoining levees (Fig. 4.3, profile *b*).

The grooves are interpreted to be submarine channels formed by erosion from turbulent flows. Channels confine the flow, acting as pathways for turbidity currents (Nichols, 2009) that are probably produced by slope failures or hyperpycnal flows (Mulder, 2011).

4.1.4. Slide scars and sediment lobes

Seven slide scars and numerous sediment lobes have been identified (Fig. 4.1). These features mostly occur in and near the middle basin of Moskusoksefjord and in the central part of the Nordfjord data set.

In Moskusoksefjord two relatively large scars are observed side by side in the outer part of the middle basin, and four smaller scars are located within a 1 km wide area on the E-NE slope in the inner basin. I Nordfjord only a single scar is observed. The slide scars vary in shape and size as well as "freshness". Their width ranges from 100-700 m, depth from 3-30 m and headwall gradient 14˚ to 30˚. At present only the scars in the inner basin of Moskusoksefjord have visible lobe shaped deposits directly downslope of the features (Fig. 4.1).

The sediment lobes vary in both size and character and are often found as sets of several superimposed lobes. They generally have lengths of 100-550 m and maximum widths from 80 m up to about 850 m (see Fig. 4.5, profile *a* and *c*). Some of the sediment lobes are not associated with observable incisions on the upper part of the slope.

Two sediment lobes located in front of slide scars and a slide scar without an associated sediment lobe has been identified in Nordfjord. The slope gradient is 6˚ in the upper, erosional scar and 2˚ in the lower, depositional zone of one of the sediment lobes (Fig. 4.5). The depth

of the incision on the upper part of the slope is 4.5 m, and the width is 115 m. The sediment lobe on the fjord bottom reaches a width >335 m and a thickness >2.7 m (Fig. 4.5, profile *c*). The surface of the sediment lobe is rugged, but due to a low resolution on the bathymetry it is not possible to determine if it is due to smaller superimposed lobes or channels (Fig. 4.5, profile c).

The slide scar headwall in figure 4.5 is ~170 m long and 10 m high. Profile *d* shows a slope gradient of maximum 14° at the headwall and an overall gentler slope inclination of 8° in the middle and 2° in the lower slope areas. The present slope inclination outside the slide scar is ~5° in the upper slope areas and 2° in the lower. Profile *e* crossing the slide scar reveals that the feature is 2.5 m deep and 153 m wide. Slope angle is 4° on both the northern and southern side walls. The slide side walls have rounded edges.
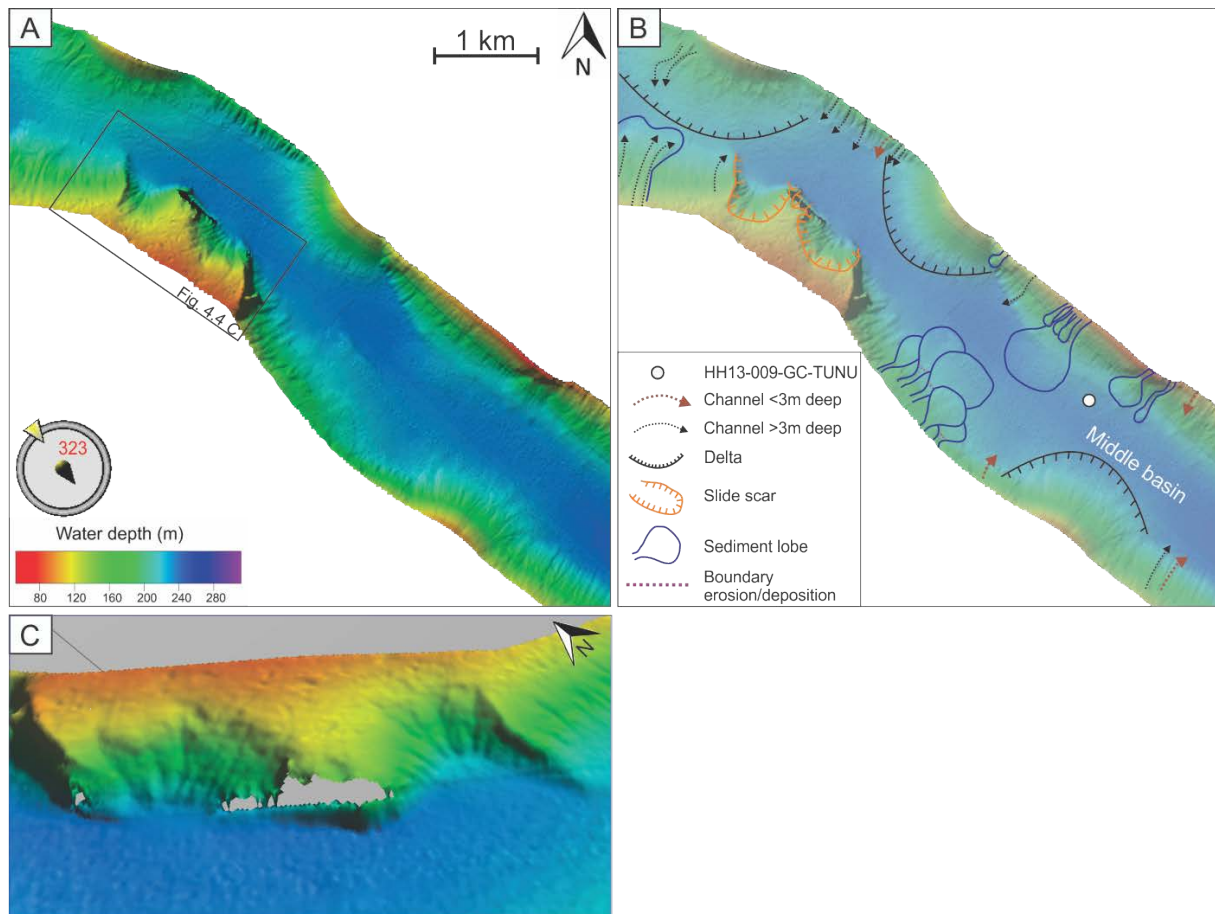
Figure 4.4: *A) Swath bathymetry data of the middle basin in Moskusoksefjord (see fig. 4.1 for location). B) Interpretation of the main morphological features of the middle basin. C) The morphology of two slide scars (see A for location), no sediment lobes have been identified in front of the scars.*

The sediment lobes are interpreted to comprise mass-transport deposits from slope failures on the steep fjord walls. Slope failures are initiated when the gravitational shear stress exceeds the sediment`s shear strength (Løseth, 1999). Factors controlling slope failures in fjords are the topography, the supply of material, the physical properties of the sediment and the triggering mechanism. Examples of triggering mechanisms are earthquakes, sediment loading, erosion, sea-level fluctuations, climate change and human activity (Syvitski et al., 1987; Forwick & Vorren, 2002; Nichols, 2009).

4.1.5. Transverse ridges

Two ridges are identified in the outer basin of Moskusoksefjord (Fig. 4.6), located at ~80m and ~260 m water depth. Ridge 1 is oriented transverse to the fjord axis, stretching 1.3 km in a general N-S direction. The ridge slopes gently towards north starting at a height of 15 m, decreasing to a minimum of 3 m. Its width narrows from 800 m in the south to 400 m in the north. A cross-profile of the ridge (Profile *a*, fig. 4.6) shows a general symmetry, with a ~3˚ slope towards the fjord mouth, and ~4˚ on the in-fjord side.

Ridge 2 stretches 770 m in a N-NE to S-SW direction and slopes from a height of 140 m and down to the sea floor. It has a steeper slope exceeding 30° on the in-fjord side and a gentler outer slope of ~20°. Its width varies between 210 m in the upper part to almost 300 m in the lower part.

Based on the bathymetry data it is difficult to determine whether the ridges are glacial moraines or of bedrock origin. According to Ottesen and Dowdeswell (2006) large transverse ridges oriented perpendicular to the fjord axis are often found in front of tidewater glaciers, marking the maximum extent of the last ice advance (e.g. on Svalbard). However, terminal moraines normally show an asymmetric shape with a steeper ice-proximal slope and a gentler distal slope (Ottesen and Dowdeswell, 2006; Winkelmann et al., 2010). The origin of the transverse ridges will be further discussed in chapter 5.
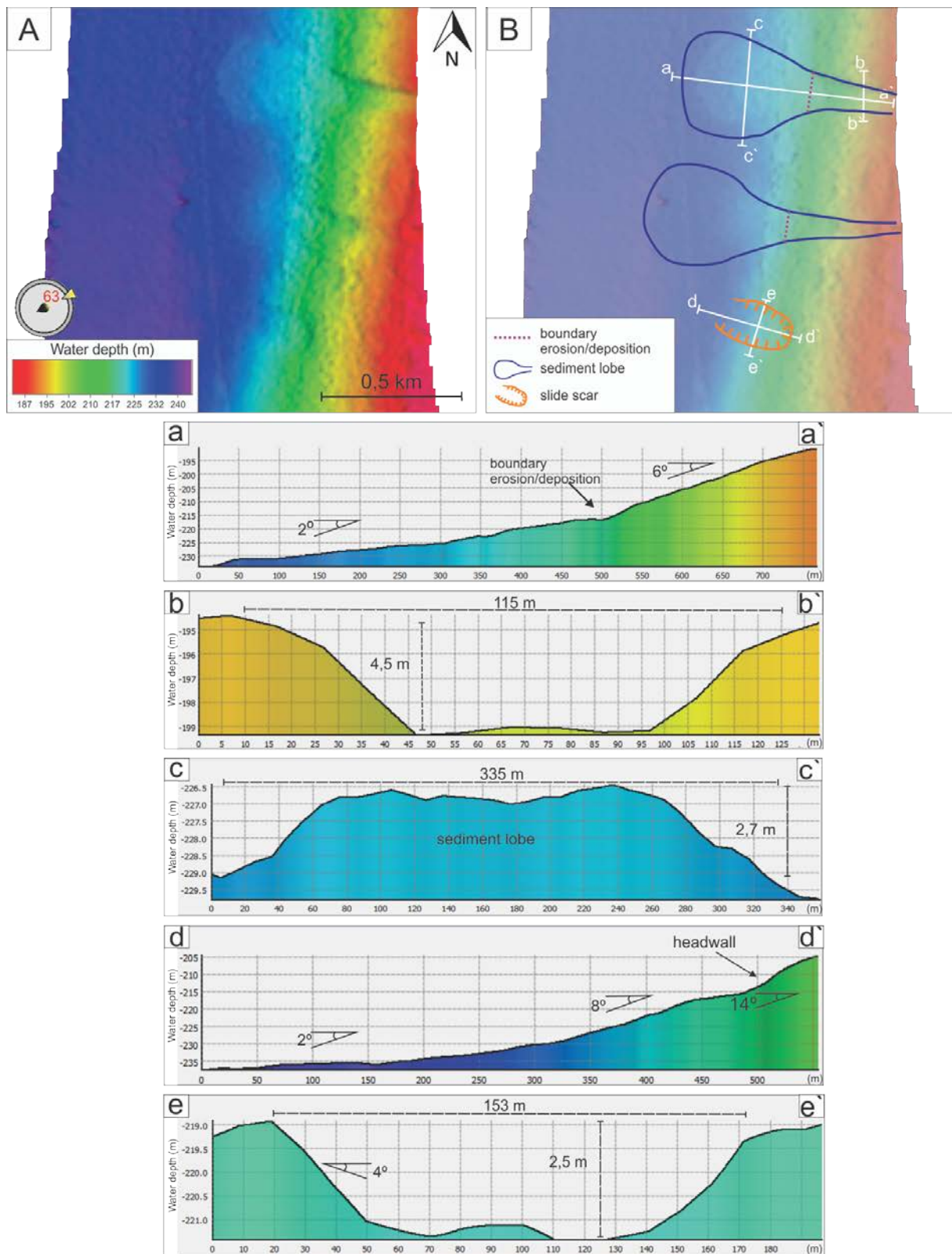
Figure 4.5: Swath bathymetry data and bathymetric profiles from Nordfjord (see Fig. 4.1 for location). *A)* A slide scar and two of the sediment lobes from Nordfjord. *B)* Interpretation of the morphological features in Nordfjord. Profile *a* show a down-slope oriented profile of the northern sediment lobe, cross profile *b* show the incision on the upper part of the slope and cross profile *c* shows the sediment lobe on the fjord bottom. Profile *d* shows the slope profile of the slide scar in Nordfjord, and *e* its cross profile.
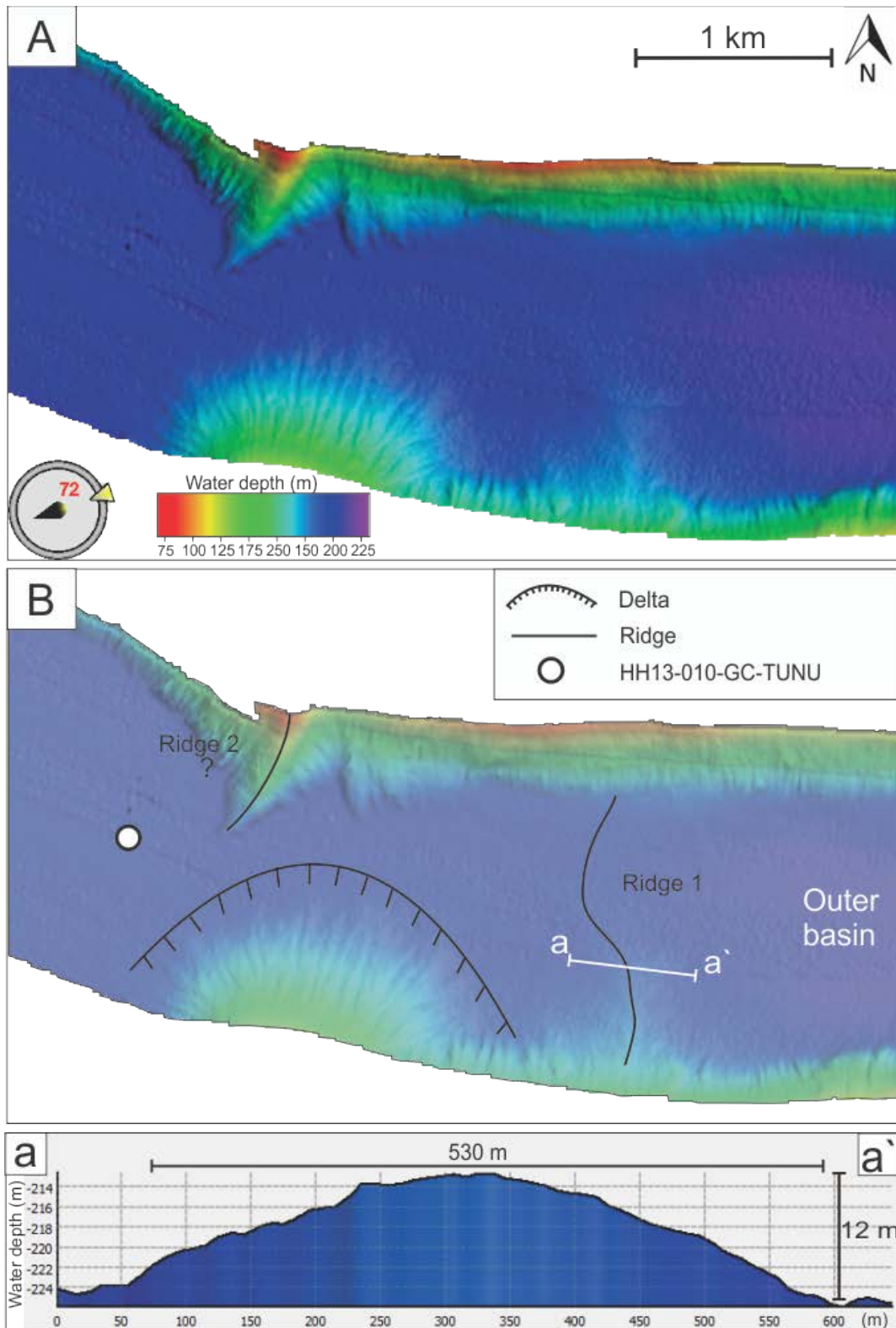
Figure 4.6: Swath bathymetry data and a bathymetric profile of the outer part of Moskusoksefjord (see Fig. 4.1 for location).
A) **A delta and two possibly partly buried transverse ridges at the fjord mouth of Moskusoksefjord.** *B)* **Interpretation of the main morphological features.**
Profile *a* show a cross-profile of Ridge 1.

5. Seismostratigraphy

5.1   Introduction

In the following chapter the available chirp sonar data from the study area will be addressed. Previously, high-resolution seismic data (Parasound sediment echo sounder) from middle-outer Kejser Franz Joseph Fjord have been described by Evans et al. (2002). Acoustic facies interpreted to be Holocene glacimarine sediments was identified, inferred to be predominantly transported by and deposited from suspension settling from meltwater plumes (Evans et al., 2002). Sediment gravity flow deposits were also identified by Evans et al. (2002).

A total of 11 chirp lines (Fig. 3.1) were collected in Nordfjord and Moskusoksefjord, all parallel to the fjord axis. Three of the lines were selected in order to study the main erosional and depositional features of the shallow sub-seafloor (for location see Fig. 5.1);

- TUNU_V_006, located along the eastern side of inner Nordfjord (Fig. 5.4)
- TUNU_V_007 which extends through the outer basin of Moskusoksefjord (Fig. 5.3)
- TUNU_V_009 stretching along the NNE side of the middle- and inner basin of Moskusoksefjord (Fig. 5.2).

The y-axis on the chirp profiles show the two-way-travel time (TWT) in seconds. When converted to sediment thickness (m) a velocity of 1600 m/s was used based on previous studies in East Greenland fjords (Andrews et al., 1994).

5.2.   Seismostratigraphic description and interpretation

The reflection patterns vary between the two fjords, as well as in the three basins of Moskusoksefjord. Therefore, the following seismostratigraphic description and interpretation is divided into four subchapters (*5.2.1 Inner basin of Moskusoksefjord, 5.2.2 Middle basin of Moskusoksefjord, 5.2.3 Outer basin of Moskusoksefjord* and *5.2.4 Nordfjord*). Also, reflections and seismic units (including mass transport deposits (MTD)) are given names accordingly to their location (*N*- Nordfjord, *O*- outer basin, *M*- middle basin and *I*- inner basin). Below the main reflections and units identified are discussed followed by a short summary.
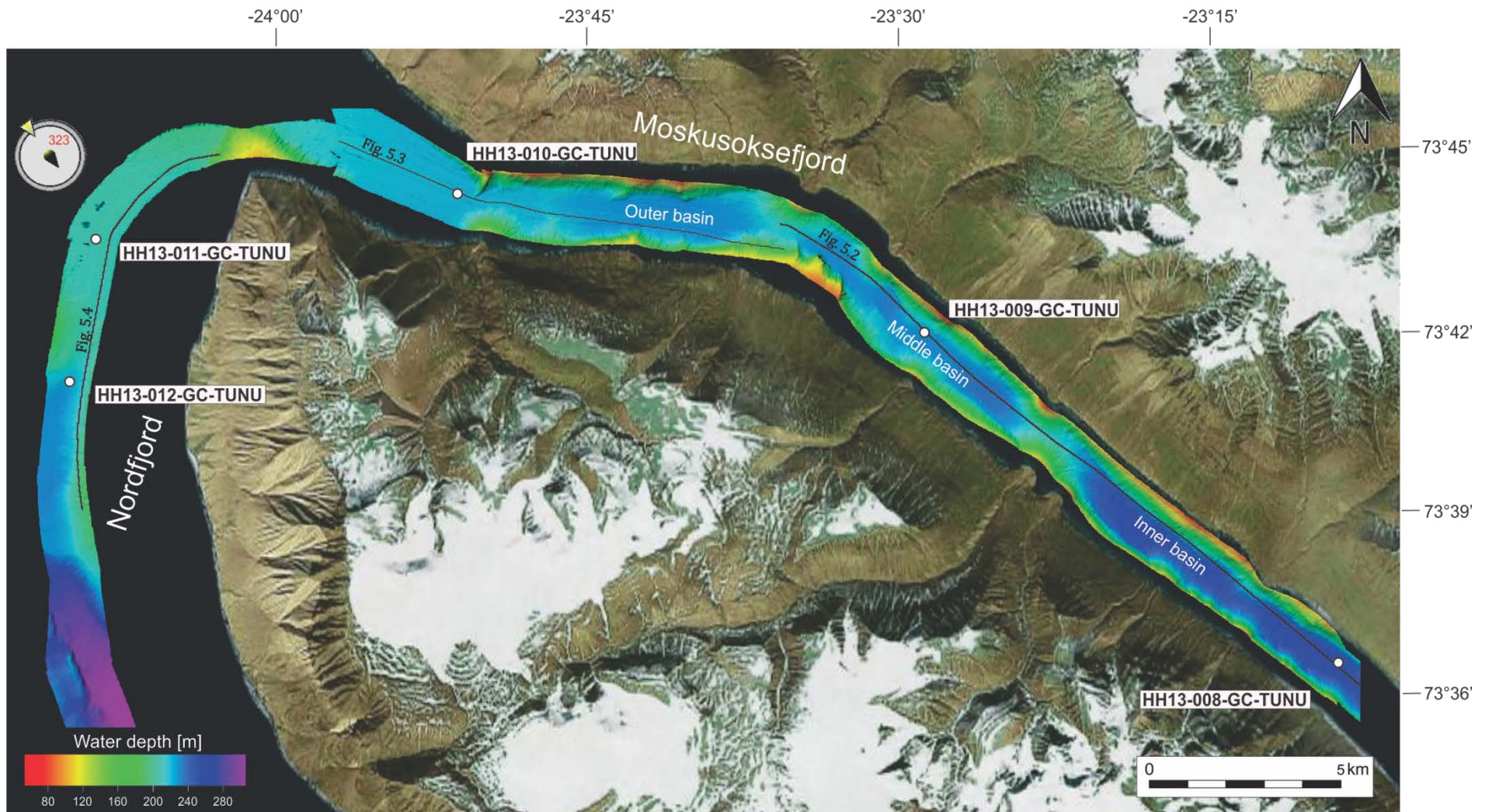
Figure 5.1: The swath bathymetry data of Nordfjord and Moskusoksefjord including the location of the gravity cores and chirp lines selected for this study. Chirp lines are displayed as black lines and core locations with white circles.

5.2.1. The inner basin of Moskusoksefjord

The seismostratigraphy of the inner basin of Moskusoksefjord is here presented by chirp line TUNU_V_009 (Fig. 5.2). The chirp line show parts of the NNW fjord sidewall, two deltas and the central part of the inner basin. The main reflections and units interpreted from the profile are *I-R1* and *I-R2,* and *Unit I-1* to *Unit I-2,* respectively (Fig. 5.2*C*).

Reflection *I-R1* is the lowermost reflection in the inner basin of Moskusoksefjord and defines the boundary between *Unit I-1* and *Unit I-2* (Fig. 5.2*C*). *Unit I-1* has an acoustically transparent signature with a rugged and undulating surface. The boundary to the overlying unit is diffuse and, in consequence, often difficult to trace. There is no lower boundary of this unit visible on the chirp line. The unit's acoustic signature indicates a relatively uniform lithological composition of the sediments. Based on this, and its proximity to the deltas, the unit is seemingly a result of unstable sediments re-deposited from the delta slope.

Above reflection *I-R1* lays *Unit I-2*, the uppermost seismostratigraphic unit of the inner basin (Fig. 5.2*C*). *Unit I-2* consists of a thick package of near-parallel, onlapping acoustic stratified sediments. Its reflections are continuous to semi-continuous, abundant and with amplitude ranging from high to low. The unit thickness exceeds 30 m in the central parts of the inner basin, and wedges out and becomes generally thin or absent over obstacles. The reflections are in some parts difficult to follow, either due to signal attenuation due strong overlying reflections casting acoustic shadows, or due to disturbance/erosion caused by mass wasting deposits (MTD). The latter seems to recur periodically in the proximity to the delta slope.

The strong acoustic stratification in *Unit I-2* is interpreted to reflect repeated changes in the lithological composition of the sediments. The proximity to several river deltas most likely contributed to acoustically stratified sediments representing lithological changes related to seasonal variations in sediment supply as documented from other areas (Forwick and Vorren, 2011). Also, in a marine fjord environment with steep slopes relatively frequent episodes of re-sedimentation of slope sediments is to be expected. These lithological changes have also been identified in sediment core HH13-008-GC-TUNU from this basin and will be further discussed in Chapter 6.

The seafloor reflection *I-R2* can be seen as a strong, continuous reflection in the lower, central part of the basin and over Delta 3 (Fig. 5.2*A*). However, on Delta 4 and the fjord sidewall *I-R2* is more diffuse due to a more irregular morphology caused by channels and slide scars (see Fig. 4.1).

5.2.2. The middle basin of Moskusoksefjord

The seismostratigraphy from the middle basin of Moskusoksefjord is also exemplified by chirp line TUNU_V_009 (Fig. 5.2). Three deltas and one MTD are seen on the profile in addition to a >27 m thick acoustically stratified sedimentary succession. Three reflections (*M-R1* to *M-R3*), three units (*Unit M-1* to *Unit M-3*) and one MTD (MTD_{M-1}) observed in the seismostratigraphy are described and interpreted below.

Unit M-1 is acoustically laminated with continuous reflections. The reflection amplitude is low to moderate, and the reflection abundance is moderate to high. The unit lies concordant below reflection *M-R2* and is seen as an infill in the sub-basin between MTD_{M-1} and *Unit M-3* (Fig. 5.2*B*). *Unit M-1* exceeds 27 meters in thickness in the lower, central parts and wedges out towards the deltas and MTD. The lower boundary of the unit was not identified on the chirp line due to the lack of penetration. The upper boundary reflection *M-R2*, however, marks a transitional, but distinctive change in the acoustic signature from low-moderate amplitude to high amplitude reflections. The internal reflection characteristics of the overlying *Unit M-2* show high, semi-continuous-continuous stratification with onlapping parallel reflections. The reflection abundance is high. *Unit M-2* has a maximum thickness of 4 m, but, like *Unit M-1*, it wedges out and becomes generally thin or absent towards the deltas and MTD. Its thickness appears even where the underlying bed is flat. The higher amplitude of the *Unit M-2* reflections compared to *Unit M-1* may indicate more frequent and/or pronounced changes in lithology as will be discussed below. In the lower part of sediment core HH13-009-GC-TUNU this change is reflected by a marked change to the occurrence of coarser material (see *Chapter 6.4.1.1. Lithology and stratigraphy*).

MTD_{M-1} is an acoustically semi-transparent to transparent unit with lobate geometries and a few chaotic internal reflections. It lies beneath parts of *Unit M-1* and *Unit M-2*, but has no lower boundary detectable on the chirp line. The unit is difficult to trace on the chirp line, but has been interpreted to consist of successive deposits of debris flows, as indicated on the bathymetry data set (see Fig. 4.4).
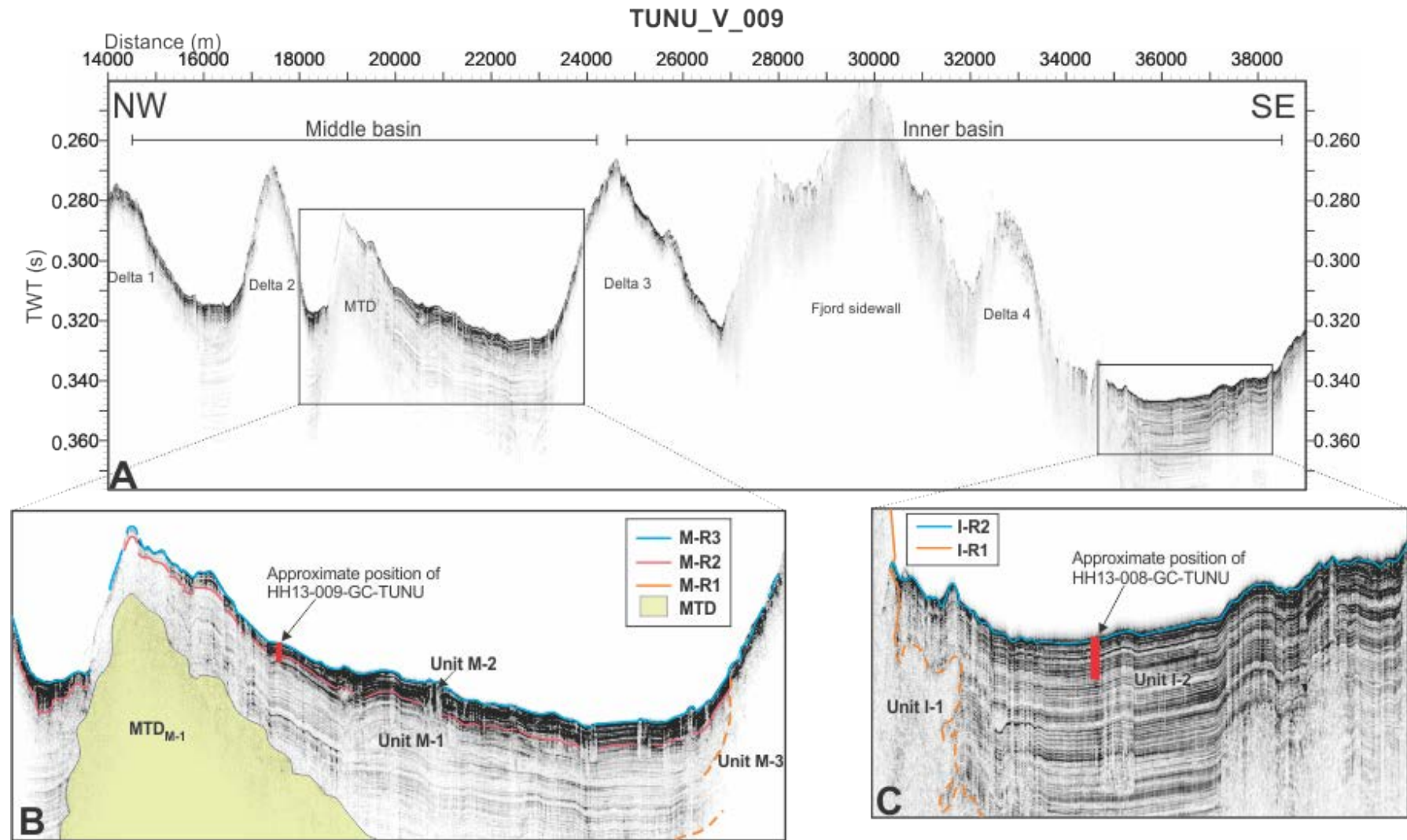
Figure 5.2: A) Chirp line TUNU_V_009 from the middle- and inner basins of Moskusoksefjord (see Fig. 5.1 for location). Four deltas, a mass-transport deposit and parts of the fjord sidewall are indicated. B) Middle basin of Moskusoksefjord. Reflection *M-R1* to *M-R3*, *Unit M-1* to *Unit M-3 and MTD$_{M-1}$* are indicated. The approximate position of sediment core HH13-009-GC-TUNU is also indicated. C) Inner basin of Moskusoksefjord. The location of reflection *I-R1* and *I-R2* and *Unit I-1* and *Unit I-2* are shown. The approximate position of sediment core HH13-008-GC-TUNU is indicated.

Unit M-3 is a semi-transparent to transparent mound-shaped unit with an irregular to very irregular upper seabed reflection (*M-R3*). The unit has no lower boundary, and the transition (*M-R1*) between *Unit M-3* and *Unit M-1* is gradual and diffuse, and therefore difficult to trace. Reflection continuity is low, and similar to *Unit I-1,* the unit also has a relatively uniform lithological composition. *Unit M-3* is interpreted to comprise delta sediments, where the presence of lobes and channels gives it an irregular upper surface.

The seabed reflection *M-R1* is strong and near-continuous, defining the upper horizon of *Unit M-2* and *Unit M-3.*

5.2.3. The outer basin of Moskusoksefjord

Chirp line TUNU_V_007 was chosen to present the seismostratigraphy of the outer basin in Moskusoksefjord (Fig. 5.3). The chirp line starts where Moskusoksefjord opens up towards Nordfjord and Waltershausen Gletscher and continuous all the way to the transitional area between the outer- and middle basin. A small ridge (see *Chapter 4.1.5 Transverse Ridges*), two distinct MTDs and a thick sedimentary succession are observed in addition to parts of the fjord sidewall, with two bedrock highs/moraines(?) separating the outer basin of Moskusoksefjord into two sub-basins. Three reflections (*O-R1* to *O-R3*), two main units (*Unit O-1* to *Unit O-2*) and two MTDs (MTD_{O-1} and MTD_{O-2}) have been discussed below.

Unit O-1 has an acoustically stratified signature with moderate to low amplitude, moderate reflection abundance and high to moderate continuity. In sub-basin 1 two MTDs also occur (MTD_{O-1} and MTD_{O-2}), while in sub-basin 2 the *Unit O-1* appears to be generally undisturbed. On the available data its thickness ranges from 3.5 m over the WNW bedrock high to reach more than 47 m in the ESE sub-basin. The unit has no lower boundary visible on the chirp line, thus the estimated sediment thickness should be regarded minimum estimates.

Concordant above *Unit O-1* lays *Unit O-2*, a package of acoustically stratified continuous to semi-continuous reflections. Both reflection amplitude and abundance is high in this unit. However, in some areas the continuity is lower. *Unit O-2* is the uppermost sediment package throughout most of the basin, but with a varying thickness. In sub-basin 1 the unit has a near uniform thickness of 6.5 m, in sub-basin 2 the unit thickness increases to 10 m. The unit consists of near-parallel onlapping sediments which either drapes or infills small depressions within the seafloor. Both *Unit O-1* and *Unit O-2* are interpreted as glacimarine sediments

transported and deposited by sediment gravity flows and suspension settling from meltwater plumes and/or rivers. This is supported by the lithology observed in sediment core HH13-010-GC-TUNU (see *Chapter 6.5.1.1. Lithology and stratigraphy*). Similar to the sedimentary succession in the middle basin of Moskusoksefjord, the *Unit O-1* to *O-2* transition represents a sudden increase in both the reflection abundance and amplitude interpreted to be due to more pronounced changes in lithology as will be further discussed below.

A package of acoustically transparent sediments, referred to as MTD_{O-1}, is located within *Unit O-1,* ~20 m below the seafloor. The MTD lies below MTD_{O-2} and is bounded by the WNW bedrock high separating the two sub-basins. The thickness of the package is 14.5 m in WNW and decreases to a minimum of 1.5 m as it reaches the WNW morain/bedrock high in ESE. The package has a hummocky upper boundary, and an erosional, lower boundary forming a disconformity to the underlying part of *Unit O-1*. Due to the geometry and internal seismic signature, MTD_{O-1} is interpreted to be a mass-transport deposit as described from previous studies of Evans et al. (2002) or other fjords (Prior et al., 1984; Hampton et al., 1996; Hogan et al., 2011; 2012).

Another package of acoustically transparent sediments is MTD_{O-2}. Its upper boundary, reflection *O-R2,* has a hummocky appearance and is semi-continuous with a varying intensity. The package has a thickness ranging from 8.7 m and up to 14.5 m and lays ~4 m below the seafloor. Similar to MTD_{O-1}, the underlying boundary is a disconformity. Both the upper hummocky boundary (reflection *O-R2*) and the lower, truncational boundary of MTD_{O-2} become unclear and chaotic towards the ridge (Ridge 1 cf. *Chapter 4.1.5.Transverse Ridges*). In conformity with the interpretation of $MTD_{O-2,}$ MTD_{O-1} has also been interpreted as a MTD which eroded into the underlying sediments of *Unit O-1*. Both MTDs are restricted to sub-basin 1.

In the ESE part of the basin is the sediment package *Unit O-3*. It is located on the fjord sidewall and lies between reflection *O-R3* (the seafloor) and *O-R1*. The unit is acoustically semi-transparent to transparent with an irregular to very irregular upper surface. The unit's basal reflection *O-R1* has a moderate to low amplitude and is like *O-R3* also diffuse on steep slopes. The unit`s irregular upper surface is believed to be a result of a complex morphology including incised channels and sediment lobes (see Fig. 4.1).

As in previous described basins (see *Chapter 5.2.1 The inner basin of Moskusoksefjord* and *5.2.2 The middle basin of Moskusoksefjord*), a strong and continuous seabed reflection (*O-R3*) which gets diffuse on steep slopes is observed in the outer basin of Moskusoksefjord.
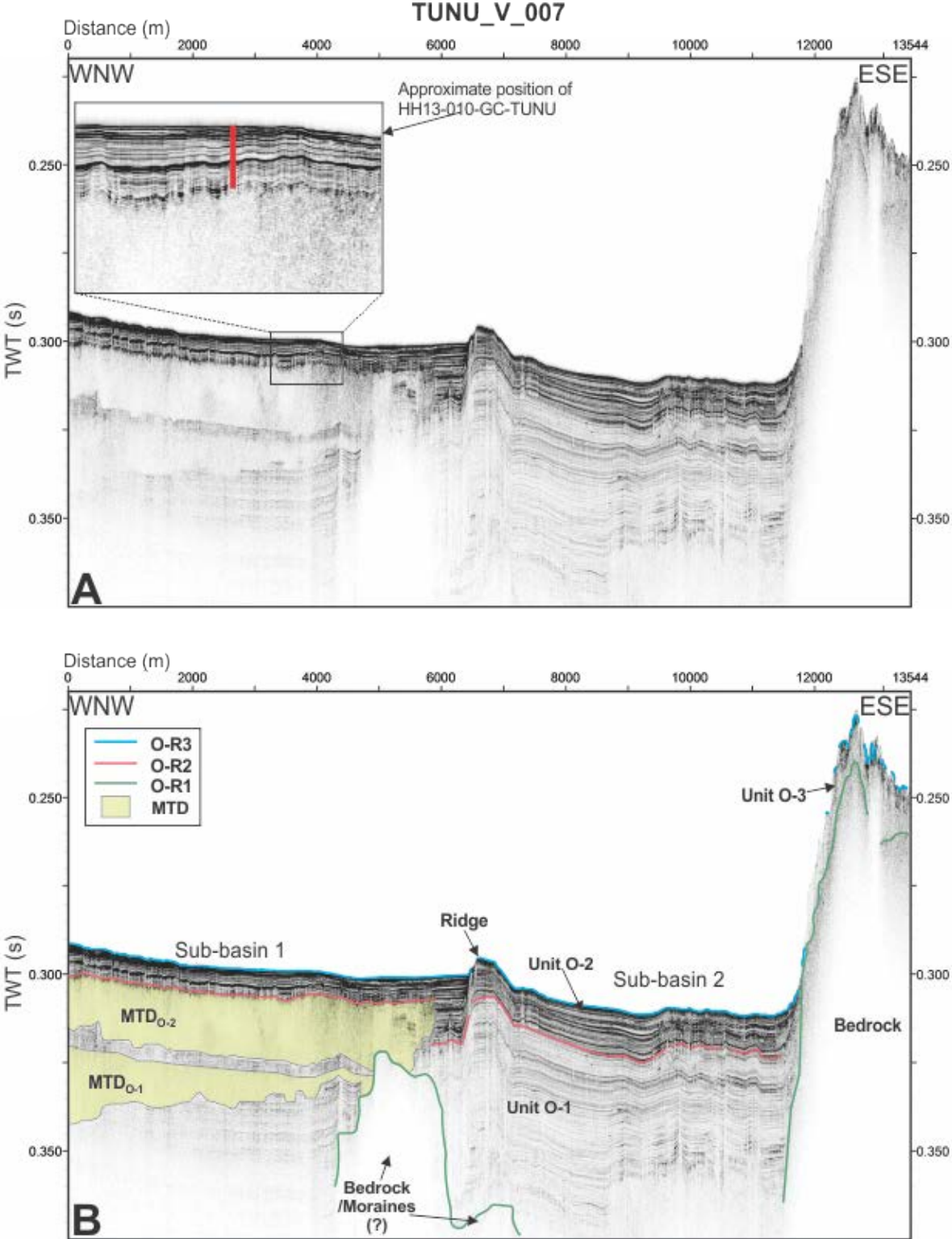
Figure 5.3: A) Chirp line TUNU_V_007 from the outer basin of Moskusoksefjord (see Fig. 5.1 for location). The approximate position of sediment core HH13-010-GC-TUNU is indicated. B) Interpretation of reflection *O-R1* to *O-R3*, *Unit O-1* to *Unit O-3* and *MTD$_{O-1}$* and *MTD$_{O-2}$*. The eastern ridge (Ridge 1) seen in Figure 4.6 is also indicated.

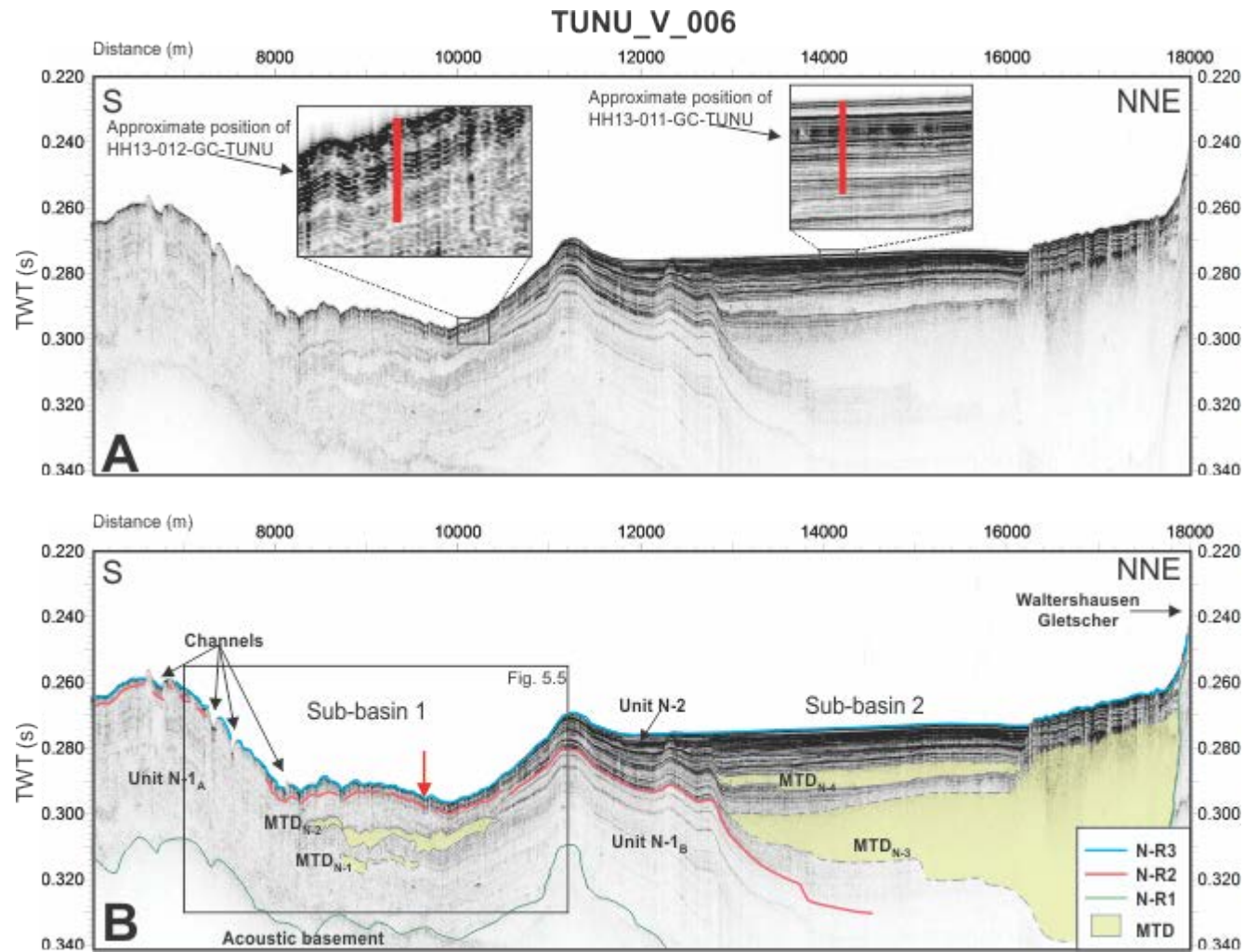**Figure 5.4: A)** Chirp line TUNU_V_006 from Nordfjord (see Fig. 5.1 for location). The approximate position of sediment cores HH13-011-GC-TUNU and HH13-012-GC-TUNU are indicated. **B)** Interpretation of reflections *N-R1* to *N-R3*, *Unit N-1* to *Unit N-2* and *MTD $_{N-1}$* to *MTD $_{N-4}$*. Channels from Figure 4.1 are also indicated. Red arrow points out the boundary between *Unit N-1$_A$* and *Unit N-1$_B$*.

5.2.4. Nordfjord

In Nordfjord chirp line TUNU_V_006 (for location, see Fig. 5.1) displays two sub-basins (sub-basin 1 and sub-basin 2) created by an elevation, interpreted to be a morainal ridge or a bedrock high (Fig. 5.4). The two main units (*Unit N-1* and *Unit N-2*) are confined by three regional seismic reflectors (*N-R1*, *N-R2* and *N-R3*). Four MTDs (MTD_{N-1} to MTD_{N-4}) have also been identified, as further described below.

Reflection *N-R1* defines the lower boundary of *Unit N-1* that lay directly upon the acoustic basement (Fig. 5.4). *Unit N-1* appears as acoustically laminated sedimentary succession comprising mainly low amplitude and continuous reflections, with some reflections having slightly higher amplitude. The unit has a thickness varying from 27 m in the deepest part of sub-basin 1 to more than 35 m in sub-basin 2. The succession gets thinner and wedges out towards the elevation between the two sub-basins. Due to the acoustic signature varying between the two sub-basins, the *Unit N-1* has been further divided into *Unit N-1$_A$* and *Unit N-1$_B$*. The continuity and amplitude of the stratification in *Unit N-1$_A$* is moderate to low, making the reflection pattern chaotic and difficult to trace. In some areas the unit appears as more transparent or massive. *Unit N-1$_B$*, on the other hand, appears as acoustically laminated with beds dipping in a NNE-direction, infilling sub-basin 2.

The uppermost *Unit N-2* lies concordant above reflection *N-R2*, marking a transitional but distinctive change in the acoustic signature of the sediment succession. *Unit N-2* consists of strong, continuous to semi-continuous onlapping reflections, becoming more chaotic and irregular in sub-basin 1. Both the reflection amplitude and reflection abundance decreases with depth. The unit thickness varies between the two sub-basins, having a near-constant thickness of ~1.5 m in sub-basin 1, and increasing to more than 40 m in the innermost part of sub-basin 2. Two large MTDs occur within *Unit N-2* (Fig. 5.4).

The acoustically laminated signature of *Unit N-1* is suggested to represent changes in the lithology. The internal seismic signature of *Unit N-2*, however, may indicate a more pronounced change in lithology relative to *Unit N-1*. Increased reflection amplitude is interpreted to indicate an increase in IRD, coarser sediments from fall-out from meltwater plumes and/or more coarse-grained turbidites that may be related to climatic fluctuations and/or a less permanent sea ice in a glacimarine environment (cf. Baeten et al., 2010; Kempf et al., 2013), as further discussed below. The southward thinning of the sedimentary

succession suggests that the main sediment sources in the area were Waltershausen Gletscher and the river coming from Broget Dal (see Fig. 2.6). The sediments in sub-basin 1 appears to be disturbed/eroded by channels and mass-wasting, as observed on the bathymetry data (see Fig. 5.1).

In the lower, central part of sub-basin 1, a small MTD (MTD_{N-1}) is observed within *Unit N-1$_A$* (Fig. 5.4 and 5.5) ~16 m below the seafloor. The MTD_{N-1} extends 0.9 km in a S-NNE direction and has a thickness varying between ~1.3-3.3 m. MTD_{N-1} is acoustically transparent and has a diffuse and undulating upper boundary reflection and a lower boundary truncating the underlying reflections. Further up in the succession, at ~8.5 m below the seafloor, MTD_{N-2} occurs. It has similar characteristics, including a transparent acoustic signature, an undulating upper- and a lower boundary truncating underlying reflections. MTD_{N-2} is larger than $_{N-1,}$ stretching ~2.2 km in a S-NNE direction with a thickness ranging from 0.5 to 6 m. It is not possible to determine whether the deposits comprise several sediment lobes. However, there seems to be traces of old channels on the upper surface of MTD_{N-2} (Fig. 5.5). Both MTDs are suggested to be debris flows originating from the eastern fjord slope. They were deposited in bathymetric lows, controlled by the sub-basins topography.
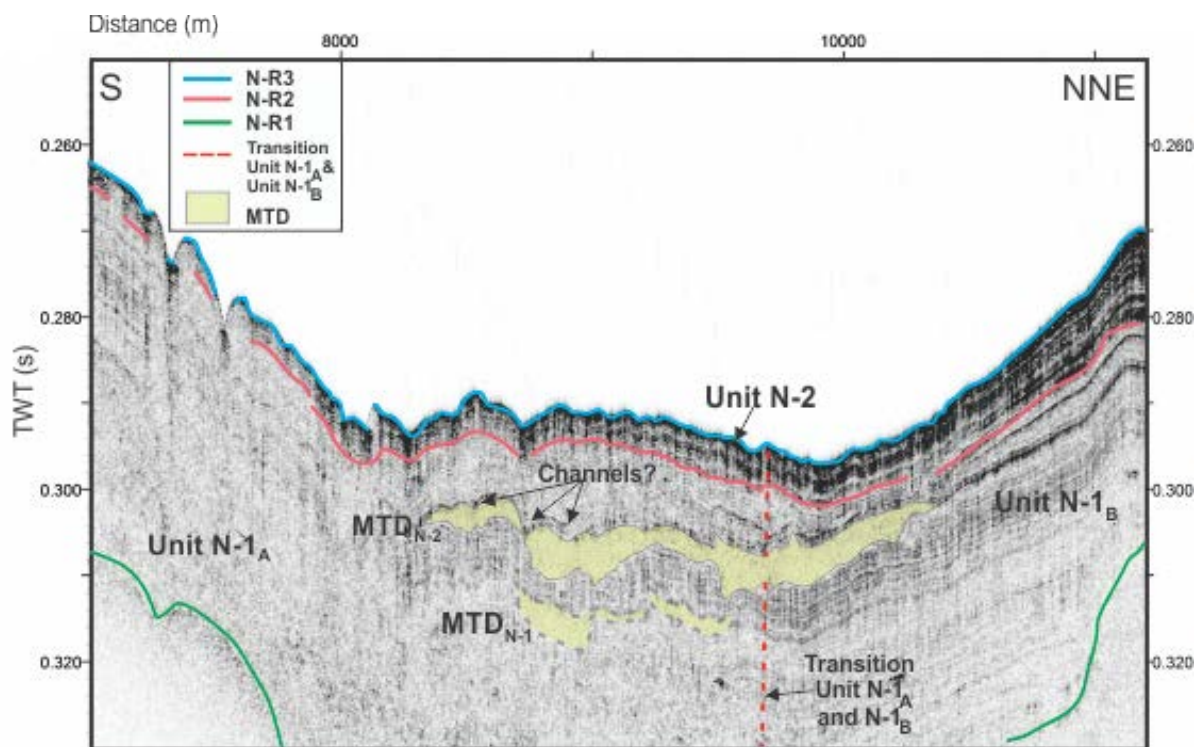

Figure 5.5: Section from chirp line TUNU_V_006 (for location, see Fig. 5.4) showing all three units observed in Nordfjord, along with *MTD$_{N-1}$* and *MTD$_{N-2}$*. The transition between the two sub-units of *Unit N-1* (*Unit N-1$_A$* and *Unit N-1$_B$*) is visible, marked with a red dotted line. Possible channel-scars on the upper surface of *MTD$_{N-2}$* are indicated.

Additional two MTDs (MTD_{N-3} and MTD_{N-4}) are restricted to sub-basin 2 where they dominate the studied part of the sub-seafloor succession, wedged in between the sedimentary successions of *Unit N-2*. MTD_{N-3}, the largest MTD identified in Nordfjord, is an acoustically transparent sediment body extending 5 km in a S-NNE direction. The MTD lays ~18-21 m below the seafloor and forms the infill of the lower part of the sub-basin. Its thickness varies from ~40 m at the NNE margin, thinning upslope in a northerly direction where it terminates. It has a diffuse and hummocky upper boundary. The lower boundary represents an unconformity as underlying sediments are truncated. Approximately 2.5 m above MTD_{N-3} lays MTD_{N-4}, the smaller MTD in sub-basin 2. The MTD has, similar to MTD_{N-3} and acoustic transparent signature with a diffuse and hummocky upper boundary and a discordant lower boundary. The MTD lies ~8 m below the seafloor, has a near-uniform thickness of ~4.5 m and extends 3.4 km in a S-NNE direction. MTD_{N-3} and MTD_{N-4} are interpreted to be mass-transport deposits, probably originating from the same area during two individual events. Triggering of slope failures in arctic fjords are interpreted to be controlled by the sea floor topography, sediment supply and properties, seismic activity, cyclic loading and sea-level fluctuations (Syvitski et al., 1987; Forwick and Vorren, 2007; 2011).

As in the previously described basins, the seabed reflection *N-R3* is strong and continuous, but more diffuse on steep slopes.

5.2.5. Summary

The uppermost unit in all three basins consists of acoustic stratified, semi-continuous to continuous reflections (Table 5-1). Both reflection amplitude and abundance are generally high, interpreted to represent more pronounced and frequent changes in lithology relative to the underlying unit of similar seismic signature but with low-medium amplitude reflections. Here the lithological changes probably have been less pronounced as the boundary between the two units follows the stratigraphy of the basin and is not purely a function of depth indicating that it not only resulted from sound attenuation as a function of depth.

Three of the basins (middle-, outer- and Nordfjord) had MTDs of various dimensions. The most extensive ones were located in the outer basin of Moskusoksefjord and in sub-basin 2 of Nordfjord which is the area nearest to the glacier. The two lowermost MTDs in each basin

(MTD_{O-1} and MTD_{N-3}) were located below the modern seafloor at ~20 m and 18 m depth, respectively, while the overlying MTDs (MTD_{O-2} and MTD_{N-4}) were located at 4 m and 8 m depth. Their location indicates that their occurrence may be related to a high sediment input from the glacier as will be discussed in more detail below.

Table 5-1: Overview of the characteristics of the seismostratigraphic units in Moskusoksefjord and Nordfjord.

Unit	Thickness range [m]	Reflection configuration	Reflection continuity	Reflection amplitude	Reflection abundance	Lower boundary	Upper boundary
Inner basin of Moskusoksefjord							
I-1	-	Transparent	-	Low	Low	No lower boundary	Gradual, diffuse
I-2	0-30+ No lower boundary	Near-parallel, stratified	Continuous to semi-continuous	High to low	High	Gradual/ No lower boundary	Modern seafloor
Middle basin of Moskusoksefjord							
M-1	0-27+ No lower boundary	Laminated, near-parallel	Continuous	Low to moderate	Moderate to high	Diffuse/ No lower boundary	Marked to gradual, concordant
M-2	0-4	Stratified, near-parallel	Continuous to semi-continuous	High	High	Marked to gradual	Modern seafloor
MTD$_{M-1}$	-	Semi-transparent to transparent. Lobate geometries	Very low	Low	Low	No lower boundary	Marked to gradual
M-3	-	Semi-transparent to transparent	Low	Low	Low	No lower boundary	Irregular, modern seafloor
Outer basin of Moskusoksefjord							
O-1	3.5-47+ No lower boundary	Stratified	High to moderate	Moderate to low	Moderate	No lower boundary	Concordant
O-2	6.5-10	Stratified, near-parallel	Continuous to semi-continuous	High to moderate	High	Concordant	Modern seafloor
MTD$_{O-1}$	1.5-14.5	Transparent	-	-	-	Diffuse, discordant	Diffuse
MTD$_{O-2}$	8.7-14.5	Transparent	-	-	-	Marked, discordant	Marked to chaotic
O-3	0-11+	Semi-transparent to transparent	Low	Low to moderate	Low	Moderate to weak, diffuse	Modern seafloor, irregular
Nordfjord							
N-1$_A$	27-36	Chaotic/ laminated	Continuous to semi-continuous	Moderate to low	Moderate to low	Acoustic basement	Concordant, diffuse
N-1$_B$	29-35+	Near-parallel, laminated	Continuous	Moderate to low	Moderate to low	Acoustic basement	Marked, concordant
N-2	1.5-40+	Laminated, near-paralell	Continuous to semi-continuous	High to low	High to low	Marked, concordant	Modern seafloor
MTD$_{N-1}$	1.3-3.3	Transparent	Low	Low	Low	Diffuse, Discordant	Diffuse
MTD$_{N-2}$	0.5-6	Transparent	Low	Low	Low	Discordant	Marked to gradual
MTD$_{N-3}$	0-40	Transparent	Low	Low	Low	Discordant	Diffuse
MTD$_{N-4}$	~4.5	Transparent	Low	Low	Low	Discordant	Marked to gradual

6. Lithostratigraphy

6.1.   Introduction

Five sediment gravity cores were retrieved from Moskusoksefjord and Nordfjord. When analyzing the cores, the methods described in Chapter 3 were applied and below the results of the analysis will be presented in order to interpret and reconstruct the depositional environment of the two fjords. Three of the sediment cores were retrieved from Moskusoksefjord (one in each basin) and two from Nordfjord (for location, see Fig. 6.1). All five sediment cores penetrate part of seismic *Unit 2*, whilst HH13-009-GC-TUNU also penetrates into the underlying *Unit 1* (Fig. 5.2, 5.3 and 5.4).
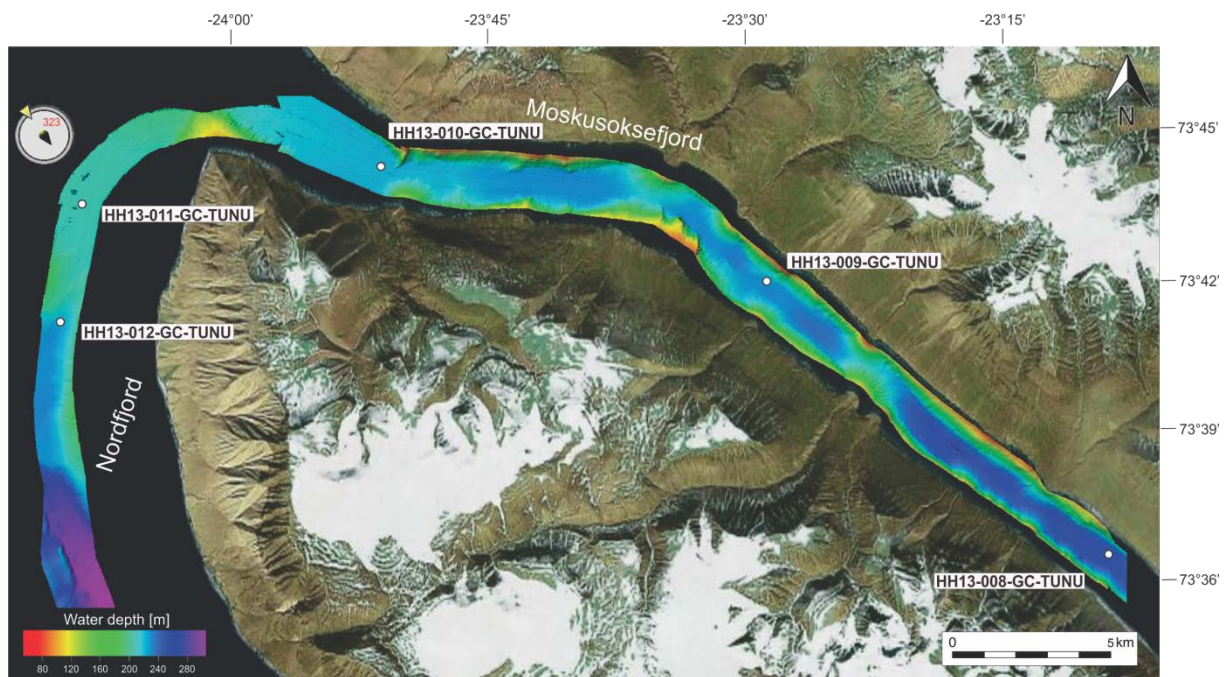
Figure 6.1: Location of the studied gravity core samples in Moskusoksefjord and Nordfjord (see Table 3-1 for more details).

6.2.   Core description

6.2.1. Grain-size analyses

The results of the grain-size analyses, i.e. volume percentages off clay, silt and sand are presented relative to depth in Figure 6.5, 6.8, 6.12, 6.17 and 6.21. All five cores show a clear dominance of the clay and silt fraction (mean values are 17-30% and 46-68%, respectively),

interrupted by relatively thin layers and lenses with a higher sand fraction than the surrounding material (mean value is 4-37%). The lower part of core HH13-009-GC-TUNU, however, stands out compared to the rest of the sampled sediments, with a 95 cm thick layer of muddy sand and sandy mud with a sand fraction ranging from 18% to 57%. The material was sampled evenly throughout the cores, with more frequent sampling in areas of interest containing either marked changes in grain-size or sediment color (on average every 6 cm). As the LS 13 320 Laser Diffraction Particle Size Analyzer Clasts only measures grains <2000 µm (<2 mm), grains that are larger are marked as individual features (clasts) in the logs. Grains larger than 2 mm will in this study be regarded as ice-rafted debris. For classification of the matrix, Folk`s (1954) classification system for sand, silt and clay is used (see *Chapter 6.2.6 Lithofacies*, below).

6.2.2. Physical properties

Physical properties of the sediments includes water content (%), wet bulk density (g/cm^3), P-wave velocity (m/s), acoustic impedance (g*m*cm^{-2}*s^{-1}), fraction porosity and magnetic susceptibility (10^{-8}SI(m^3/kg)). The results are presented as continuous plots for all five cores (Fig. 6.5, 6.8, 6.12, 6.17 and 6.21). Measurements from the top, bottom and at section boundaries occasionally protrude being unusually high or low, and are therefore removed from the plots. The water content shows a normal trend of downcore decrease due to the effect of sediment consolidation, with peaks to lower values in areas containing coarser material. The MSCL physical properties are generally zigzag-shaped around constant values with clear increases or decreases around lithological boundaries with changes in either the grain-size or color of the sediment. All measured physical properties either show a general trend of increasing or decreasing due to compaction caused by the weight of overlying sediments. The measured physical properties are described relative to the general trend of the cores. The minimum, maximum and mean value for each core is given in Table 6-1.

6.2.3. Element geochemistry (XRF core scanning)

The excited sediments of all five cores provided a good response for element Si, Cl, K, Ca, Ti, Fe and Rh, while Al and Zr provided a moderate response. Also, in core HH13-008-GC-TUNU and HH13-009-GC-TUNU element Rb was sufficiently excited to be accounted for in the interpretations below. The element geochemistry is expressed with selected element/element ratios and elements/sum ratios (see *Chapter 3.4.3; XRF scan*). This includes

Ca/Fe, Al/Sum, Zr/Rb, Fe/Sum, Ti/Sum, Ca/Sum, K/Sum and Si/Sum (Fig. 6.6, 6.9, 6.13, 6.18 and 6.22). The mean values can be found in Table 6.1 below. Changes within the element ratios are described relative to the general trend of the cores and the mean values of the graphic plots.

6.2.4. Radiocarbon dating

The results from the AMS radiocarbon dating and calibrated ages are presented in Table 6-2. The calibrated ages are based on a mean of the 1σ range. Due to the limited amount of material available for radiocarbon dating, several of the samples taken proved to be too small for dating. As a result, only a few radiocarbon dates could be obtained from our cores and ages for core HH13-010-GC-TUNU sediments have therefore not been determined.

The results from the radiocarbon dating of core HH13-008-GC-TUNU provided a reversed age model, with an age of 1010 cal. yr. BP at 115-114 cm depth and 610 cal. yr. BP at 202 cm depth (Table 6-2). We interpret the dated sample from 115-114 cm depth comprising diverse benthic foraminifera to be the incorrect age. The sample of diverse benthic foraminifera may have been influenced by vital effects (e.g. Erez, 1978; Grossman, 1987), resulting in the dated age being too high. Another possibility is reworking of the sediments producing old ages on top (Forsberg et al., 2007) The sample from 115-114 cm depth is therefore not taken into account in the further discussion. We consider the other ages in this study provided by diverse benthic foraminifera to be reliable, keeping in mind that also them could have too high ages. In addition, the sample from 219-218 cm depth in core HH13-011-GC-TUNU failed and is therefore also excluded from the further discussion.

6.2.5. ^{210}Pb and ^{137}Cs dating

The results from the ^{210}Pb and ^{137}Cs dating of cores HH13-008-GC-TUNU and HH13-012-GC-TUNU are presented in Table 6-3. As mentioned previously, the data must be treated as the first order approximation. Particularly the ^{210}Pb dating gave a variable result, making the ^{137}Cs dating more reliable. Calculations of the sediment accumulation rates for the two cores are based on a simplified dating based on the ^{210}Pb model and the presence of ^{137}Cs. The results are reported within a 2 σ standard deviation uncertainty range (Szczuciński, 2015).

6.2.6. Visual description

The lithofacies was identifies and the lithological logs were created based on the study of the sediment surface, X-ray photographs and the grain-size analyses data. The composition of the matrix is indicated by the widths of the logs. After opening, black spots were observable for a few days before they disappeared. They have been interpreted to be sulphide traces caused by bacteria during sulphide reduction (Forwick, 2001).

Multiple lithofacies are distinguished (see *Chapter 6.2.6 Lithofacies*, below). Together they represent one lithological unit in all cores, except for HH13-009-GC-TUNU, which mentioned previously sampled both seismic *Unit M-1* and M-*2* in the middle basin of Moskusoksefjord (see Fig. 5.2). Core HH13-009-GC-TUNU is therefore divided into two lithological units where the boundary between lithological *Unit 9-1* and 9-*2* correspond to the reflection separating seismic *Unit 1* and *2* (Fig. 6.7).

The logs, including color images of the sediment surfaces, are presented in Figure 6.4, 6.7, 6.10, 6.16 and 6.19. All cores are described relative to the depth, from the bottom and up.

6.2.7. Lithofacies

The lithofacies codes are based on Folk`s (1954) classification system for sand, silt and clay (Fig. 6.2). The system divides the sediments into ten groups based on the percentage of sand and the silt:clay ratio: Sand (*S*), clayey sand (*cS*), muddy sand (*mS*), silty sand (*siS*), sandy clay (*sC*), sandy mud (*sM*), sandy silt (*sSi*), clay (C), mud (*M*) and silt (*Si*). In addition, codes for laminated (*l*) upward fining *(-uf)*, upward coarsening *(-uc)* and clasts *(c)* are used.

Massive mud (*M*) is the most dominant lithofacies in the investigated cores, except for in core HH13-010-GC-TUNU where silt (*S*) dominates. Sediments are classified as mud when the silt:clay ratio is between 1:2 and 2:1 (Fig. 6.2). The coarser sediments in all five cores are characterized by being one or two shades darker than the surrounding material, however, Munsell Soil Color Chart doesn`t always distinguish between them.
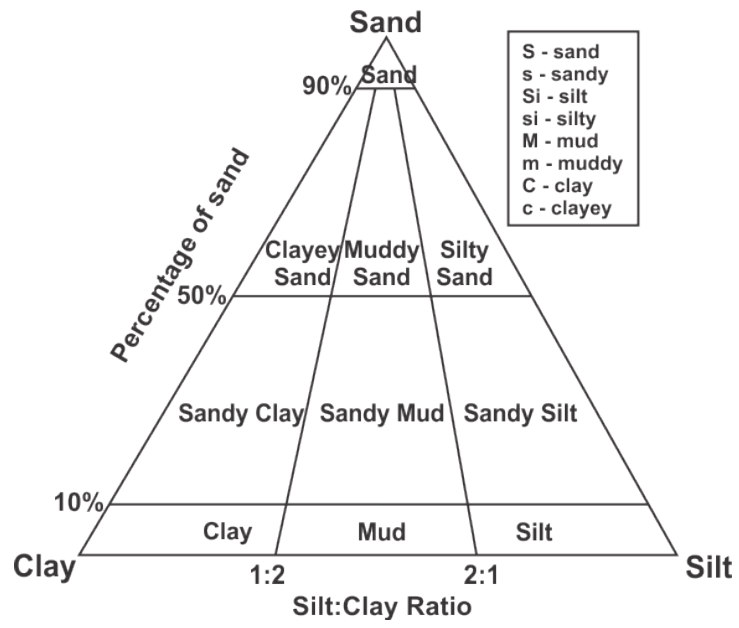
Figure 6.2: Folk`s (1954) classification system for sand, silt and clay.

Table 6-1: Mean values for the measured physical properties and element geochemistry.

	Outer Nordfjord	*Inner Nordfjord*	*Outer Moskusoksefjord*		*Inner Moskusoksefjord*
	HH13-012-GC-TUNU	**HH13-011-GC-TUNU**	**HH13-010-GC-TUNU**	**HH13-009-GC-TUNU** 9-1 9-2	**HH13-008-GC-TUNU**
P-wave velocity (m/s)					
Minimum	1470	1345	1356	1503 1442	1405
Maximum	1593	1802	1749	1629 1634	1623
Mean	1509	1532	1532	1560 1502	1509
Wet bulk density (g/cm^3)					
Minimum	1.6	1.6	1.6	1.7 1.6	1.5
Maximum	2.0	2.1	2.0	1.9 1.9	1.9
Mean	1.8	1.8	1.8	1.8 1.7	1.7
Acoustic Impedance (g*m*cm^{-2}*s^{-1})					
Minimum	2431	2340	2214	2554 2350	2243
Maximum	3022	3840	3535	3129 3061	3113
Mean	2665	2486	2708	2863 2545	2560
Fraction porosity					
Minimum	0.4	0.4	0.4	0.5 0.5	0.5
Maximum	0.7	0.7	0.7	0.6 0.7	0.7
Mean	0.6	0.5	0.6	0.5 0.6	0.6
Mag.sus. (10-8 SI (m3/kg))					
Minimum	33	70	33	11 20	15
Maximum	63	96	69	27 33	32
Mean	44	87	45	17 30	22
Ca/Fe ratio					
Mean	0.30	0.35	0.35	0.35 0.39	0.22
Al/Sum					
Mean	0.01	0.01	0.01	0.01 0.01	0.01
Zr/Rb ratio					
Mean	-	-	-	2.64 1.61	1.44
Fe/Sum ratio					
Mean	0.43	0.40	0.41	0.39 0.43	0.43
Ti/Sum ratio					
Mean	0.04	0.04	0.04	0.04 0.04	0.04
Ca/Sum ratio					
Mean	0.13	0.13	0.14	0.11 0.11	0.01
K/Sum ratio					
Mean	0.13	0.13	0.13	0.15 0.13	0.15
Si/Sum ratio					
Mean	0.11	0.13	0.14	0.13 0.10	0.12

Table 6-2: Results from the radiocarbon dating and calibrated ages.

Lab reference	Core	Sampling depth (cm)	Species	14C age BP	Cal. yr BP Calib 7.1 1 σ range	Cal. yr BP Calib 7.1 2 σ range	Cal. yr BP Calib 7.1 1 σ mean
60276.1.1	HH13-008-GC-TUNU	115-114	Benthic foraminifera	1620 ± 65	914-1101	819-1206	1010
60277.1.1	HH13-008-GC-TUNU	202	*Buccinum hydrophanum*	1205 ± 60	541-664	492-743	610
60278.1.1	HH13-009-GC-TUNU	118-117	Ostracoda	1790 ± 300	879-1508	612-1845	1190
-	HH13-011-GC-TUNU	219-218	Ostracoda /shell	Failed	-	-	-
60280.1.1	HH13-011-GC-TUNU	593-592	Benthic foraminifera	1750 ± 130	991-1270	824-1410	1130
60281.1.1	HH13-012-GC-TUNU	196-195	Benthic foraminifera	1295 ± 70	614-777	537-871	690
60282.1.1	HH13-012-GC-TUNU	455-454	Benthic foraminifera	7470 ± 130	7644-7911	7500-8036	7770

Table 6-3: Results from the ^{210}Pb and ^{137}Cs dating of cores HH13-008-GC-TUNU and HH13-012-GC-TUNU. The measured total ^{210}Pb and ^{137}Cs activities with 2-sigma uncertainty ranges are presented. Excess ^{210}Pb (ex ^{210}Pb), used for sediment accumulation rates calculations, are calculated using supported activity taken from the sample below the region of radioactive decay.

HH13-008-GC-TUNU

Sampling depth (cm)	Lab reference	^{137}Cs Bq/g	^{137}Cs uncertainty	^{210}Pb Bq/g	^{210}Pb uncertainty	ex ^{210}Pb Bq/g
0-2	IG0968	0.0047	0.0014	0.0625	0.0185	0.0063
10-12	IG0969	0		0.0557	0.0162	-
20-22	IG0970	0		0.0620	0.0174	0.0058
150-152	IG0967	0		0.0562	0.0154	-

HH13-012-GC-TUNU

Sampling depth (cm)	Lab reference	^{137}Cs Bq/g	^{137}Cs uncertainty	^{210}Pb Bq/g	^{210}Pb uncertainty	ex ^{210}Pb Bq/g
0-2	IG0972	0		0.0581	0.0194	0.0113
10-12	IG0971	0.0010	0.0010	0.0461	0.0139	
20-22	IG0973	0.0019	0.0010	0.0609	0.0156	0.0141
50-52	IG0974	0.0008	0.0010	0.0402	0.0155	
100-102	IG0975	0		0.0453	0.0014	
150-152	IG0976	0		0.0465	0.0157	
200-202	IG0977	0		0.0550	0.0181	

Table 6-4: Estimated sedimentation rates.

Core	Depth interval (cm)	Age interval ^{14}C cal. yr. BP	Age yr	Sedimentation rate (cm/ka)
HH13-008-GC-TUNU	202-0	610-0	610	316
HH13-009-GC-TUNU	117-0	1190-0	1190	90
HH13-011-GC-TUNU	592-0	1130-0	1130	533
HH13-012-GC-TUNU	454-195	7770-690	7080	36
	195-0	690-0	690	279
	454-0	7770-0	7770	58

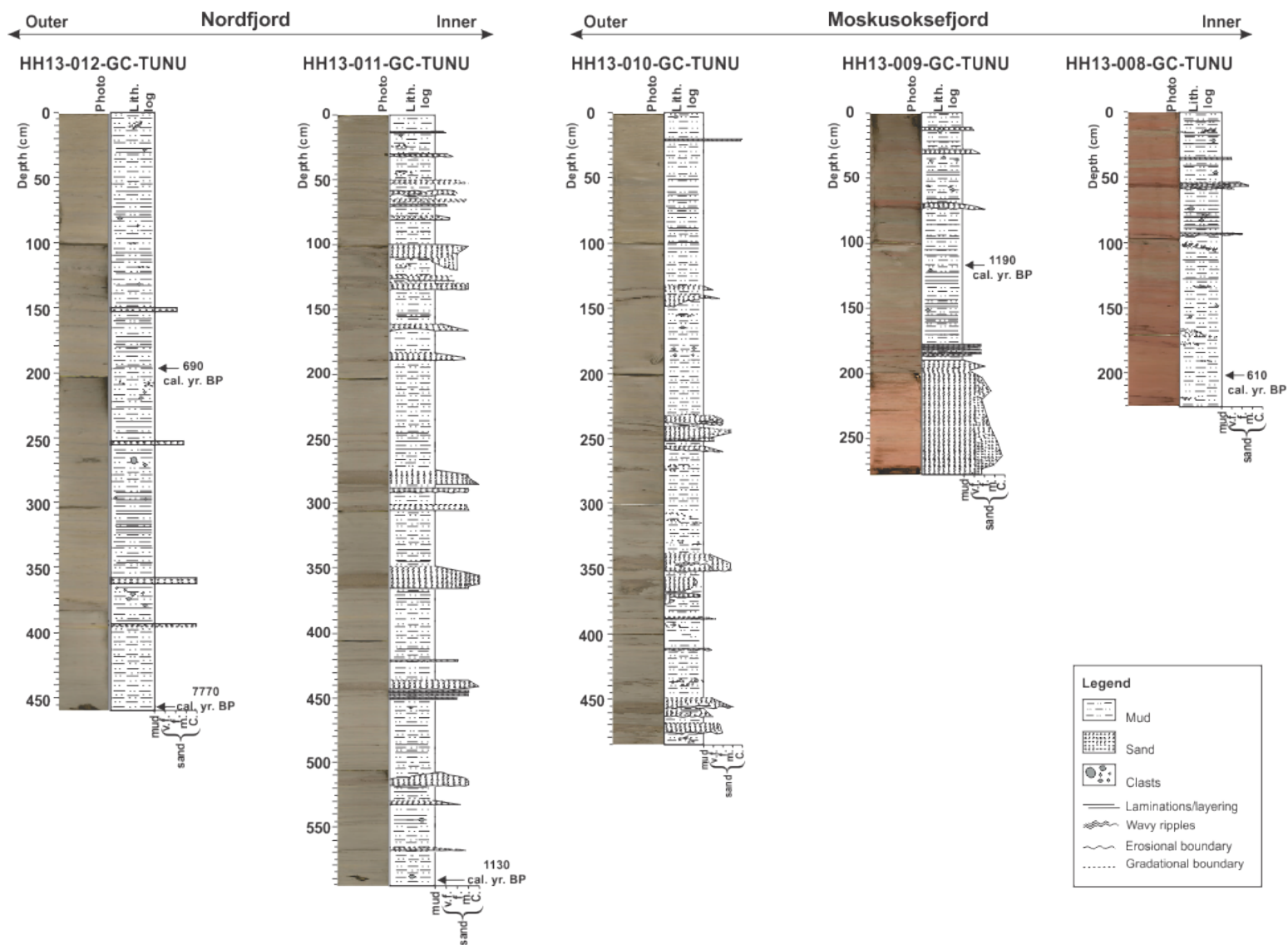| Core	Depth interval (cm)	Age interval ^{210}Pb and ^{137}Cs 2 σ mean	Age yr	Sedimentation rate (cm/ka)
HH13-008-GC-TUNU	10	~200-0	~200	<50
HH13-012-GC-TUNU	50	~50-0	~50	<1000

Figure 6.3: Lithological logs from all five sediment cores displayed in a transect from inner Moskusoksefjord (right) to outer Nordfjord (left). Core columns show core photos and lithological logs with sediment structures and distribution of clasts. The depth of the dated intervals are indicated by arrows. Radiocarbon ages are presented in calibrated years BP.

71

6.3.   The inner basin of Moskusoksefjord - Core HH13-008-GC-TUNU

Core HH13-008-GC-TUNU was retrieved from the inner basin of Moskusoksefjord (Fig. 6.1) at 256 m water depth. The core length is 226 cm (Table 3-1). The core comprises one lithological unit (*Unit 8-1*) containing lithofacies *M* (mud), *sM* (sandy mud) and *mS* (muddy sand) in addition to lamination *(l)* and sporadic clasts (*c*).

6.3.1. Unit 8-1 (226-0 cm)

6.3.1.1.   Lithology and stratigraphy

Frequent color changes characterize the unit, the changes are both gradual and sharp and are often (but not always) related to variations in the lithofacies (Fig. 6.4). The lowermost 98 cm (226-128 cm) is characterized by brown (7.5YR 4/3) mud with lenses of dark reddish brown (5YR 3/2) sandy mud and muddy sand. From ~128 cm and up the sediment colour of the mud changes frequently, creating laminations/layering alternating between brown (7.5YR 5/3) and reddish brown (5YR 4/3) with 4-12 cm thick bands of weak red colour (2.5YR 4/2). Irregular and sub-horizontal layers of coarser material (2-8 cm thick) with dark reddish brown (5YR 3/2) color occurs periodically throughout the core. Also, a single layer of dark grayish brown (10YR 4/2) sandy mud can be seen between 105-97 cm (Fig. 6.4).

The grain-size distribution shows clay and silt being the dominant fractions in the core, ranging from 6-42% and 33-68%, respectively (Fig. 6.5). Several peaks in the sand fraction occur throughout the core, containing either sandy mud (sand fraction up to 46%) or muddy sand (up to 61%). These increases in the sand fraction (>10%) are seen as sub-horizontal layers or as lenses. There are three layers and six lenses of sandy mud seen on the core surface, in addition to a single lens of muddy sand. The first layer is located at 95-92 cm and has a sand fraction reaching 31%. It has an erosional lower boundary, a sharp upper boundary and is fining upwards. The second layer, located at 58-54 cm, consists of three stacked layers of sandy mud with a maximum sand fraction of 22%. All three layers have an erosional lower boundary and a gradational upper boundary and are fining upwards. The sandy mud layer located furthest up in the core at 36-34 cm has a maximum sand fraction of 18%. Unlike the two previous layers, the third layer has sharp upper- and lower boundaries and shows no signs of fining upwards. The lenses containing sandy mud are located at around 220 cm (13%),192 cm (15%), 170 cm (42%),135 cm (14%), 104 cm (16%) and 15 cm (46%), whilst the muddy
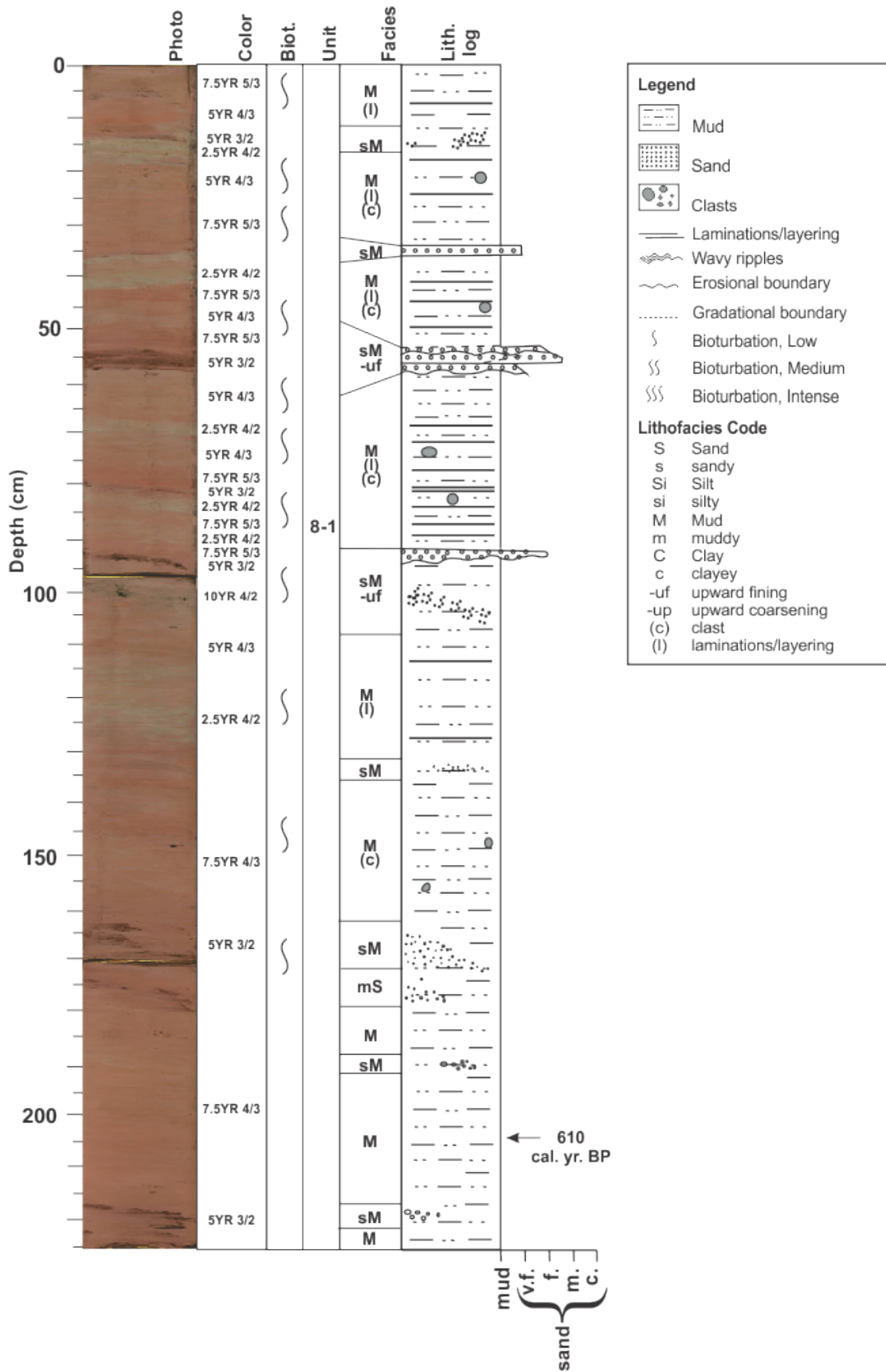
Figure 6.4: Lithological log of core HH13-008-GC-TUNU showing the core surface, color image, Munsell color codes, bioturbation, lithological units, lithofacies codes and structures. The depth of the dated interval is indicated by an arrow.

73
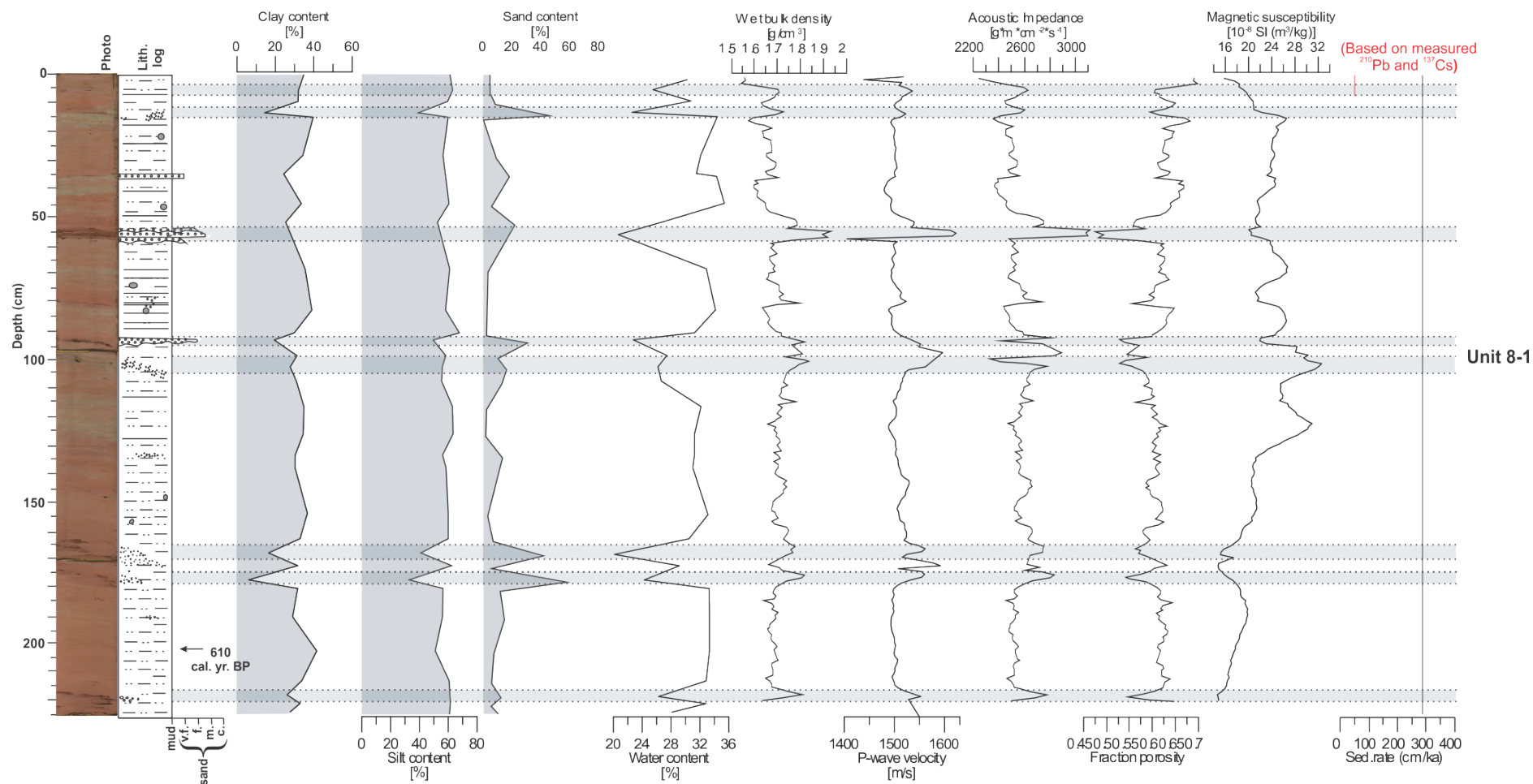
Figure 6.5: Grain-size distribution, the measured physical properties and the estimated linear sediment rates (dotted line is the average sedimentation rate) of core HH13-008-GC-TUNU. Color image and lithological log are included for reference. Unit is indicated. The depth of the dated interval is indicated by an arrow, while the largest fluctuations in the measured physical properties are indicated by gray horizontal lines.

Figure 6.6: Measured element geochemistry for core HH13-008-GC-TUNU. Color image and lithological core is included for reference. Unit is indicated. The depth of the dated interval is indicated by an arrow, while the largest fluctuations in the element geochemistry are indicated by gray horizontal lines.

sand lens is located at 179 cm (61%). Clasts are randomly distributed within the mud.

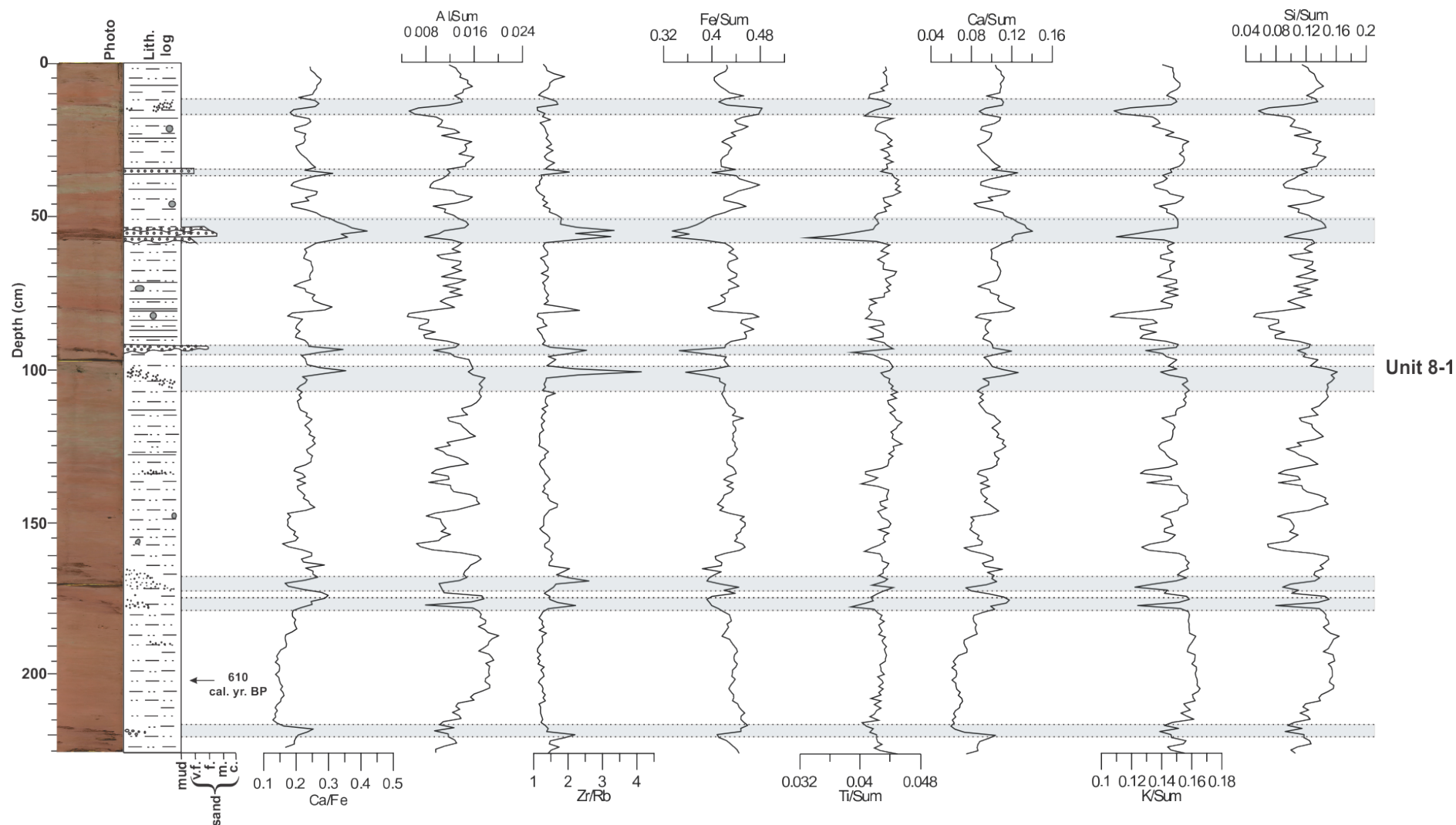Bioturbation in the core is low, except for in the lowermost ~50 cm and in the intervals containing sandy mud or muddy sand, where it is absent (Fig. 6.4).

6.3.1.1.   Physical properties

All five physical properties follow the sediment composition, with peaks within the sandy mud or muddy sand intervals occurring around 220 cm, 179 cm, 170 cm, 95 cm, 58 cm, 15 cm and 6 cm (Fig. 6.5). The wet bulk density, p-wave velocity and acoustic impedance generally follow the same trend with positive peaks within the coarser material, whereas the fraction porosity mirrors the other properties and have negative peaks. The magnetic susceptibility of the core varies between 15 ($*10^{-8}SI(m^3/kg)$) and 33, with a mean of 22. A marked decrease in the magnetic susceptibility occurs from approximately 128 cm depth and downcore.

6.3.1.2.   Element geochemistry

The Ca/Fe ratio fluctuates around a mean of 0.22 and is characterized by numerous oscillations (Fig. 6.6 and Table 6-1). Element Fe and Ca have a reversed relationship with concentrations of Fe decreasing where Ca increases. Positive peaks in Ca occur in relation to intervals with dark reddish brown sandy mud and muddy sand or with the presence of clasts, whilst Al increases within the brown and reddish brown mud intervals (see *Chapter 6.3.1.1 Lithology and stratigraphy*, above). Similar to Fe, concentrations of Ti, K and Si decreases within intervals with increased fractions of sand or clasts, whilst Zr/Rb follows Ca and increases (Fig. 6.6).

6.3.1.3.   Chronology and sedimentation rates

The variable downward concentration of ^{210}Pb makes it impossible to do a reliable assessment of the sediment accumulation rates (Table 6-3 and 6-4). Given the results of ^{137}Cs and assuming a constant initial concentration, an approximate sediment accumulation rate of about 0.04 cm/year may be calculated for the upper 10 cm. With the ^{137}Cs activity only being documented at the top core sample (0-2 cm), it is suggested that the sediment accumulation is in the range of 0.01 to 0.14 cm/year. Comparison the two results, the likely sediment

accumulation rate for the upper 10 cm is less than 50 cm/ka (Table 6-4). However, some more samples needs to be dated to get a more reliable assessment of the sediment accumulation rate (Szczuciński, 2015).

For radiocarbon dating a single gastropod sample and one sample of benthic foraminifera from core HH13-008-GC-TUNU were collected (Table 6-2). But, as mentioned previously (see *Chapter 6.2.4 Radiocarbon dating*), the sample comprising diverse benthic foraminifera is excluded from the study. The gastropod sample was collected at 202 cm depth and provided an age of 610 cal. yr. BP (calibrated years before present). Assuming a linear sedimentation rate and that the top of the core represents the modern seafloor, the average sedimentation rate for the interval between 202-0 cm is 316 cm/ka (Table 6-4). It should be noted that the sedimentation rates were exclusively calculated for deposits that were assumed to be from suspension fallout, i.e. thickness of the coarser layers were excluded.

6.3.1.4.   Interpretation

The dominance of massive or laminated mud with randomly distributed sandy layers and lenses and the presence of occasional dropstones indicate a glacimarine environment (e.g. Dowdeswell and Scourse, 1990; Powell and Domack, 1995) with rain-out from sediment laden glacial meltwater plumes. The repeatedly changing sediment color within the massive mud is suggested to represent input from multiple source areas (e.g. Forwick and Vorren, 2009) while the lenses containing increased sand fractions are interpreted to be deformed layers from synsedimentary deformation (Nichols. 2009). The sediment source area delivering the weak red sediment was initiated approximately 435 cal. yr. BP during the Little Ice Age (LIA), whilst the most frequent color changes occurred later in the LIA. Clasts and sand lenses observed in the core are suggested to be ice rafted debris (IRD) originating from either ice rafting by icebergs and/or by sea ice (cf. Forwick and Vorren, 1997; Reeh et al., 1999). The occurrence of bioturbation in the intervals containing mud further indicates that the sediments have not been reworked (Forwick and Vorren, 1997).

As mentioned previously, the core is located in a fjord environment with steep slopes and in the proximity to several river- and fan deltas. The observed irregular, sub-horizontal layers of coarser material with dark reddish brown or dark grayish brown color may reflect mass transport events such as turbidity or debris flows. The presence of deposits with erosional lower boundaries, fining upward sediments and the absence of bioturbation may represent

parts of a Bouma Sequence (e.g. Bouma, 1962; Nichols, 2007; Leeder, 2011), which is further discussed in *Chapter 6.5.1.5 Bouma sequence* below. The missing erosional lower boundary of the uppermost sand layer may be due to a non-eroding turbidity flow or a hydroplaning debris flow (cf. Mohrig et al., 1998; Mulder and Alexander, 2001).

The increasing trend of the water content and fraction porosity from the bottom and up (Fig. 6.5), along with a subsequently decreasing wet bulk density, p-wave velocity and acoustic impedance are expected to be a result of compaction due to the weight of the overlying sediments. Both the measured physical properties and element geochemistry can be correlated to changes in the lithology and sediment color. As a general trend the dark reddish brown sandy sediment contains increased amounts of Ca and Zr whilst the brown and reddish brown mud has an increase in Al, K and Si relative to the surrounding material. The weak red mud shows, along with the clasts, an increase in Fe.

6.4. The middle basin of Moskusoksefjord - Core HH13-009-GC-TUNU

Core HH13-009-GC-TUNU was recovered from the middle basin of Moskusoksefjord in the proximity to a MTD (Fig. 5.2). The core was retrieved at 233 m water depth approximately 13 km NNW of HH13-008-GC-TUNU (Fig. 6.1 & Table 3-1). The core length is 283 cm. The core penetrated into seismic *Unit M-2* and upper part of *Unit M-1* where the boundary between seismic *Unit M-1* and *M-2* correspond to the reflection separating lithological *Unit 9-1* and *9-2* (Fig. 5.2) and is therefore divided into two lithological units (*Unit 9-1* and *9-2*) below. There are three lithofacies; *M* (mud), *sM* (sandy mud) and *mS* (muddy sand). Lamination (*l*) and occasional clasts occur (*c*).

The photo of the lowermost core section photo (283-198 cm) (see Fig. 6.7) was taken at another occasion than the upper two and may therefore have been taken with different settings. Also, some measurements from the bottom of the core are missing or are incorrect due to lacking sediments creating a gap (283-273 cm).

6.4.1. Unit 9-1 (283-188 cm)

6.4.1.1. Lithology and stratigraphy

Sediment color varies little from the bottom to the top of *Unit 9-1*, changing gradually at ~207 cm depth (Fig. 6.7). The bottom sediments (283-207 cm) comprises relatively sandy, dark

reddish gray (5YR 4/2) sediments overlain by slightly finer sandy sediments of weak red color (2.5YR 4/2). The unit is dominated by sandy mud (*sM*) with a sand fraction ranging from 18% to 46%. In addition, an interval comprising muddy sand (*mS*) (57% sand) occurs between 275-267 cm. Coarsening upwards (inverse grading) from fine or medium sand to coarse sand occurs at three intervals (274-263 cm, 220-213 cm and 197-194 cm), while fining upwards (normal grading) occurs in between. There are no clasts or bioturbation present in the unit.

6.4.1.2. Physical properties

The physical properties of the unit are zigzag-shaped around the mean values (Table 6-1). The water content show little variation with a minimum of 20%, a maximum of 29% and a mean value of 23% (Fig. 6.8). From ~270 cm and up to 250 cm the wet bulk density, p-wave velocity and acoustic impedance show a general decreasing trend while the fraction porosity shows an increasing trend. The magnetic susceptibility increases upcore with a mean of 17 ($*10^{-8}$SI(m^3/kg)) (Table 6-1).

6.4.1.3. Element geochemistry

All element ratios fluctuate, varying somewhat from the mean values. From the bottom of the core and up to 252 cm depth the element ratios of Ca/Fe, Zr/Rb and Ca/Sum show a general decreasing trend meanwhile Fe/Sum, Ti/Sum and K/Sum increase (Fig. 6.9).

6.4.1.4. Interpretation

The unit comprises three stacked intervals of reverse- and subsequent normal graded sandy mud and no bioturbation. Based on this, we suggest that the unit comprises three turbidites. The presence of both normal and inverse grading within a turbidite is a result of an unsteady flow (Kneller, 1995; Kneller and McCaffrey, 2003). Sediment reworking in this area is also indicated (Fig. 5.2). Given that the core is located in the proximity of a MTD (see *Chapter 5.2.2 Middle basin of Moskusoksefjord*), it is suggested that *Unit 9-1* was deposited from several turbidity currents.
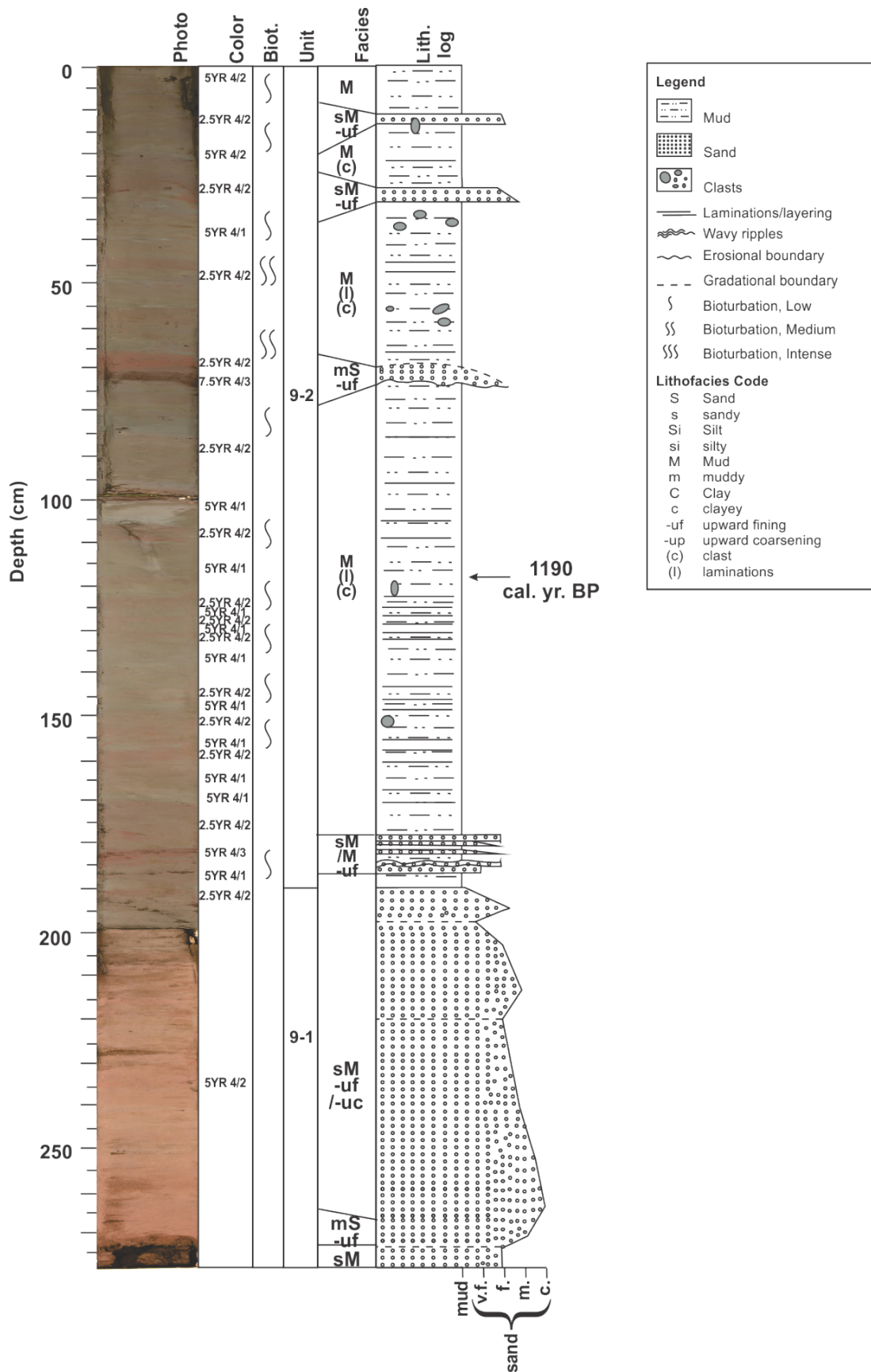
Figure 6.7: Lithological log of core HH13-009-GC-TUNU showing color image, Munsell color codes, bioturbation, units, lithofacies codes and structures. The depth of the dated interval is indicated by an arrow.

80

6.4.2. Unit 9-2 (188-0 cm)

From 188-25 cm depth the sediment color of the mud (*M*) changes repeatedly, alternating between dark gray (5YR 4/1) and weak red (2.5YR 4/2) creating laminations (*l*) (Fig. 6.7). In the upper 25 cm of the core the dark gray intervals become more dark reddish gray (5YR 4/2). In addition, single layers of reddish brown (5YR 4/3) sandy mud (*sM*) and brown (7.5YR 4/3) muddy sand (*mS*) occurs at 184-182 cm and 74-71 cm depth, respectively.

The unit is dominantly made up by massive mud (*M*) containing clasts (*c*) (Fig. 6.7 & 6.8). Layers of fining upwards sandy mud (*sM*) occur between 187-178 cm (up to 46% sand fraction), 31-27 cm (20% sand) and 13-11 cm depth (24% sand). All layers have sharp upper- and lower boundaries and are fining upwards. The upper layer (13-11 cm) also contains a single clast. A four cm thick layer of fining upwards muddy sand (*mS*) with a sand fraction reaching 65% occurs at 74-70 cm depth. The layer has an erosional lower boundary, a gradational upper boundary and is fining upwards. Clasts located within the mud occur as single features at 152 cm and 121cm, and as clusters between 60-55 cm and 37-33 cm.

The intervals comprising massive mud (*M*) have a low amount of bioturbation, with an increase in the interval at 70-43 cm.

6.4.2.1. Physical properties

A peak occurs in all five physical properties at 73 cm depth (Fig. 6.8). The water content has positive peaks at 168 cm and 108 cm and negative peaks at 183 cm and 73 cm, where all the peaks but one (108 cm) are related to changes in the lithology. The magnetic susceptibility generally increases from the bottom of the unit to approximately 136 cm depth. Above this, there are little fluctuations except for two negative peaks around 96 cm and 73 cm that are related to changes in the lithology. The mean value of the magnetic susceptibility is 30 (*10^{-8}SI(m^3/kg)), and is therefore considerably higher than the underlying *Unit 9-1* (see *Chapter 6.4.1.2. Physical properties*).

6.4.2.2. Element geochemistry

The element ratios vary considerably throughout the unit, and appear to be related to bedrock composition in the source area (Fig. 6.9). Concentrations of Al, Ca, Ti, K and Si decrease within the weak red layers of mud (*M*), while Zr and Fe show a minimal increase. In the brown layer of muddy sand (*mS*) between 74-70 cm, a marked increase in the concentrations of Zr and Ca occurs, accompanied by a marked decrease in Fe.
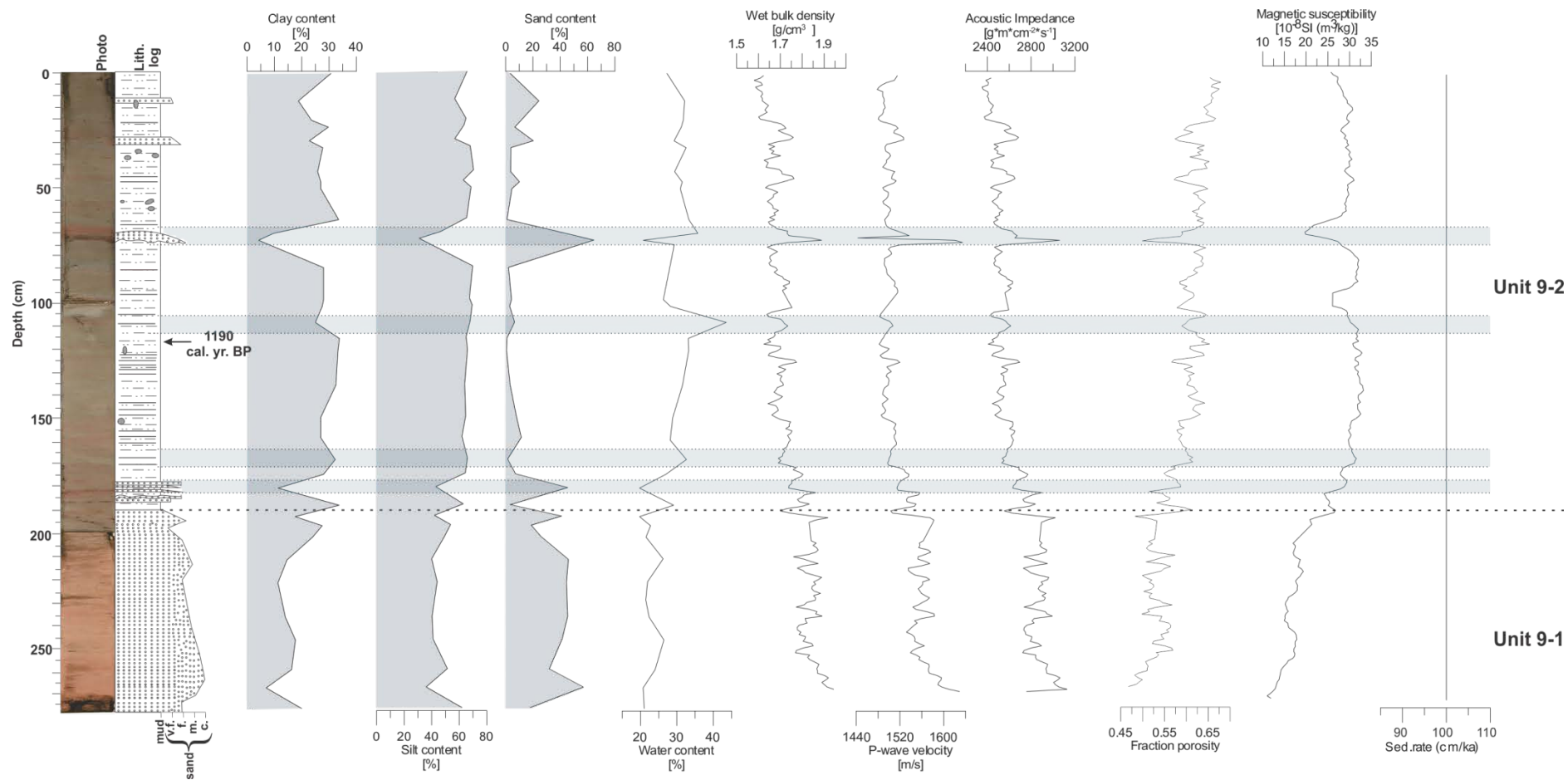
Figure 6.8: Grain-size distribution, the measured physical properties rate of core HH13-009-GC-TUNU and the estimated linear sedimentation. Color image and lithological log are included for reference. Units are indicated. The depth of the dated intervals is indicated by an arrow, while the largest fluctuations in the measured physical properties are indicated by gray horizontal lines.
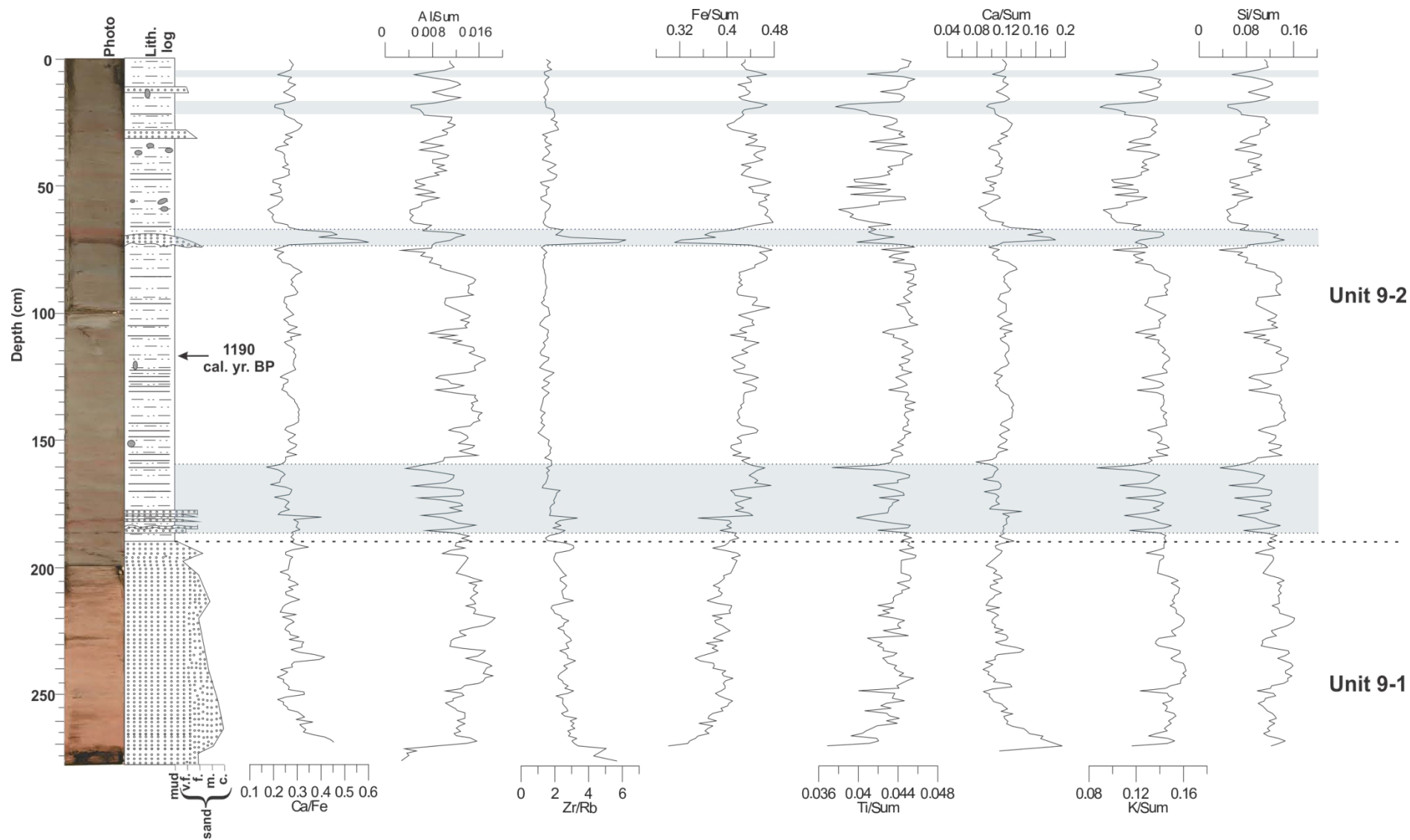
Figure 6.9: Measured element geochemistry for core HH13-009-GC-TUNU. Color image and lithological core is included for reference. Units are indicated. The depth of the dated intervals is indicated by an arrow, while the largest fluctuations in the element geochemistry are indicated by gray horizontal lines.

6.4.2.3. Chronology and sedimentation rates

A single sample of ostracoda was prepared for radiocarbon dating. The sample was collected at 118-117 cm depth, providing an age of 1190 cal. yr. BP (Table 6-2). A sedimentation rate of 90 cm/ka (Table 6-4) has been estimated assuming preservation of the present day seabed in the top of the core and a linear sedimentation rate from 117 cm depth and up to the top of the core. Only the sediments assumed to be deposited from suspension fall-out were included in the calculations. Based on this, the sediments from the bottom of *Unit 9-2* and up to approximately 99 cm are suggested to have been deposited during the Neoglaciation. The sediments from ~99 cm and up to ~81 cm represent the Medieval Warm Period, ~81 cm to ~9 cm the LIA and 9 cm and up the period after the LIA during the present day warming.

6.4.2.4. Interpretation:

The massive and laminated/layered mud containing clasts and layers of sandy mud and muddy sand is interpreted to represent a glacimarine environment (cf. Powell and Domack, 1995). The layer of sandy mud located between 13-11 cm containing a single clast is, along with the other single or clustered clasts are suggested to be IRD deposited by either sea ice or icebergs (e.g. Vorren et al., 1983; Forwick and Vorren, 1997; Reeh et al., 1999). The layers located at 187-178 cm, 74-70 cm and 31-27 cm are suggested to be parts of turbidites (for further discussion about turbidites, see *Chapter 6.5.1.4 Interpretation* below).

The physical factors and element geochemistry seem to correlate with the lithology to a certain degree with a large peak at 73 cm depth at the base of the interval containing muddy sand. However, it appears to be a larger correlation with the sediment colors (i.e. bedrock composition of the source area) representing sediment input from multiple sources.

6.5. Outer basin of Moskusoksefjord - Core HH13-010-GC-TUNU

Core HH13-010-GC-TUNU was retrieved in the outer basin of Moskusoksefjord (Fig. 6.1), approximately 11.5 km from the ice front of Waltershausen Gletscher and in the proximity to a delta (~570 m) prograding into the fjord from the south. The core length is 486 cm (Table 3-1). The sediment core comprises one single unit (*Unit 10-1*) containing five lithofacies (*M* (mud), *sM* (sandy mud), *sSi* (sandy silt), *Si* (silt) and *siS* (silty sand)) in addition to laminations (*l*) and clasts (*c*) (Fig. 6.10).

The uppermost 20-30 cm was lost during core retrieval, in addition do heavily disturbance of the upper >20 cm of the core.
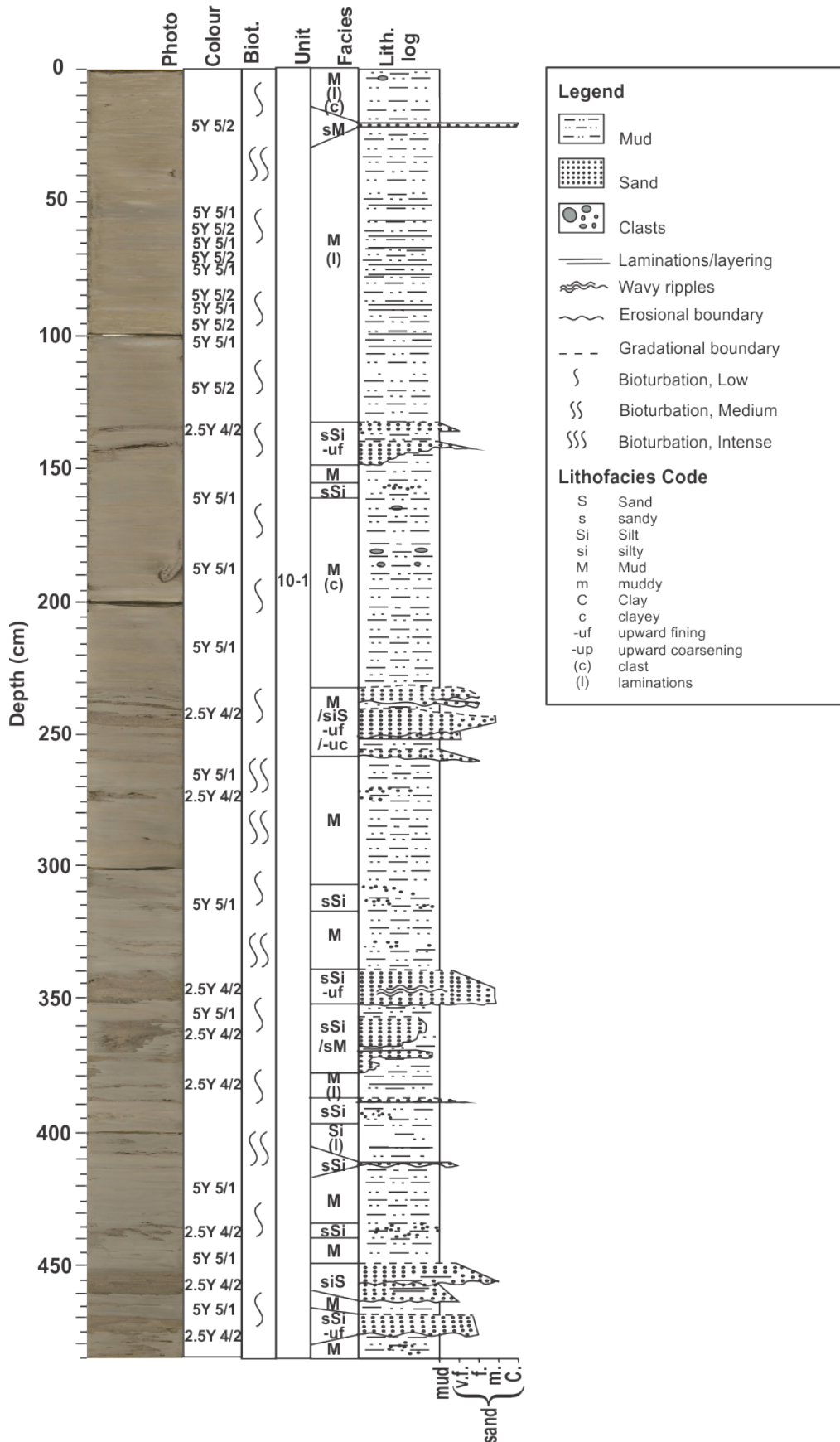
6.5.1. Unit 10-1 (486-0 cm)

6.5.1.1. Lithology and stratigraphy

There are three different colors appearing in the core that are related to the lithofacies; gray (5Y 5/1), dark grayish brown (2.5Y 4/2) and olive gray (5Y 5/2) (Fig. 6.10). The gray color dominates the mud (*M*) from the bottom and up to approximately 115 cm depth where it is followed by olive gray mud (*M*). The coarser intervals of the core have a dark grayish brown color (2.5Y 4/2).

The matrix of the core consists mainly of massive mud (*M*) (Fig. 6.10 and 6.12). However, multiple sub-horizontal layers of either sandy mud (17-31% sand), sandy silt (14-39% sand), or silty sand (51-77% sand) also occur throughout the core. A single interval of silt (63-74% silt) occurs between 411-397 cm. Sections with very little variations in the measured lithology show clear signs of lamination on the X-ray photographs (Fig. 6.11). Clasts (*c*) occur in a cluster between 193-180 cm and as single features at 165 cm and 3 cm.

There are several features classified as silty sand that show characteristics of a classic Bouma Sequence (Bouma, 1962). These features are located between 476-468 cm, 462-451 cm, 372-358 cm, 353-339 cm, 260-254 cm, 249-240 cm, 148-141 cm and 139-134 cm depth (Fig. 6.10). Their lower boundaries are erosional, whereas their upper are gradual. Grain-size analysis show that they are fining upward and some show signs of parallel lamination or wavy ripples. The feature located between 462-451 cm depth is further described below (see *Chapter 6.5.1.4. Interpretation*).
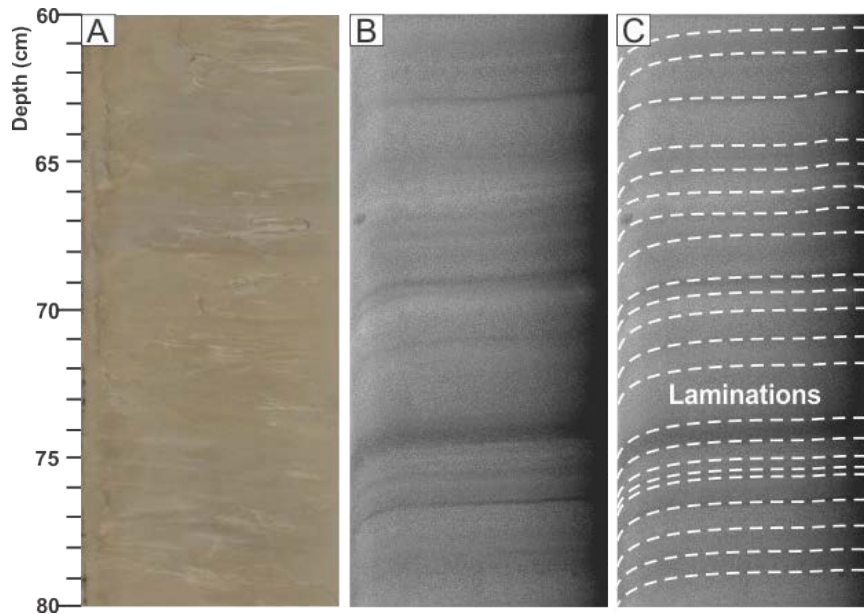
Figure 6.10: Lithological log of core HH13-010-GC-TUNU showing color image, Munsell color codes, degree of bioturbation, units, the lithofacies codes and sedimentary structures.

Figure 6.11: *A)* **Color image of the splitted core surface,** *B)* **X-ray photograph of the splitted core surface and** *C)* **X-ray photograph of the splitted core surface with interpretations of core HH13-010-GC-TUNU between 80cm and 60 cm depth. Laminations are indicated by white dotted lines.**

6.5.1.2. Physical properties

The water content show, as mentioned previously, a general decreasing trend downcore due to compaction of the underlying sediments with a maximum and minimum value of 39% and 14%, and a mean value of 25%. The graphic plots of the wet bulk density, p-wave velocity, acoustic impedance and fraction porosity generally show small oscillations around the mean values with fluctuations related to variations in the lithology (Fig. 6.12 & Table 6-1). Relatively marked peaks occur within the coarse layers of the core, with the fraction porosity having negative peaks. The largest peaks occur between 476-468 cm, 462-451 cm, 353-339 cm, 260-254 cm, 249-240 cm and 139-134 cm. The magnetic susceptibility varies throughout from 33 (*10^{-8}SI(m^3/kg)) to 69, with a mean value of 45.

6.5.1.3. Element geochemistry

The element ratios of Ca/Fe, Fe/Sum, Ti/Sum, Ca/Sum, K/Sum and Si/Sum generally show little variations from the mean value (Fig. 6.13 & Table 6-1). The most pronounced fluctuations occur, similarly to the physical properties above, within the coarse layers of the core. Ca/Fe, Ca/Sum and Si/Sum follow the same trend of positive peaks and are mirrored by Fe/Sum, Ti/Sum and K/Sum having negative peaks. Al/Sum shows fluctuations seemingly unrelated to the grain-size variations.
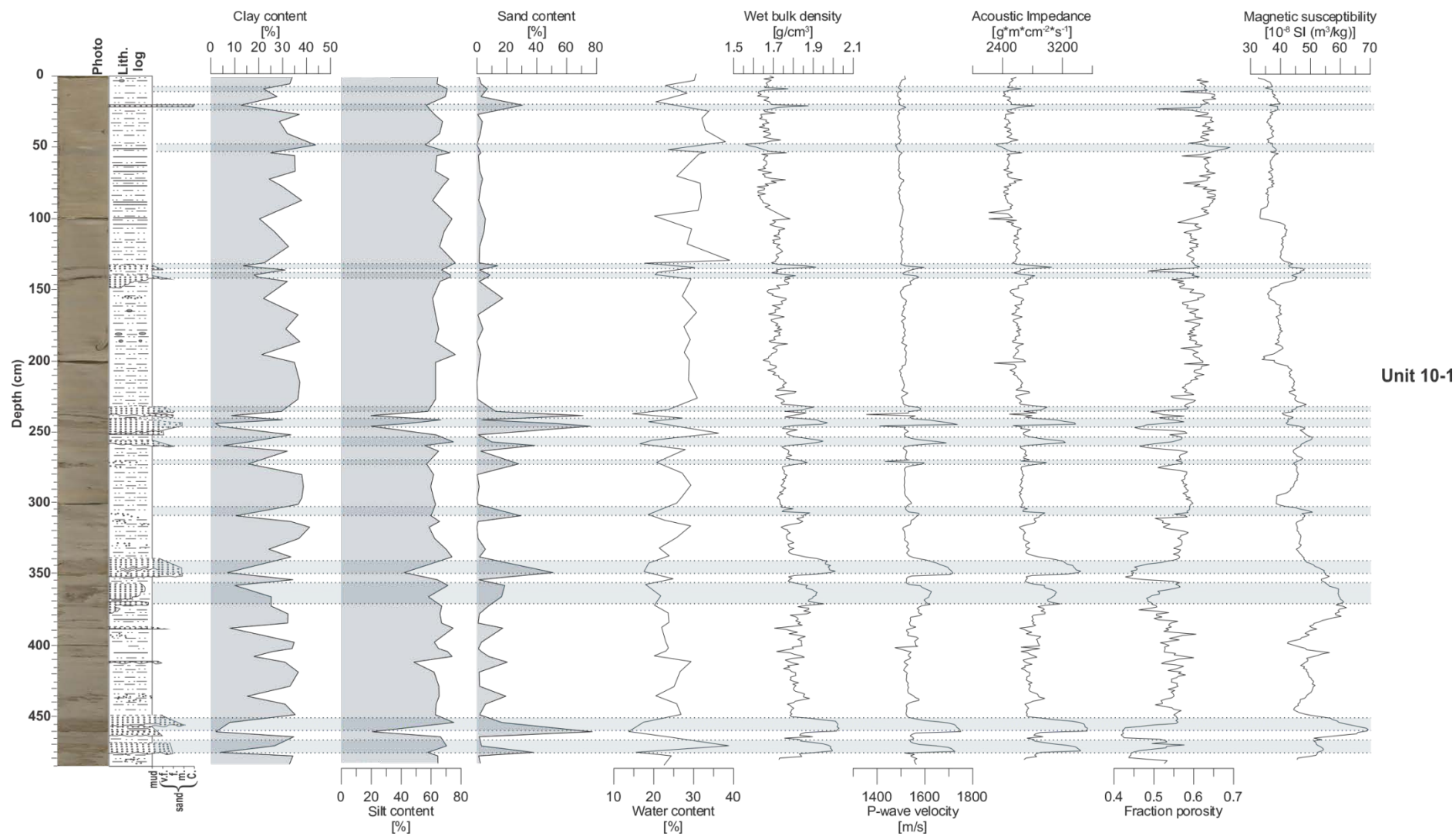
Figure 6.12: Grain-size distribution and the measured physical properties of core HH13-010-GC-TUNU. Color image and lithological log are included for reference. Unit is indicated. The largest fluctuations in the measured physical properties are indicated by gray horizontal lines.

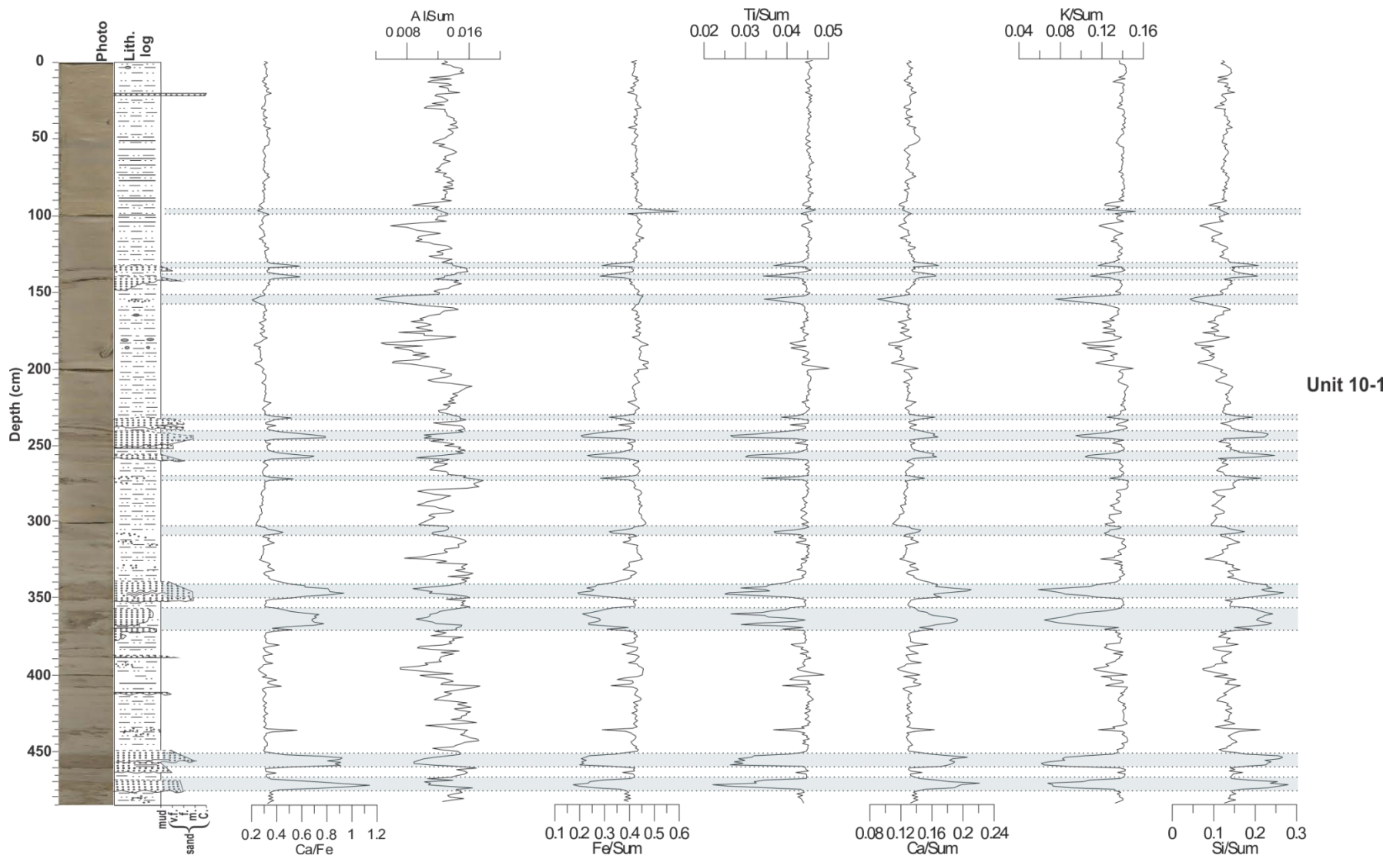**Figure 6.13: Measured element geochemistry for core HH13-010-GC-TUNU. Color image and lithological core is included for reference. Unit is indicated. The largest fluctuations in the element geochemistry are indicated by gray horizontal lines.**

6.5.1.4. Interpretation

Core HH13-010-GC-TUNU is dominated by muddy sediments with signs of periodical mass-transport activity. The most likely source is the nearby glacier Waltershausen Gletscher, making the sediments of glacimarine origin. Rain-out from sediment laden glacial meltwater plumes originating from Waltershausen Gletscher dominates the core along with intervals containing turbidites.

A turbidity flow, or current, is a "subgroup of gravity flows whose changed density compared to ambient fluid is due to grains suspended by turbulence" (Leeder, 2011). Turbidity flows can originate in a number of ways; transformation from a debris flow caused by sediment failure, as river outflows, ignitive flows in canyons or due to storm surges causing shelf turbidity currents (Kneller and Buckee, 2000; Meiburg and Kneller, 2010; Leeder, 2011). A turbidity flow can be divided into three zones: head, body and tail. At the head of the flow, the coarsest grains erode the underlying bed and mixes with the ambient fluid. This further forces the sediments into suspension, which are in turn further incorporated into the body and tail of the current. The flows density contrast is reduced, the velocity decelerates and the sediments are deposited by suspension fallouts from the body and tail as the flow comes to a halt (Kneller and Buckee, 2000; Nichols, 2009; Leeder, 2011).

The Bouma Sequence divides low- and medium grained turbidites into five distinct divisions (T_a-T_e) (Nichols, 2009; Leeder, 2011) (Fig. 6.14):

- T_a: The lowermost layer comprises massive to normally graded, fine- to coarse grained structureless sand, often with pebbles near the base. The sediments are deposited rapidly, and the base is often eroded.
- T_b: Planar-laminated sand, often finer and more sorted grains than in T_a. Represents the upper flow regime.
- T_c: Ripple-laminated layer containing medium to very fine sand. Indicative of moderate flow velocities within the lower flow regime.
- T_d: Parallel-laminated silt and interlaminated silts and mud. Deposited by a waning flow. Lamination is commonly less well defined than in T_b.
- T_e: The uppermost layer comprising homogenous, structureless hemipelagic silts and clays. Deposited as suspension fallout after the current has come to rest.
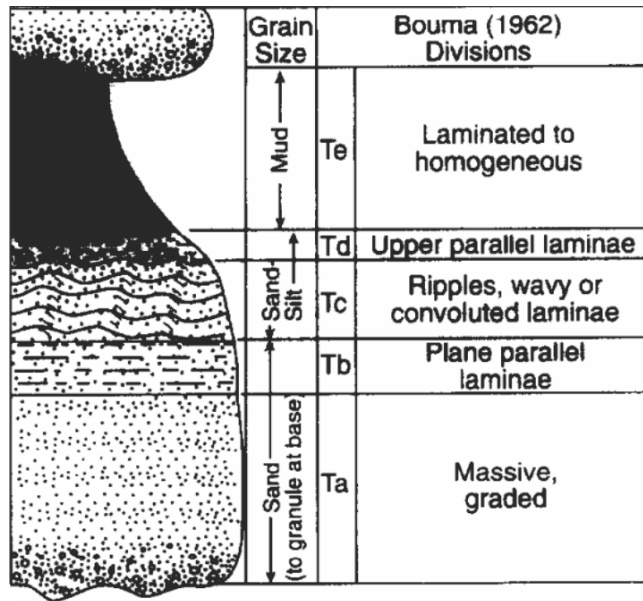
Figure 6.14: A graphic presentation of the ideal Bouma Sequence showing the T_a, T_b, T_c, T_d and T_e divisions and their characteristics. (From Bouma (1962) in Shanmugam (1997).
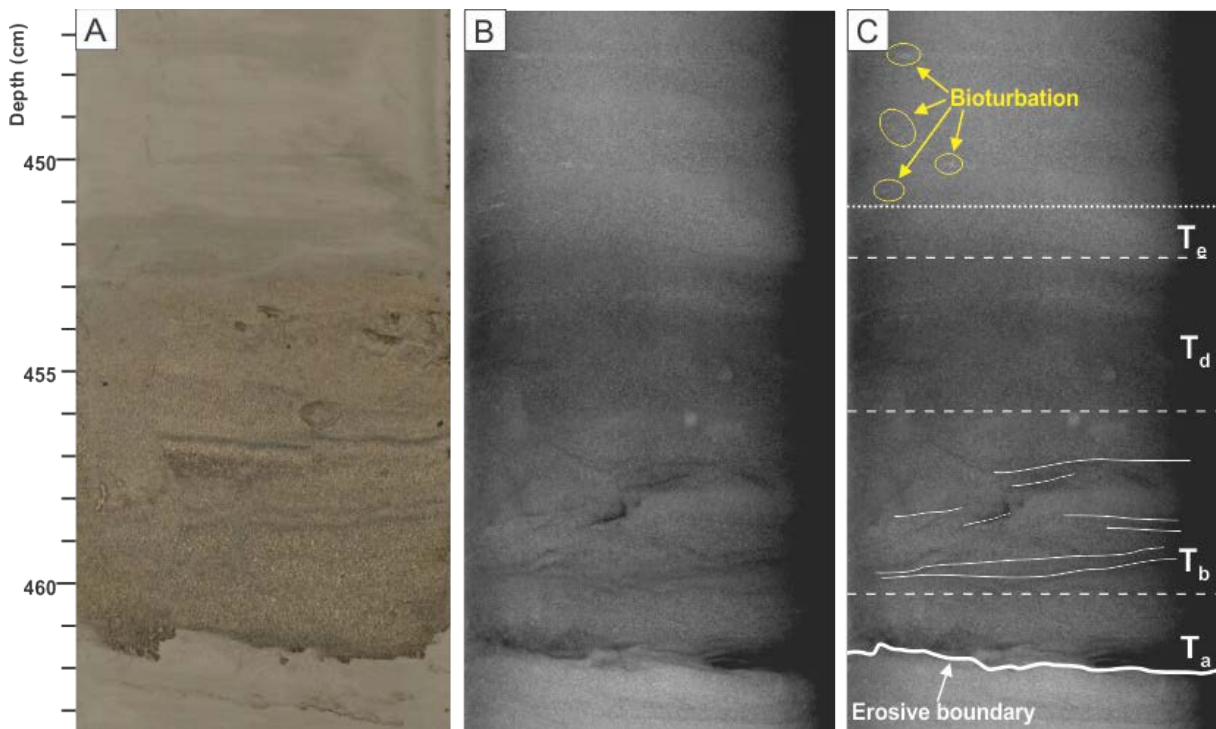

Figure 6.15: *A*) Color image, *B*) X-ray photograph and *C*) X-ray photograph with interpretations of core HH13-010-GC-TUNU between 463.5 cm and 446.5 cm depth. Turbidites with intervals from the Bouma Sequence are indicated in white, bioturbation by yellow.

The feature located between 462-451 cm has a distinctive erosional lower boundary and a gradational upper boundary (Fig. 6.15). The executed grain-size analysis revealed that the feature has massive medium sand at the base and fines upwards to mud. The feature has been interpreted to represent parts of the Bouma Sequence. The massive, structureless sand above the erosive base (~462-460 cm) is suggested to represent interval T_a. Above lies T_b, an interval (~460-456 cm) with sub-horizontal, near-parallel laminae composed of fine sand. Aligned mica minerals contribute to the visualization of the laminas on the core surface. Interval T_d spans from ~456 cm and up to ~452.2 cm and contains very fine sand to silty sediments. However, no laminas are observed on the sediment surface. The uppermost interval, T_e, comprises massive mud and stretches up to ~451 cm.

The clasts are, as mentioned previously, suggested to be IRD deposited by either icebergs or sea ice (cf. Forwick & Vorren, 1997; Reeh et al., 1999). With the little amount of clasts present in the core, we suggest that it either was a little amount of ice calving during the period of deposition, or the icebergs floated out of Nordfjord.

The sparse amount of biological material suggests an unfavorable environment for macrofauna caused by high sedimentation rate. This is not supported by available radiocarbon dates, but the proximity to Waltershausen Gletscher makes this likely (cf. Andrews et al., 1994). However, bioturbation occurs in the muddy intervals of the core indicating some biological activity in the area and no reworking of the sediments (e.g. Forwick and Vorren, 2007).

The physical properties and element geochemistry correlate well with the lithology, but a closer relation should not be excluded as the core was sampled on average every 6 cm. The intervals with increased grain-sizes and sand fraction are accompanied by a darker, more brownish gray sediment color, along with increases in the wet bulk density and marked peaks in the element geochemistry. Both the increase in Ca and Si within the coarser intervals and the change to olive gray in the upper 115 cm may are likely to be caused by a change in the sediment provenance.

6.6. Nordfjord - Cores HH13-011-GC-TUNU and HH13-012-GC-TUNU

Cores HH13-011-GC-TUNU and HH13-12-GC-TUNU were both acquired in Nordfjord, but in two different sub-basins (for location, see Fig. 5.4 & 6.1). Their distance from the front of Waltershausen Gletscher is ~10 km and ~14 km, respectively. The uppermost 10 cm of the sediments were lost during core retrieval, in addition to the uppermost 10-20 cm being heavily disturbed.

6.6.1. Unit 11-1 (597-0 cm)

Core HH13-011-GC-TUNU was retrieved at 210 m water depth in sub-basin 2 (Fig. 5.4) and is 597 cm long. It is made up by one single unit (*Unit 11-1*), containing lithofacies *M* (mud), *sM* (sandy mud), *Si* (silt)*, sSi* (sandy silt), and *siS* (silty sand) along with laminations (*l*) and a few clasts (*c*).

6.6.1.1. *Lithology and stratigraphy*

Like core HH13-010-GC-TUNU, the sediment colors of core HH13-011-GC-TUNU change frequently between gray (5Y 5/1), dark grayish brown (2.5Y 4/2) and olive gray (5Y 5/2) (Fig. 6.16). The gray color dominates the fine sediments from the bottom of the core and up to approximately 150 cm depth. From here and up the fine sediment has dominantly an olive gray color. Thin laminas of dark grayish color containing higher sand fractions are present throughout the core.

Large fluctuations in grain-size are observed throughout the core, accompanied with dark grayish brown color (Fig. 6.16 & 6.17). The grain-size distribution shows average dominant volumes of silt (67%), with clay and sand having 21% and 12%, respectively. The core consists of massive silt (*Si*) interrupted by thin layers of lamina comprising mud (*M*), sandy mud (*sM*), sandy silt (*sSi*) and silty sand (*siS*). The largest sand fractions are seen near the bottom of the intervals between 515-503 cm (up to 62% sand), 443-432 cm (72%), 362-348 cm (78%), 289-271 cm (74%) and 114-99 cm (67%). Clasts (*c*) are identified at 587 cm, 541 cm, 455 cm and 16 cm.
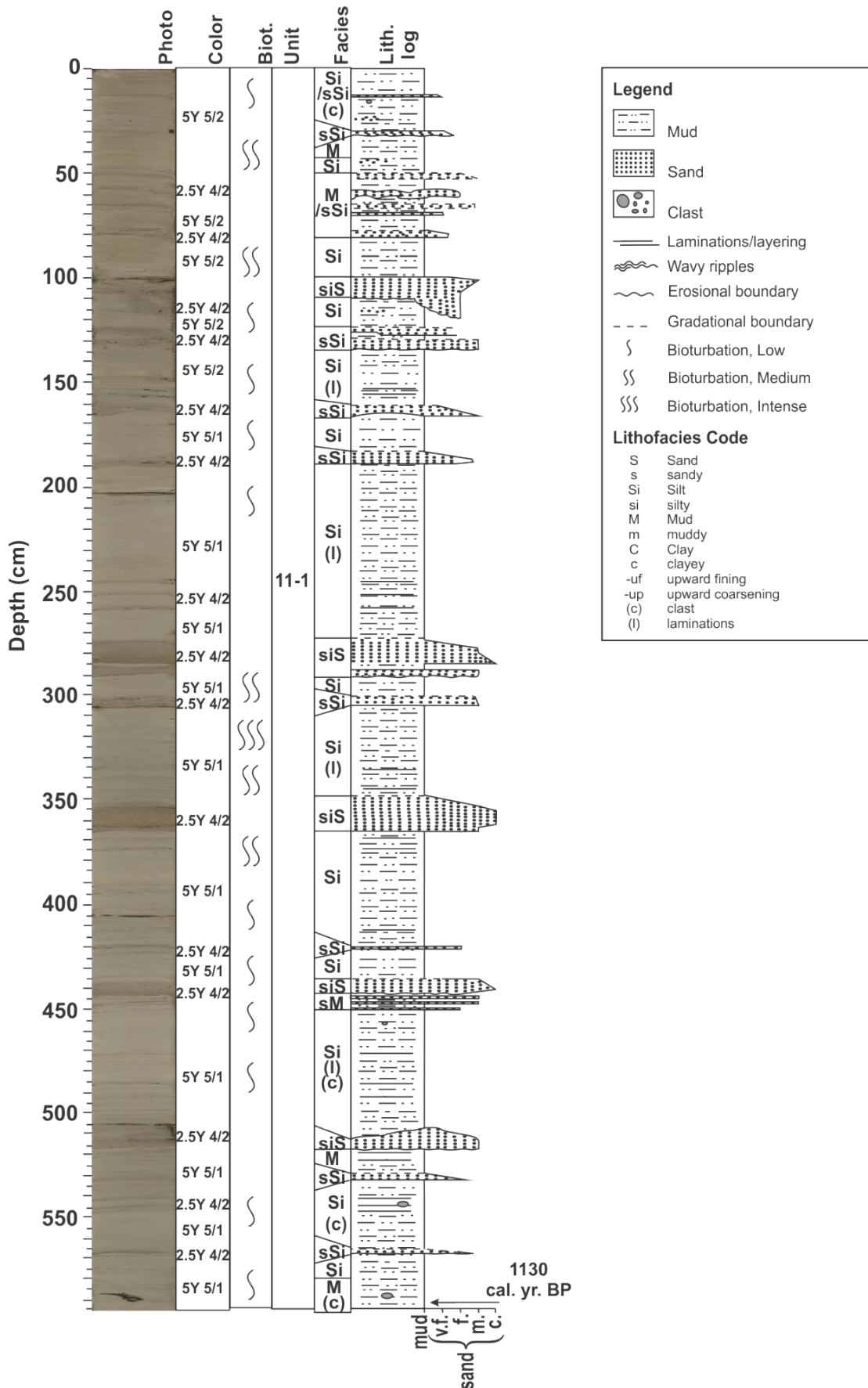
Figure 6.16: Lithological log of core HH13-011-GC-TUNU showing color image, Munsell color codes, bioturbation, units, lithofacies codes and structures. The dated interval is indicated by an arrow.

94

Bioturbation occurs in the intervals containing mud or silt, with the most pronounced degree of bioturbation in the intervals between 385-364 cm, 357-289 cm, 99-91 cm and 48-32 cm (Fig. 6.16).

6.6.1.2. Physical properties

The water content shows relatively large fluctuations with a minimum of 10%, a maximum of 37% and a mean value of 24% (Fig. 6.17). However, unlike the previous described sediment cores, the measured water content fluctuates around a relative constant value, increasing slightly with depth. This indicates that the sediments have not gone through normal consolidation and are therefore suggested to have been deposited rapidly. The wet bulk density, p-wave velocity, acoustic impedance and fraction porosity vary only slightly around the mean values in the fine-grained intervals of the core. In the top ~190 cm of the core, however, more frequent layers containing sand fractions up to 10% leads to increased fluctuations in the fine-grained intervals. In the coarser intervals more noticeable changes and large peaks occur due to changes in the P-wave velocity and higher density of the sediments. The magnetic susceptibility of the core show more frequent fluctuations than in the aforementioned cores (see Fig. 6.5, 6.8 and 6.12), influenced by the grain-size distribution with negative peaks in the coarser intervals. The magnetic susceptibility is high compared to the other sediment cores studied (see Table 6.1) with a minimum of 70 ($*10^{-8}SI(m^3/kg)$), a maximum of 96 and a mean value of 87.

6.6.1.3. Element geochemistry

Fluctuations in element geochemistry are observed in all of the plotted graphs (Fig. 6.18). The Ca/Fe, Ti/Sum and K/Sum reflect the variations in grain-size and color of the deposits with larger peaks in intervals with higher fractions of dark grayish brown sand. Fe, Ti and K decrease in the coarser intervals. Si shows small peaks in the coarser intervals, whereas Al and Ca appear to be unrelated to the sediments grain-size distribution.

6.6.1.4. Chronology and sedimentation rates

Three samples were collected for radiocarbon dating for this core, located at 593-592 cm, 401-400 cm and 219-218 cm depth. The material sampled at 401-400 cm contained too little carbonates and was therefore not further prepared for radiocarbon dating. Also, the sample at

219-218 cm, containing ostracoda and shell fragments was prepared and attempted to be dated but failed due to too little material available.

The sample containing diverse benthic foraminifera at 593-592 cm has been dated to 1130 cal. yr. BP (Table 6-2). If assuming a linear sedimentation rate from 592-0 cm (in addition to the 10 cm lost during core retrieval), the average sedimentation rate is 533 cm/ka (Table 6-4).

With the bottom of the core (593-592 cm) being dated to be 1130 cal. yr. BP and the estimated average sedimentation rate being 533 cm/ka., the sediments from the bottom and up to ~416 cm have been deposited during the Medieval Warm Period, from ~416 cm to ~43 cm in the Little Ice Age, while the upper ~53 cm are of modern times.

6.6.1.5.   Interpretation

Core HH13-011-GC-TUNU is interpreted to comprise sediments representing a glacimarine environment where Waltershausen Gletscher is the dominant sediment source. The mud is interpreted to be essentially deposited by suspension settling from overflows, whereas the sand content is deposited by density-currents related to underflows (Benn & Evans, 2010). The clasts and some of the laminas are related to IRD. As the content of thin sand layers increases upcore, the upper part of the core represents a period of enhanced glacial activity compared to the underlying sediments (cf. Forwick and Vorren, 2009, Baeten et al., 2010; Jessen et al., 2010).
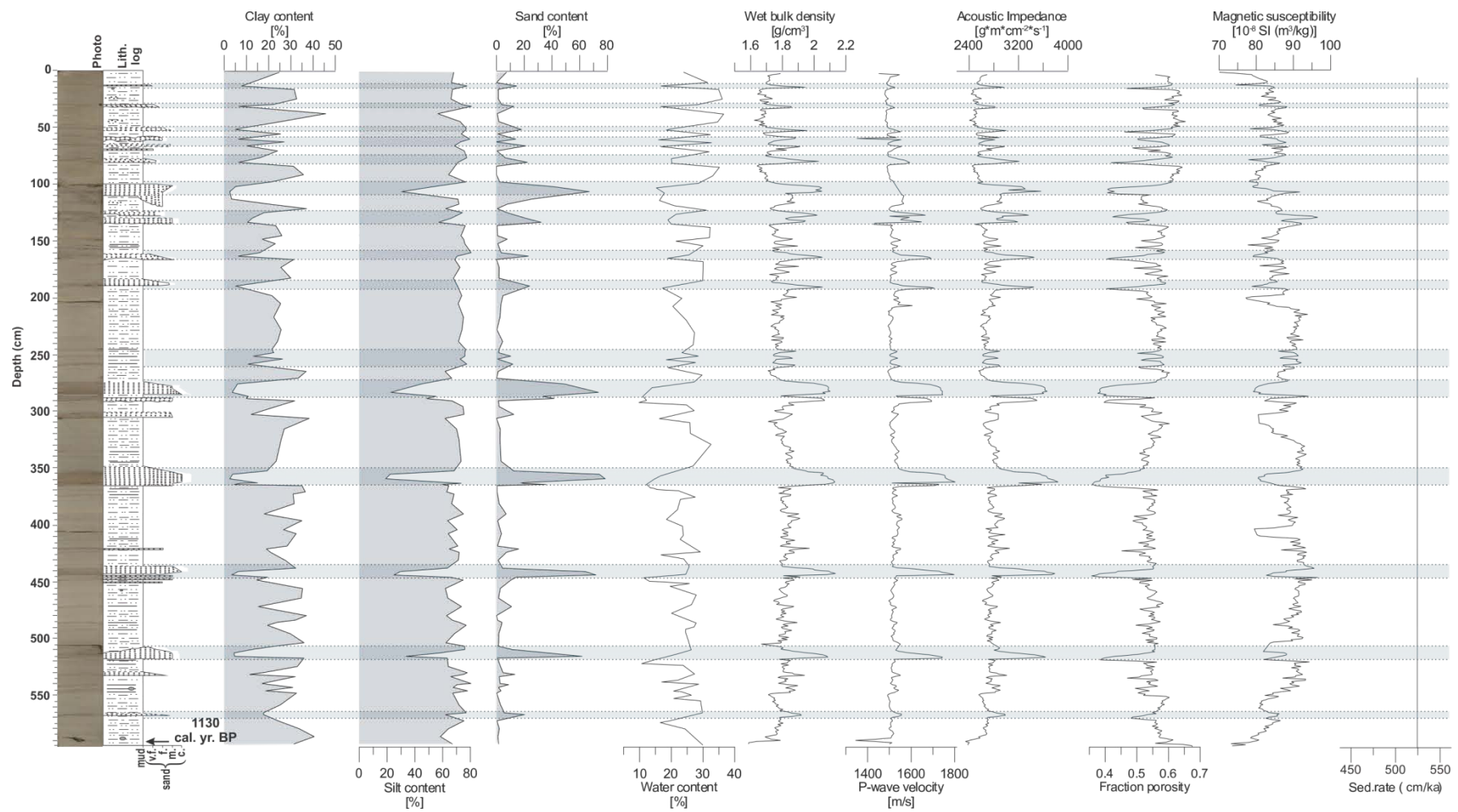
Figure 6.17: Grain-size distribution, estimated linear sedimentation rate and the measured physical properties of core HH13-011-GC-TUNU. Color image and lithological log are included for reference. Unit is indicated. The depth of the dated intervals is indicated by an arrow, while the largest fluctuations in the measured physical properties are indicated by gray horizontal lines.
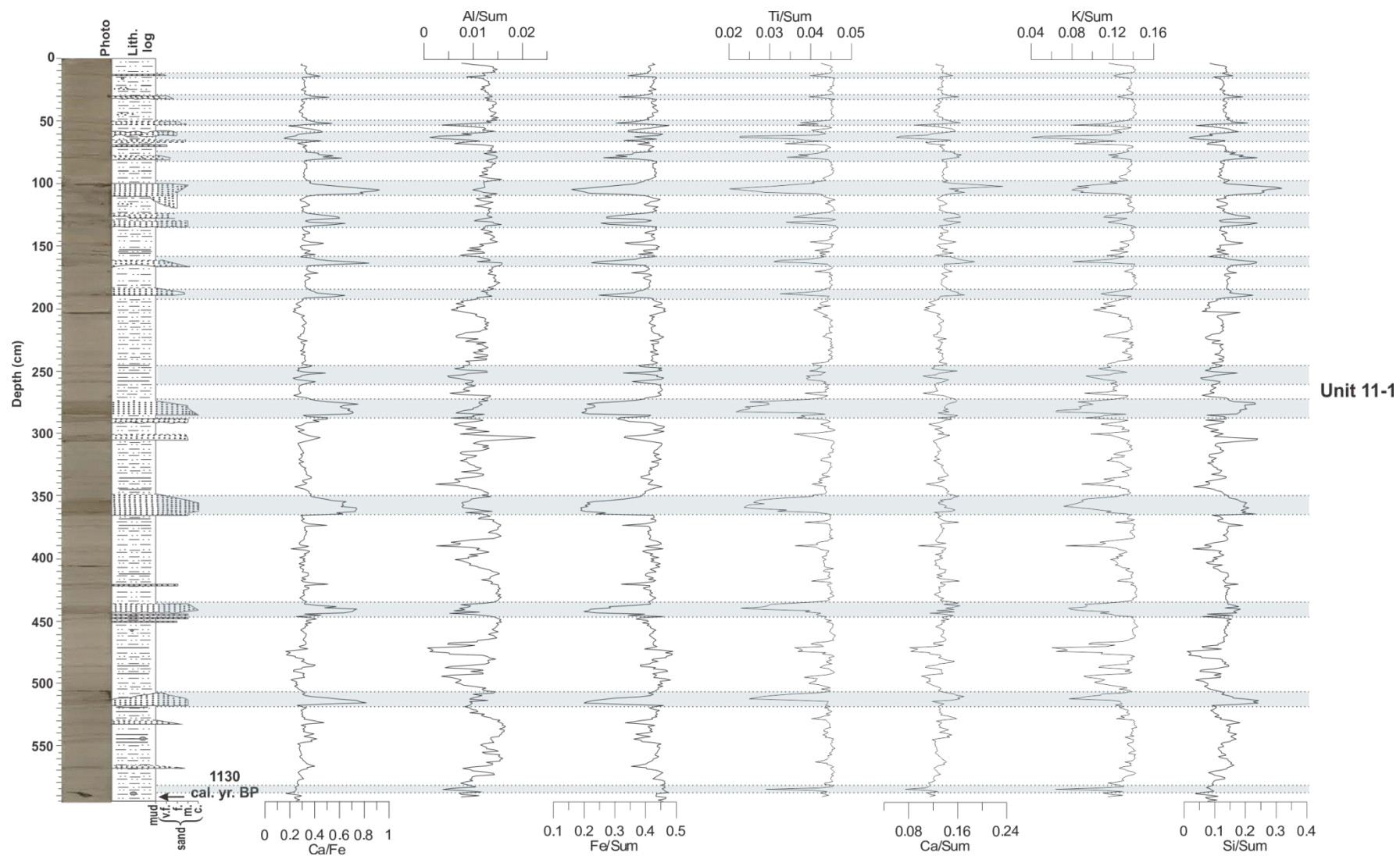
Figure 6.18: Measured element geochemistry for core HH13-011-GC-TUNU. Color image and lithological core is included for reference. Unit is indicated. The depth of the dated intervals is indicated by an arrow, while the largest fluctuations in the element geochemistry are indicated by gray horizontal lines.

6.6.2. Unit 12-1 (459-0 cm)

Core HH13-012-GC-TUNU is 459 cm long and was retrieved at ~209 m water depth in sub-basin 1 (Fig. 5.4). The core includes *Unit 12-1* and lithofacies *M* (mud), *sM* (sandy mud), *sSi* (snady silt) and *mS* (muddy sand) along with laminations (*l*) clusters of clasts (*c*).

The uppermost 10 cm of sediments were heavily disturbed during core retrieval.

6.6.2.1.   Lithology and stratigraphy

The sediment color changes frequently throughout the core, alternating between gray (5Y 5/1) and olive gray (5Y 5/2) (Fig. 6.19). Color changes are generally gradual. In addition, a single layer of weak red (2.5YR 4/2) occurs at depth of 393-390 cm.

The grain-size distribution shows relatively little fluctuation compared to the previously discussed sediment cores (see *Chapter 6.3.1, 6.4.1, 6.5.1 & 6.6.1*). The core is mainly composed of mud with four relatively thin (3-6 cm thick) layers of either sandy silt or muddy sand and numerous sand lenses. Average grain-size volumes are 4% sand, 69% silt and 27% clay (Fig. 6.19). Two large peaks of muddy sand occur between 394-391 cm (43% sand) and 360-356 cm (49%), whilst smaller peaks of sandy silt and sandy mud occur between 255-253 cm (15%), 152-150 cm (13%) and 15-5 cm (up to 15%). Clasts occur mainly in clusters, between 380-366 cm, 298-296 cm, 273-265 cm, 221-214 cm, 133-132 cm, 120-119 cm, 101-100 cm and 87-81 cm (Fig. 6.21).

Bioturbation is absent from the bottom and up to approximately 390 cm (Fig. 6.19). From 390 cm and up to 195 cm the bioturbation occurs as low with a slight increase to medium around 310 cm depth, whilst from 190 cm and up to the core top the bioturbation is intense and disturbs the sediments (Fig. 6.20).

6.6.2.2.   Physical properties

The water content of the core fluctuates between 15% and 44% with a mean value of 24% (Fig. 6.21). The general trend of the water content remains constant with depth, with decreases occurring in correlation with increases in the sand fraction. The wet bulk density, p-wave velocity, acoustic impedance and fraction porosity all have a zigzag-shaped appearance, with a general trend reflecting the sediments consolidation with depth. The largest peaks occur in accordance with clasts. The magnetic susceptibility varies throughout the core from
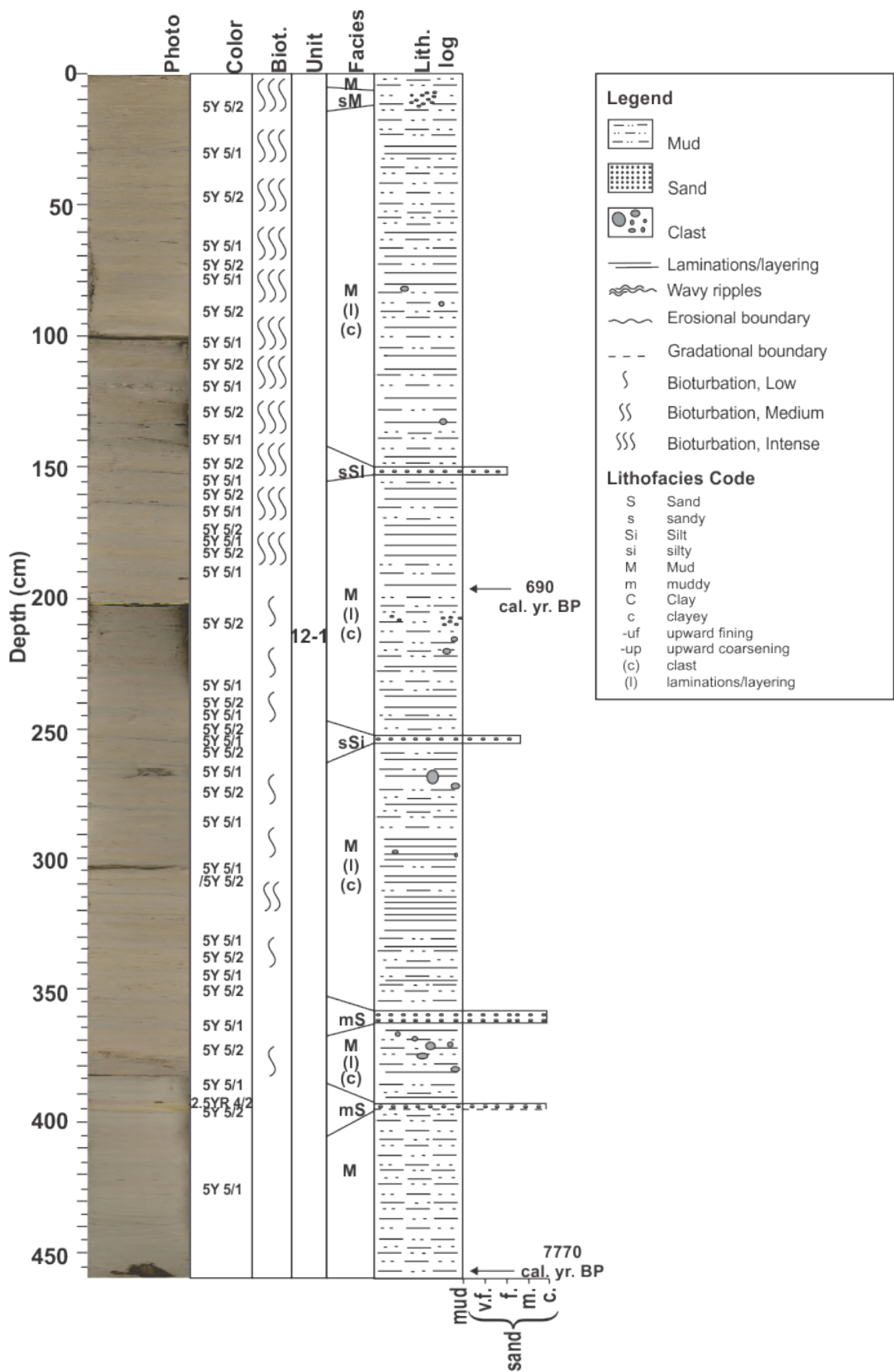
Figure 6.19: Lithological of for core HH13-012-GC-TUNU showing color image, Munsell color codes, bioturbation, units, lithofacies codes and structures. The dated intervals are indicated by arrows.
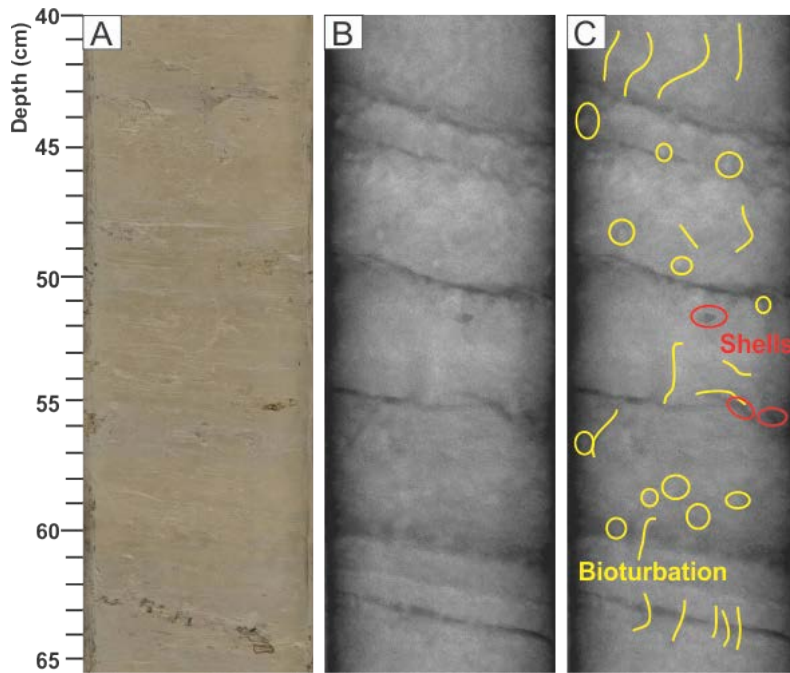
Figure 6.20: Detail image of bioturbated mud comprising some laminations/layering. *A*) Color image. *B*) X-ray photograph and *C*) X-ray photograph with interpretations from core HH13-012-GC-TUNU between 65.5 cm - 40 cm depth. Bioturbation is indicated by yellow circles and lines, shells by red circles.

33 (*10^{-8}SI(m^3/kg)) to 63, with a mean value of 44. The graph shows a decreasing trend from the bottom and up with jumps to lower values in and around section boundaries.

6.6.2.3. Element geochemistry

All of the plotted element geochemistry fluctuates around the mean values, with some peaks related to lithological variations and/or sediment color (Fig. 6.21 & 6.22). Ca, K, Ti and Si follow each other with marked decreases in the same depths. Ca and Si have abrupt increases at 117 cm. An abrupt decrease in Ca simultaneously with increases in Al, Fe and K occurs within the weak red interval at 393-390 cm.

6.6.2.4. Chronology and sedimentation rates

The results from ^{210}Pb dating provided an unsteady decrease of activities with depth, making it difficult to do a reliable assessment of the sediment accumulation rates. However, the samples from the upper 50 cm show higher activities suggesting that the sediments accumulated during less than 100 years. The calculated sediment accumulation rate using the ^{210}Pb activity from 20 and 50 cm depth is likely bigger than 300 cm/ka assuming a constant initial concentration. The ^{137}Cs activities are observed down to at least 50 cm depth, but is absent at 100 cm deep, suggesting that the sediment accumulation is in range of 800 to 1600

cm/ka. The maximum activity at 20 cm depth makes it more likely that the lower range of values is the correct. However, comparing the results from both ^{210}Pb and ^{137}Cs the most likely sediment accumulation rate for the uppermost ~50 cm is about 1000 cm/ka (Table 6-4). However, some more samples needs to be dated to get a more reliable assessment of the sediment accumulation rate (Szczuciński, 2015).

Three samples were collected from core HH13-012-GC-TUNU for radiocarbon dating, located at 455-454 cm, 196-195 and 98-97 cm depth. Only two of the samples (455-454 cm and 196-195 cm) contained enough material for preparation and radiocarbon dating. They both contained diverse benthic foraminifera. The deepest interval from 455-454 cm provided an age of 7770 cal. yr. BP while 690 cal. yr. BP was measured for 196-195 cm (Table 6-2). Following sedimentation rates have been estimated based on the ^{14}C dating assuming a linear sedimentation rate and that the top of the core represents the present seafloor: 36 cm/ka between 454-195 cm and 279 cm/ka between 195 cm and to the top (Table 6-4). This gives an estimated average linear sedimentation rate of 58 cm/ka for the whole core.

Based on the sedimentation rates provided by the obtained radiocarbon ages, the sediments from the bottom of the core and up to ~261 cm were deposited from approximately 7770 cal. yr. BP to 4500 cal. yr. BP during the Holocene Climate Optimum. The interval between ~261-58 cm represents the Neoglaciation, ~58-46 cm the Medieval Warm Period, ~46-6 cm the LIA and ~6 cm and up to the top of the core the post LIA – modern day deposits.

6.6.2.5. *Interpretation*

Similar to the previously discussed sediment cores, core HH13-012-GC-TUNU is also interpreted to represent a glacimarine environment due to the presence of scattered clasts. The sediment core is made up by massive and laminated/layered bioturbated mud and coarser sediments interpreted to be deposited as fall-out from meltwater plumes and/or coarse-grained turbidites. The high radiocarbon date at the bottom of the core (7770 cal. yr. BP at 455-454 cm depth) indicates a very low average sedimentation rate compared to the previously discussed core HH13-011-GC-TUNU (58 cm/ka vs. 533 cm/ka). Syvitski (1989) postulated that as much as 70% of the sediment load from glaciers are deposited glacifluvially or from suspension within the first 500 m from the glacier front. This marked decrease in average sedimentation rate is caused by an increasing distance to the main sediment source

Waltershausen Gletscher and, as observed in Fig. 5.4, an elevation creating an obstacle for sediment transportation along the seafloor.

The intense bioturbation in the upper ~190 cm of the core have caused displacement within the sediments. The primary laminations in the sediments have been altered and are therefore difficult to visualize on the sediment surface and may only be observed on the X-ray photographs (Fig. 6.20). An increase in the degree of bioturbation may indicate an environmental stability with slow suspension fallout sedimentation (e.g. Gingras et al., 2015).
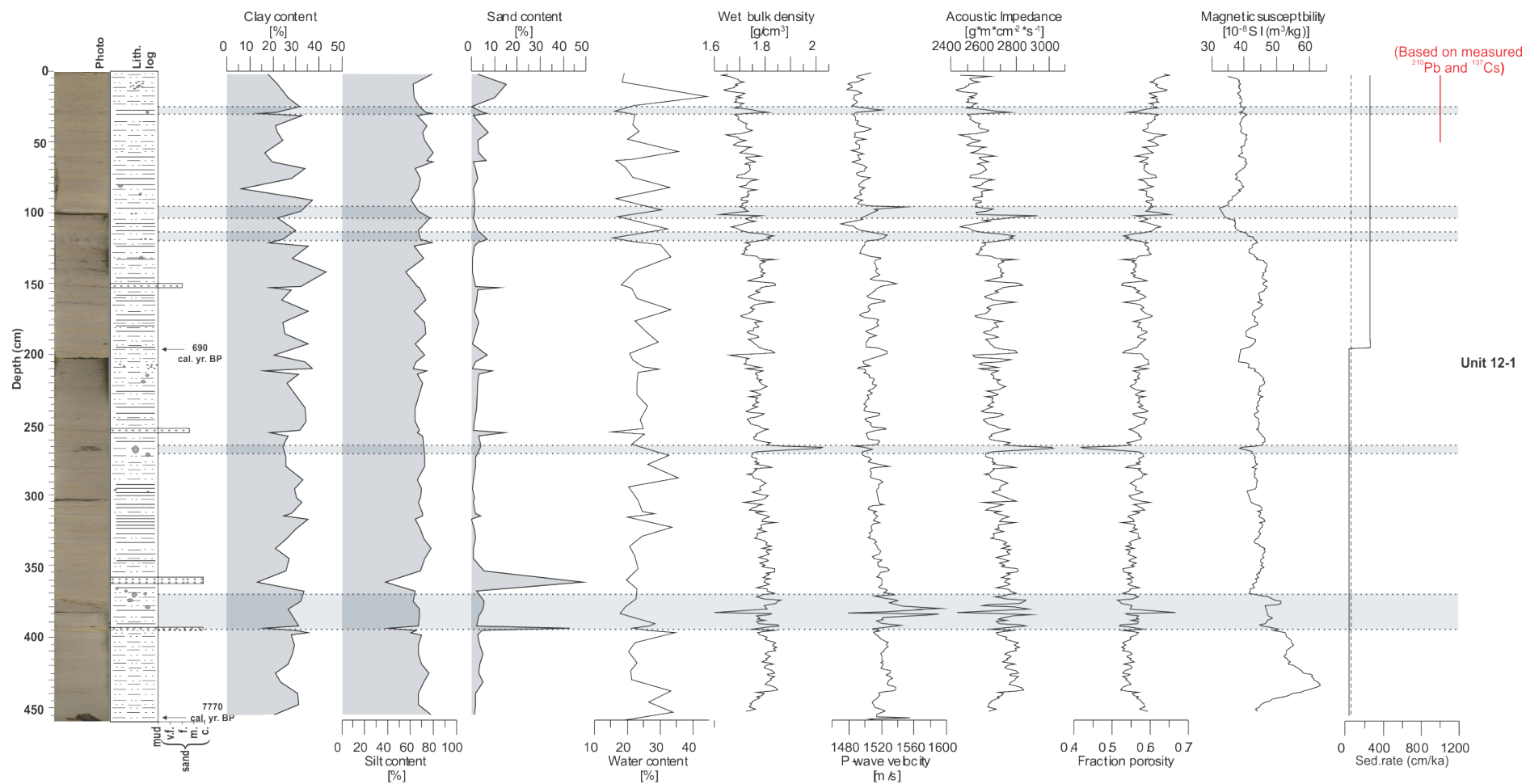
Figure 6.21: Grain-size distribution, estimated linear sedimentation rate (dotted line is the average sedimentation rate) and the measured physical properties of core HH13-012-GC-TUNU. Color image and lithological log are included for reference. Unit is indicated. The depths of the dated intervals are indicated by arrows, while the largest fluctuations in the measured physical properties are indicated by gray horizontal lines.

Figure 6.22: Measured element geochemistry for core HH13-012-GC-TUNU. Color image and lithological core is included for reference. Unit is indicated. The depths of the dated intervals are indicated by arrows, while the largest fluctuations in the element geochemistry are indicated by gray horizontal lines.

7. Discussion

In this chapter the results from the previous three chapters will be compiled and compared in order to reconstruct the sedimentary paleoenvironment of the study area during the Holocene. The acoustic data (comprisi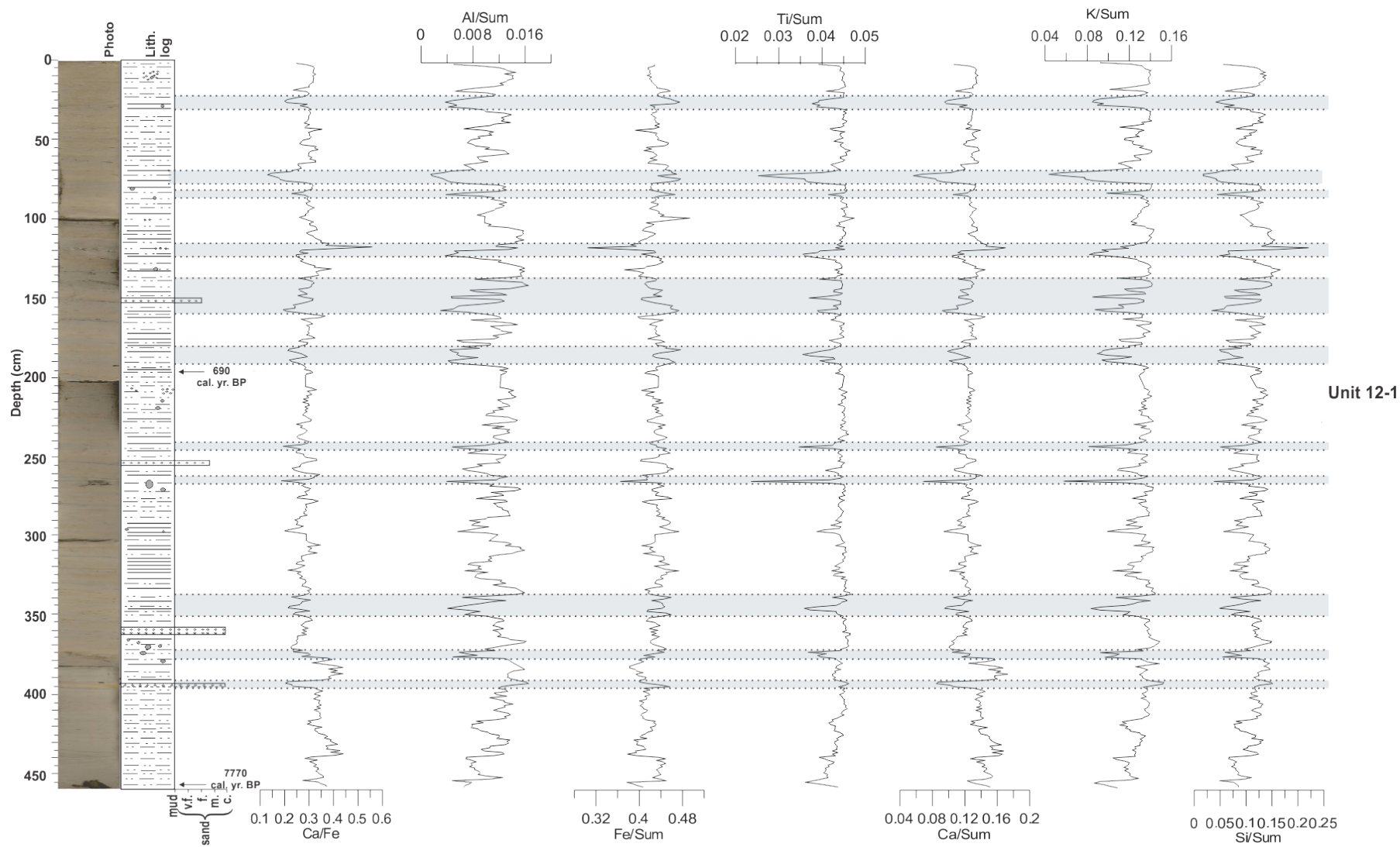ng the swath bathymetry and chirp profiles) will be discussed in order to correlate and classify the morphology and origin of the submarine landforms. Moskusoksefjord and Nordfjord will here be discussed separately with a short summary at the end. Further, the lithostratigraphy and seismostratigraphy will be correlated. Sediment distribution (thickness) and sediment rates in the two fjords will be addressed in addition to the sedimentary processes and provenance. The different rates will be compared and to sedimentation rates found in other East Greenland fjords. Fjords from Spitsbergen and Northern Norway will be compared as well in regards to sedimentation rates. Finally, the Holocene glacial history and sedimentary paleoenvironment of Moskusoksefjord and Nordfjord will be discussed.
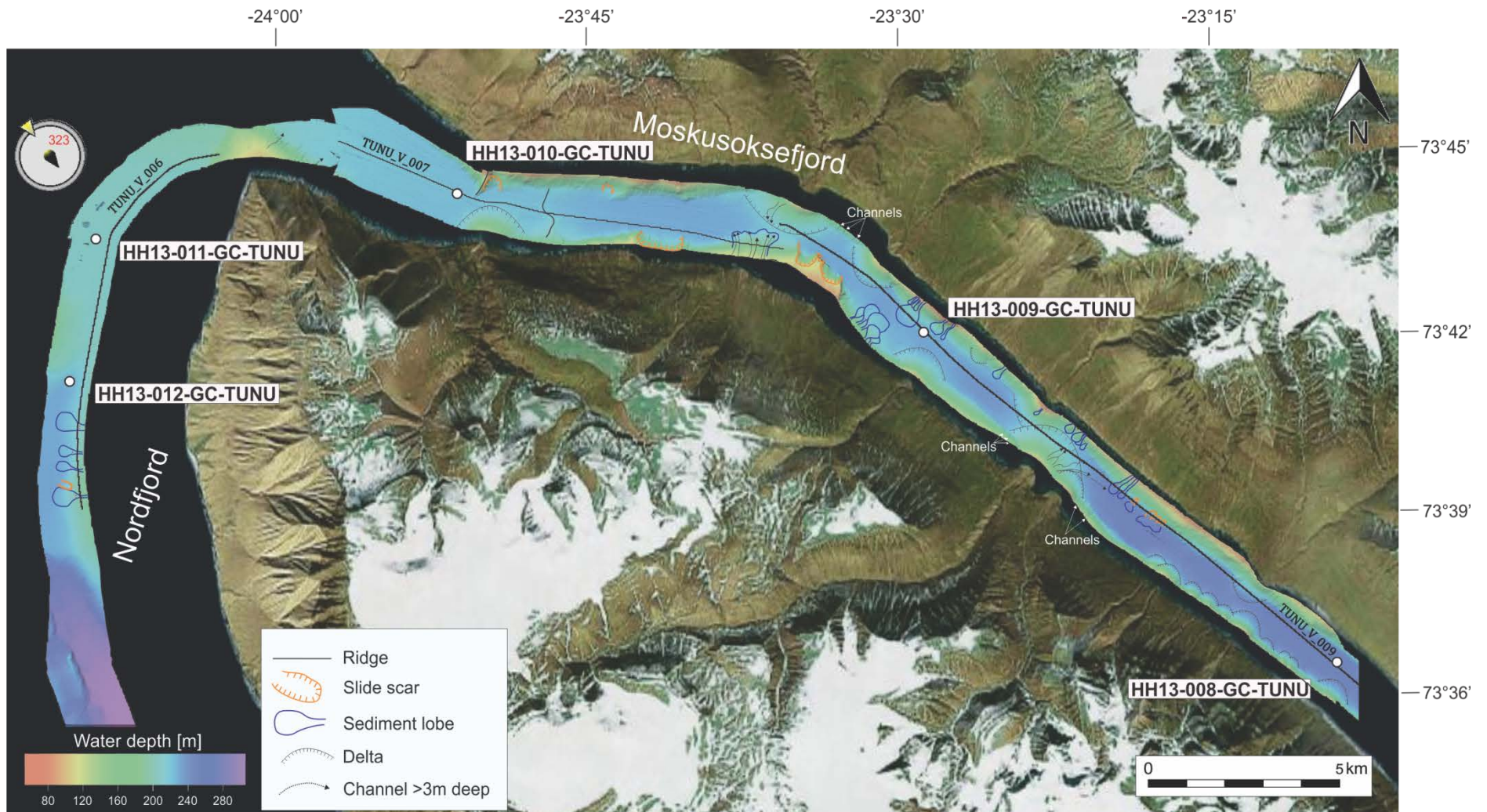
Figure 7.1: Swath bathymetry with interpretation of the large-scale features, position of chirp lines and core locations.

7.1. Morphology and origin of the submarine landforms

In this chapter Moskusoksefjord and Nordfjord will be discussed separately based on a geographical division of the two fjords. Both fjords` large-scale morphology is summarized in Figures 7.1 and 7.2. No glacial landforms have been observed in the study area apart from two transverse ridges in the outer basin of Moskusoksefjord which may represent buried glacial moraines. The lack of observable glacial landforms is probably due to high sedimentation rates in the fjord and thereby thick sediment cover (see *Chapter 7.3 Sedimentation rates and distribution*, below). In addition, a study of the northern part of Nordfjord proximal to the present glacier front has not been carried out. A conceptual model of the main landforms is found in Fig. 7.3.
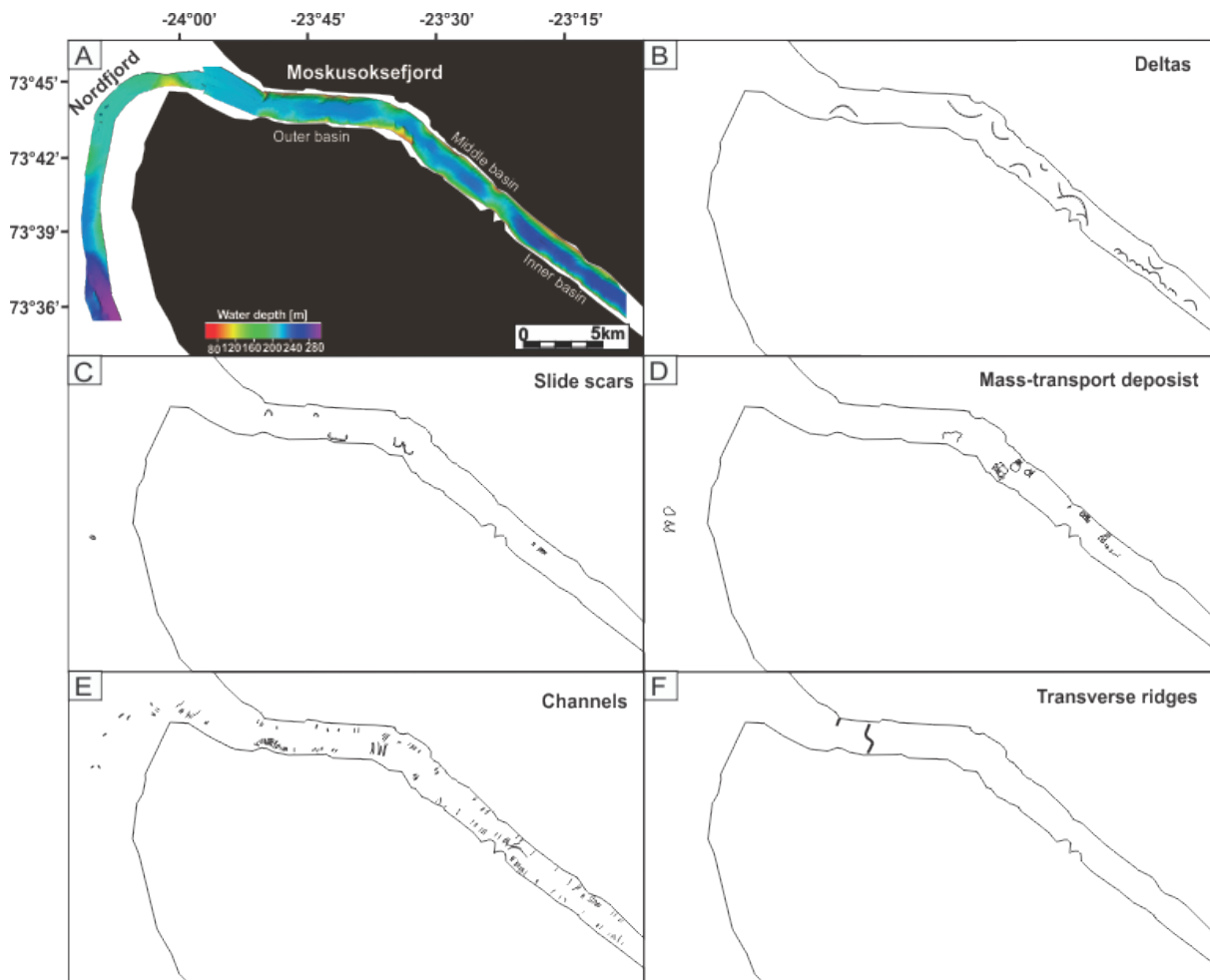

Figure 7.2: The different morphological features and their distribution in Moskusoksefjord and Nordfjord, North-East Greenland. *A*) An overview map of the swath bathymetry of the two fjords; *B*) Deltas; *C*) Slide scars; *D*) Sediment lobes; *E*) Channels; *F*) Transverse ridges.

7.1.1. Moskusoksefjord

The dominant submarine landforms identified on the swath bathymetry and chirp data in Moskusoksefjord are relatively large river deltas in addition to smaller fan deltas (Fig. 7.2). The acoustic data also reveals that both the N-NE and S-SW fjord sides includes slide scars, sediment lobes and deep channels, landforms interpreted to be a result of sediment gravity flows (Fig. 7.1 and 7.2). A single ridge is observed in the outer basin of Moskusoksefjord. The main morphological features of the fjord are further discussed below.
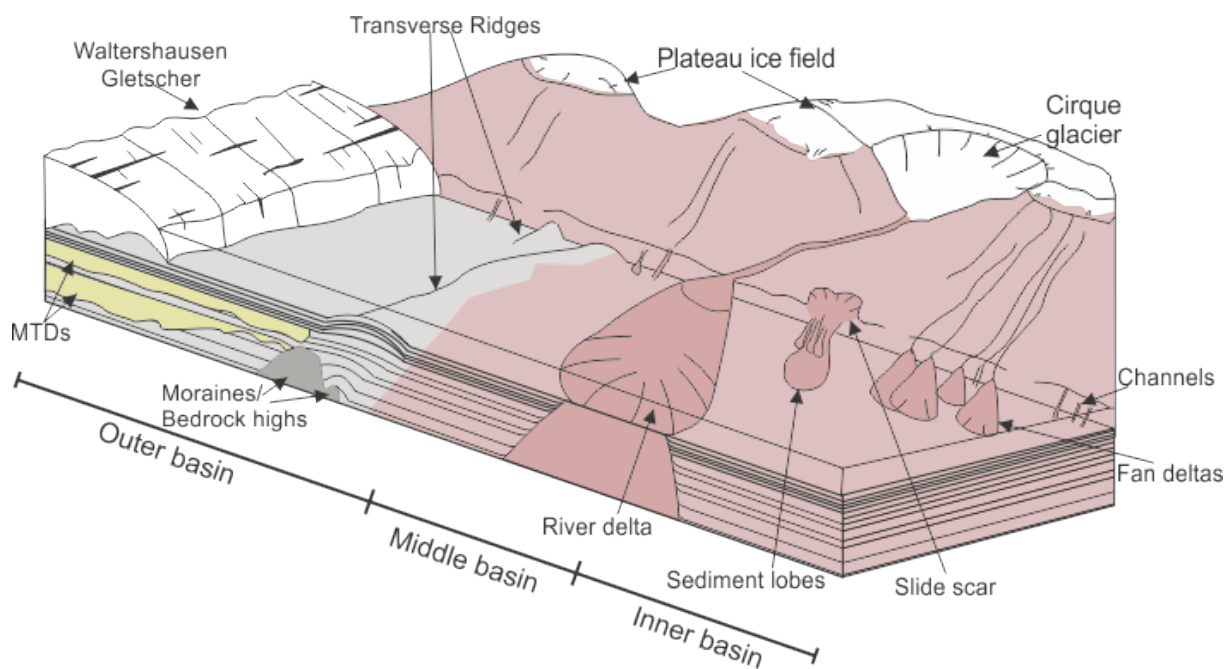
Figure 7.3: Conceptual model of the main landforms observed in Moskusoksefjord. Note that the landforms are not to scale and that the model is a generalization.

7.1.1.1.   Transverse ridges

Two transverse ridges (ridge 1 and 2) are identified in the outer basin of Moskusoksefjord (Fig. 7.1 and 7.2) approximately 13 km and 14 km from the present front of Waltershausen Gletscher. On the bathymetry data Ridge 1 is only observable on the northern fjord side (Fig. 4.6). However, seismic data reveals that both ridges extend across the fjord basin. Both ridge 1 and 2 occur below seismic *Unit O-1* and are buried by 18 m and 57 m of sediments, respectively. Whilst ridge 1 shows an asymmetric shape with a steeper ice-distal slope and a gentler proximal slope, ridge 2 shows a general symmetry. However, the steep distal slope of

ridge 1 appears to have been exposed to slope failure. Due to the lack of additional data it is difficult to determine whether the ridges represent terminal moraines or bedrock highs. One interpretation is that they were formed during the deglaciation of the fjord during the final phase of the last glacial or during a later glacial readvance. The ridges can be compared with similar landforms in other glacial fjords interpreted as recessional moraines (e.g. Plassen et al., 2004; Ottesen and Dowdeswell, 2006; Baeten et al., 2010).

7.1.1.2. Slide scars and sediment lobes

The bathymetric data reveals that both fjord sides have been exposed to slope failures, with slide scars and MTDs present on the slopes (Fig. 7.1, 7.2*C* and *D*). Although the majority of the slide scars on the bathymetry data are identified in and around the outer basin of Moskusoksefjord (with some smaller occurring in the inner basin), the identified MTDs are located in the middle- and inner basin (Fig. 7.2*C* & *D*). Given that the two transverse ridges identified in the outer basin of Moskusoksefjord are glacial moraines, they reveal the position of the glacier front during stillstand. Thus, we suggest relatively high sedimentation rates in the proximity to the glacier front to have resulted in unstable fjord slopes and subsequent slide scars. The MTDs, which are often found superimposed, appear as lensoid/lobate packages of sediment on the bathymetry data (Fig. 7.3), whereas the chirp data also reveals two relatively thick packages infilling the topography in the outer basin of Moskusoksefjord (MTD_{O-1} and MTD_{O-2}). The two features are located ~20 m and ~4 m below the modern seafloor. They are bounded by the local topographic relief and extend from the bathymetric high located in the outer part of the outer basin of Moskusoksefjord and continue outside of the available acoustic data (Fig. 5.3). Both features are interpreted to be formed by cohesive debris flows based on their sharp bed boundaries, acoustic transparent signature and lobate geometry (cf. Laberg & Vorren, 1995). The lack of internal reflectors is a common characteristic of mass-flow deposits due to the deformational homogenization of the sediments during submarine slope failure (Nardin et al., 1979). The source for the cohesive debris flows are difficult to reconstruct, however, we suggest that they may have been initiated as a result of an unstable grounding-line in front of Waltershausen Gletscher. A high sediment input may result in the buildup of steep, unstable slopes at the glacier margin (Benn and Evans, 2010). The cohesive debris flows are associated with a smooth seafloor topography indicating subsequently erosion or draping of younger sediments, suggesting that the features are old events (cf. Bøe et al., 2000).
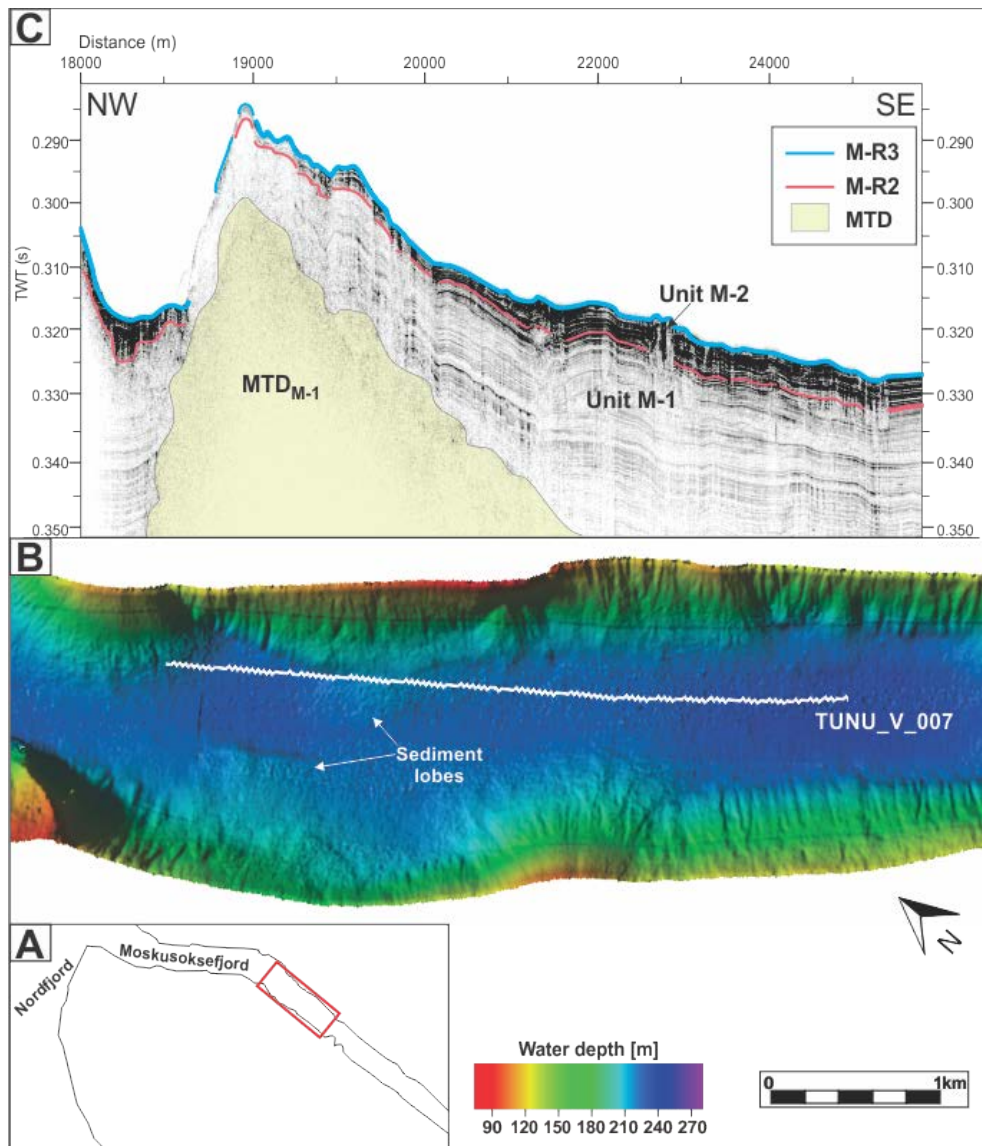
Figure 7.4: *A) Overview map of the location of the swath bathymetry data shown in B. B) Swath bathymetry data of the middle basin in Moskusoksefjord. Sediment lobes visible on the modern seafloor are indicated. Vertical exaggeration is x3. C) The figure shows a part of chirp line TUNU_V_007 in the middle basin of Moskusoksefjord. Reflection M-R2 to M-R3, Unit M-1 to Unit M-3 and MTD$_{M-1}$ are indicated.*

The MTDs located in the middle basin appears to be sourced by channels which are suggested to have acted as pathways for failed sediments initiated outside the available bathymetry data. Comparing the smaller, more recent slide scars with adjoining MTDs in the middle- and inner basin with the buried MTDs of the outer basin, it appears to be a change in the functioning of gravity-driven processes in Moskusoksefjord. The frequency of slope failures is related to the sediment accumulation rate of the area in addition to the force and frequency of potential triggering mechanisms (Syvitski & Shaw, 1995).

Mass movements in middle-outer Nordfjord (for location, see Fig. 1.2) are suggested to have been caused by sediments deposited along the margins, by rock-fall, deltas and alluvial fans and by melt-water processes (Evans et al., 2002). The irregular and steep topography of Moskusoksefjord and Nordfjord, in addition to the high sedimentation rates, makes the sediments of the area predisposed for failure (Evans et al., 2002).

7.1.1.3.   Deltas

Deltas are found to occur in all three basins of Moskusoksefjord (Fig. 7.1 and 7.2*B*). Out of the 18 observed deltas, 13 are located on the S-SW fjord slope, whilst five are observed on the N-NE fjord slope. As aforementioned, deltas are deposits produced on slopes where rivers or streams enter a standing body of water (Nemec, 1990; Howe et al., 2010). The coarsest material is deposited immediately from underflows, causing the deltas to prograde into the fjord basins while the deposition of the suspended load occurs over a larger area affected by the ocean circulation of the fjord basin (Nichols, 2009). Often fjord deltas are found at the fjord-head, however, in Moskusoksefjord the observed deltas occur as side-entry deltas.

The deltas are supplied with glacifluvial sediments from meltwater draining both the plateau ice fields and cirque glaciers located on both Gauss Halvø and Hudson Land (Fig. 2.1). The glaciers present in the fjord today are believed to be remnants after the GIS. Thus the formation of the river deltas is suggested to have been initiated following the deglaciation of the fjord (cf. Hansen, 2004).

Out of the 11 fan deltas identified in Moskusoksefjord, ten of them are located on the S-SW slope in the inner basin and a single on the N-NE slope in the middle basin (for location, see Fig. 4.1, 7.1 and 7.2). Here both the offshore and onshore slope gradients are steep (>30°) and coarse-grained alluvial fans enter the fjord. Isolated ice masses located on mountain plateaus drives subglacial erosion and thereby proglacial sedimentation, feeding alluvial fans (Lønne and Nemec, 2004). Satellite imagery reveals that the alluvial fans located along the fjord margins are presently active. The active channels are here recognized by the void of vegetation and paler, "fresher" bedrock surfaces.

7.1.1.4.   Channels

Numerous channels are identified in Moskusoksefjord, occurring on the fjord slopes in association with either deltas or slope failures (Fig. 7.1 and 7.2E). The channels are formed by

erosion from turbulent flows. Other studies have found that similar features have acted as pathways for both hyperpycnal flows originating from glacial meltwater streams and as a result of mass flows (e.g. turbidity flows or erosive debris flows) (Stoker et al., 2010). The high amount of channels present in the fjord suggests that there is a high amount of erosion and sedimentary activity keeping the channels active and preventing sedimentary infill. The presence of randomly distributed turbidites in all three sediment cores suggest that meltwater may have been supplied to the fjord basins through the whole time interval presented by the cores as will be further discussed below.

7.1.2. Nordfjord

Only a few submarine landforms are observed on the bathymetric data in Nordfjord. This is at least partly due to the limited amount of data available. Nordfjord is wider compared to Moskusoksefjord and only the central, deepest part of the fjord basin has been surveyed. Here, a single slide scar, a few sediment lobes and some accompanying channels are identified and interpreted, all located in sub-basin 1 (Fig. 4.5). However, the chirp data reveals four mass-transport deposits (MTD_{N-1} to MTD_{N-4}) of various dimensions (Fig. 5.4).

The single slide scar observable in Nordfjord has an escarpment with rounded edges and associated smooth seafloor topography. The accompanying slide deposit may have been eroded or draped by younger glacimarine sediments, indicating that the slide scar represents an older event.

The two smaller MTD`s located in sub-basin 1 have been interpreted to be cohesive debris flows originating from the eastern fjord slope. Satellite images reveal that several streams draining the local plateau ice field enters the east side of the fjord not far from the available acoustic data. The MTDs are probably deposited after a collapse of the fjord side as observed in Moskusoksefjord. Another two MTDs are identified in sub-basin 2, lying 18m and 5.5 m below the modern seafloor. They have, like to the two relatively large features located in sub-basin 1, also been interpreted as cohesive debris flows interpreted to have been initiated by a high sediment input from Waltershausen Gletscher resulting in slope instabilities.

7.1.3. Summary

Both fjords are characterized by landforms originating from a high sediment input. The high amount of sediments supplied by Waltershausen Gletscher may cause slope instabilities at the

114

glacier front, resulting in mass flows. The two lowermost cohesive debris flows and the two overlying cohesive debris flows located in the outer basin of Moskusoksefjord and in sub-basin 2 of Nordfjord are suggested to have originated from the same two events initiated in the proximity of Waltershausen Gletscher. Also, rivers and streams draining the plateau ice fields and cirque glaciers in the fjords catchment area contributes to delta progradation and slope failures in the more distal areas from the glacier front.

7.2.   Correlation of acoustic data and sediment cores

The interpreted swath bathymetry data, seismostratigraphy and lithostratigraphy will be correlated in the following chapter. In order to project the sediment cores onto the chirp lines an average sediment velocity of 1600 m/s was assumed, as estimated from previous studies in East Greenland fjords (Andrews et al., 2004) and Spitsbergen fjords (Plassen et al., 2004).

Core shortening is a common problem during marine gravity coring (Lee, 1985; Morton and White, 1997). During coring the core sediments may experience physical compaction and sediment bypassing. Also, water currents formed as the core barrel strikes the seafloor may erode the soft surface of the seafloor, preventing sampling of the upper few cm (Lee, 1985). There is often a combination of these processes causing the observed shortening. Physical compaction of the sediments involves expulsion of air and water from the pore spaces, in addition to rearrangement of the sediment grains to a closer packing (Morton and White, 1997). The result is a measured core shortening relative to the sediment interval being cored. This may cause a problem when correlating the sediment cores with seismic data, in addition to a less accurate estimation of the sedimentation rates on the core site.

7.2.1. The inner basin of Moskusoksefjord - core HH13-008-GC-TUNU

Core HH13-008-GC-TUNU was retrieved in the inner basin of Moskusoksefjord in the proximity to both river- and fan deltas (Fig. 7.1). The approximate position of the core is indicated on chirp line TUNU_V_009 in Fig. 7.5. The core is 226 cm long and penetrated seismic *Unit I-2*, a thick package of near-parallel, onlapping acoustic stratified sediments. The lower boundary of *Unit I-2* was not identified on the chirp line due to the lack of penetration. However, the unit sediment thickness at the core site exceeds 30 m. The seismic unit is interpreted to be acoustically stratified due to lithological variations. The core comprises massive and laminated/layered bioturbated mud with randomly distributed sandy layers and lenses and occasional dropstones (see *Chapter 6.3.1.1 Unit 8.1*). It is interpreted to consist of

glacimarine sediments deposited mainly as rain-out from sediment laden glacial meltwater plumes during and after the Little Ice Age (see *Chapter 7.3 Sediment rates and distribution*). The internal reflections in the seismic unit can to a small degree be correlated with the acoustic impedance of the sediment core, however, this is inferred to be difficult because of the high abundance of reflections.
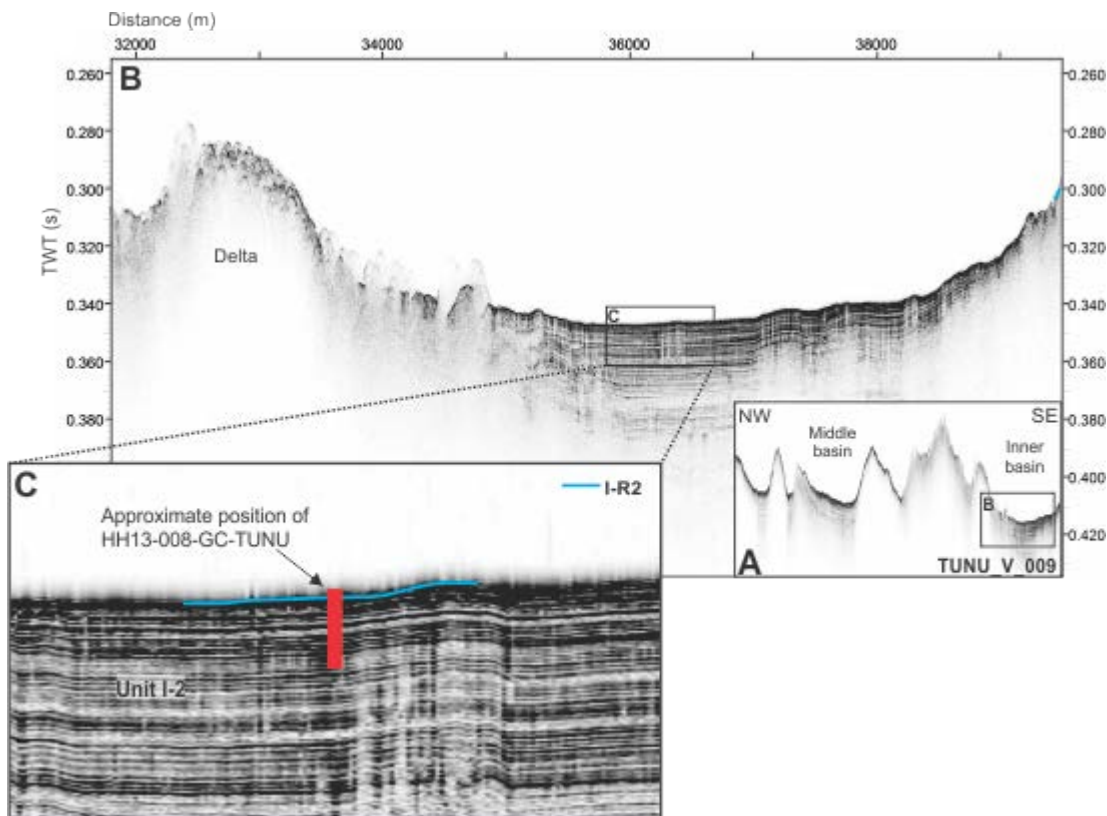

Figure 7.5: *A*) Chirp line TUNU_V_009 from the middle- and inner basins of Moskusoksefjord (see Fig. 7.1 for location). *B*) The approximate position of core HH13-008-GC-TUNU in the inner basin of Moskusoksefjord on seismic data. *C*) Close-up of the coring site. Seismic *Unit I-1* and reflection *I-R2* (the sea floor) are indicated.

7.2.2. The middle basin of Moskusoksefjord - core HH13-009-GC-TUNU

The chirp profile in Figure 7.6 shows the approximate position of core HH13-009-GC-TUNU. The core is 283 cm long and was retrieved from the middle basin of Moskusoksefjord superior the distal slope of a MTD. The MTD, referred to as seismic unit *MTD$_{M-1}$*, has been identified on the bathymetric data as well as on chirp line TUNU-V-009 (Fig. 7.4). The core penetrated into seismic *Unit M-2* and the upper part of *M-1* where the boundary reflection *M-R2* between seismic *Unit M-1* and *M-2* (pink line in Fig. 7.X) corresponds to the boundary

separating lithological *Unit 9-1* and *9-2*. The boundary reflection (*M-R2*) marks a transitional, but distinctive change in the acoustic signature with higher amplitude of the reflections above than below *M-R2*, interpreted to indicate a more frequent and/or pronounced change in lithology going from lithological *Unit M-1* to *M-2*. The lower lithological *Unit 9-1,* interpreted as three stacked, normal-graded sandy turbidites, correlates with the uppermost part of seismic *Unit M-1,* which on the chirp line TUNU_V_009 shows a few internal reflections with low to moderate amplitude. Above this lies seismic *Unit M-2* containing a high abundance of internal reflections with high amplitudes. It is correlated with lithological *Unit 9-2* comprising glacimarine sediments consisting of massive and laminated/layered bioturbated mud deposited from suspension fall-out in addition to three relatively thin turbidites and occasional IRD originating from either ice rafting by icebergs and/or sea ice (e.g. Forwick & Vorren, 1997; Reeh et al., 1999). The high amplitude and high abundance of reflections seen in seismic *Unit M-2* are suggested to correlate with color changes as well as with lithological changes in lithological *Unit 9-2*. Dated ostracods at 118-117 cm depth provides an age of 1190 cal. yr. BP, suggesting that the sediments in the core were deposited from late Neoglaciation and up to present. Assuming an average sedimentation rate of 85 cm/ka (see *Chapter 7.3. Sedimentation rates and distribution*) for lithological *Unit 9-2* (and seismic *Unit M-2*), the transition to lithological *Unit 9-1* (seismic *Unit M-1*) occurred approximately 1930 cal. yr. BP. The boundary between the lithological units is associated with a marked increase in the acoustic impedance in the lower part of the sediment core. A marked peak in acoustic impedance at 73 cm depth, however, is proved difficult to correlate with the chirp data, possibly due to the core site not being precise or sediment compaction introduced during sampling as discussed above.

7.2.3. The outer basin of Moskusoksefjord - core HH13-010-GC-TUNU

Figure 7.7 shows chirp line TUNU_V_007, located parallel to the fjord axis (for location, see Fig. 7.1), and the approximate position of core HH13-010-GC-TUNU. The core is 486 cm long and was retrieved outside of the ridge in the outer basin of Moskusoksefjord (Fig. 7.2*F*). Core HH13-010-GC-TUNU penetrates seismic *Unit O-2* which has, similar to *Unit M-2* and *Unit I-2*, been interpreted to comprise mainly massive or laminated/layered bioturbated mud interbedded with turbidites and occasional IRD. The most important sediment source is the nearby glacier Waltershausen Gletscher, thus most of the sediments are inferred to be of glacimarine origin (cf. Powell & Domack, 1995). Directly beneath *Unit O-2* in sub-basin 1 lay

a relatively thick acoustic transparent package (*MTD* $_{O-2}$) which has, as mentioned previously, been interpreted to be a cohesive debris flow (Fig. 7.7). Since the total length of the core is 4.86 m (+ the 0.2-0.3 m lost during retrieval), the sedimentary package was not captured within the core. It appears as *MTD* $_{O-2}$ eroded the upper part of *Unit O-1* and the lower part of *Unit O-2*. The high abundance of internal reflections in the penetrated seismic unit can be correlated with fluctuations in the measured physical properties and changes in the lithology within the cored sediments.

Figure 7.6: *A*) **Chirp line TUNU_V_009 from the middle- and inner basins of Moskusoksefjord (see Fig. 7.1 for location).** *B*) **The approximate position of core HH13-009-GC-TUNU in the middle basin of Moskusoksefjord on seismic data. Mass transport deposit MTD$_{M-1}$ is indicated.** *C*) **Close-up of the coring site. Seismic *Unit M-1* and *M-2* and reflections *M-R2* to *M-R3* (the sea floor) are indicated.**
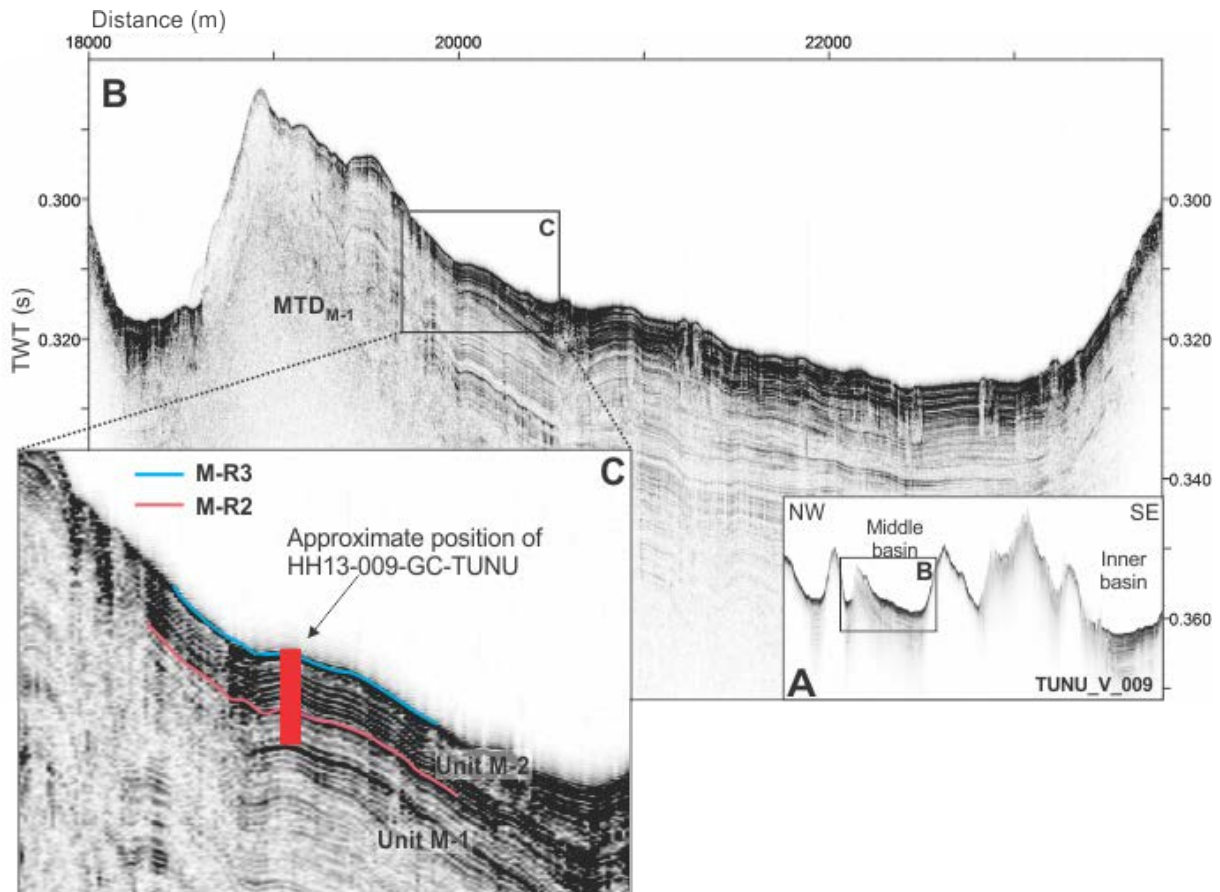
Figure 7.7: A) Chirp line TUNU_V_007 from the outer basin of Moskusoksefjord (see Fig. 7.1 for location). B) The approximate position of core HH13-010-GC-TUNU on seismic data. Seismic *Unit O-2*, mass transport deposit *MTD$_{O-2}$* and reflections *O-R2* to *O-R3* (the sea floor) are indicated.

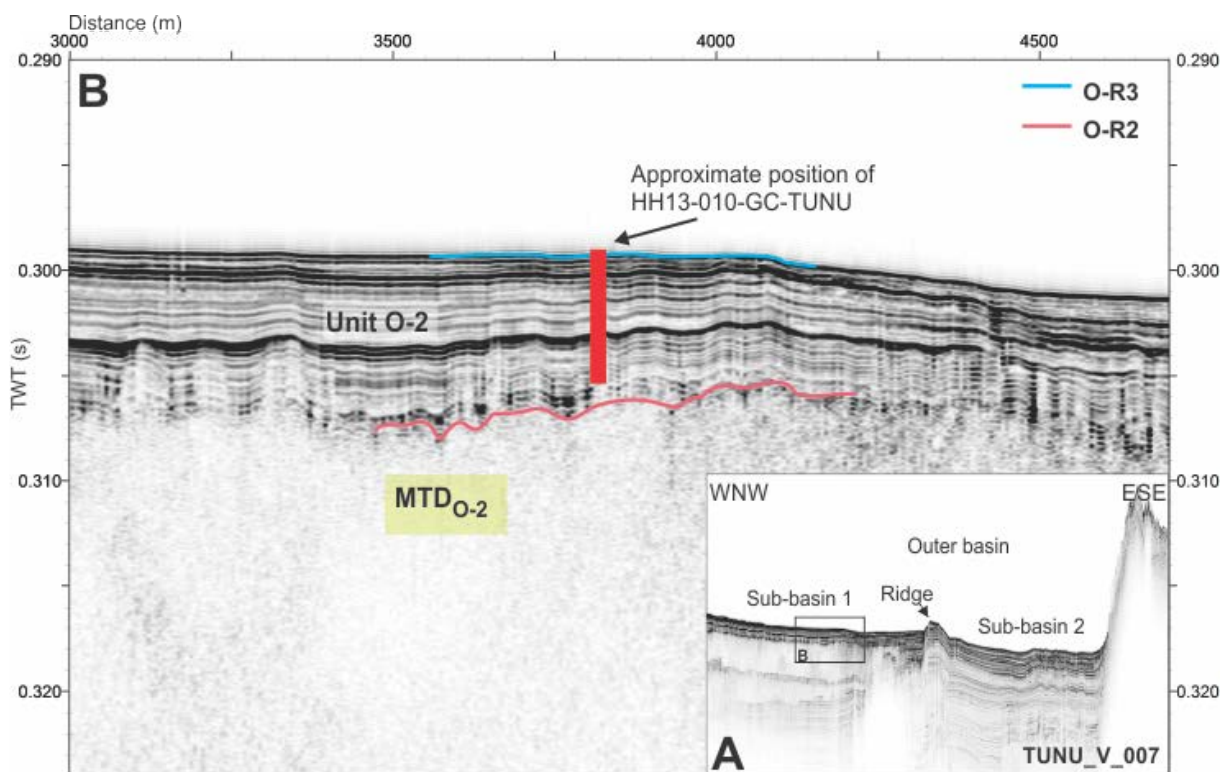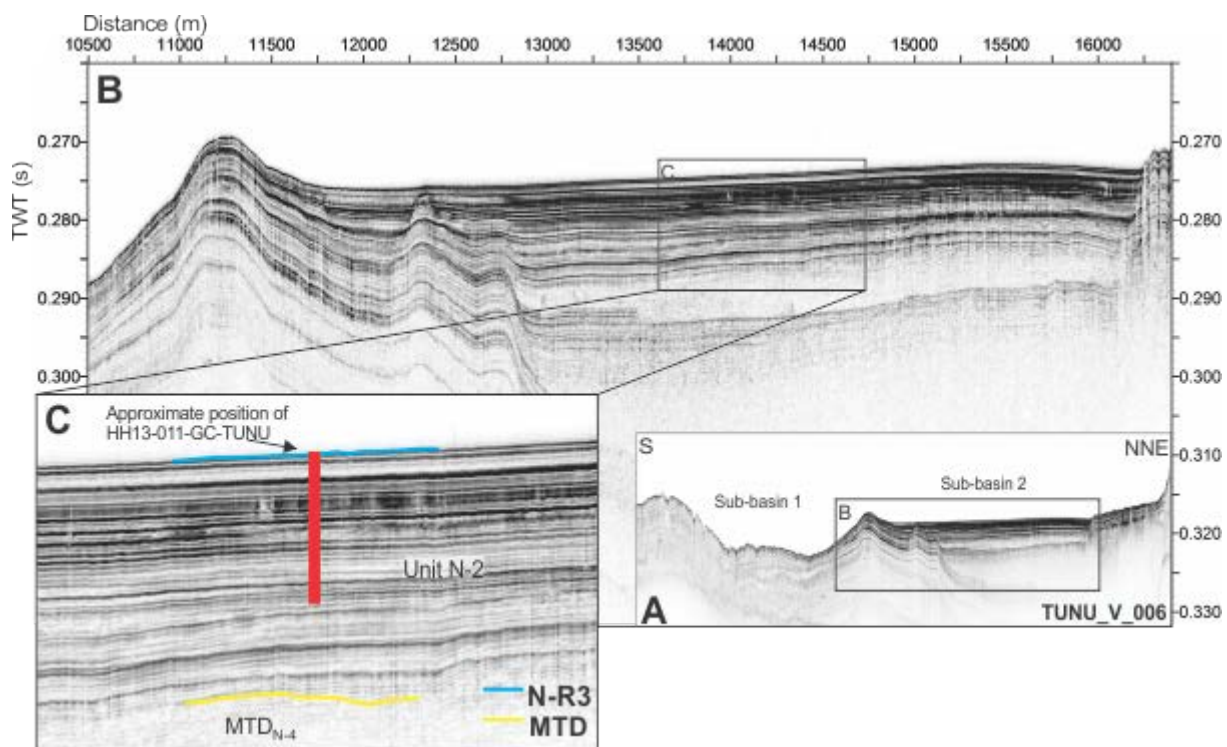**Figure 7.8: *A*) Chirp line TUNU_V_006 from Nordfjord (see Fig. 7.1 for location). *B*) The approximate position of core HH13-011-GC-TUNU in sub-basin 2 in Nordfjord on seismic data. *C*) Close-up of the coring site. Seismic *Unit N-2*, mass transport deposit MTD$_{N-4}$ and reflection *N-R3* (the sea floor) are indicated.**

7.2.4. Sub-basin 2 of Nordfjord - core HH13-011-GC-TUNU

Chirp line TUNU_V_006 shows the two sub-basins in the middle- and inner part of Nordfjord (for location, see Fig. 7.1). Core HH13-011-GC-TUNU was retrieved approximately 400 m west of the chirp line, and is therefore projected onto the nearest chirp line TUNU_V_006. Figure 7.8 indicates the approximate position of the core located in sub-basin 2. The core penetrated into seismic *Unit N-2*, a >40 m thick sedimentary succession containing strong, continuous to semi-continuous onlapping reflections which decreases in both amplitude and reflection abundance with depth. The succession becomes thinner and wedges out towards the elevation between the two sub-basins. However, two acoustic transparent packages (MTD_{N-3} and MTD_{N-4}) dominate the studied part of the sub-seafloor succession, interbedded with the sedimentary successions of *Unit N-2*. MTD_{N-3} and MTD_{N-4} are interpreted as cohesive debris flows, located at approximately 18-20 m and 8 m below the seafloor, respectively. Thus, with the core being 597 cm (in addition to 10 cm lost during core retrieval), the core did not capture any of the sediments from the MTDs. *Unit N-2* is interpreted to reflect frequent changes in lithology, with IRD, coarse-grained turbidites and mud deposited as suspension fall-out from meltwater plumes mainly originating from Waltershausen Gletscher. The dated interval at 592 cm depth provided an age of 1130 cal. yr. BP, providing a relatively high estimated sedimentation rate of 446 cm/ka (see *Chapter 7.3 Sedimentation rates and distribution*, below). The high sedimentation rate reflects the thickness of the sedimentary succession and is suggested to be a result of the proximity to the present day glacier front of Waltershausen Gletscher (~10 km). The glacier supplies the fjords with sediments throughout the year. Even though the core was retrieved further west of the chirp line, the internal reflections of the seismic unit can most likely be correlated with both the increases in sand fraction corresponding to the peaks in the measured acoustic impedance of the cored sediment.

7.2.5. Sub-basin 1 of Nordfjord - core HH13-012-GC-TUNU

Similar to the previously described core (see *Chapter 7.2.4 Core HH13-011-GC-TUNU – Nordfjord*), core HH13-012-GC-TUNU was retrieved approximately 400 m west of chirp line TUNU_V_006 and is therefore also projected onto the nearest chirp line (Fig. 7. 9). The core site for HH13-012-GC-TUNU is in sub-basin 1, located 4 km further south of core HH13-011-GC-TUNU and approximately 14 km from the glacier front of Waltershausen Gletscher. The lithology of the core includes bioturbated mud with small lenses of poorly sorted sand and a few clasts. The core penetrated seismic *Unit N-2*, which at the core site has a thickness

of ~4.8 m. The southward thinning of the sedimentary succession suggests that the main sediment sources in the area were Waltershausen Gletscher and the river coming from Broget Dal (see Fig. 2.6). South of the elevation separating the two sub-basins the unit appears to be disturbed/eroded by channels and mass-wasting, as observed on the bathymetry data (Fig. 5.1 and 7.9). Concordant below seismic *Unit N-2* lays *Unit N-1*. Here two additional debris flows are observed in the central, lower part of sub-basin 1 within *Unit N-1$_A$* (Fig. 5.4 and 5.5). Correlation between the internal reflections of the penetrated unit and the measured physical properties and lithological variations are proven to be difficult. We suggest the reason to be that the core was projected onto the chirp line and that there may be local variations in the sediment stratigraphy. Core HH13-012-GC-TUNU may be correlated with core *PS2633* described by Evans et al. (2002). The distance between the two cores is ~27 km.
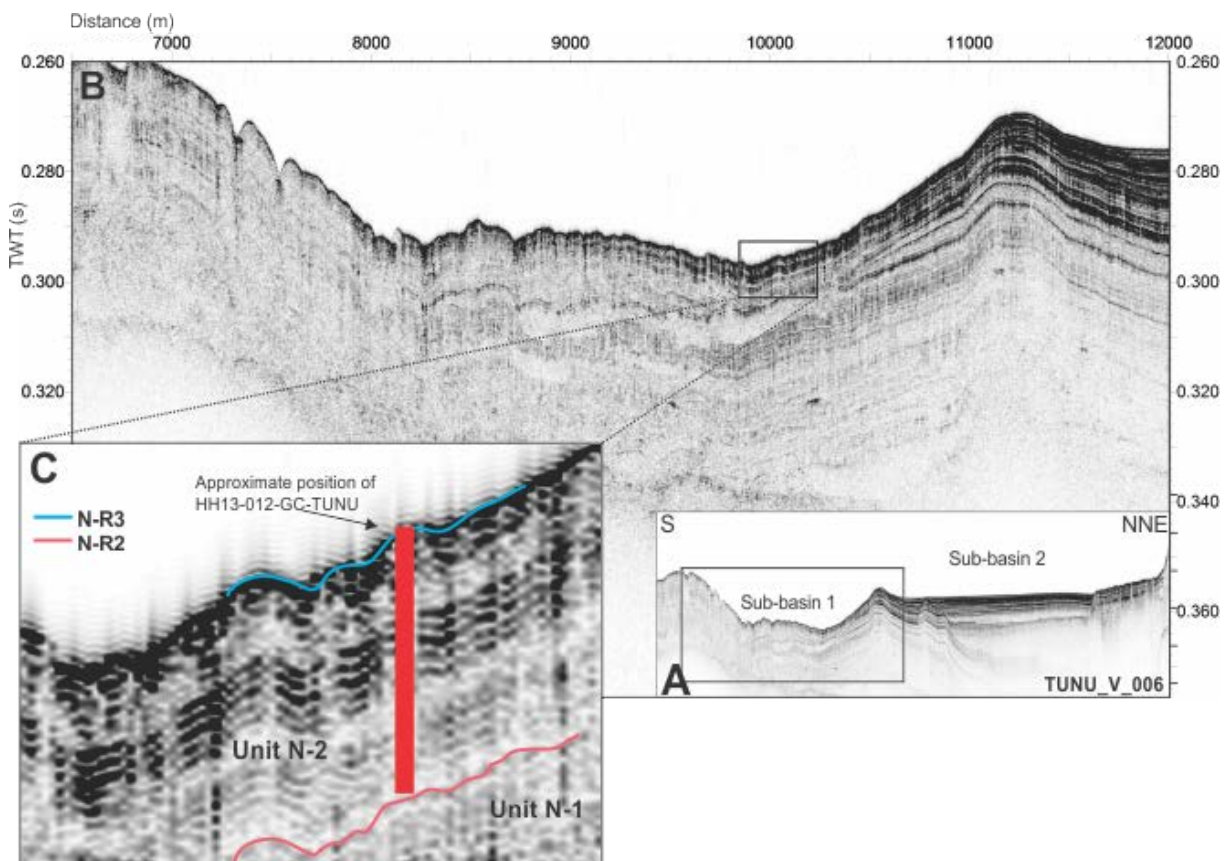

Figure 7.9: *A*) Chirp line TUNU_V_006 from Nordfjord (see Fig. 7.1 for location). *B*) The approximate position of core HH13-012-GC-TUNU in sub-basin 1 in Nordfjord on seismic data. *C*) Close-up of the coring site. Seismic *Unit N-1* to *N-2* and reflections *N-R2* to *N-R3* are indicated.

7.3.   Sedimentation rates and distribution

The sedimentation rate and river discharge in Greenland fjords in general are regarded as medium to high (Syvitski et al., 1987). Evans et al. (2002) recorded a Holocene sediment flux up to 111 cm/ka in the middle and outer part of Nordfjord and attributed this to the narrow fjord physiography with the proximity to meltwater sources. Below, both the obtained ^{14}C ages and the measured ^{210}Pb and ^{137}Cs will be used to estimate the sedimentation rates in the studied parts of Moskusoksefjord and inner Nordfjord. Then the results will be compared to previous work from the outer part of Nordfjord, other Greenland fjords and Spitsbergen- and north Norwegian fjords.

For the estimation of linear sedimentation rates, a constant accumulation of sediments between the dated intervals was assumed. However, by applying an age model using calibrated years BP, one assumes the top of the core to be deposited in AD 1950 (0 cal. yr. BP). To get a more correct estimation of the sedimentation rates, the discussed age intervals will be given in cal. yr. AD, with the top of the cores assumed to be AD 2013 (year of acquisition). For cores HH13-010-GC-TUNU and HH13-011-GC-TUNU, 25 and 10 cm of sediments, respectively, were added to the top of the core to compensate for the sediments lost during retrieval. In addition, the sedimentation rates were exclusively calculated for deposits that were assumed to be from suspension fallout, i.e. thickness of the coarser layers comprising reworked sediments were excluded. Eventual erosion, core shortening and uncertainties in the dating methods have not been taken into account, so these rates should therefore be regarded as minimum rates. The estimated linear sedimentation rates (in cm/ ka) are summarized in Table 7-1.

Table 7-1: Sedimentation rates (cm/ka), based on cal. yr. AD. * Average sedimentation rates are calculated for the whole core length.

Core	Depth interval (cm)	Age interval (cal. yr. BP 1 σ mean)	Age yr (^{210}Pb and ^{137}Cs: 2 σ mean)	Age interval (cal. yr. AD)	Age yr	Sedimentation rate (cm/ka)
HH13-008-GC-TUNU	10-0	-	~200-0	1814-2014	~200	<50
	202-0	610-0	-	1340-2013	673	287*
HH13-009-GC-TUNU	117-0	1190-0	-	760-2013	1253	85*
HH13-011-GC-TUNU	592-0	1130-0	-	820-2013	1193	446*
HH13-012-GC-TUNU	50-0	-	~50-0	1964-2014	~50	<1000
	195-0	690-0	-	1260-2013	753	256
	454-195	7770-690	-	(-)5820-1260	7080	36
	454-0	7770-0	-	(-)5820-2013	7833	58*

7.3.1. Moskusoksefjord

7.3.1.1. Inner basin of Moskusoksefjord

Core HH13-008-GC-TUNU was collected in the inner basin of Moskusoksefjord approximately 40 km from the present day glacier terminus of Waltershausen Gletscher and approximately 32 km away from a large braided river located at the fjord head. The sediments in the top of the core are expected to be intact, representing the present seafloor. A single age from radiocarbon dating was obtained from the core at 202 cm depth, giving an age of 610 cal. yr. BP. The linear sedimentation rate, based on cal. yr. AD, is 287 cm/ka (Table 7.1). The estimated sediment rate for the core is based on one date and is therefore the average of the whole core length. It is, however, expected to have been changes in the sedimentation rate through time, as seen in other comparable fjord studies (Hald et al., 2004). The sedimentation rate in the core is comparatively high given the distance to the glacier front, but is of the same order of magnitude as reported for other East Greenland fjords south of the study area. Average sedimentation rates in three East Greenland fjords have been estimated by Andrews et al. (1994), with Kangerdlussuaq Fjord, Mikis Fjord and Nansen Fjord having average sedimentation rates of 110-340 cm/ka during the last 1 ka based on cores collected from the fjord heads to the fjord mouths. In Scoresby Sund, however, an average sedimentation rate of 20-30 cm/ka has been estimated for the deeper parts of the fjord (Marienfeld, 1991).

The measured ^{210}Pb and ^{137}Cs provided a sediment accumulation rate of less than 50 cm/ka in the upper 10 cm of the sediment core. This is a fraction markedly lower than the average sedimentation rate provided by the radiocarbon dating, revealing that the sedimentation rate has varied through time. If correct, the inner basin has experienced a relatively low sedimentation accumulation rate during the last ~200 years.

Based on the established chronology the studied sediments can be related to the paleoclimate of East Greenland as reconstructed by previous studies (see *Chapter 1.2.2. Holocene paleoclimate of East Greenland)*. Assuming that the estimated sedimentation rate based on the provided radiocarbon age is correct (287 cm/ka), the sediments from the bottom of the core and up to ~29 cm have been deposited during the LIA (Levy et al., 2014). The mud and sandy mud from ~29 cm and to the top of the core represents the period after the LIA and up to present. However, applying the measured ^{210}Pb and ^{137}Cs, only the upper 5 cm of the core would represent the period after the LIA.

7.3.1.2. Middle basin of Moskusoksefjord

The core site for HH13-009-GC-TUNU is located approximately 13 km from core HH13-008-GC-TUNU and 27 km from the present day terminus of Waltershausen Gletscher. The age obtained from radiocarbon dating was found at 117 cm depth, giving an age of 1190 cal. yr. BP. The estimated linear sedimentation rate is 85 cm/ka (Table 7-1), making it more than 3 timed lower than in core HH13-008-GC-TUNU located further away from the glacier front. A reason for the difference in sedimentation rate may be the braided river located at the fjord head acting as an important sediment source for the inner part of Moskusoksefjord.

7.3.1.3. Outer basin of Moskusoksefjord

No ages were obtained from core HH13-010-GC-TUNU. However, we suggest that the smooth seafloor and the thickness of the sedimentary successions observed on the chirp data reflect a high sedimentation rate in the area, also confirmed by the closest dated core (011, see below). The core site is located 11.5 km from the ice front of Waltershausen Gletscher, which is interpreted to act as the main sediments source for the outer Moskusoksefjord basin. It appears that the inflow of suspended material coming from the river delta is transported in-fjord away from the core site. The water flow is interpreted to be controlled by the circulation pattern in the fjord, with the water flowing inwards on the southern side of Moskusoksefjord.

This is supported by the observation of gray mud inferred to have derived from Waltershausen Gletscher being deposited in the two innermost basins.

7.3.2. Nordfjord

7.3.2.1. Sub-basin 2 of Nordfjord

At core site HH13-011-GC-TUNU in Nordfjord one of the highest sedimentation rates of this study was estimated. The sample from 592 cm depth provided an age of 1130 cal. yr. BP implying an average linear sedimentation rate of 446 cm/ka (Table 7-1). The smooth nature of the seafloor in sub-basin 2 of Nordfjord reflects to a great extent the relatively thick succession of sediments as seen in other Greenland fjords (Andrews et al., 1994). The maximum thickness of the seismic unit in which the core penetrates (*Unit N-2*) exceeds 40 m (see *Chapter 5.2.4 Nordfjord*). However, the two thick cohesive debris flows occurring within this succession contribute to the total thickness. The proximity to the present day glacier front of Waltershausen Gletscher (~10 km) is inferred to be the reason for the high sedimentation rate at the core site as high sedimentation rates characterizes this type of setting (Calabrese & Syvitski, 1987; Cowan and Powell, 1991; Andrews et al., 1994).

7.3.2.2. Sub-basin 1 of Nordfjord

Core HH13-012-GC-TUNU was collected in sub-basin 1 in Nordfjord (for location, see Fig. 5.4 and 7.1), approximately 14 km from the present day glacier front of Waltershausen Gletscher. The samples for radiocarbon dating taken at 454 cm and 195 cm depth provided ages of 7770 cal. yr. BP and 690 cal. yr. BP, respectively. Further, ^{210}Pb and ^{137}Cs measuring suggested that the upper 50 cm were deposited during a ~50 year period. The lowest sedimentation rate from this study was estimated for the interval between 454-195 cm with a linear sedimentation rate of 36 cm/ka (Table 7-1). The sedimentation rate increases to 256 cm/ka in the interval from 195 cm depth and up to the modern seafloor. The average linear sedimentation rate for the whole core is calculated to be 56 cm/ka.

7.3.3. Sedimentation rates – compared to Spitsbergen- and north Norwegian fjords

A Holocene sedimentation rate of up to 111 cm/ka was estimated by Evans et al. (2002) for the outer part of Kejser Franz Joseph Fjord. The average linear sedimentation rates in this study can be compared to other rates found in East Greenland fjords, with Kangerdlugssuaq

Fjord, Mikis Fjord and Nansen Fjord having average sedimentation rates of 110-340 cm/ka during the last 1 ka (Andrews et al., 1994), while Syvitski et al. (1996) reported a rate of 700 cm/ka for the last ~1400 yr. BP in the outer part of Kangerdlugssuaq fjord. In Scoresby Sund, however, an average sedimentation rate of 20-30 cm/ka has been estimated for recent deposited sediments in the deeper parts of the fjord (Marienfeld, 1991). Sedimentation rates in other East Greenland fjords are estimated to range from ~10 to 600 cm/ka in ice-distal settings and approximately 2400 cm/ka in ice-proximal settings (Marienfield, 1991; Dowdeswell et al., 1994; Syvitski et al., 1996). As a conclusion, the estimated sedimentation rates obtained in this study is of the same magnitude or smaller than previously reported for East Greenland fjords.

In Spitsbergen fjords, however, the sedimentation rates are a magnitude higher. A sedimentation rate in the range of 5000-10 000 cm/ka was estimated at a distance of approximately 10 km from the modern calving front of Kongsvegen glacier in Kongsfjorden (Elverhøi et al., 1983), while an average sedimentation rate of 1700 cm/ka was estimated in Tempelfjorden for the last ca. 130 years (Plassen et al., 2004). In van Mijenfjorden (also Spitsbergen) the pattern of sedimentation rates shows the highest sedimentation rates during the early Holocene, lowest during the middle Holocene and an increase during the late Holocene (Hald et al., 2004). The estimated sedimentation rates obtained from this study are significantly smaller compared to the rates in Spitsbergen fjords.

The north Norwegian fjords Andfjord and Vågsfjord had estimated sedimentation rates of 173 cm/ka and 456 cm/ka, respectively, during the deglaciation of the Fennoscandian Ice Sheet (approximately 17.5-11.2 cal. kyr. BP). Ullsfjorden, however, had sedimentation rates of 21800 cm/ka in an ice-proximal environment and 1100-1900 cm/ka in a more ice-distal environment during the deglaciation (Plassen and Vorren, 2003). The rates from Andfjrod and Vågsfjord are of the same magnitude as the rates obtained in Moskusoksefjord and Nordfjord, whereas the rates obtained from Ullsfjorden are a magnitude or two higher.

In summary, it is evident that the sedimentation rates in glacimarine environments vary greatly. The estimated average sedimentation rates in this study are 58 cm/ka for the last ~8 ka and 85-446 cm/ka for the last 1 ka. The rates can be compared with both the rates from the deglaciation of both Andfjord and Vågsfjord in northern Norway as well as the estimated rates in other East Greenland fjords for the same time period. However, they are a magnitude

smaller than the rates in Spitsbergen fjords and in Ullsfjorden. Based on this, we suggest the sedimentation rates in East Greenland fjords through the Holocene to be of medium rate rather than medium to -high as suggested by Syvitski et al. (1987).

7.4. Sedimentary processes and provenance

The distribution of sediments in a fjord environment is affected by the hydrographic regime (tidal activity, waves, Coriolis effect), the bathymetry (depth and morphology) and the distance to sediment sources (Syvitski, 1987; Howe et al., 2010). The sediments entering a fjord can be distributed by four primary sets of transport mechanisms; ice-contact processes, fluvial processes, rafting by icebergs and sea ice or by deep-water currents. After the initial deposition, redistribution may occur through mass-transport (e.g. slide and sediment gravity flows) and wave/tidal activity (Syvitski, 1989). A summary of all the main processes and deposits in glaciated fjords inferred to have influenced on the deposition within the study area is presented in Figure 7.10.

Greenland fjords are well-known for having large outlet glaciers from the GIS (Hambrey, 1994), with the dominant sediment source being glacial flour generated from tidewater glaciers (Heling, 1974). After studying the sediments cores and acoustic data from both Moskusoksefjord and Nordfjord we suggest that the dominant sedimentary processes in this area were suspension fall-out of glacial flour from turbid overflows, deposition from turbidity currents generated from melt-water underflows, mass-wasting and IRD. These processes will be further discussed below.
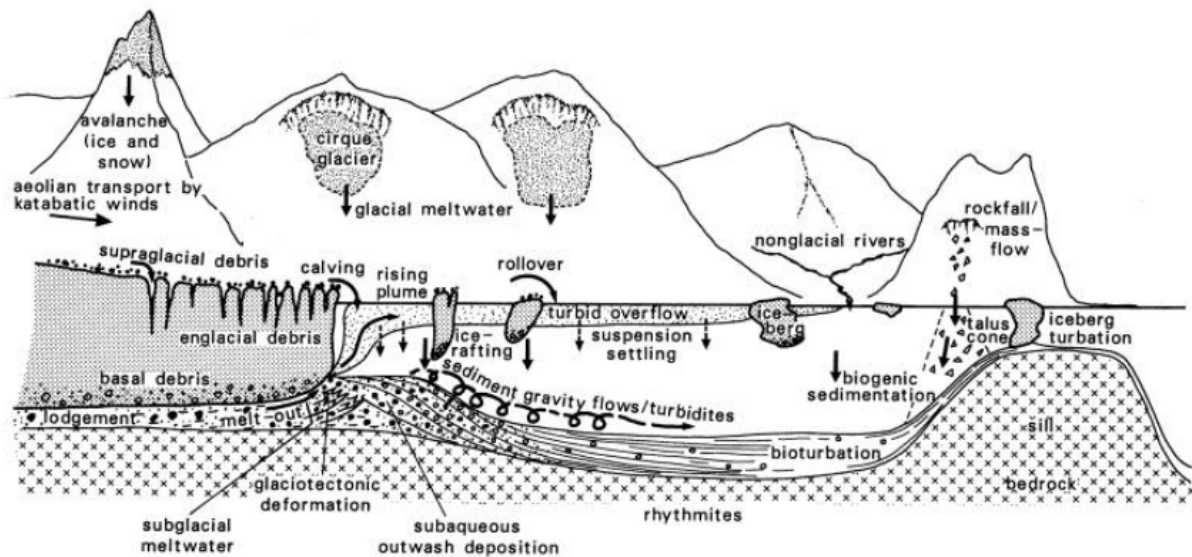
Figure 7.10: Main processes and deposits in glaciated fjords (by Hambrey, 1994).

7.4.1. Suspension fall-out

All five sediment cores are dominated by massive or laminated/layered mud and high sedimentation rates, suggesting that the main sedimentary process is suspension fall-out of fine-grained sediments from sediment-laden meltwater plumes, where glacial meltwater acts as the main sediment sources to both Moskusoksefjord and Nordfjord´s sedimentary environment. Suspension fall-out from meltwater plumes has previously been documented as a significant sedimentary process in East Greenland fjords based on the observed high amount of fine-grained lithofacies (Andrews et al., 1994; Evans et al., 2002).

The suspended sediments enter the fjords through either sub- or englacial meltwater outlets at the front of Waltershausen Gletscher (Fig. 7.10), as well as from tributary valley glacial meltwater rivers. Meltwater from the glacier can carry as much as 30 g litre^{-1} and still remain buoyant enough to form hypopycnal flows (overflows) due to the higher density of seawater (Powell and Domack, 1995). However, up to 50 g litre^{-1} sediment in suspension has been observed in Kongsfjorden, Spitsbergen (Elverhøi et al., 1980). Sediment deposition is controlled by the upper column water circulation in the fjord, with the surface plume velocity and particle removal processes determining the distance a particle is carried before it is deposited (Syvitski, 1989). The coarsest material is deposited in the immediate vicinity to the glacier front, whereas the finer material is held in suspension and transported further out-fjord (Syvitski et al., 1987). As mentioned previously, as much as 70% of the sediment load from glaciers are deposited glacifluvially or from suspension within the first 500 m from the glacier

128

termini. Thus, sedimentation rates show a general decreasing trend away from the sediment source (Calabrese & Syvitski, 1987; Cowan and Powell, 1991; Andrews et al., 1994). None of the cores retrieved in this study were collected within 500 m from the present glacier front, however, its position may have varied through time (e.g. during the Little Ice Age). Thus, it should not be excluded that the core sites closest to the glacier front may have periodically been localized in the ice-proximal environment.

The (glaci-) fluvial discharges are important contributors to deposition from suspension, especially in the inner part of Moskusoksefjord. However, due to the rivers being frozen during the winter season, most river runoff occurs during the summer months (July to September). As the meltwater discharge to the fjord basin can vary on diurnal, seasonal and annual basis, the amount of sediment or the sediment grain-size introduced to the fjord system fluctuates (Menzies, 1995). The estimated sedimentation rates from the study also reveals that another important point source is the river coming from Badlandal located at the fjord head of Moskusoksefjord (Fig. 2.6 and 7.11). Core HH13-008-GC-TUNU located closest to the sediment source has a higher sedimentation rate relative to core HH13-009-GC-TUNU situated further out the fjord but closer to Waltershausen Gletscher.

Considering there are no chirp lines located in the central, deepest parts of the fjord basins and no cross-lines in the two fjords, it is difficult to determine thickness variations of the sediment succession. However, differences in the sediment thickness on the available chirp lines suggest that deposition of sediment vary not only with distance to large sediment sources like Waltershausen Gletscher and the river coming from the fjord head of Moskusoksefjord (Fig. 7.11), but it is also controlled by the topography. The sediment succession is thinner over bathymetric highs and typically thicker in basins (e.g. Fig. 5.4). This is inferred to be related to the circulation pattern and ocean currents in the fjords (Syvitski et al., 1987).
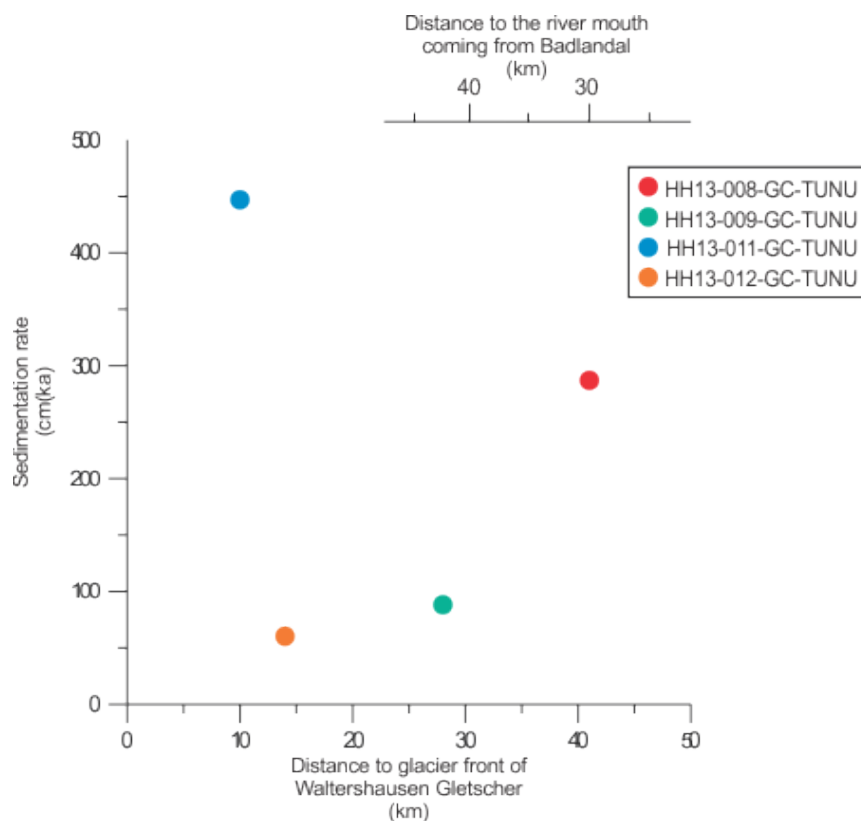
Figure 7.11: Sedimentation rates of this study relative to the distance to the glacier front of Waltershausen Gletscher and the river coming from Badlandal (for location, see Fig. 2.6).

7.4.2. Mass-transport deposits

Mass wasting has been identified in various forms in both the studied fjords as well as in other East Greenland fjords (e.g. Smith and Andrews, 2000; Ó Cofaigh, 2001). There are several factors controlling slope failure in fjords, with most slope failures occurring in conjunction with a high sediment input and sediment loading adjacent to glacier fronts and delta areas (Syvitski et al., 1987; Forwick & Vorren, 2002; Nichols, 2009). Slope failures are common at the front of tidewater glaciers, and are often caused by high sedimentation rates, iceberg calving impacts and glacier-push of the grounding-line depositional system (Powell, 2003). Whereas smaller events (1-2 km run-out distance) may occur at intervals of days, hours, or even continuously, larger events carrying large volumes of sediments tens of kilometers occur more sporadically (Powell, 1991).

Although the majority of the slide scars on the bathymetry data are identified in and around the outer basin of Moskusoksefjord (with some smaller occurring in the inner basin), the identified MTDs are located in the middle- and inner basin (Fig. 7.2*C* & *D*). The observed

MTDs from the available acoustic data are indicated in Figure 4.1*B*, 5.2, 5.3 and 5.4, and are discussed in *Chapter 7.1.1.2. Slide scars and sediment lobes*.

The MTD located in the middle basin (MTD_{M-1}) consisting of successive deposits of debris flows contains no internal reflections and is therefore inferred to have been deposited either during a single event or within a relatively short period of time. Since core HH13-009-GC-TUNU does not penetrate into MTD_{M-1} it is difficult to determine when it was deposited. However, due to the feature occurring within seismic *Unit M-1* and the estimated sedimentation rate in core HH13-009-GC-TUNU determining the approximate age of the upper boundary reflection, it is suggested to have been deposited prior to 1920 cal. yr. BP.

The MTDs located in the outer basin of Moskusoksefjord (MTD_{O-1} and MTD_{O-2}) and in sub-basin 2 of Nordfjord (MTD_{N-3} and MTD_{N-4}) are suggested to represent episodically events related to slope failures near the glacier front of Waltershausen Gletscher. The two MTDs in sub-basin 2 are both deposited within seismic *Unit N-2*. A dated interval at the lowermost part of core HH3-011-GC-TUNU penetrating seismic *Unit N-2* in sub-basin 2 (593-592 cm) provided an age of 1130 cal. yr. BP. Another date obtained from the bottom of core HH13-012-GC-TUNU (455-454 cm) in sub-basin 1 provided a higher age of 7770 cal. yr. BP. With the bottom of core HH13-012-GC-TUNU being located ~20 cm above the reflection boundary *N-R2* and by assuming a linear average sedimentation rate, the unit boundary at the core site is inferred to be deposited ~8200 cal. yr. BP. Given that the unit boundary is of the same age in both sub-basins, MTD_{N-3} and MTD_{N-4} are inferred to be deposited within the period 8200-1130 cal. yr BP. However, we suggest them to be deposited within the highest age range due to them lying relatively deep within the unit. As mentioned previously, the two lowermost MTDs (MTD_{O-1} and MTD_{N-3}) and the two overlying MTDs (MTD_{O-2} and MTD_{N-4}) in each basin are thought to have originated from the same two events.

The last two MTDs in Nordfjord (MTD_{N-1} and MTD_{N-2}) are located in the lower, central part of sub-basin 1 within seismic *Unit N-1*. They are inferred to have originated through episodically slope failures along the eastern fjord side in Nordfjord. Based on the age estimated for the unit's upper boundary reflection, the MTDs are most likely deposited prior ~8200 cal. yr. BP.

In all five sediment cores turbidites have been identified based on two or more of the following parameters; an erosional lower- and gradational upper boundary, particles fining upwards from coarse sand to mud and/or the lack of bioturbation (for further information, see *Chapter 6.5.1.4. Interpretation*). Whereas the two cores in the inner part of Moskusoksefjord and the core in sub-basin 1 in Nordfjord only have turbidites in certain levels of the cores, the two cores located closest to the glacier front have turbidites identified throughout their cores.

The first identified turbidite in core HH13-008-GC-TUNU is located at 95 cm depth, which assuming a linear average sedimentation rate was deposited approximately 240 cal. yr. BP. The frequencies of the identified turbidites in core HH13-008-GC-TUNU are 2 per 100 years over the last 240 years and 1.4 per 100 years over the last 700 years. In core HH13-009-GC-TUNU the stacked turbidites in the bottom of the core are, based on estimated sedimentation rates, suggested to be deposited around 1920 cal. yr. BP. In this core the frequencies of turbidites are 0.67 per 100 years over the last 450 years and 2.4 per 100 years over the last 1920 years. Their origins are suggested to be related to fluvial input/processes on the nearby deltas.

The high frequency turbidites in the two cores located closest to the glacier front (HH13-010-GC-TUNU and HH13-011-GC-TUNU) are suggested to be related to glacial meltwater coming from Waltershausen Gletscher. The frequency in core HH13-010-GC-TUNU is unknown due to the lack of radiocarbon dating, whilst the calculated frequency of turbidites in core HH13-011-GC-TUNU is 2 per 100 years over the last 1130 years. Although the turbidites identified in core HH13-012-GC-TUNU also are inferred to be related to meltwater coming from Waltershausen Gletscher, the frequency of turbidites in the core are several magnitude lower with 1 per 2000 years over the last 8000 years (0.05 per 100 years).

7.4.3. Ice-rafted debris (IRD)

Icebergs calving off the front of tidewater glaciers are important for transport of ice-rafted debris (IRD) into the marine environment (e.g. Dowdeswell and Murray, 1990). Icebergs can carry a significant volume of debris with particles from clay to boulder size, contributing to the total volume of glacimarine sediments. The main mechanisms of debris release from icebergs are fall-out, drop as the iceberg melts and dumping by overturning icebergs (Fig. 7.12). Another important agent for rafting of debris is sea ice (Powell and Domack, 1995).

Sea-ice rafted debris has often been subjected to an increased amount of weathering relative to the debris transported by icebergs, thus having a more rounded appearance and an absence of striations (St.John et al., 2015). During the winter season (October to June) the sea ice cover suppresses iceberg calving in addition to trapping the icebergs that are calved off. When the sea ice breaks up the icebergs are released to the fjord (Dowdeswell and Dowdeswell, 1989; Evans et al., 2002).

IRD is observed in all five sediment cores with an increasing influence away from the glacier margin. Evans et al. (2002) suggested that the high sedimentation rates of meltwater processes in middle-outer Nordfjord exceed the amount of debris deposited from icebergs. Thus, the high amount of suspension settling from glacier meltwater tends to overwhelm the iceberg-dropped component proximal to the glacier front (Boulton, 1990).

Iceberg calving is the dominant ablation mechanism for the GIS in East Greenland, with approximately 8 km^3 yr^{-1} calving into the Kejser Franz Joseph Fjord system (Reeh, 1985; Reeh et al., 1999). However, rafting of material from icebergs and sea ice has proven to be of less importance in the two studied fjords than in other East-Greenland fjords (e.g. Kangerlussuaq Fjord, Miki Fjord and Nansen Fjord in East-Greenland; Smith and Andrews, 2000) based on the amount of IRD relative to other sediments in the cores. Estimated volume of iceberg melt relative to ice sheet meltwater is 4:1 in Kangerlussuaq Fjord and 2:1 in Nansen Fjord (Andrews et al., 1994). The Scoresby Sund fjord system has an estimated flux of icebergs of about 15 km^3 yr^{-1} (Dowdeswell et al., 1997), whilst Kangerlussuaq Gletscher (Kangerlussuaq Fjord) alone calves approximately 15 km^3 yr^{-1} (Reeh, 1985). In Spitsbergen fjords, however, the amount of calving is several orders of magnitude lower, with a total mass loss in the whole archipelago due to calving is estimated to be 5.0–8.4 km^3 yr^{-1} (water equivalent – w.e.), with a mean value 6.75 ± 1.7 km3 yr−1 (w.e.) (Błaszczyk et al., 2009).
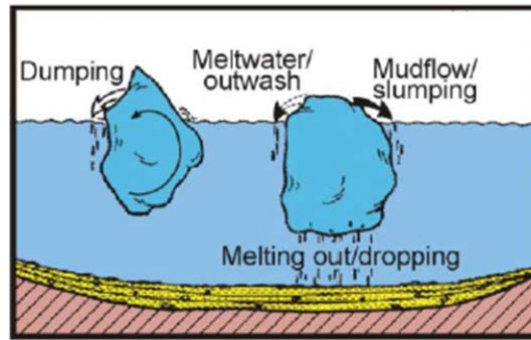
Figure 7.12: Modes of iceberg rafting (modified from Vorren et al., 1983).

7.4.4. Sediment provenance

The mid-late Holocene deposits in Moskusoksefjord and Nordfjord are interpreted to be dominated by glacimarine sediments mainly deposited through suspension fall-out, mass-wasting and ice rafting. Therefore, the sediments are thought to derive from the surrounding land areas including the catchment areas of the glaciers.

Of all the analyses performed on the sediment cores, the XRF core scanning and the measured magnetic susceptibility of the sediments appear to be the most useful when interpreting the provenance of the sediments. Both methods provide high-resolution records of the sediments, giving information about the geochemical elements as well as materials ability to be magnetized. Below, the magnetic susceptibility will be discussed first, followed by the XRF.

The magnetic susceptibility of the sediments in core HH13-008-GC-TUNU and HH13-009-GC-TUNU located in the inner and middle basins of Moskusoksefjord range between 11-33 ($*10^{-8}$ SI(m^3/kg)) (Table 6-1). These values are relatively low compared with the other studied sediment cores of this study. Two additional cores that show similar values in terms of the measured magnetic susceptibility are cores HH13-010-GC-TUNU and HH13-012-GC-TUNU located in the outer basin of Moskusoksefjord and in sub-basin 1 in Nordfjord. Their values range from 33-69 ($*10^{-8}$ SI(m^3/kg)) and have means of 45 and 44 ($*10^{-8}$ SI(m^3/kg)), respectively. Core HH13-011-GC-TUNU, however, stands out with comparatively high values ranging from 70-96 ($*10^{-8}$ SI(m^3/kg)). As the magnetic susceptibility generally decreases with distance from Waltershausen Gletscher, it is suggested that sediments with higher magnetic susceptibility are derived from the catchment area of Waltershausen

Gletscher. The bedrock located below the glacier is made up of Neoproterozoic to Ordovician Caledonian fold belts comprising pale sandstones and darker mudstones with local granite formation. The area surrounding Moskusoksefjord consists of Devonian continental siliciclastic sediments mainly comprising red sandstones (Henriksen et al., 2000; Henriksen, 2008).

The application of XRF scanning of fjord sediments is a generally new research area and little is known about the interpretation within these environments. Authors performing studies in other settings have attempted to correlate their results with sediment provenance, composition and nature and the degree of terrestrial sediment discharge (Croudace et al., 2006; Rothwell et al., 2006; Calvert & Pedersen, 2007; Bertrand et al., 2012). In this study the XRF data has been used to i) correlate the cores and ii) relate the sediments with the surrounding bedrock.

The Ca/Fe ratio is thought to be an indicator of biogenic carbonate:detrial clay indicator (Rothwell et al., 2006). The amount of Ca decreases with distance from Waltershausen Gletscher and in the in-fjord direction of Moskusoksefjord, meaning that the abundance of carbonate material is highest proximal to the glacier front. However, study of the five sediment cores reveals that there is very little carbonate microfossils available in the cores closest to the glacier front. Thus, the brownish/reddish sediments derived from the surrounding land areas of Moskusoksefjord have a lower amount of Ca than the grayish sediments coming from Waltershausen Gletscher. However, the coarse dark reddish brown sediments from the two inner cores of Moskusoksefjord have a higher amount of Ca compared to the finer sediments within the cores, indicating that the brownish sediments in core HH13-008-GC-TUNU and HH13-009-GC-TUNU were derived from at least two separate sediment input sources. The concentration of Fe within the sediments decreases slightly with distance to the glacier front, making the bedrock located beneath the glacier slightly deficient in Fe. Unlike the other measured elements, Zr occurs exclusively in the two innermost cores, with the ratio Zr/Rb providing marked increases in the base of turbidites. Both cores contain weak red intervals of mud with small decreases in Al compared to the surrounding brown mud.

The three cores located in the outer basin of Moskusoksefjord and in Nordfjord contain mostly fine gray sediments with layers or lenses of coarser dark grayish brown sediments. K

is thought to be associated with clay minerals, which can be seen in all three cores. Thus, the layers containing coarse dark grayish brown sediments are characterized by decreases in K, Ti and Fe and subsequent increases in both Ca and Si.

In summary, the coarser dark reddish brown sediments observed in the inner- and middle basins of Moskusoksefjord are inferred to have come from the fjord side walls whereas the finer brown mud is suggested to have mainly come from the river entering the fjord head. The weak red/grayish sediments in the inner-and middle basins of Moskusoksefjord are interpreted to have derived from Waltershausen Gletscher. The three outer cores in the study area, located in the outer basin of Moskusoksefjord and in sub-basin 1 and 2 of Nordfjord, are assumed to contain sediments mainly originating from Waltershausen Gletscher.

Finally, the previously suggested application of the different geochemical elements for sediment provenance has proven to be partly incorrect for the study area of this thesis. Whereas the concentration of Ti is thought to show an increase in the base of turbidites, it has proven to be the opposite for the turbidites present in all five cores. Also, the element ratio Ca/Fe has in this study shown to be applicable for indicating sediments derived from the glacier rather than for variations in biogenic carbonate:detrial clay. A possible interpretation is that the carbon derived from the bedrock beneath Waltershausen Gletscher overprints the carbonate production in the area.

7.5. Mid-late Holocene history and sedimentary paleoenvironment of Moskusoksefjord and Nordfjord

In the following sections the results from the previously discussed chapters will be presented in order to reconstruct the mid-late Holocene glacial history and sedimentary paleoenvironment in Moskusoksefjord and Nordfjord. The reconstruction is based on the IRD content, lithological changes, sedimentation rates and sediment provenance as well as comparison to published data. A schematic overview of the main sedimentary processes and paleoenvironments in Moskusoksefjord and Nordfjord from the Holocene Climate Optimum and up to present are presented in Fig. 7.17.

The division into five main time periods is based on the paleoclimate of the area as there were no marked boundaries in the lithology, measured physical properties or the geochemical elements of the cores. The dates of the boundaries were approximated using an age model assuming constant sediment accumulation rates between the provided radiocarbon dates (Fig. 7.13). It is proven to be a spatial variation in the onset of major climatic events (e.g. Medieval Warm Period, Little Ice Age etc.) (e.g. Mann, 2002). However, the following time period divisions are based on previous studies conducted in East Greenland (see *Chapter 1.2.2. Holocene paleoclimate of East Greenland*).

The oldest dated sediments are from the bottom of core HH13-012-GC-TUNU and have an age of 7770 cal. yr. BP, suggesting that the core sediments were deposited during the last ~8000 years. Core 012 is therefore used as a key core for the Holocene Climate Optimum, Neoglaciation and Medieval Warm Period. Core HH13-011-GC-TUNU provides the most detailed representation of the sedimentary paleoenvironment of the study area and is therefore used as the key core for the Little Ice Age and Modern Maximum, whereas core HH13-008-GC-TUNU, HH13-009-GC-TUNU and HH13-012-GC-TUNU are used as supplements.
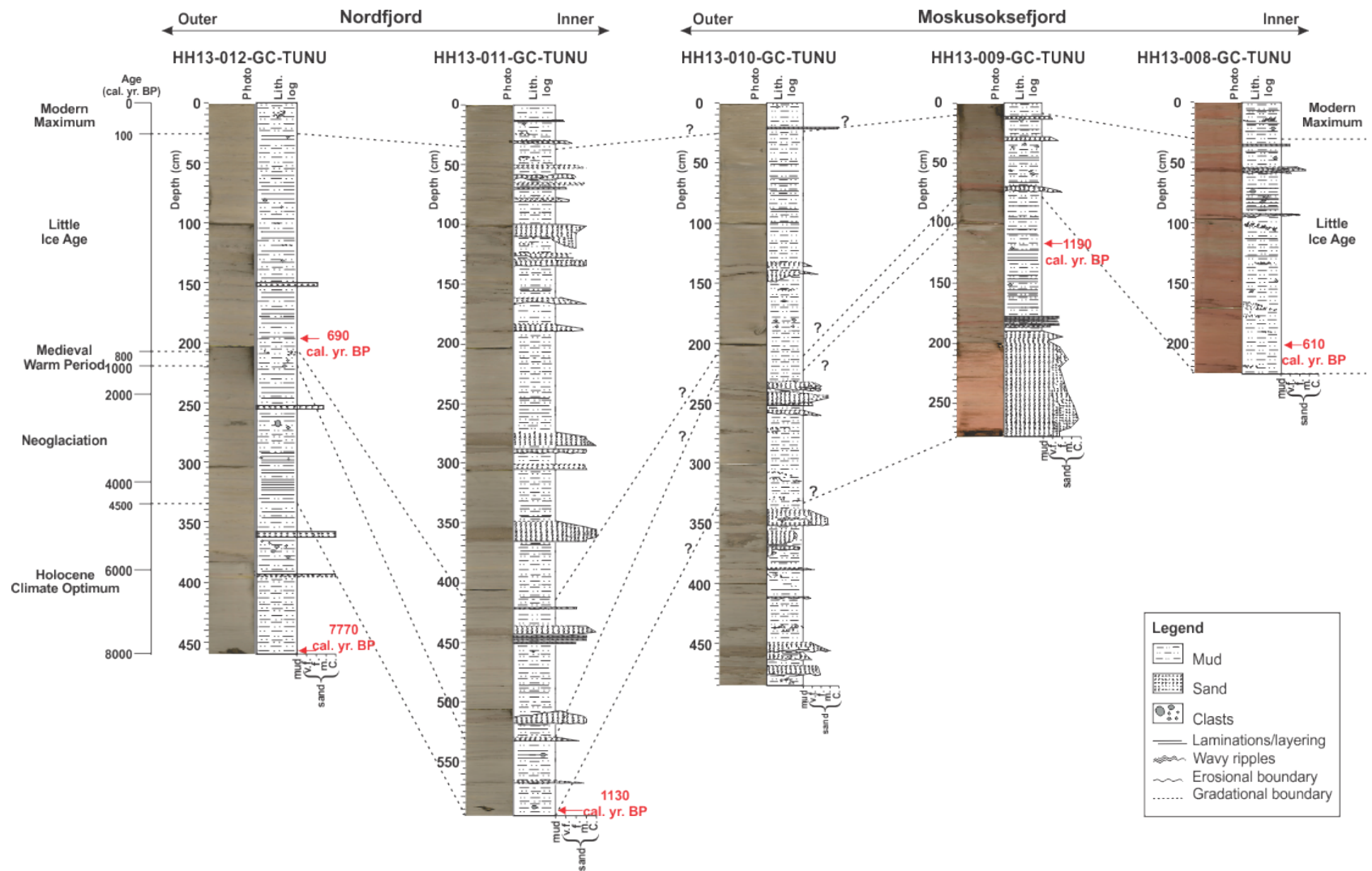
Figure 7.13: Lithological logs from all five sediment cores displayed in a transect from inner Moskusoksefjord (right) to outer Nordfjord (left), along with the results from correlation and calculations of sedimentation rates. A linear age model based on the ^{14}C AMS and ^{210}Pb/^{137}Cs dating result is indicated on the left., with dotted lines correlating the time intervals. Calibrated ages BP from radiocarbon ages are given in red.

138

7.5.1. Holocene Climate Optimum (>8000–4500 cal. yr. BP)

Sediments deposited during the Holocene Climate Optimum are represented in the lower part (459 cm- ~345 cm) of core 012 (Fig. 7.14). A sample of diverse benthic foraminifera collected between 455-454 cm depth provided an age of 7770 cal. yr. BP. The lower part of the interval (459-394), estimated to represent ~8000-5700 cal. yr. BP, is characterized by massive gray mud and no bioturbation. The absence of bioturbation is suggested to be a result of one of two factors; i) the mud represents the uppermost part of a turbidite (division T_a – see *Chapter 6.5.1.4. Interpretation*) or ii) high sedimentation rates resulting in an unfavorable environment for macrofauna (Gingras et al., 2015). However, the latter is considered unlikely based on the estimated sedimentation rate of 36 cm/ka for the time interval.
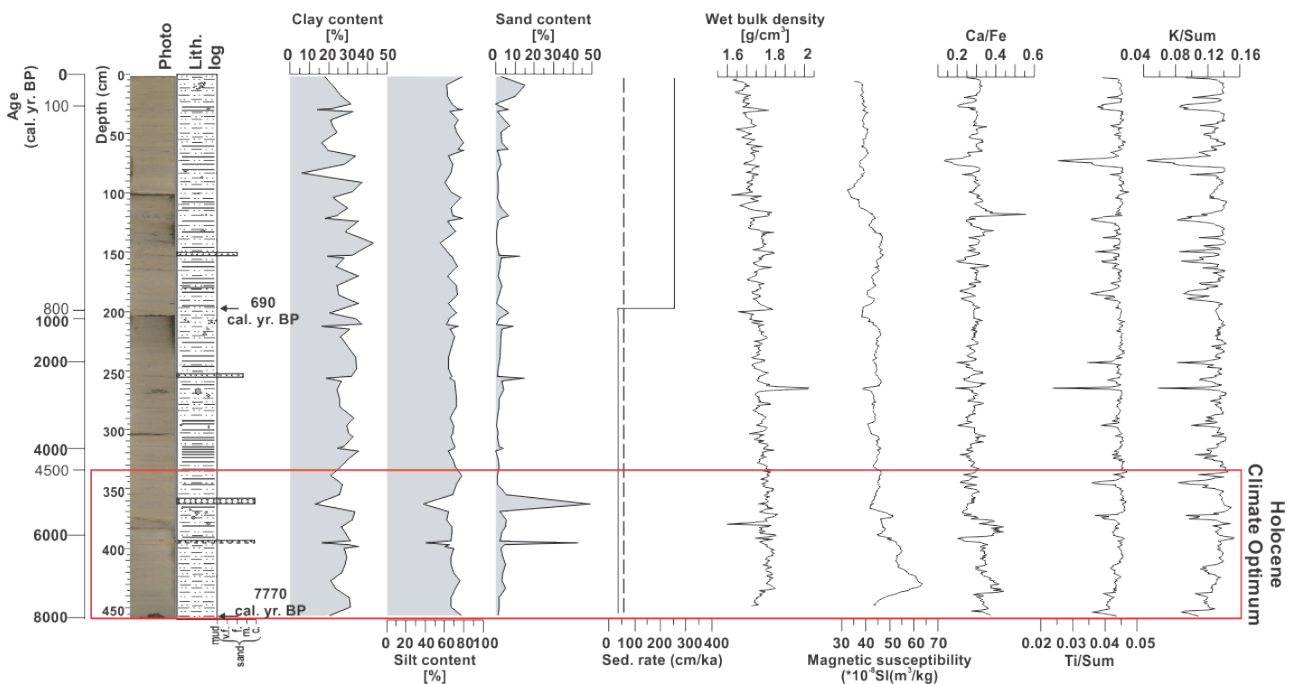
Figure 7.14: Lithological log, grain-size distribution, sedimentation rates (dotted line is the average sedimentation rate), measured physical properties and element geochemistry for core HH13-012-GC-TUNU plotted against depth. Radiocarbon ages are given in calibrated years BP. A linear age model is presented to the left. The inferred interval of the Holocene Climate Optimum is marked with a red box.

In East Greenland, the Holocene Climate Optimum is characterized by drier and warmer summer temperatures than present with the ice sheet retreated behind the present day limit (Fig. 7.17). Modeling estimates shows that the GIS shrunk to 0.17 m (sea-level equivalent) smaller than present around 5-4 ka BP and retreated up to 80 km behind the present day ice limit at Hvalrosodden, north of Kejser Franz Joseph Fjord (Simpson, 2009). However, a study

performed in lake sediments in Kejser Franz Joseph Fjord revealed that the regional climate cooled around 6500 cal. yr. BP with an adjoining increase in precipitation and snow accumulation (Wagner et al., 2000). This cooling is suggested to have caused Waltershausen Gletscher to advance into tidewater, resulting in a more ice-proximal environment with deposition from meltwater plumes, turbidity currents and iceberg rafting. Also, increased precipitation would have resulted in increased erosion in the catchment areas of the two fjords and higher transport energy of the meltwater streams. The result is a relative increase in the amount of coarse-grained sediments transported to the basins, as can be seen in the sediments retrieved from sub-basin 1 of Nordfjord. Similar observations have been made in lake sediments at Geographical Society Ø (Wagner et al., 2000). A cooling climate could also result in a sea-surface cooling and a year-round sea-ice formation with subsequent trapping of icebergs within a sikkusaq (cf. Dwyer, 1995; Syvitski et al., 1996).

7.5.2. Neoglaciation – Medieval Warm Period (~4500-800 cal. yr. BP)

The climate continued to cool into the Neoglaciation and glaciers expanded all over Greenland (Fig. 7.17) (Bennike and Weidick, 2001). Lake sediments from outer Kejser Franz Joseph Fjord indicated a gradual decrease in the temperature since 5000 cal. yr. BP (Wagner et al., 2000), in alignment with the GRIP palaeotemperature record (Dahl-Jensen et al., 1998), culminating in a very cold and dry climate. The onset of the middle Holocene cooling has been argued to be caused by the retreat of warm Atlantic water masses to the southern central parts of Greenland along with a strengthening of the EGC and subsequent southwards shift of the sea-ice margin (Wagner et al., 2000). The renewed glacier expansion is inferred to have occurred ca. 5800 cal. yr. BP in the North-East Greenland (Hjort, 1997), whilst the advance in Scoresby Sund region occurred about 2000 years later (Funder, 1989).

The renewed climatic cooling can tentatively be correlated with a change in the acoustic signature in the middle basin of Moskusoksefjord, going from low-moderate amplitude to high amplitude reflections. The reflection boundary between seismic *Unit M-1* to *Unit M-2* is estimated to be formed around 2000 cal. yr. BP. The internal seismic signature of *Unit M-2* is inferred to indicate a more pronounced change in lithology relative to *Unit M-1*. Increased reflection amplitude is interpreted to indicate an increase in ice rafting, coarser sediments from fall-out from meltwater plumes and/or more coarse-grained turbidites related to an associated higher glacial activity in the fjord.

An increase in the amount of laminations is characteristic for the Neoglaciation time period in both fjords (Fig. 7.15), indicating an advance of the glacier front and a subsequent more ice-proximal environment (Fig. 7.17). The frequent laminations deposited by suspension settling and turbidity currents demonstrate variations in the meltwater discharge coming from Waltershausen Gletscher, in addition to shorefast sea-ice suppressing iceberg rafting. Laminated mud and the presence of sea-ice have previously been described for similar settings (Vorren et al., 1983; Marienfeld, 1991; Ó Cofaigh and Dowdeswell, 2001). In the middle basin of Moskusoksefjord the laminations observed are a result of frequent changes in the sediment provenance. The red mud coming from the fjord sides of Badlandal in the innermost part of Moskusoksefjord is periodically overwhelmed by suspension fall-out of gray mud transported by meltwater plumes coming from Waltershausen Gletscher. The mixing of the two sediments produces a laminated/layered appearance of the sediments.

The relatively small amount of IRD during the Neoglaciation is postulated to be caused by perennial sea-ice suppressing iceberg drift. Sea-ice impacts both the stability of the glacier front as well as iceberg production and mobility (Jennings and Weiner, 1996). Similar settings have been documented in other East Greenland fjords (Smith and Andrews, 2000). However, a steady delivery of IRD to the east-central Greenland margin has been documented for the late Holocene (e.g. Jennings et al., 2002), indicating that some fjords were not ice covered?

The Medieval Warm Period followed the Neoglaciation and is thought to have been warmer and more stable than today (Jennings and Weiner, 1996). Studies from Nansen Fjord revealed that the sea surface was mostly free from sea-ice in the summer during the Medieval Warm Period (Fig. 7.17) (Jennings and Weiner, 1996). The climatic event is regarded to have lasted from ~1000-800 cal. yr. BP (Johnsen et al., 1992; Wagner et al., 2000). As aforementioned, the onset of the climatic event shows spatial variations. Records of dwarf shrub pollen in Basaltsø in Kejser Franz Joseph Fjord indicated a short warming between ~900 and 500 cal. yr. BP (Wagner et al., 2000). It is difficult to identify the timing of the Medieval Warm Period in Moskusoksefjord and Nordfjord from the limited data available in this study. This will be further discussed below.
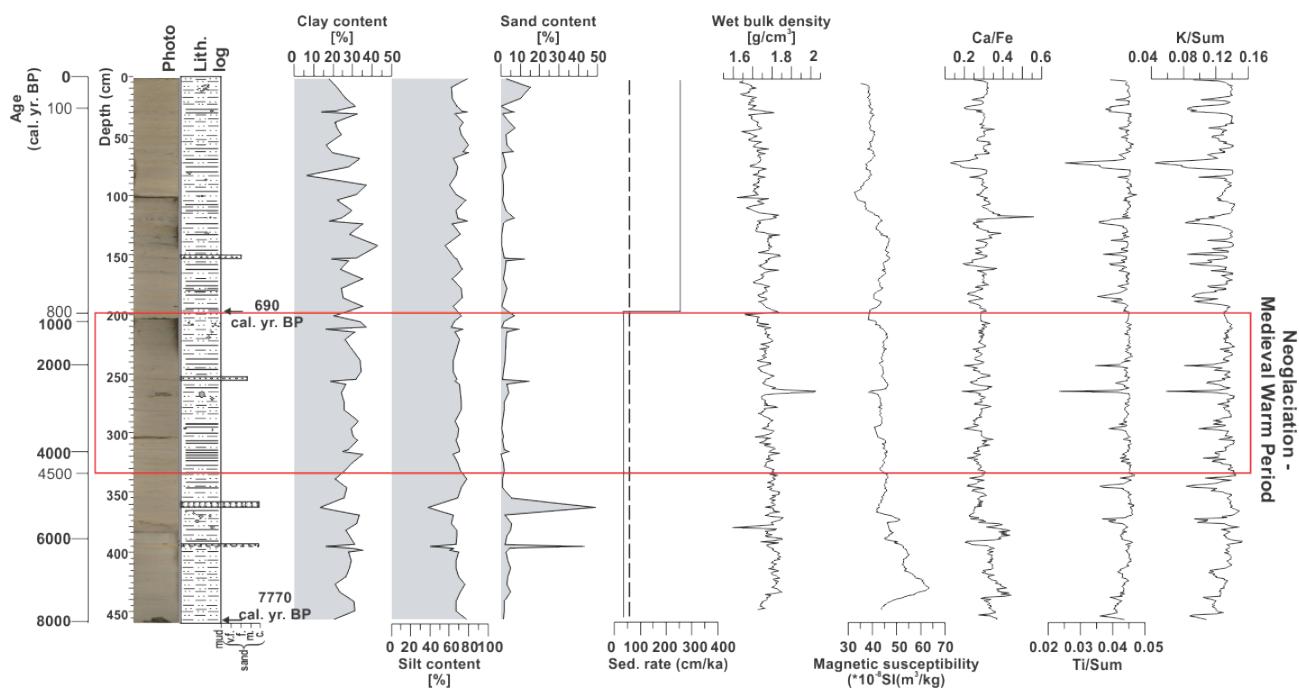
Figure 7.15: Lithological log, grain-size distribution, sedimentation rates (dotted line is the average sedimentation rate), measured physical properties and element geochemistry for core HH13-012-GC-TUNU plotted against depth. Radiocarbon ages are given in calibrated years BP. A linear age model is presented to the left. The inferred interval of the Neoglaciation – Medieval Warm Period is marked with a red box.

7.5.3. The Little Ice Age (~800-100 cal. yr. BP)

Following the Medieval Warm Period the climate cooled again, culminating in the Little Ice Age (Fig. 7.16 and 7.17). The Little Ice Age in East Greenland was characterized by a relatively cold climate and glacier expansion along with changes in $\delta^{18}O$ values (Benn & Evans, 2010) and low values of biogeochemical parameters from lake sediments (Wagner et al., 2000). According to Wagner et al. (2000), the Little Ice Age started about 800 cal. yr. BP. Several factors have been suggested for its onset, with changes in the solar activity causing a prolonged minimum in sunspot activity and solar output being the main theory along with volcanic eruptions and changes in the ocean circulation of the North Atlantic (e.g. Mann et al., 1998, Mann, 2000; Benn and Evans, 2010).

The acoustic signature within seismic *Unit N-2* changes gradually from medium to strong amplitude reflections around the beginning of the Little Ice Age (Fig. 7.8), interpreted to reflect an increase in the glacial activity with frequent changes in lithology, with IRD, coarse-grained turbidites and mud deposited as suspension fall-out from meltwater plumes mainly originating from Waltershausen Gletscher. Even though the Little Ice Age is known for being
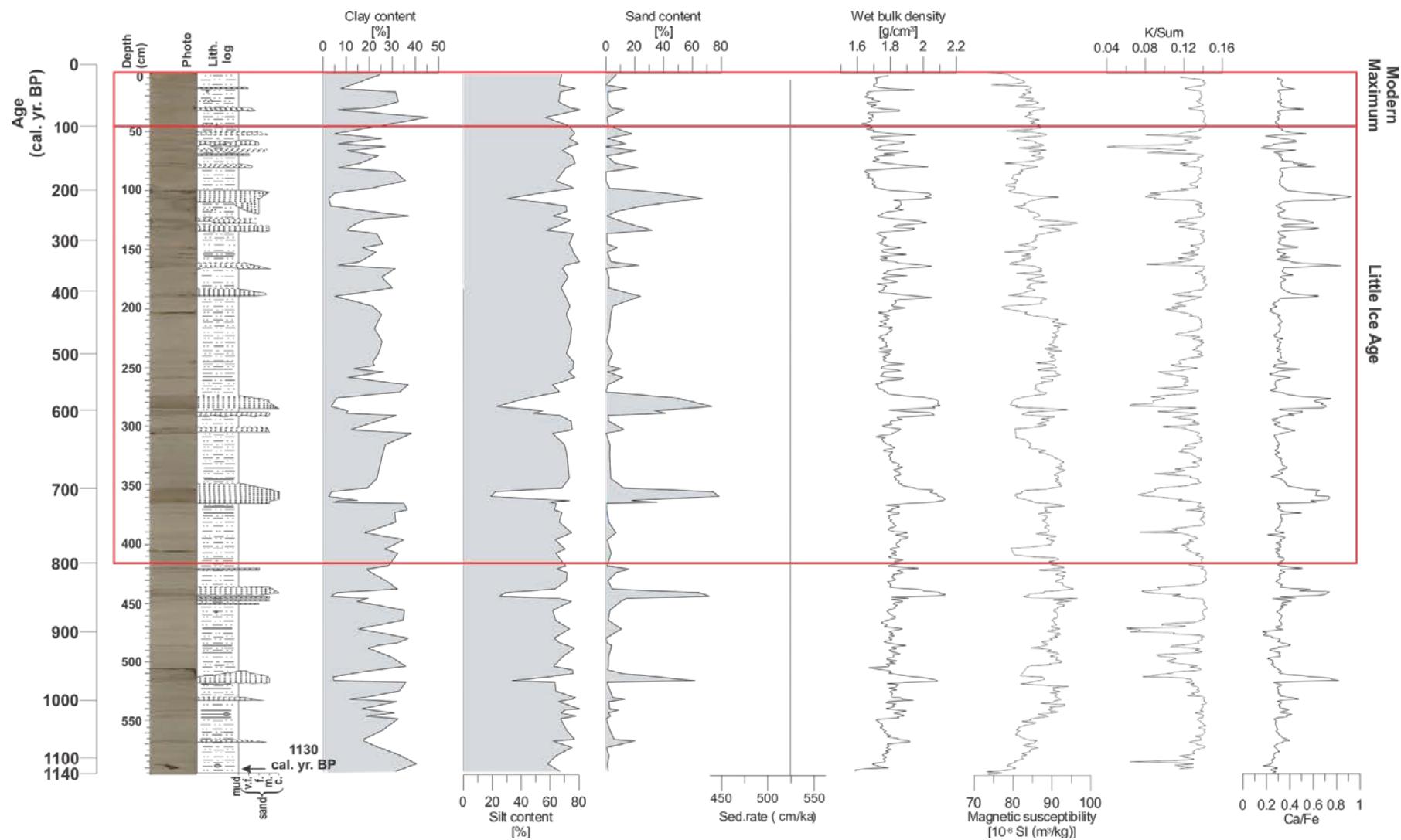
Figure 7.16: Lithological log, grain-size distribution, sedimentation rate, measured physical properties and element geochemistry for core HH13-011-GC-TUNU plotted against depth. Radiocarbon age is given in calibrated years BP. A linear age model is presented to the left. The inferred intervals of the Little Ice Age and Modern Maximum are marked with red box.

143

the coldest period in Holocene, IRD is nearly absent in core 011. In core 008 and 009, however, the IRD content increases a little towards the top. In addition to the late cooling signal in the sediment cores, it is interpreted to indicate a late onset of the Little Ice Age in Moskusoksefjord and Nordfjord.

The end of the Little Ice Age (~400-100 cal. yr. BP) is characterized by an increase in the general frequency of turbidites in sub-basin 2 of Nordfjord and in the two innermost basins of Moskusoksefjord. The frequency of occurrence (events per 100 years) during the Little Ice Age is estimated to have been 0.4 for core 009, 1.9 for core 011 and 0.14 for core 012. Core 008, which is estimated to contain sediments deposited up to ~700 cal. yr. BP, had 0.8 per 100 years for the time period 700-100 cal. yr. BP. It appears to be a change in the characteristics of the turbidites towards the end of the time period with an increase in the frequency and an associated general thinning of the turbidites. A suggestion for the increases in events is a climate worsening with intervening warm intervals, causing more frequent instabilities at the glacier front.

The gray mud inferred to have derived from sediment-laden glacial meltwater plumes originating from Waltershausen Gletscher was either insignificant or absent in the inner basin of Moskusoksefjord for more than 250 years. The gray mud was introduced to the inner basin ~360 cal. yr. BP and is inferred to reflect either a stronger meltwater signal coming from Waltershausen Gletscher as a result of a small glacier advance or a decrease in the meltwater production within the catchment area of the river at the fjord head of Moskusoksefjord. A change in the fjord circulation is inferred to be unlikely. Overall, sedimentation in the inner basin appears to be dominated by meltwater coming from the fjord head over the last ~700 years.

Compared with e.g. Spitsbergen and Norway, little is known about the Little Ice Age in East Greenland. Whilst glacier on Svalbard and in Norway advanced during the climatic cooling (e.g. Mangerud and Landvik, 1997; Svendsen and Mangerud, 1997; Plassen et al., 2004), the response of East Greenland glaciers remains unclear. The measured physical properties (e.g. wet bulk density) of the cores in the proximity to Waltershausen Gletscher show no signs of the core sites being overridden by a glacier. A potential advance of the glacier front must then have been less than 10 km from the present day glacier margin. However, more data is

required to confirm/deny this hypothesis. However, a sill in Kangerdlussuaq Fjord is proposed to have formed during the Little Ice Age (Syvitski et al., 1996).
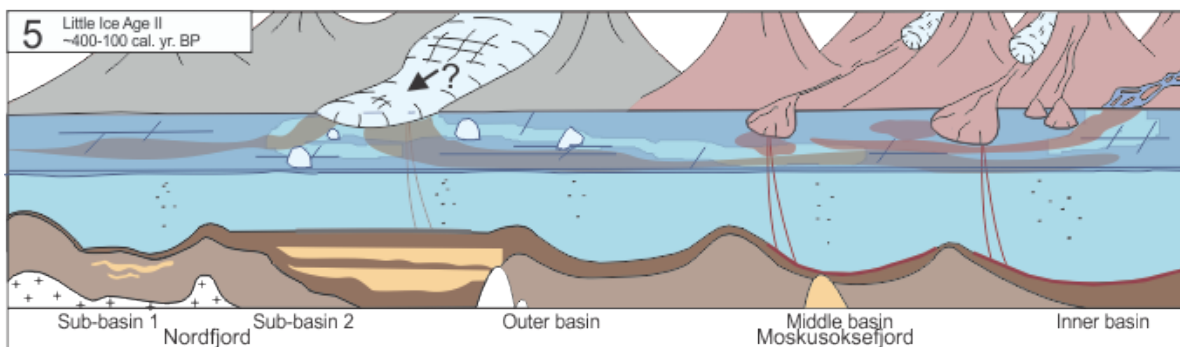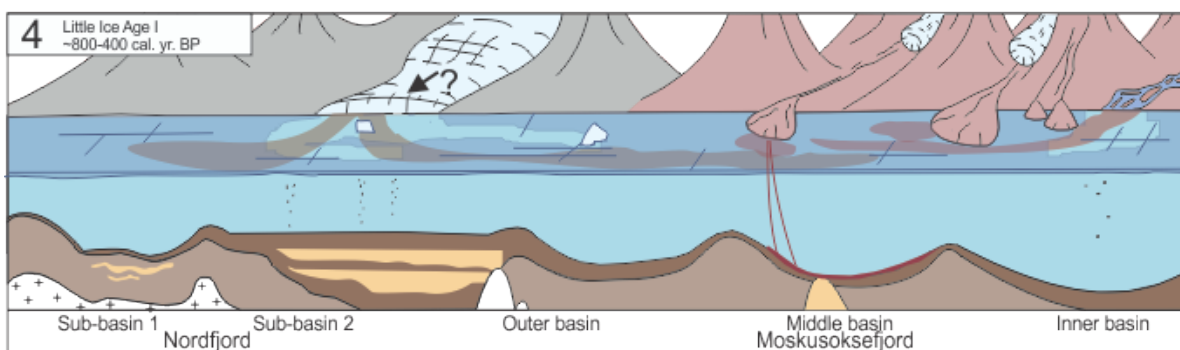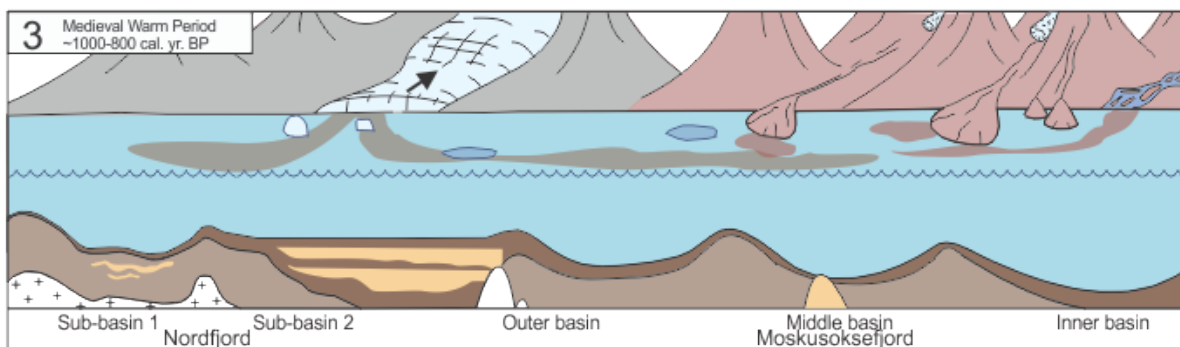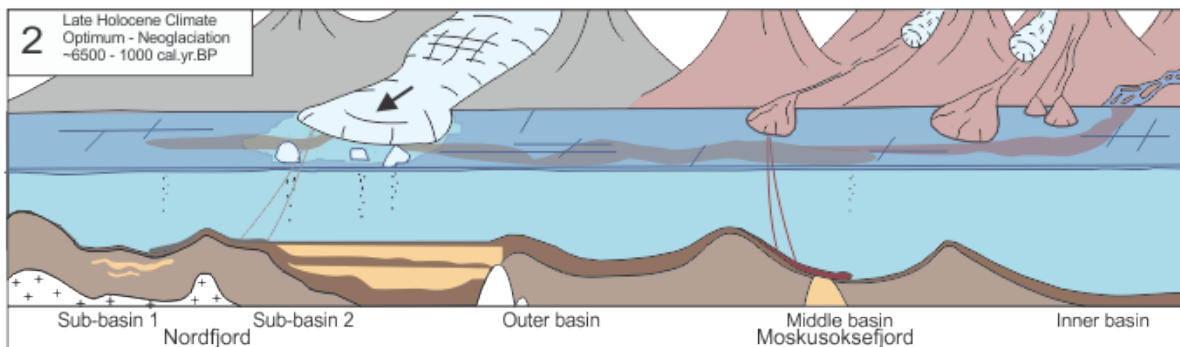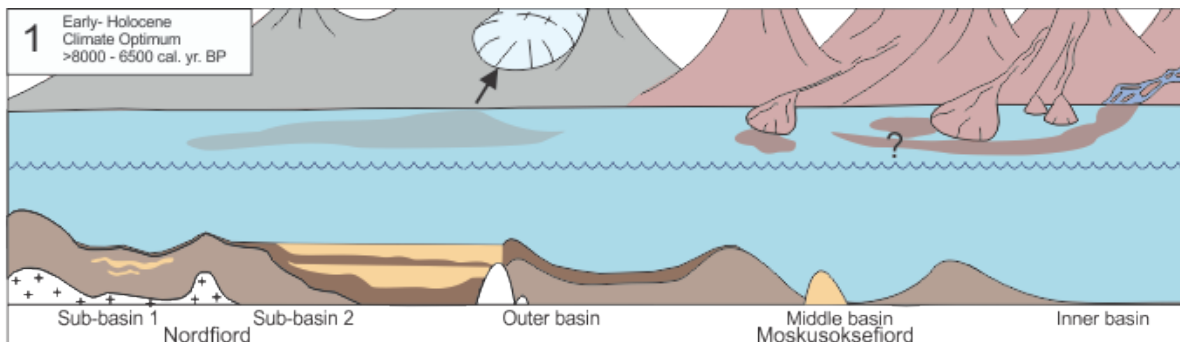
In summary, no clear advances of the glacier front of Waltershausen Gletscher have been documented for the Little Ice Age in Moskusoksefjord and Nordfjord. The sedimentary environment appears to have been stable throughout the Little Ice Age with randomly distributed turbidites throughout the whole time interval as seen in the two cores closest to the glacier front.
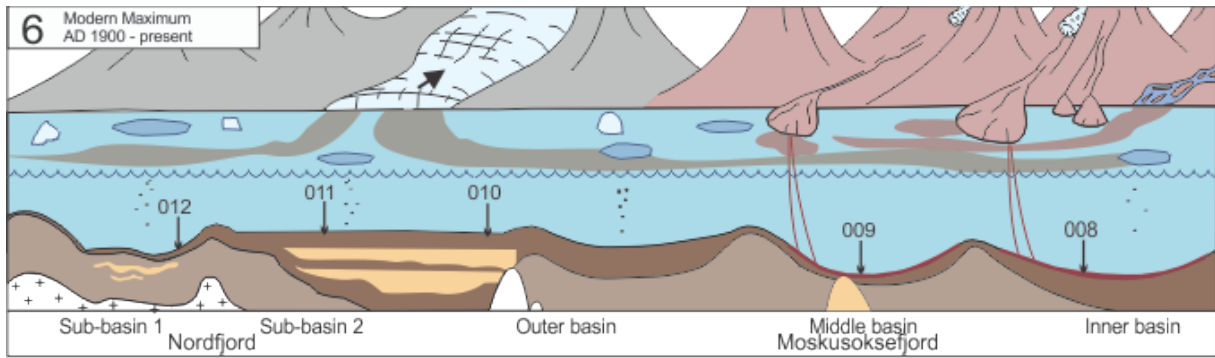
7.5.4. Modern Maximum (AD 1900-present)

The Modern Maximum represents the present warming period (Fig. 7.17). After the Little Ice Age temperatures on Greenland increased and reached a maximum in the 1930s, cooled, and have increased again since the 1980s. A warming of 1.1°C was observed at the ice sheet summit from 1991-2000 (Box, 2002).

A possible glacier retreat and increased river meltwater discharge after the Little Ice Age is seen as a relative increase in the amount of sand in the upper part of all five sediment cores. The measured ^{210}Pb and ^{137}Cs revealed the highest sedimentation rate of <1 cm/yr (<1000 cm/ka) during the time interval of this study for the upper part of core 012, suggesting an increase in subglacial melting and river run-off. It is uncertain whether the glacier front of Waltershausen Gletscher has retreated since the Little Ice Age. Further south of the study area, however, studies show that Kangerdlussuaq Glacier began its retreated from its Little Ice Age maximum extent (LIA$_{max}$) between 1930 to 1932 and retreated more than 7 km from 1932 to 1933. The glacier thinned by 230-265 m between its LIA$_{max}$ and up to 1981 (Khan et al., 2014).

Satellite monitoring of the glacier front from of 2001-2009 Waltershausen Gletscher revealed very limited change in the front position. Fluctuations of the glacier front was relatively minor with -0.13 km interannual front change from 2001-2005 and +0.15 km front change from 2005-2008 (Seale et al., 2011) (Fig. 2.4). This is in agreement with other glaciers in North-East Greenland (Seale et al., 2011).

Figure 7.17: Schematic overview of the main sedimentary processes and paleoenvironments in Moskusoksefjord and Nordfjord from the Holocene Climate Optimum and up to present. The sediment cores from this study are indicated.

8. Summary and conclusions

Swath bathymetry, high-resolution seismic data and five sediment cores were analyzed in order to reconstruct the Holocene glacial history, sedimentary processes and paleoenvironment of Moskusoksefjord and inner parts of Nordfjord, North-East Greenland.

- In Moskusoksefjord the large-scale bathymetry was divided into an inner-, middle- and outer basins, separated by relatively large deltas prograding into the fjord from both sides. The studied part of inner Nordfjord is divided into two sub-basins. No glacial landforms have been observed in the study area apart from two transverse ridges in the outer basin of Moskusoksefjord which may represent buried glacial moraines. The lack of observable glacial landforms is probably due to a relatively high sedimentation rates in the fjord and thereby thick sediment cover.

- The seafloor of the central parts of the basins appears as generally smooth, while a number of small- and large-scale landforms characterize the basin side walls. Here several slide scars and sediment lobes are found, and together with numerous channels, they contribute to the rugged appearance of the fjord slopes.

- The chirp data reveals a general distinction of two seismostratigraphic units, both dominated by acoustically stratified, semi-continuous to continuous reflections. The uppermost unit is interpreted to represent more pronounced and frequent changes in lithology relative to the underlying unit of similar seismic signature but with lower amplitude reflections. The timing of the change in acoustic signature is inferred to vary between the two fjords as well as within the fjords, and may tentatively be related to the climatic variations prior to the Little Ice Age.

- Mass-transport activity in Moskusoksefjord and Nordfjord probably occurred episodically throughout the Holocene. Types of mass-transport deposits present in the two fjords are cohesive debris flows and turbidites. The most extensive MTDs were interpreted as cohesive debris flows located in the outer basin of Moskusoksefjord and in sub-basin 2 of Nordfjord, the area closest to the present glacier front of Waltershausen Gletscher. They are tentatively suggested to have been deposited during late Holocene Climate Optimum, representing episodical events related to the development of oversteepened slopes due to high sediment supply and/or pushing of sediments at or near the grounding line of the glacier.

- The dominating sedimentary process in Moskusoksefjord and Nordfjord are suspension settling from turbid meltwater plumes derived from Waltershausen Gletscher and the river coming from Badland at the fjord head of Moskusoksefjord.

- The frequency of turbidites increases towards the end of the Little Ice Age and is highest in the proximity to the glacier front. Whereas the turbidites identified in the outer basin of Moskusoksefjord and in Nordfjord are suggested to be related to glacial meltwater coming from Waltershausen Gletscher, the turbidites in the inner- and middle basins of Moskusoksefjord are inferred to be related to fluvial input and subsequent resedimentation-processes on the nearby deltas.

- IRD is observed in all five sediment cores with a relatively increasing influence away from the glacier margin. However, rafting of material from icebergs and sea ice has proven to be of less importance in the two studied fjords than in other East-Greenland fjords (cf. Smith and Andrews, 2000) based on the amount of IRD.

- The estimated average sedimentation rates in this study are 58 cm/ka for the last ~8 ka and 85-446 cm/ka for the last 1 ka. Based on this, we suggest the sedimentation rates in East Greenland fjords through the Holocene to be of medium rate rather than medium to -high as suggested by Syvitski et al. (1987).

- Magnetic susceptibility and quantitative element geochemistry from XRF are useful proxies and can be used to reconstruct the sediment provenance within the two fjords. The grayish Neoproterozoic to Ordovician Caledonian bedrock beneath Waltershausen Gletscher has a higher Ca content and magnetic susceptibility values than the reddish Devonian continental siliciclastic sediments in the area surrounding Moskusoksefjord.

- After retreating onto land during the warm Holocene Climate Optimum, Waltershausen Gletscher advanced into the fjord after a climate cooling ~6500 cal. yr. BP. An increasing in glacial activity continued through the Neoglaciation with shorefast sea-ice suppressed iceberg rafting.

- No clear glacial advance and little IRD are observed related to the Little Ice Age. In addition to the late cooling signal in the sediment cores, it is interpreted to indicate a late onset and a restricted advance of the Little Ice Age ice front in Moskusoksefjord and Nordfjord.

9. Recommended further work

The results from this study have provided new information about the sedimentary paleoenvironment and glacial history of Moskusoksefjord and Nordfjord during the Holocene. However, the research has highlighted a number of areas on which further research is recommended in order to improve our understanding and to get more complete and accurate results. The recommended directions of further work are:

- Gather acoustic data closer to the glacier front of Waltershausen Gletscher in order to map the maximum extent of the glacier front during the Little Ice Age.
- Mapping the remaining parts of Nordfjord and the outer part of Kejser Franz Joseph Fjord would contribute to a better understanding of the deglaciation of the fjord system.
- Recovery of additional sediment cores:
  - Longer sediment cores would allow us to penetrate into the underlying seismic Unit -1 as well as the interpreted MTDs in the area closest to the present glacier front of Waltershausen Gletscher. The periods of their formations could then be dated.
  - Develop a spatial and temporal pattern of IRD in Nordfjord.
- Additional radiocarbon dates would improve the inferred age models for the sediment cores in addition to correct for potential changes in sedimentation rates.

10.Bibliography

Aagaard, K., & Coachman, L. (1968). The East Greenland Current north of Denmark Strait, Part I. *Arctic, 21*, 181-200.

Alley, R. B. (2007). Wally Was Right: Predictive Ability of the North Atlantic "Conveyor Belt" Hypothesis for Abrupt Climate Change. *Annual Review of Earth and Planetary Sciences , 35*, 241-272.

Alley, R. B., Andrews, J., Brigham-Grette, J., Clarke, G., Cuffey, K., Fitzpatrick, J., . . . White, J. (2010). History of the Greenland Ice Sheet: paleoclimatic insights. *Quaternary Science Reviews*, 1728-1756.

Alley, R., Mayewski, P., Stowers, T., Stuvier, M., Taylor, K., & Clark, P. (1997). Holocene climatic instability: A prominent, widespread event 8200 yr ago. *Geology, 25*, 483-486.

Andresen, A., Rehnström, E. F., & Holte, M. (2007). Evidence for simultaneous contraction and extension at different crustal levels during the Caledonian orogeny in NE Greenland. *Journal of the Geological Society, 164*, 869-880.

Andrews, J. T., Milliman, J. D., Jennings, A. E., Rynes, N., & Dwyer, J. (1994). Sediment thickness and Holocene glacial marine sedimentation rates in three East Greenland fjords (ca. 68°N). *The Journal of Geology, 102*, 669-683.

Appleby, P. G. (2008). Three decades of dating recent sediments by fallout radionuclides: a review. *Holocene, 18*, 83-93.

Baeten, N., Forwick, M., Vogt, C., & Vorren, T. O. (2010). Late Weichselian and Holocene sedimentary environments and glacial activity in Billefjorden, Svalbard. In Howe.J.A., W. Austin, M. Forwick, & M. Paetzel, *Fjord Systems and Archives* (Vol. 344, pp. 207-223). London: Geological Society, Special Publications.

Bard, E., Tuna, T., Fagault, Y., Bonvalot, L., Wacker, L., Fahrni, S., & Synal, H.-A. (2015 (in press)). AixMICADAS, the accelerator mass spectrometer dedicated to 14C recently installed in Aix-en-Provence, France. *Nuclear Instruments and Methods in Physics Research B*.

Beckhoff, B., Kanngiesser, B., Langhoff, N., Wedell, R., & Wolff, H. (2006). *Handbook of Practical X-Ray Fluorescence Analysis.* Berlin Heidelberg: Springer-Verlag GmbH.

Benn, D. I., & Evans, D. J. (2010). *Glaciers & Glaciation* (2nd ed.). Hodder Arnold Publication - Routledge.

Bennike, O. (2008). An early Holocene Greenland whale from Melville Bugt, Greenland. *Quaternary Science, 69*, 72-76.

Bennike, O., & Björck, S. (2002). Chronology of the last recession of the Greenland Ice Sheet. *Journal of Quaternary Science, 17*(3), 211-219.

Bennike, O., & Weidick, A. (2001). Late Quaternary history around Nioghalvfjersfjorden and Jøkulbugten, North-East Greenland. *Boreas, 30*, 205-227.

Bersch, M. (1995). On the circulation of the northeastern North Atlantic. *Deep-Sea Research, 42*, 1583-1607.

Bertrand, S., Hughen, K., Sepúlveda, J., & Pantoja, S. (2012). Geochemistry of surface sediments from the fjords of Northern Chilean Patagonia (44–47°S): Spatial variability and implications for paleoclimate reconstructions. *Geochimica et Cosmochimica Acta, 76*, 125-146.

Błaszczyk, M., Jania, J. A., & Hagen, J. O. (2009). Tidewater glaciers of Svalbard:Recent changes and estimates of calving fluxes. *Polish polar research, 30*(2), 85-142.

Boulton, G. S. (1990). Sedimentary and sea level changes during glacial cycles and their control on glacimarine facies architecture. In J. A. Dowdeswell, & J. D. Scourse, *Glacimarine environments: Processes and sediments* (Vol. 53, pp. 15-52). Geological Society Special Publication.

Bouma, A. (1962). *Sedimentology of some Flysch deposits.* Amsterdam: Elsevier.

Bourke, R., Newton, J. L., Paquette, R. G., & Tunnicliffe, M. D. (1987). Circulation and Water Masses of the East Greenland Shelf. *Journal of Geophysical Research, 92*, 6729-6740.

Bowman, S. (1990). *Radiocarbon dating.* Berkley and Los Angeles: University of California Press.

Box, J. (2002). Survey of Greenland instrumental temperature records 1873-2001. *International Journal of Climatology, 22*, 1829-1847.

Burger, R., Sheehan, A., & Jones, C. (2006). *Introduction to Applied Geophysics: Exploring the Shallow Subsurface.* New York: W. W. Norton & Company.

Böcher, T., Fredskild, B., Holmen, K., & Jakobsen, K. (1978). *Grønlands flora (The flora of Greenland)* (3rd ed.). Copenhagen: P. Haase.

Bøe, R., Hovland, M., Instanes, A., Rise, L., & Vasshus, S. (2000). Submarine slide scars and mass movements in Karmsundet and Skudenesfjorden, southwestern Norway: morphology and evolution. *Marine Geology, 167*(1-2), 147-165.

Calabrese, E. A., & Syvitski, J. P. (1987). *Modelling the growth of a prograding delta.* Geological Survey of Canada Report 1624.

Calvert, S., & Pedersen, T. (2007). Elemental proxies for palaeoclimatic and palaeoceanographic variability in marine sediments: Interpretation and application. In C. Hillaire-Marcel, & A. de Vernal (Eds.), *Proxies in Late Cenozoic paleoceanography* (pp. 567-644). Montreal: Elsevier.

Cappelen, J., Jørgensen, B. V., Laursen, E. V., Stannius, L. S., & Thomsen, R. S. (2001). *The Observed Climate of Greenland, 1958-99 - with Climatological Standard Normals, 1961-90.* Copenhagen: Danish Meterological Institute.

Carter, L. (2012, 07 13). *Charting the seafloor: Multibeam echo sounding*. Retrieved from Te Ara – the Encyclopedia of New Zealand: www.TeAra.govt.nz/en/charting-the-sea-floor/page-4

Cattaneo, A., Babonneau, N., Déverchère, J., Domzig, A., Gaullier, V., Lepillier, B., . . . Yelles, K. (2010). Submarine landslides along the algerian margin: A review of their occurrence and potential link with tectonic structures. In D. C. Mosher, *Submarine mass movements and their consequences* (Vol. 28, pp. 515-525). Springer.

CIA. (2014). *The World Factbook*. Retrieved 05 16, 2014, from "Greenland": https://www.cia.gov/library/publications/the-world-factbook/geos/gl.html

Cowan, E. A., & Powell, R. D. (1991). Ice-proximal sediment accumulation rates in a temperate glacial fjord, southeastern Alaska. (J. B. Anderson, & G. M. Ashley, Eds.) *Glacial marine sedimentation: Paleoclimatic significance, 261*, pp. 61-74.

Croudace, I. W., Rindby, A., & Rothwell, G. (2006). ITRAX: description and evaluation of a new multi-function X-ray core scanner. In R. G. Rothwell, *New techniques in sediment core analysis* (Vol. 267, pp. 51-63). London: Geological Society, Special Publications.

Dahl-Jensen, D., Bamber, J., Bøggild, C., Buch, E., Christensen, J., Dethloff, K., . . . Veen, C. v. (2009). *The Greenland Ice Sheet in a Changing Climate: Snow, Water, Ice and Permafrost in the Arctic (SWIPA).* Oslo: Arctic Monitoring and Assessment Programme (AMAP).

Dahl-Jensen, D., Mosegard, K., Gundestrup, N., Clow, G., Johnsen, S. J., & Balling, A. W. (1998). Past temperatures directly from the Greenland Ice Sheet. *Science, 282*, 268-271.

Den Store Danske. (2014). *Den Store Danske; Gyldendals åbne encyklopædi*. Retrieved 05 16, 2014, from "Kejser Franz Joseph Fjord": http://www.denstoredanske.dk/Geografi_og_historie/Gr%C3%B8nland/Gr%C3%B8nl ands_geografi/Kejser_Franz_Joseph_Fjord

Denbigh, P. N. (1989). Swath Bathymetry: Principles of Operation and an Analysis of Errors. *IEEE Journal of Oceanic Engineering, 14*(4), 289-298.

Domack, E., & McClennen, C. (1996). Accumulation of glacial marine sediments in fjords of the Antarctic Peninsula and their use as late Holocene paleoenvironmental indicators. In R. Ross, E. Hofmann, L. Quetin, R. Ross, E. Hofmann, & L. Quetin (Eds.), *Foundations for ecological research west of the Antarctic Peninsula.* (Vol. 70, pp. 135-154). Antarctic Research Series.

Dowdeswell, J. A. (1987). Processes of glacimarine sedimentation. *Progress in Physical Geography, 11*, 52-90.

Dowdeswell, J. A., & Dowdeswell, E. K. (1989). Debris in icebergs and rates of glaci-marine sedimentation: observations from Spitsbergen and a simple model. *Journal of Geology, 97*, 221-231.

Dowdeswell, J. A., & Murray, T. (1990). Modelling rates of sedimentation from icebergs. *Geological Society, London, Special Publications, 53*, 121-137.

Dowdeswell, J. A., & Scourse, J. D. (1990). On the description and modelling of glacimarine sediments and sedimentation. *Geological Society, London, Special Publications, 53*, pp. 1-13.

Dowdeswell, J. A., Hagen, J. O., Bjørnsson, H., Glazovsky, A. H., Holmlund, P., Jania, J., . . . Thomas, B. (1997). The mass balance of circum-Arctic glaciers and recent climate change. *Quaternary Research, 48*, 1-14.

Dowdeswell, J. A., Whittington, R. J., & Marienfeld, P. (1994). The origin of massive diamicton facies by iceberg rafting and scouring, Scoresby Sund, East Greenland. *Sedimentology, 41*, 21-35.

Dwyer, J. (1995). Mapping tide-water glacier dynamics in East Greenland using Landsat data. *Journal of Glaciology, 41*(139), 584-595.

Elverhøi, A., Liestøl, O., & Nagy, J. (1980). Glacial erosion, sedimentation and microfauna in the inner part of Kongsfjorden, Spitsbergen. *Norsk Polarinstitutt Skrifter, 172*, 33-58.

Elverhøi, A., Lønne, Ø., & Seland, R. (1983). Glaciomarine sedimentation in a modern fjord environment, Spitsbergen. *Polar Research, 1*, 127-149.

Erez, J. (1978). Vital effect on stable-isotope composition seen in foraminifera and coral skeletons. *Nature, 273*, 199-202.

Evans, J., Dowdeswell, J., Grobe, H., Niessen, F., Stein, R., Hubberten, H.-W., & Whittington, R. (2002). Late Quaternary sedimentation in Kejser Franz Joseph Fjord and the continental margin of East Greenland. *Geological Society, London, Special Publications*, 149-179.

Evans, J., Ó Cofaigh, C., Dowdeswell, J., & Wadhams, P. (2009). Marine geophysical evidence for former expansion and flow of the Greenland Ice Sheet across the northeast Greenland continental shelf. *Journal of Quaternary Science, 24*(3), 279-293.

Farmer, D. M., & Freeland, H. J. (1983). The Physical Oceanography of Fjords. *Progress in Oceanography, 12*(2), 147-194.

Farmer, D. M., & Freeland, H. J. (1983). The Physical Oceanography of Fjords. *Progress in Oceanography, 12*(2), 147-194.

Foldvik, A., Aagaard, K., & Torresen, T. (1988). On the velocity field of the East Greenland Current. *Deep-Sea Research, 35*, 1335-1354.

Folk, R. (1954). The distinction between grain size and mineral composition in sedimentary-rock nomenclature. *The Journal of Geology, 62*(4), 344-359.

Forsberg, C. F., Solheim, A., & Kvalstad, T. J. (2007). Slope instability and mass transport deposits on the Godavari river delta, east indian margin form a regional geological perspective. In V. Lykousis, D. Sakellariou, & J. Locat, *Submarine mass movementsand their consequences* (pp. 19-28). Springer.

Forwick, M. (2001). Development of the sedimentary environment in Balsfjord (northern Norway). *Cand. scient. thesis in geology*. Department of Geology, University of Tromsø.

Forwick, M. (2013a). *How to use XRF core scanner data aquired with the Aavatech XRF core scanner at the Department of Geology, University of Tromsø.* Tromsø: Department of Geology.

Forwick, M. (2013b). Fjords. *GEO-3121 Marine Geology*. Department of Geology, University of Tromsø.

Forwick, M., & Vorren, T. O. (2002). Deglaciation history and post-glacial mass movements in Balsfjord, northern Norway. *Polar Research, 21*(2), 259-266.

Forwick, M., & Vorren, T. O. (2007). Holocene mass-transport activity and climate in outer Isfjorden, Spitsebergen: marine and subsurface evidence. *The Holocene, 17*(6), 707-716.

Forwick, M., & Vorren, T. O. (2009). Late Weichselian and Holocene sedimentary environments and ice rafting in Isfjorden, Spitsbergen. *Palaeogeography, Palaeoclimatology, Palaeoecology, 280*, 258-274.

Forwick, M., & Vorren, T. O. (2011). Mass wasting in Isfjorden, Spitsbergen. In Y. Yamada, K. Kawamura, K. Ikehara, Y. Ogawa, R. Urgeles, D. Mosher, . . . M. Strasser, *Submarine mass movements and their consequences. Advances in Natural and Technological Hazards Research* (Vol. 31, pp. 711-722). New York: Springer-Verlag.

Fujifilm. (2014). *Fujifilm Technical Handbook: The Fundamentals of Industrial Radiography.* Tokyo: Fujifilm Corporation.

Funder, S. (1989). Quaternary geology of the ice free areas and adjacent shelves of Greenland. In R. J. Fulton, *Quaternary Geology of Canada and Greenland* (pp. 743-792). Toronto: Geological Survey of Canada.

Funder, S., & Hansen, L. (1996). The Greenland Ice Sheet: a model for its culmination and decay during and after the last glacial maximum. *Bulletin of the Geological Society of Denmark, 42*, 137-152.

Funder, S., Hjort, C., Landvik, J., Nam, S.-I., Reeh, N., & Stein, R. (1998). History of a stable ice margin - East Greenland during middle and upper Pleistocene. *Quaternary Science Reviews, 17*, 77-123.

Funder, S., Jennings, A., & Kelly, M. (2004). Middle and late Quaternary glacial limits in Greenland. In J. Ehlers, & P. Gibbard, *Quaternary glaciations - extent and chronology II* (pp. 425-430). Amsterdam: Elsevier.

Funder, S., Kjeldsen, K. K., Kjær, K. H., & Cofaigh, C. Ò. (2011). The Greenland Ice Sheet During the Past 300,000 Years: A Review. *Quaternary Science Reviews*, 699-713.

GEOTEK. (2000). *Geotek Multi-Sensor Core Logger (MSCL) Manual.*

GEOTEK. (2014a). Retrieved 05 13, 2014, from "Manual; Multi-Sensor Core Logger": http://www.geotek.co.uk/sites/default/files/MSCLmanual.pdf

GEOTEK. (2014b). *"GEOTEK X-ray Core Imaging with CT MSCL-XCT: Linear images & 3D reconstruction of sediment and rock cores*. Retrieved 05 14, 2014, from http://www.geotek.co.uk/sites/default/files/Geotek_MSCL-XCT.pdf

GEUS. (2003, 06 20). *Geological Survey of Denmark and Greenland - GEUS*. Retrieved 05 16, 2014, from "Geological map of Greenland 1 : 2 500 000": http://www.geus.dk/program-areas/raw-materials-greenl-map/greenland/gr-map/anhstart-uk.htm

Gingras, M. K., Pemberton, S. G., & Smith, M. (2015). Bioturbation: Reworking of sediments for better or worse. *Oilfield Review, 26*(4), pp. 46-58.

Gregory, J. M., Huybrechts, P., & Raper, S. C. (2004). Climatology: Threatened loss of the Greenland ice-sheet. *Nature, 428*(6983), 616.

Grossmann, E. L. (1987). Stable isotopes in modern benthic foraminifera: a study of vital effects. *Journal of Foraminifera Research, 17*(1), 48-61.

Hald, M., Ebbesen, H., Forwick, M., Godtliebsen, F., Khomenko, L., Korsun, S., . . . Vorren, T. O. (2004). Holocene paleoceanography and glacial history of the West Spitsbergen area, Euro-Arctic margin. *Quaternary Science Reviews, 23*, 2075-2088.

Hambrey, M. (1994). *Glacial Environments.* London: UCL Press.

Hampton, M., Lee, H., & Locat, J. (1996). Submarine landslides. *Reviews of Geophysics, 34*(1), 33-59.

Hanna, E., Huybrechts, P., Janssens, I., Cappelen, J., Steffen, K., & Stephens, A. (2005). Runoff and mass balance of the Greenland ice sheet: 1958—2003. *Journal of Geophysical Research, 110*.

Hansen, L. (2004). Deltaic infill of a deglaciated arctic fjord, East Greenland: Sedimentray facies and sequence stratigraphy. *Journal of sedimentary research, 74*(3), 422-437.

Hansen, L., Funder, S., Murray, A., & Mejdahl, V. (1999). Luminescence dating of the last Weichselian Glacier advance in East Greenland. *Quaternary Geochronology, 18*, 179-190.

Hass, H., Kuhn, G., Monien, P., Brumsack, H.-J., & Forwick, M. (2010). Climate fluctuations during the past two millennia as recorded in sediments from Maxwell Bay, South Shetland Islands, West Antarctica. *Geological Society, Special Publications, 344*, 243-260.

Heling, D. (1974). Investigations on recent sediments in the Fiskenæset region, southern West Grenland. *Rapport Grønlands Geologiske Undersøgelse, 65*, 66-68.

Hennekam, R., & de Lange, G. (2012). X-ray fluorescence core scanning of wet marine sediments:methods to improve quality and reproducibility of high-resolution paleoenvironmental records. *Limnology and Oceanography: Methods, 10*, 991-1003.

Henriksen, N. (2008). *Geological History of Greenland - Four billion years of earth evolution.* Copenhagen: Geological Survey of Denmark and Greenland (GEUS).

Henriksen, N., Higgins, A., Kalsbeek, F., & Pulvertaft, T. C. (2000). Greenland from Archaen to Quaternary; Descriptive text to the Geological map of Greenland. 1:2 500 000. *Geology of Greenland Survey Bulletin, 185*.

Higgins, A., Elvevold, S., Escher, J., Frederiksen, K., Gilotti, J., Henriksen, N., . . . Watt, G. (2004). The foreland-propagating thrust architecture of the East Greenland Caledonides 72˚-75˚. *Journal of the Geological Society, 161*, 1009-1026.

Higgins, A., Leslie, A., & Smith, M. (2001). Neoproterozoic–Lower Palaeozoic stratigraphical relationships in the marginal thin-skinned thrust belt of the East Greenland Caledonides: comparisons with the foreland in Scotland. *Geological Magazine, 138*(2), 143-160.

Higham, T., Ramsey, C., Hogg, A., Petchey, F., & Cresswell, R. (2014, 10 30). *Accelerator mass spectrometry (AMS) measurement*, 149. Retrieved 11 20, 2014, from Radiocarbon Web-Info: https://c14.arch.ox.ac.uk/embed.php?File=ams.html

Hjort, C. (1973). A sea correction for East Greenland. *GFF, 95*(1), 132-134.

Hjort, C. (1997). Glaciation, climate history, changing marine levels and the evolution of the Northeast Water Polynya. *Journal of marine systems, 10*, 23-33.

Hogan, K., Dix, J., Lloyd, J., Long, A., & Cotterill, C. (2011). Seismic stratigraphy records the deglacial history of Jakobshavn Isbræ, West Greenland. *Journal of Quaternary science, 26*(7), 757-766.

Hogan, K., Dowdeswell, J., & Ó Cofaigh, C. (2012). Glacimarine sedimentary processes and depositional environments in an embayment fed by West Greenland ice streams. *Marine Geology, 311-314*, 1-16.

Hopkins, T. S. (1991). The GIN Sea - A synthesis of its physical oceanography and literature review 1972-1985. *Earth-Science Reviews, 30*, 175-318.

Howe, J., Austin, W., Forwick, M., Paetzel, M., Harland, R., & Cage, A. (2010). Fjord systems and archives: a review. In J. Howe, Austin, W.E.N., M. Forwick, & M. Paetzel, *Fjord Systems and Archives* (Vol. 344, pp. 5-15). London: Special Publications.

Hubberten, H., Grobe, H., Jokat, W., Melles, M., Niessen, F., & Stein, R. (1995). Glacial history of East Greenland explored. *EOS, Transactions American Geophysical Union, 76*(36), 353-356.

Håkansson, S. (1973). University of Lund Radiocarbon dates VI. *Radiocarbon, 15*(3), 493-513.

Jakobsen, B. H. (2009). Holocene climate change and environmental reconstruction in East Greenland. *IOP Conf. Series: Earth and Environmental Science*, *6*.

Jakobsen, B., Fredskild, B., & Pedersen, J. (2008). Holocene changes in climate and vegetation in the Ammassalik area, East Greenland, recorded in lake sediments and soil profiles. *Geologisk Tidsskrift - Danish Journal of Geography, 108*(1), 21-50.

Jennings, A. E., & Weiner, N. J. (1996). Environmental change in eastern Greenland during the last 1300 years: evidence from foraminifera and lithofacies in Nansen Fjord, 68N. *The Holocene, 6*(2), 179-191.

Jennings, A. E., Knudsen, K. L., Hald, M., Hansen, C. V., & Andrews, J. T. (2002). A mid-Holocene shift in Arctic sea-ice variability on the East Greenland Shelf. *The Holocene, 12*(1), 49-58.

Jessen, S. P., Rasmussen, T. L., Nielsen, T., & Solheim, A. (2010). A new Late Weichselian and Holocene marine chronology for the western Svalbard slope 30,000-0 cal years BP. *Quaternary Science Reviews, 29*, 1301-1312.

Johnsen, S., Clausen, H., Dansgaard, W., Gundestrup, N., Hansson, M., Jonsson, P., . . . Sveinbjørnsdottir, A. (1992). A "deep" ice core from East Greenland. Meddelelser om Grønland. *Geoscience, 29*, 3-22.

Kempf, P., Forwick, M., Laberg, J.-S., & Vorren, T. O. (2013). Late Weichselian and Holocene sedimentary palaeoenvironment and glacial activity in the high-arctic van Keulenfjorden, Spitsbergen. *The Holocene, 23*(11), 1607-1618.

Kneller, B. (1995). Beyond the turbidite paradigm: physical models for deposition of turbidites and their implications for reservoir prediction. In A. J. Hartley, & D. J. Prosser, *Characterization of Deep Marine Clastic Systems* (Vol. 94, pp. 31-49). Geological Society Special Publications.

Kneller, B., & Buckee, C. (2000). The structure and fluid mechanics of turbidity currents: a review of some recent stuudies and their geological implications. *Sedimentology, 41*(1), 62-94.

Kneller, B., & McCaffrey, W. (2003). The interpretation of vertical sequences in turbidite beds: the influence of longitudinal flow structure. *Journal of sedimentary research, 73*(5), 706-713.

Kongsberg Maritime. (2003). *EM 300: 30 kHz multibeam echo sounder for depths reaching 5000 meters.* Horten: Kongsberg Maritime AS.

Laberg, J.-S., & Vorren, T. O. (1995). Late Weichselian submarine debris flow deposits on the Bear Island Trough Mouth Fan. *Marine Geology, 127*, 45-72.

Landvik, J. (1994). The last glaciation of Germania Land and adjacent areas, northeast Greenland. *Journal of Quaternary Science, 9*(1), 81-92.

Lee, H. J. (1985). State of art: Laboratory stermination of the strength of marine soils. In R. C. Chaney, & K. R. Demars, *Strength testing of marine sediments: Laboratory and in-situ measurements ASTM STP 883* (pp. 182-250). Philadelphia: American Society for Testing and Materials.

Lee, H., & Clausner, J. (1979). *Seafloor soil sampling and geotechnical parameter determination - Handbook: Technical Report R873.* Civil Engineering Laboratory, Naval Construction Battalion Center, Port Hueneme, CA.

Lee, H., Locat, J., Desagnés, P., Parsons, J. D., McAdoo, G., B., . . . Boulanger, E. (2007). Submarine mass movements on continental margins. In C. A. Nittrouer, J. A. Austin, M. E. Field, J. H. Kravitz, P. M. Syvitski, & P. L. Wiberg, *Continental margin sedimentation: from sediment transport to sequence stratigraphy* (Vol. 37). Blackwell Publishing.

Leeder, M. (2011). *Sedimentology and sedimentary basins; From tubulence to tectonics* (2nd ed.). Wiley-Blackwell.

Levy, L., Kelly, M., Lowell, T., Hall, B., Hempel, L., Honsaker, W., . . . Axford, Y. (2014). Holocene fluctuations of Bregne ice cap, Scoresby Sund, east Greenland: a proxy for climate along the Greenland Ice Sheet margin. *Quaternary Sciene Reviews, 92*, 357-368.

Lowe, J., & Walker, M. (1997). *Reconstructing Quaternary Environments* (2nd ed.). Routledge.

Lønne, I., & Nemec, W. (2004). High-arctic fan delta recording deglaciation and environment disequilibrium. *Sedimentology, 51*, 553-589.

Løseth, T. M. (1999). *Submarine massflow sedimentation: computer modelling and basin-fill stratigraphy.* Springer.

Mangerud, J. (1972). Radiocarbon dating of marine shells, including a discussion of apparent age of Recent shells from Norway. *Boreas, 1*, 143-172.

Mangerud, J., & landvik, J. Y. (2007). Younger Dryas cirque glaciers in western Spitsbergen: smaller than during the Little Ice Age. *Boreas, 36*, 278-285.

Mann, M. E. (2002). Little Ice Age. In M. C. MacCracken, & J. S. Perry, *Encyclopedia of Global Environmental Change, Volume 1, The Earth system: physical and chemical dimensions of global environmental change* (pp. 504-509). John Wiley & Sons.

Mann, M. E., Bradley, R. S., & Hughes, M. K. (1998). Global-scale temperature patterns and climate forcing over the past six centuries. *Nature, 392*, 779-787.

Marienfeld, P. (1991). 14C-dates of glacimarine sediments from Scoresby Sund, East Greenland. In P. Möller, C. Hjort, & O. Ingólfsson, *The last interglacial-glacial cycle: Preliminary report on the PONAM fieldwork in Jameson Land and Scoresby Sund* (Vol. 33, pp. 165-168). LUNDUAQ Report.

Marienfeld, P. (1992). Postglacial sedimentary history of Scoresby Sund, East Greenland. *Polarforschung, 60*, 181-195.

Marum. (2013a, 06 19). *Marum; Center for Marine Environmental Science*. Retrieved 05 13, 2014, from "Multi-sensor core logger (MSCL)": https://www.marum.de/en/Multi-sensor_core_logger_MSCL.html#Section3742

Marum. (2013b, 09 26). *Marum; Center for Marine Environmental Science*. Retrieved 05 12, 2014, from "XRF Core Scanner": http://www.marum.de/en/XRF_Core_Scanner.html

McKee, B. A., Nittrouer, C., & DeMaster, D. J. (1983). Concepts of sediment deposition and accumulation applied to the continental shelf near the mouth of the Yangtze River. *Geology, 11*, 631-633.

McLennan, S. M., Bock, B., Hemming, S. R., Hurowitz, J. A., Lev, S. M., & K., M. D. (2003). The roles of provenance and sedimentary processes in the geochemistry of sedimentary rocks. In D. R. Lentz, *Geochemistry of Sediments and Sedimentary Rocks: Evolution Considerations to Mineral Deposit-Forming Environments* (pp. 7-38). St. John`s, Newfoundland: Geological Association of Canada, Geotext 4.

Meiburg, E., & Kneller, B. (2010). Turbidty currents and their deopsits. *Annual review of fluid mechanics, 42*, 135-156.

Menzies, J. (1995). Glaciers and ice sheets. In J. Menzies, *Modern glacial environments: Processes, dynamics and sediments* (pp. 101-138). Butterworth-Heinemann.

Mohrig, D., Whipple, K., Hondzo, M., Ellis, C., & Parker, G. (1998). Hydroplaning of subaqueous debris flows. *The Geological Society of America Bulletin, 110*(3), 387-394.

Moon, T., Joughin, I., Smith, B., & Howat, I. (2012). 21st-Century Evolution of Greenland Outlet Glacier Velocities. *Science, 336*, 576-578.

Morton, R. A., & White, W. A. (1997). Characteristics of and corrections for core shortening in unconsolidated sediments. *Journal of Coastal Research, 13*(3), 761-769.

Mosher, D. C., & Simpkin, P. G. (1999). Enironmental Marine Geoscience 1. Status and Trends of Marine High-Resolution Seismic Profiling: Data Aquisition. *Geoscience Canada, 26*(4), 174-188.

Mulder, T. (2011). Gravity processes and deposits on continental slope, rise and abyssal plains. In H. Hüneke, & T. Mulder, *Deep-sea sediments* (pp. 25-148). Amsterdam: Elsevier.

Mulder, T., & Alexander, J. (2001). The physical character of subaqueous sedimentary density flows and their deposits. *Sedimentology, 48*, 269-299.

Nardin, T. R., Hein, F. J., Gorsline, D. S., & Edwards, B. D. (1979). A review of mass movement processes, sediment and acoustic characteristics, and contrasts in slope and base-of-slope systems v. Canyon-fan-basin floor systems. *Society of Economic Palaeontologists and Mineralogists Special Publication, 27*, 61-73.

Nelson, C., Escutia, C., Damuth, J., & Twichell, D. (2011). Interplay of mass-transport and turbidite-system deposits in different active tectonic and passive continental margin settings: external and local controlling factors. *Mass-transport deposits in deepwater settings. SEPM Spec Publ, 96*, pp. 39-66.

Nemec, W. (1990). Aspects of sediment movement on steep delta slopes. *Coarse-grained deltas*, 29-73.

Nichols, G. (2009). *Sedimentology and stratigraphy* (2nd ed.). Wiley-Blackwell.

Nielsen, T., & Andersen, C. (2002). Plankton community structure and production along a freshwater-influenced Norwegian fjord system. *Marine Biology, 141*, 707-724.

Ó Cofaigh, C., & Dowdeswell, J. A. (2001). Laminated sediments in glacimarine environments: diagnostic criteriea for their interpretation. *Quaternary Science Reviews, 20*, 1411-1436.

Ó Cofaigh, C., Dowdeswell, J. A., & Grobe, H. (2001). Holocene glacimarine sedimentation, inner Scoresby Sund, East Greenland: the influence of fast-flowing ice-sheet outlet glaciers. *Marine Geology, 175*, 103-129.

Ó Cofaigh, C., Dowdeswell, J., Evans, J., Kenyon, N., Taylor, J., Mienert, J., & Wilken, M. (2004). Timing and significance of glacially influenced mass-wasting in the submarine channels of the Greenland Basin. *Marine Geology, 207*, 39-54.

Ohmura, A., & Reeh, N. (1991). New precipitation and accumulation maps for Greenland. *Journal of Glaciology, 37*(125), 140-148.

Ottesen, D., & Dowdeswell, J. (2006). Assemblages of submarine landforms produced by tidewater glaciers in Svalbard. *Journal of geophysical research, 111*(F1).

Pickrill, R., & Barnes, P. (2003). Managing the seabed with multibeam mapping: learning from Canadian experience. *Water & Atmorphere, 11*, 7-9.

Pittauerova, D. (2009, July 6). *Sediment chronology using 210Pb and 137Cs.* Retrieved April 29, 2015, from Alfred-Wegener-Institut: Helmholtz-zentrum für polar- und meeresforschung: http://www.awi.de/fileadmin/user_upload/Research/Research_Divisions/Climate_Scie nces/Paleoclimate_Dynamics/Modelling/Lessons/Blockseminar_2009/Daniela_Pittaue rova.pdf

Plassen, L., & Vorren, T. O. (2002). Late Weichselian and Holocene sediment flux and sedimentation rates in Andfjord and Vågsfjord, North Norway. *Journal of Quaternary Science, 17*(2), 161-180.

Plassen, L., & Vorren, T. O. (2003). Sedimentary processes and the environment during deglaciation of a fjord basin in Ullsfjorden, North Norway. *Norwegian Journal of Geology, 83*, 23-36.

Plassen, L., Vorren, T. O., & Forwick, M. (2004). Integrated acoustic and coring investigation of glacigenic deposits in Spitsbergen fjords. *Polar Research, 23*(1), 89-110.

Powell, R. D. (1991). Grounding-line systems as second-order controls on fluctuations of tidewater termini of temperate glaciers. *Geological Society of America Special Papers, 261*, 75-94.

Powell, R. D. (2003). Subaquatic Landsystems; Fjords. In D. Evans, & L. Gooster, *Glacial Landsystems.* Routledge.

Powell, R., & Domack, E. (1995). Modern glaciomarine environments. In J. Menzies, *Modern glacial environments: Processes, dynamics and sediments* (pp. 445-486). Butterworth-Heinemann.

Prior, D., & Bornhold, B. (1990). The underwater development of Holocene fan deltas. In A. Colella, & D. Prior, *Coarse-grained deltas* (pp. 75-90).

Prior, D., Bornhold, B., & Johns, M. (1984). Depositional characteristics of a submarine debris flow. *The Journal of Geology, 92*(6), 707-727.

Quinn, R., Bull, J. M., & Dix, J. K. (1998). Optimal Processing of Marine High-Resolution Seismic Reflection (Chirp). *Marine Geophysical Researches, 20*, 13-20.

Reeh, N. (1985). Greenland Ice-Sheet mass balance and sea-level change. In *Report DOE/EV/60235-1 Glaciers, ice sheets and sea level: Effect of a CO2-induced climatic change* (pp. 155-171). Washington D.C.

Reeh, N., Mayer, C., Miller, H., Thomsen, H., & Weidick, A. (1999). Present and past climate control on fjord glaciations in Greenland: Implications for IRD-deposition in the sea. *Geophysical Research Letters, 20*(8), 1039-1042.

Reimer, P. J., Bard, E., Bayliss, A., Beck, W. J., Blackwell, P., Ramsey, C. B., . . . Hogg, A. (2013). INTCAL13 and MARINE13 radiocarbon age calibration curves 0-50 000 years cal BP. *Radiocarbon, 55*(4), 1869-1887.

Robbins, J. A., & Edgington, D. N. (1975). Determination of recent sedimentation in Lake Michigan using Pb-210 and Cs-137. *Geochim. Cosmochim. Acta, 39*, 285-304.

Rothwell, R., Hoogakker, B., Thomson, J., Croudace, I., & Frenz, M. (2006). Turbidite emplacement on the southern Balearic Abyssal Plain (western Mediterranean Sea) during Marine Isotope Stages 1-3: an application of ITRAX XRF scanning of sediment cores to lithostratigraphic analysis. In R. Rothwell, *New techniques in sediment core analysis* (Vol. 267, pp. 79-98). London: Geological Society.

Sakuna, D., Szczuciński, W., Feldens, P., Schwarzer, K., & Khokiattiwong, S. (2012). Sedimentary deposits left by the 2004 Indian Ocean tsunami on the inner continental shelf offshore of Khao Lak, Andaman Sea (Thailand). *Earth Planets Space, 64*, 931-943.

Schad, L. (2008, 09 12). *Physics of Imaging Systems Basic Prinsiples of X-Ray Diagnostic I [PowerPoint Slides]*. Retrieved 05 14, 2014, from http://www.umm.uni-heidelberg.de/inst/cbtm/ckm/lehre/techniquesofimagingsystems/2_medphys_roen_1_2sw.pdf

Schock, S. G., LeBlanc, L. R., & Mayer, L. A. (1989). Chirp subbottom profiler for quantitative sediment analysis. *Geophysics*, 445-450.

Seale, A., Christoffersen, P., Mugford, R. I., & O´Leary, M. (2011). Ocean forcing of the Greenland Ice Sheet: Calving fronts and patterns of retreat identified by automatic satellite monitoring of eastern outlet glaciers. *Journal of Geophysical Reseach, 116*.

Shanmugam, G. (1997). The Bouma Sequence and the turbidite mind set. *Earth-Science Reviews, 42*, 201-229.

Simpson, M. J., Milne, G., Huybrechts, P., & Long, A. (2009). Calibrating a glaciological model of the Greenland ice sheet from the Last Glacial Maximum to present-day using field observations of relative sea level and ice extent. *Quaternary Science Reviews, 28*, 1631-1657.

Smith, L. M., & Andrews, J. T. (2000). Sediment characteristics in iceberg dominated fjords, Kangerlussuaq region, East Greenland. *Sedimebtray Geology*, 11-25.

St.John, K., Passchier, S., Tantillo, B., Darby, D., & Kearns, L. (2015). Microfeatures of modern sea-ice rafted sediment and implications for paleo-sea-ice reconstructions. *Annals of Glaciology, 56*(69), 83-93.

Stigebrandt, A. (1976). Vertical Diffusion Driven by Internal Waves in a Sill Fjord. *Journal of Physical Oceanography, 6*, 486-495.

Stoker, M. S., Wilson, C. R., Howe, J., Bradwell, T., & Long, D. (2010). Paraglacial slope instability on Scottish fjords: examples from Little Loch Broom, NW Scotland. In J. A. Howe, W. E. Austin, & M. Forwick, *Fjord systems and archives* (Vol. 344, pp. 225-242). London: Geological Society Special Publication.

Stoner, J., Channell, J., & Hillaire-Marcel, C. (1996). The magnetic signature of rapidly deposited detrital layers from the deep Labrador Sea: Relationship to North Atlantic Heinrich layers. *Paleoceanography, 11*(3), 309-325.

Stuvier, M., Reimer, P., & Reimer, R. (2015, April 09). *CALIB Radiocarbon Calibration*. Retrieved from Marine Reservoir Correction Database: http://calib.qub.ac.uk/calib/

Suckow, A. (2014). *210Pb Dating of Sediments*. Retrieved November 19, 2014, from Leibniz Institute for Applied Geophysics: http://www.liag-hannover.de/fileadmin/user_upload/pix/Geochronologie_Isotopenhydrologie/allgemeines/Principles_210Pb.pdf

Svendsen, J. I., & Mangerud, J. (1997). Holocene glacial and climatic variations on Spitsbergen, Svalbard. *The Holocene, 7*(1), 45-57.

Syvitski, J. (1989). On the deposition of sediment within glacier-influenced fjords: Oceanographic controls. *Marine Geology*, 301-329.

Syvitski, J. P., & Shaw, J. (1995). Sedimentology and geomorphology of fjords. In G. M. Perillo, *Geomorphology and sedimentology of estuaries. Developments in Sedimentology* (Vol. 53, pp. 113-178). Amsterdam: Elsevier.

Syvitski, J. P., Andrews, J. T., & Dowdeswell, J. A. (1996). Sediment deposition in an iceberg-dominated glacimarine environment, East Greenland: basin fill implications. *Global and Planetary Change, 12*, 251-270.

Syvitski, J., Burrell, D., & Skei, J. (1987). *Fjords: Processes and Products.* New York: Springer Verlag.

Szczuciński, W. (2015). *The preliminary assessment of sediment accumulation rates in core HH13-008-GC-TUNU and HH13-012-GC-TUNU from Kejser Franz Joseph Fjord system.* Adam Mickiewicz University, Institute of Geology, Poznań, Poland.

Szczuciński, W., Stattegger, K., & Scholten, J. (2009). Modern sediments and sediment accumulation rates on the narrow shelf off central Vietnam, South China Sea. *Geo-Marine Letters, 29*(1), 47-59.

Telford, R. J., Heegaard, E., & Birks, H. J. (2004). All age-depth models are wrong: but how badly? *Quaternary Science Reviews, 23*, 1-5.

Tjallingii, R., Röhl, U., Kölling, M., & Bickert, T. (2007). Influence of the water content on X-ray fluorescence core-scanning measurements in soft marine sediments. *Geochemistry, Geophysics, Geosystems, 8*(2), 1-12.

Udden, J. (1914). Mechanical composition of clastic sediments. *The Geological Society of America Bulletin, 25*, 543-548.

Vorren, T. O., Hald, M., Edvardsen, M., & Lind-Hansen, O. (1983). Glacigenic sediments and sedimentary environments on continental shelves: General principles with a case study from the Norwegian shelf. In J. Ehlers, *Glacial deposits in north-west Europe* (pp. 61-73). Rotterdam: Balkema.

Wacker, L., Lippold, J., Molnár, M., & Schulz, H. (2013). Towards radiocarbon dating of single foraminifera with a gas ion source. *Nuclear Instruments and Methods in Physics Research B, 294*, 307-310.

Wagner, B., Bennike, O., Cremer, H., & Klug, M. (2010). Late Quaternary history of the Kap Mackenzie area, northeast Greenland. *Boreas, 39*, 492-504.

Wagner, B., Melles, M., Hahne, J., Niessen, F., & Hubberten, H.-W. (2000). Holocene climate history of Geographical Society Ø, East Greenland — evidence from lake sediments. *Palaeogeography, Palaeoclimatology, Palaeoecology, 160*, 45-68.

Wassmann, P., Svendsen, H., Keck, A., & Reigstad, M. (1996). Selected aspects of the physical oceanography and particle flux in fjords of northern Norway. *Journal of Marine Systems, 8*, 53-71.

Watts, A. (2010). *Greenland glaciers – melt due to sea current change, not air temperature.* Retrieved October 09, 2014, from Watts Up With That?: http://wattsupwiththat.com/2010/02/16/greenland-glaciers-melt-due-to-sea-current-change-not-air-temperature/

Weidick, A. (1993). Neoglacial change of ice cover and related response of the Earth´s crust in West Greenland. *Grønlands Geologiske Undersøgelse Rapport, 159*, 121-126.

Weidick, A. (1995). Landsat Images of Greenland. In R. S. Williams, & J. G. Ferrigno, *Greenland; Satellite Image Atlas of Glaciers of the World. U.S. Geological Survey Professional Paper* (Vols. 1386-C). Washington: U.S. Government Printing Office.

Weidick, A., & Bennike, O. (2007). Quaternary glaciation history and glaciology of Jakobshavn Isbræ and the Disko Bugt region, West Greenland: a review. *Geological Survey of Denmark and Greenland Bulletin, 14*, p. 78.

Weltje, G. J., & Tjallingii, R. (2008). Calibration of XRF core scanners for quantitative geochemical logging of sediment cores: Theory and application. *Earth and Planetary Science Letters, 274*, 423-438.

Wentworth, C. (1922). A scale of grade and class terms for clastic sediments. *Journal of Geology, 30*, 377-392.

Wilken, M., & Mienert, J. (2006). Submarine glacigenic debris flows, deep-sea channels and past ice-stream behaviour of the East Greenland continental margin. *Quaternary Science Reviews, 25*, 784-810.

Winkelmann, D., Jokat, W., Jensen, L., & Schenke, H.-W. (2010). Submarine end moraines on the continental shelf off NE Greenland - Implications for Lateglacial dynamics. *Quaternary Science Reviews, 29*, 1069-1077.